

**Spectroscopic and functional investigations of the
[FeFe]-hydrogenase from *Chlamydomonas
reinhardtii* and its natural electron donor**

Inaugural-Dissertation

zur Erlangung des Doktorgrades
der Mathematisch-Naturwissenschaftlichen Fakultät
der Heinrich-Heine-Universität Düsseldorf

vorgelegt von

JUDITH FRIEDERIKE SIEBEL

aus Karlsruhe

Düsseldorf, April 2015

erstellt am Max-Planck-Institut für Chemische Energiekonversion
in Mülheim an der Ruhr

Gedruckt mit der Genehmigung der
Mathematisch-Naturwissenschaftlichen Fakultät der
Heinrich-Heine-Universität Düsseldorf

Referent: Prof. Dr. Wolfgang Lubitz

Korreferent: Prof. Dr. Karl-Erich Jaeger

Tag der mündlichen Prüfung: 8. Juni 2015

TABLE OF CONTENTS

ABBREVIATIONS.....	1
DECLARATION.....	2
LIST OF PUBLICATIONS.....	3
ABSTRACT.....	5
ZUSAMMENFASSUNG.....	6
1 INTRODUCTION	7
1.1 The energy problem.....	7
1.1.1 General.....	7
1.1.2 The hydrogen issue.....	7
1.2 Hydrogenases.....	9
1.2.1 General.....	9
1.2.2 [FeFe]-hydrogenases.....	10
1.2.3 [FeFe]-hydrogenases in green algae.....	12
1.2.4 HydA1 – the [FeFe]-hydrogenase from <i>Chlamydomonas reinhardtii</i>	13
1.3 Artificial maturation of hydrogenases.....	15
1.3.1 [FeFe]-hydrogenase model complexes.....	15
1.3.2 Artificial maturation assisted by HydF.....	16
1.3.3 Unassisted artificial maturation.....	17
1.4 Aim and outline of the research.....	19
2 APPLIED METHODS	21
2.1 Heterologous protein overexpression and purification.....	21
2.2 H ₂ conversion activity measurements.....	23
2.3 Infrared spectroscopy.....	24
2.3.1 Basic concepts.....	24
2.3.2 Infrared spectroscopy on proteins.....	24
2.4 Magnetic resonance spectroscopy.....	26
2.4.1 Basic concepts.....	26
2.4.2 Nuclear magnetic resonance spectroscopy.....	28

2.4.2.1	General	28
2.4.2.2	2D NMR.....	29
2.4.2.3	3D NMR.....	30
2.4.2.4	Applications	31
2.4.3	Electron paramagnetic resonance spectroscopy	32
2.5	Mössbauer spectroscopy	34
2.5.1	Basic concepts	34
2.5.2	⁵⁷ Fe Mössbauer spectroscopy.....	36
2.5.3	The Mössbauer spectrum	36
3	SUMMARY OF JOURNAL ARTICLES	39
3.1	Paper I.....	39
3.2	Paper II.....	41
3.3	Paper III	43
3.4	Paper IV	45
4	JOURNAL ARTICLES.....	47
4.1	Paper I.....	47
4.1.1	Journal article	48
4.1.2	Supporting information	58
4.2	Paper II.....	75
4.2.1	Journal article	76
4.2.2	Supporting information	82
4.3	Paper III	93
4.3.1	Journal article	94
4.3.2	Supporting information	101
4.4	Paper IV	111
4.4.1	Journal article	112
4.4.2	Supporting information	120
5	CONCLUSIONS & OUTLOOK	133
6	REFERENCES	137
7	ACKNOWLEDGEMENTS	143

ABBREVIATIONS

adt	azadithiolate, [(SCH ₂) ₂ NH] ²⁻	HYSCORE	hyperfine sublevel correlation
<i>C. reinhardtii</i>	<i>Chlamydomonas reinhardtii</i>	IPTG	isopropyl β-D-1-thiogalacto- pyranoside
COSY	correlation spectroscopy	NADP ⁺	nicotinamide adenine dinucleotide phosphate
CW	continuous wave	NMR	nuclear magnetic resonance
DFT	density functional theory	NOESY	nuclear Overhauser and exchange spectroscopy
DNA	deoxyribonucleic acid	NRVS	nuclear resonance vibrational spectroscopy
<i>E. coli</i>	<i>Escherichia coli</i>	PRE	paramagnetic relaxation enhancement
ENDOR	electron nuclear double resonance	PetF	photosynthetic electron transport ferredoxin
EPR	electron paramagnetic resonance	SAM	S-adenosyl-L-methionine
FNR	ferredoxin-NADP ⁺ - oxidoreductase	tRNA	transfer ribonucleic acid
FTIR	Fourier transform infrared	TOCSY	total correlation spectroscopy
HABA	2-(4-hydroxyphenylazo)- benzoic acid	UV/Vis	ultraviolet-visible
H ₄ MPT	tetrahydromethanopterin	wt	wild-type
HSQC	heteronuclear single quantum coherence		

DECLARATION

I, Judith Siebel, declare that this thesis and the work presented herein has been generated by myself. Contributions of others have been made clear when the work has been done jointly with others. All sources and references that I used are given. Parts of the thesis are already published (see “List of Publications”).

Hiermit erkläre ich, Judith Siebel, dass die vorliegende Arbeit und die darin präsentierten Ergebnisse von mir selbst erstellt wurden. Der Beitrag anderer in Teilen der Arbeit, die in Zusammenarbeit erstellt wurden, ist kenntlich gemacht. Ich habe alle von mir benutzten Hilfsmittel und Quellen angegeben. Teile der Arbeit sind bereits veröffentlicht (siehe „List of Publications“).

Judith Friederike Siebel

LIST OF PUBLICATIONS

This thesis is based on the following publications, which are referred to in the text by the numerals I–IV.¹⁻⁴ They are based on work done by myself jointly with others. My contributions of each paper are indicated in chapter 4.

I “Hybrid [FeFe]-hydrogenases with modified active sites show remarkable residual enzymatic activity”

J. F. Siebel, A. Adamska-Venkatesh, K. Weber, S. Rumpel, E. Reijerse, W. Lubitz, *Biochemistry* **2015**, *54*, 1474–1483.

II “Enhancing hydrogen production of microalgae by redirecting electrons from photosystem I to hydrogenase”

S. Rumpel, J. F. Siebel, C. Farès, J. Duan, E. Reijerse, T. Happe, W. Lubitz, M. Winkler, *Energy & Environmental Science* **2014**, *7*, 3296–3301.

III “Structural insight into the complex of ferredoxin and [FeFe] hydrogenase from *Chlamydomonas reinhardtii*”

S. Rumpel, J. F. Siebel, M. Diallo, C. Farès, E. J. Reijerse, W. Lubitz, *ChemBioChem* **2015**, accepted, DOI: 10.1002/cbic.201500130.

IV “Spectroscopic investigations of [FeFe] hydrogenase matured with $[\text{}^{57}\text{Fe}_2(\text{adt})(\text{CN})_2(\text{CO})_4]^{2-}$ ”

R. Gilbert-Wilson, J. F. Siebel, A. Adamska-Venkatesh, C. C. Pham, H. Wang, E. Reijerse, S. P. Cramer, W. Lubitz, T. B. Rauchfuss, *Journal of the American Chemical Society* **2015**, accepted, DOI: 10.1021/jacs.5b03270.

ABSTRACT

Hydrogenases are enzymes that catalyze the reversible reaction of electrons and protons to molecular hydrogen (H₂). In the research field of future renewable energy systems, hydrogen is often considered as ideal energy carrier since its combustion generates only water. Therefore, hydrogenases are of potential technological interest. However, in order to be able to use hydrogenases in technological applications, their mechanisms and the factors that affect their activities need to be better understood. This work addresses these points in different ways by studying the [FeFe]-hydrogenase from *Chlamydomonas reinhardtii*, HydA1.

- Paper I: Several non-native cofactors were inserted into unmaturation HydA1 using the recently discovered unassisted artificial maturation procedure. H₂ production rates were not improved, but interesting insight into the functionality of HydA1 was shown.
- Paper II: NMR investigations of HydA1, its natural electron donor PetF and its natural competitor FNR revealed PetF amino acid residues that are only important for FNR-binding and not for HydA1-binding. Substitution of those amino acid residues led to an increased H₂ production activity of HydA1 in the presence of FNR.
- Paper III: Gallium-substitution of the two iron atoms in PetF revealed the structure of the whole PetF interface with HydA1. Calculation of a PetF-HydA1 docking model indicates several amino acid residues as targets for mutagenesis aiming at increased H₂ production.
- Paper IV: The novel synthesis of $[\text{}^{57}\text{Fe}_2(\text{adt})(\text{CN})_2(\text{CO})_4]^{2-}$ and its insertion into unmaturation HydA1 affords active HydA1 selectively labeled with ⁵⁷Fe, opening multiple spectroscopic investigations that were not accessible this way before.

Taken together, this work provides different approaches to understand the catalytic activity of HydA1 in detail and to improve its H₂ production rate. Overall, engineering of the HydA1-PetF interface seems to be a more promising target for increasing H₂ production than engineering of the binuclear iron core of the active site.

ZUSAMMENFASSUNG

Hydrogenasen sind Enzyme, die die chemische Reaktion von Elektronen und Protonen zu molekularem Wasserstoff (H₂) katalysieren. Wasserstoff wird oft als idealer Energieträger der Zukunft betrachtet, da bei seiner Verbrennung lediglich Wasser entsteht. Um Hydrogenasen technisch einsetzen zu können, muss ihre Funktionsweise zunächst besser verstanden und ihre katalytische Effizienz optimiert werden. Diese Arbeit befasst sich mit Untersuchungen an der [FeFe]-Hydrogenase HydA1 von *Chlamydomonas reinhardtii*.

- Paper I: Die kürzlich entwickelte artifizielle Maturierung wurde genutzt, um verschiedene unnatürliche Cofaktoren in HydA1 einzubringen. Die dabei entstandenen Hybrid-Hydrogenasen zeigten zwar geringere H₂-Produktionsraten, es konnten jedoch interessante Erkenntnisse über die Funktionalität von HydA1 gewonnen werden.
- Paper II: Durch NMR-spektroskopische Untersuchungen an HydA1, seinem natürlichen Elektronendonator PetF und seinem Elektronen-Konkurrenten FNR wurden PetF-Aminosäuren identifiziert, die wichtig für die Bindung von FNR, aber nicht von HydA1 sind. Ein Austausch dieser Aminosäuren führte zu einer erhöhten PetF-abhängigen H₂-Produktionsrate von HydA1 in Anwesenheit von FNR.
- Paper III: Durch Gallium-Substitution der Eisenatome von PetF wurde das gesamte Interface zwischen PetF und HydA1 entschlüsselt. Die Berechnung eines PetF-HydA1-Komplexes gibt Hinweise auf verschiedene Aminosäurereste, die als Ziel für Mutagenese benutzt werden können, um die H₂-Produktionsrate zu verbessern.
- Paper IV: Die neu entwickelte Synthese von $[\text{}^{57}\text{Fe}_2(\text{adt})(\text{CN})_2(\text{CO})_4]^{2-}$ ermöglicht die Herstellung von aktivem, ⁵⁷Fe-angereichertem HydA1. Dadurch werden verschiedene spektroskopische Untersuchungen zugänglich, die vorher so nicht möglich waren.

In dieser Arbeit werden verschiedene Ansätze gezeigt, um die katalytische Aktivität von HydA1 im Detail zu verstehen und zu verbessern. Veränderungen an dem HydA1-PetF-Interface erscheinen dabei vielversprechender als Änderungen an dem aktiven Zentrum.

1 INTRODUCTION

1.1 The energy problem

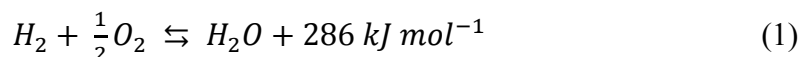
1.1.1 General

The so-called *energy transition* is permanently present in the media: after the Fukushima nuclear disaster in Japan in March 2011, Germany has decided to shut down all its nuclear power plants until 2022. Additionally, it is planned to reduce the CO₂ emission. Therefore, the use of non-renewable energy sources such as oil and coal has to be abandoned and the future energy demand has to be generated using renewable energies like solar and wind energy.

To date, this is still a vision. Day by day, we use enormous amounts of oil (more than 100,000 liter per second worldwide).⁵ Although the crude oil prize was increasing in the past, it recently decreased to about 0.40 \$ per liter, making oil cheaper than mineral water. Oil is liquid and, therefore, easy to extract and to transport.⁶ Additionally, our energy infrastructure is highly optimized for fossil fuel use.⁷ Right now, oil *is* still available at low costs and thus intensively used. However, in the foreseeable future, we will run out of oil. Coal will last longer, but it is the dirtiest of all fossil fuels.⁸ The use of fossil fuels as main energy source leads to pollution and global warming – severe, probably irreversible damage to Earth's atmosphere. The worldwide energy demand is above 120,000 TWh ($432 \cdot 10^{18}$ J) per year and rises constantly due to increasing world population and higher living standards.⁹ It is estimated to roughly double by midcentury.¹⁰ If we want to satisfy our future energy demand and still live on a planet with a functioning ecosystem, we need abundant, clean, and secure renewable energy sources.

1.1.2 The hydrogen issue

Hydrogen, the first element of the periodic table, is the most abundant element in the universe and exists as invisible, light and nontoxic diatomic gas H₂. It has an extremely high energy content of 120 MJ per kg (gasoline: 44 MJ per kg) and its combustion generates only water:¹¹



Water, an inexpensive and abundant molecule, is a “green carrier” of hydrogen. Hence, hydrogen is often considered as the ideal “green energy carrier” for the future.¹² Unfortunately, molecular hydrogen is only present on Earth in very low amounts and, therefore, it has to be produced under energy consumption. The global hydrogen production is 50 million tons per year, less than 2% of the world’s energy demand, but it is mainly used as a feedstock for the chemical industry and rarely used as fuel.^{11,13} Also, the hydrogen generation is often not carbon-neutral, because it is produced from fossil fuels (natural gas, liquid hydrocarbons and coal), hence polluting the atmosphere, or requires catalysts containing rare and expensive metals such as platinum.^{14,15}

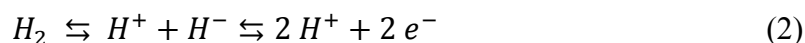
Hydrogen as a gas comprises an inconveniently high volume at room temperature and normal pressure (11,250 L per kg), which can be reduced by pressurizing in a high-pressure (350 atm) steel tank (56 L per kg) or by liquefying at 20 K (14 L per kg). However, these procedures also require energy.¹¹ Furthermore, safety aspects of hydrogen as fuel are often discussed since ≈4% hydrogen per volume form a flammable mixture with air. The disaster of the *Hindenburg* airship in 1937 and the space shuttle *Challenger* in 1986 are lasting memories, but one has to consider that also gasoline is flammable and explosive. Additionally, in contrast to gasoline, hydrogen is volatile and it has a high detonation limit, meaning that it burns most likely before it comes to an explosion.¹⁶

It would be ideal to produce hydrogen on demand using water splitting and solar energy as energy source as nature has developed: in some green algae, chlorophyll captures incoming sunlight and its energy is used to split water into oxygen, electrons and protons. The electrons can be used for hydrogen production, a reaction catalyzed by so-called hydrogenases.¹⁷ Hydrogen could then be used to produce energy in a fuel cell equipped with catalysts based on cheap and abundant metals such as iron or nickel.

1.2 Hydrogenases

1.2.1 General

Hydrogenases are metallo-enzymes that catalyze the “simple” conversion from molecular hydrogen into electrons and protons as well as the reverse reaction, the generation of hydrogen:¹⁸



Hydrogenases occur in various different microorganisms of which most are prokaryotes belonging to the bacteria and archaea life domains. However, some of them belong to the third domain of life, the eukaryotes.^{19,20} Altogether, around 450 hydrogenases are known (status in 2007), which show a wide diversity in size, quaternary structure and electron donors/acceptors.²¹ They can be classified according to the metal content of their active site, where the catalytic reaction takes place. The two main groups are the [FeFe]-hydrogenases and the [NiFe]-hydrogenases.²² The third class are the [Fe]-hydrogenases, which are only found in methanogenic archaea.²³ They do not directly catalyze the reversible splitting of hydrogen, but need a hydride transfer substrate for their hydrogen converting functionality, *i.e.* methenyltetrahydromethanopterin (methenyl- H_4MPT^+). It reversibly reacts with H_2 to methylene- H_4MPT and H^+ .²⁴ Figure 1 shows the active sites of all three hydrogenase classes.

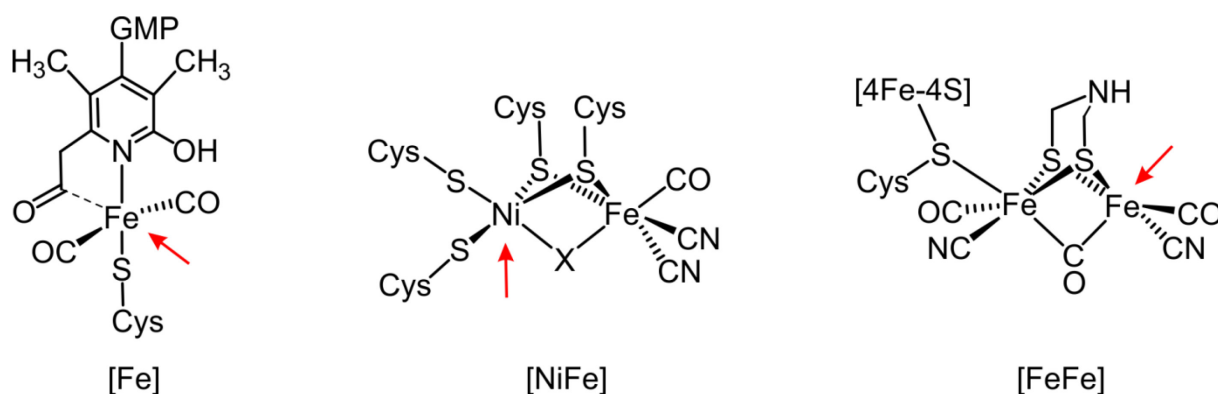


Figure 1. Active sites of the three different classes of hydrogenases: the [Fe]-hydrogenase, the [NiFe]-hydrogenase and the [FeFe]-hydrogenase. GMP is a guanylate residue (deprotonated guanosine monophosphate). The red arrows indicate the H_2 binding sites. The nature of X depends on the redox state of the enzyme and can be O, OH^- or H^- .

[FeFe]-hydrogenases and [NiFe]-hydrogenases share the characteristic feature of carrying the small inorganic ligands cyanide (CN^-) and carbonyl (CO) at iron. Furthermore, they both possess thiolates bridging between their binuclear cores. In general, [NiFe]-hydrogenases are more involved in hydrogen oxidation and [FeFe]-hydrogenases in hydrogen production.²⁵ Most of the [NiFe]-hydrogenases can be purified aerobically in an inactive state, whereas almost all [FeFe]-hydrogenases have to be purified anaerobically.²⁶ Additionally, some [NiFe]-hydrogenases show oxygen tolerance that is not found in [FeFe]-hydrogenases, e.g. the membrane-bound [NiFe]-hydrogenase from the proteobacterium *Ralstonia eutropha*.²⁷

1.2.2 [FeFe]-hydrogenases

Until the beginning of the 80's, when hydrogenases were already known for many decades, it was not unequivocally proven that hydrogenases exist that do not contain nickel.²⁶ In 1984, it was demonstrated that the hydrogenases from the bacteria *Desulfovibrio vulgaris* and *Clostridium pasteurianum* lacked nickel.^{28,29} The first crystal structure of an [FeFe]-hydrogenase was published in 1998 by the group of Peters.³⁰ As already shown in Figure 1, the active center of [FeFe]-hydrogenases consists of a [4Fe-4S]-cluster connected via the thiolate of a cysteine residue to a unique binuclear [2Fe]-subsite.³¹ This unit is called the "H-cluster". The two Fe atoms of the [2Fe]-subsite are referred to as the proximal iron (Fe_p) and the distal iron (Fe_d) relative to the [4Fe-4S]-cluster. They are connected via an azadithiolate bridge and each iron is coordinated by a CO and a CN^- ligand.³² CO and CN^- are strong field ligands that keep the iron center in a low spin-state.³³ Additionally, there is a CO ligand that can be bridging (as shown in Figure 1) or terminal depending on the redox state of the H-cluster (see below, Figure 2).³⁴ Fe_p is six-coordinated, whereas Fe_d is five-coordinated, leaving an open coordination site where the catalytic reaction occurs.²² In addition to the H-cluster, many [FeFe]-hydrogenases contain additional [FeS]-clusters,

so called “F-clusters”. The H-cluster is buried within the protein, whereas the F-clusters form a chain from the H-cluster to the protein surface (or *vice versa*) for electron transport.

The catalytic mechanism of the [FeFe]-hydrogenases is intensively examined already over quite a long time, but is still a matter of debate. It has been studied using many different spectroscopic techniques such as Fourier-transform infrared (FTIR),³⁴ electron spin resonance (EPR),³⁵ ⁵⁷Fe-Mössbauer,³⁶ nuclear resonance vibrational (NRVS)³⁷ and X-ray absorption spectroscopy.³⁸ Also, electrochemical studies³⁹ and density functional theory calculations (DFT)⁴⁰ have been performed to shed light on the catalytic mechanism.

Figure 2 shows the catalytic mechanism proposed by Adamska *et al.* in 2012.⁴¹

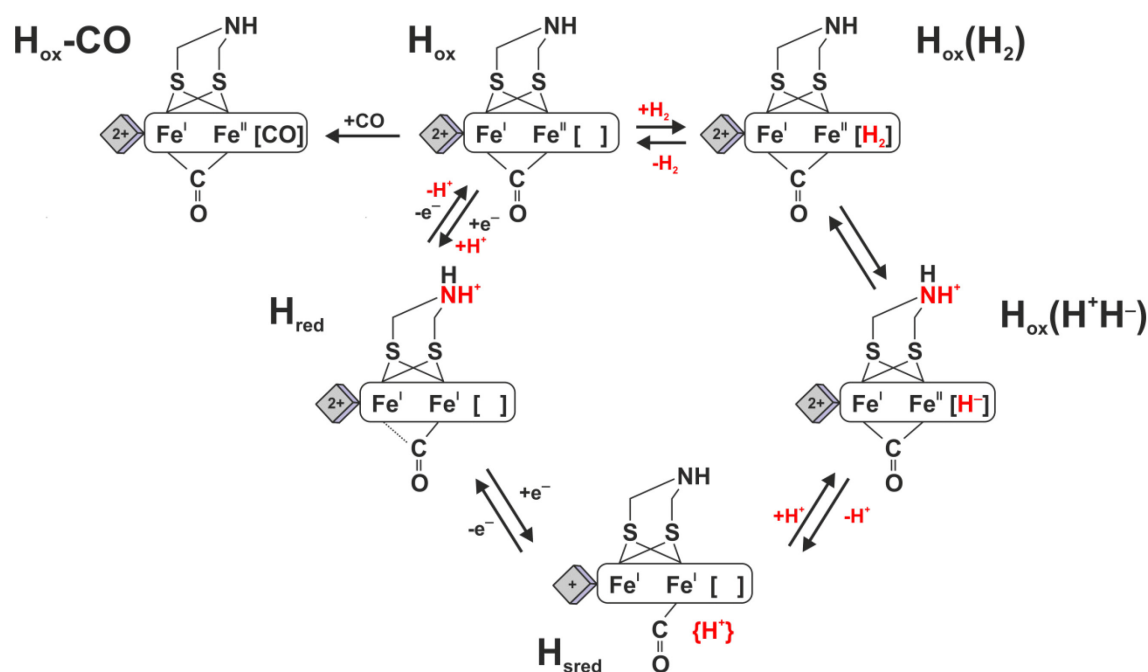


Figure 2. Catalytic hydrogen splitting and production mechanism of [FeFe]-hydrogenases as proposed by Adamska *et al.* including the inactive H_{ox-CO} state.⁴¹ The [2Fe]-subsite is depicted schematically and the [4Fe-4S]-cluster is shown as a square with the overall charge indicated.

In general, Fe_d and the [4Fe-4S]-cluster are redox active and the amine bridgehead functions as a Brønsted base. The hydride is terminally bound to Fe_d and a flexible CO ligand can either be bridging or terminal. Describing the catalytic cycle for H_2 splitting, the oxidized state (H_{ox}) can be seen as starting point, where molecular hydrogen can bind to the distal iron. There, it is split heterolytically into a hydride and a proton; the latter is binding to the amine bridge. A

proton is released, Fe_d and the [4Fe-4S]-cluster get reduced and the former bridging CO is terminally bound to Fe_d . This super-reduced state (H_{sred}) is the only state with the [4Fe-4S]-cluster in its reduced $[\text{4Fe-4S}]^{+1}$ form. In the next step to the reduced state (H_{red}), an oxidation of the [4Fe-4S]-cluster and back-formation of the bridging CO take place. Finally, after a further oxidation and loss of a proton, the catalytic cycle is closed. H_{ox} , H_{red} and H_{sred} are stable intermediates. Another characterized state is the CO-inhibited state ($\text{H}_{\text{ox-CO}}$), which is formed upon CO exposure of the oxidized state. The CO binds to the open coordination site of the distal iron and blocks the catalytic activity.³²

1.2.3 [FeFe]-hydrogenases in green algae

Green algae are photosynthetically active algae and belong to the eukaryote life domain. Together with cyanobacteria, green algae are the only organisms currently known that are capable of both oxygenic photosynthesis and hydrogen production.⁴² In cyanobacteria, hydrogen is produced by nitrogenases or in a dark anaerobic reaction by hydrogenases, whereas green algae produce hydrogen photosynthetically,¹⁷ where hydrogen evolution is observed as a consequence of anaerobiosis or nutrient deprivation.^{43,44} Although algae usually carry out oxygenic photosynthesis, they can adopt to anaerobic conditions by switching their metabolism to fermentation.^{45,46} Under these metabolic conditions, however, harmful end-products such as ethanol can be produced.⁴⁷ Also, the respiratory chain is only partially active and the Calvin cycle is inhibited, both functioning as an electron sink under normal metabolic conditions.⁴⁵ Therefore, in the fermentative metabolism, hydrogenase production is upregulated,¹⁷ because the hydrogenase catalyzes the reaction from electrons and protons to molecular hydrogen and thereby serves as an electron sink. The formed end product, hydrogen, is volatile and harmless.

Figure 3 shows a schematic overview of the photoproduction of hydrogen in the green algae *Chlamydomonas reinhardtii*.⁴⁸ Its hydrogenase HydA1 (see also next chapter 1.2.4) is located

in the stroma of chloroplasts.⁴⁹ Electrons, originating from light-induced water splitting at photosystem II, are transported via an electron transport chain, including several proteins, to photosystem I and from there to the ferredoxin PetF (photosynthetic electron transport ferredoxin). This small protein contains a [2Fe-2S]-cluster that is reduced upon electron delivery.⁵⁰ PetF can distribute the photosynthetic electrons to a variety of proteins, including HydA1.⁴⁸ PetF is, therefore, the natural electron donor of HydA1.⁵¹ However, the most important electron acceptor of PetF is the ferredoxin-NADP⁺-oxidoreductase (FNR), a key enzyme between photosynthetically produced electrons and the Calvin cycle.⁵² The subject of FNR and HydA1 competing for the electrons of PetF is addressed in paper II.²

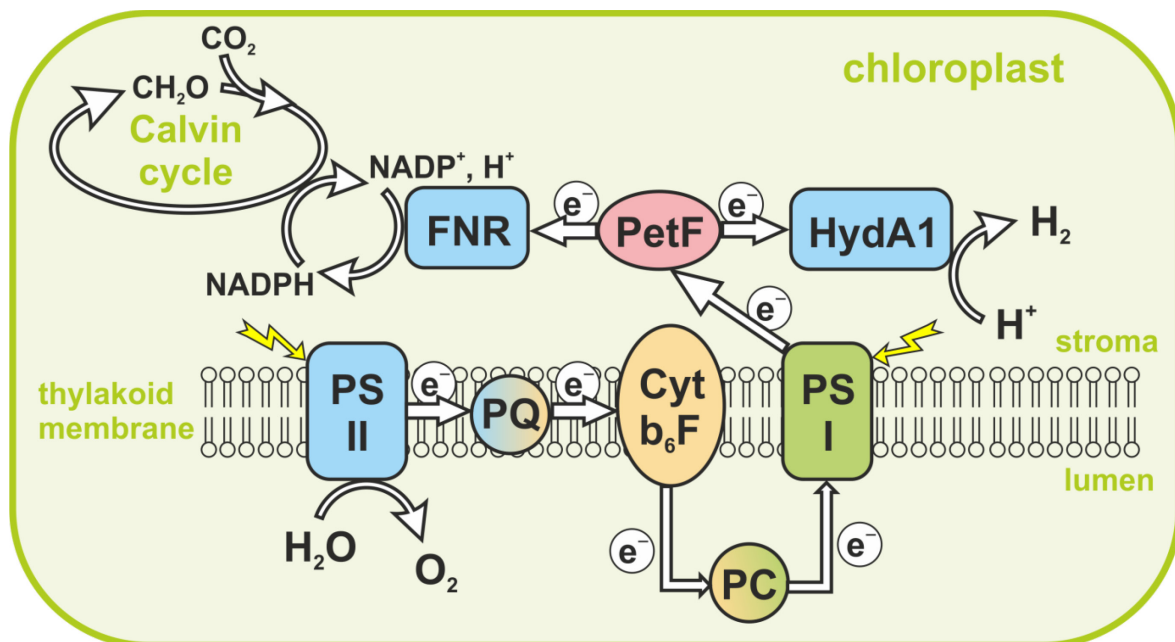


Figure 3. Schematic overview of the photoproduction of hydrogen in *Chlamydomonas reinhardtii*.⁴⁸ Further electron acceptors of PetF are omitted for clarity. PSII: photosystem II, PQ: plastoquinone pool, Cyt b₆f: cytochrome b₆f, PC: plastocyanin, PSI: photosystem I, PetF: photosynthetic electron transport ferredoxin, FNR: ferredoxin-NADP⁺-oxidoreductase.

1.2.4 HydA1 – the [FeFe]-hydrogenase from *Chlamydomonas reinhardtii*

Chlamydomonas reinhardtii (*C. reinhardtii*) is a single-cell green alga living in fresh water. It is widely used as a model system in many different subfields in biology.⁵³ Its hydrogenase HydA1 is a ≈50 kDa protein consisting of a single unit. Like all [FeFe]-hydrogenases from green algae, HydA1 does not contain F-clusters in addition to the H-cluster.^{43,54} It, therefore,

represents the minimal core unit that is necessary for H₂ conversion and is most suitable for spectroscopic investigations, because no signals from the F-clusters can interfere with H-cluster signals. In this work, exclusively HydA1 has been studied.

So far, active HydA1 has not been crystallized. However, a crystal structure of the unmaturation inactive form containing only the [4Fe-4S]-cluster is available (Figure 4).⁵⁵ Although the [2Fe]-subsite is not present in the crystal structure, its position can be estimated by comparing the crystal structure to previously characterized, similar structures of other [FeFe]-hydrogenases.^{31,56} Also, the amino acids that coordinate the [2Fe]-subsite are known.⁵⁷ The crystal structure indicates that the H-cluster synthesis occurs stepwise. First, the [4Fe-4S]-cluster is assembled and then the [2Fe]-subsite is inserted through a positively charged, 8–15 Å wide and about 25 Å deep channel. The [4Fe-4S]-cluster is located at the base of the channel. Presumably, this channel collapses following incorporation of the [2Fe]-subsite as a result of conformational changes in two loop regions.⁵⁵

As a consequence of the absence of the F-clusters in HydA1, electrons for the catalytic reaction are directly transferred from its redox partner, the ferredoxin PetF (see also previous chapter 1.2.3). Therefore, an electron transfer complex between HydA1 and PetF is formed. This complex has been studied (paper III).³

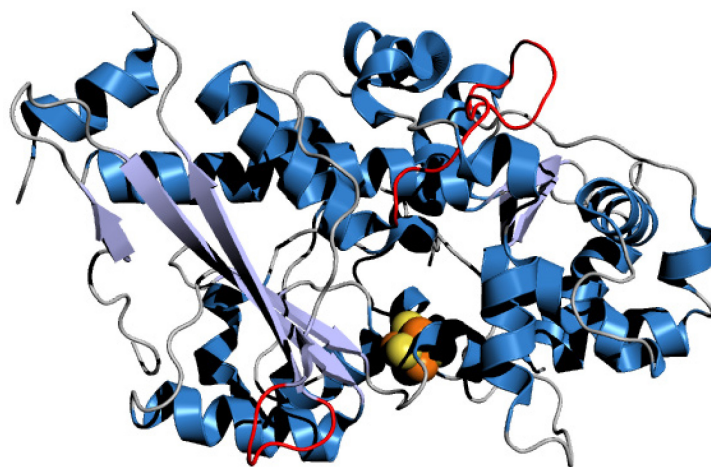


Figure 4. Crystal structure of the unmaturation inactive form of HydA1. The [4Fe-4S]-cluster is shown as spheres (iron in orange and sulfur in yellow), the two loop regions presumably involved in H-cluster maturation (see text) are colored red. α -helices are shown in blue and β -sheets in light blue.⁵⁵

1.3 Artificial maturation of hydrogenases

1.3.1 [FeFe]-hydrogenase model complexes

Since the crystal structures of [FeFe]-hydrogenases were solved,^{30,32,58} chemists started to synthesize model compounds that mimic the active site. The number of [FeFe]-hydrogenase model compounds has grown enormously in the past 15 years. The review of Tard and Pickett from 2009 gives an overview of different hydrogenase models.⁵⁹ For a more recent review, see Simmons *et al.*, 2014.⁶⁰

In 1999, three groups individually reported the [FeFe]-hydrogenase [2Fe]-subsite model $[\text{Fe}_2((\text{SCH}_2)_2\text{CH}_2)(\text{CO})_4(\text{CN})_2]^{2-}$ (Figure 5a) derived from the precursor diiron carbonyl compound.⁶¹⁻⁶³ At this time, the nature of the bridgehead was not yet identified, since carbon, nitrogen, and oxygen could not be distinguished crystallographically. Therefore, the mimics $[\text{Fe}_2((\text{SCH}_2)_2\text{NH})(\text{CO})_4(\text{CN})_2]^{2-}$ and $[\text{Fe}_2((\text{SCH}_2)_2\text{O})(\text{CO})_4(\text{CN})_2]^{2-}$ were also synthesized (Figure 5b and 5c).^{64,65} None of these complexes showed promising catalytic activity and they are, therefore, considered as structural rather than functional models. In thiolate-bridged binuclear [FeFe] models, apart from variations of the bridgehead, the carbonyl and cyanide ligands can easily be substituted, *e.g.* by phosphines, isocyanides, nitrosyl ligands and *N*-heterocyclic carbenes.⁵⁹ All in all, there is a huge toolbox for modifying the [2Fe]-core.

In order to design a functional [FeFe]-hydrogenase active site mimic, several features of the natural H-cluster have to be taken into account: i) an open coordination site for substrate binding, ii) a proton-shuttling system, iii) a contact site for the external redox partner.¹⁸ An example of a model compound featuring all these elements was published by Camara *et al.* in 2012 (Figure 5d).⁶⁶ In this complex, the modified ferrocene acts as a redox-active unit, therefore mimicking the [4Fe-4S]-cluster. The *N*-benzyl bridgehead group functions as a proton relay and there is a potential substrate binding site. Indeed, hydrogen oxidation could be observed for this complex.⁶⁶

Biomimetic [FeFe]-hydrogenase models help to understand the catalytic mechanism by featuring certain structural and electronic aspects. However, their electrocatalytic performance in hydrogen production and oxidation is generally rather poor.⁶⁷ For the design of a functional and robust hydrogen conversion catalyst for future technological applications, *bioinspired* models may be more promising than mere *biomimetic* models, although the distinction between the two is ambiguous. One example of a rather bioinspired model is a mononuclear iron compound that mimics only the distal iron (designed by the Ott group, Figure 5e).⁶⁸ The stable, penta-coordinated Fe(II) complex provides an open coordination site for substrate binding and catalyzes the electrochemical reduction of protons at a mild overpotential.

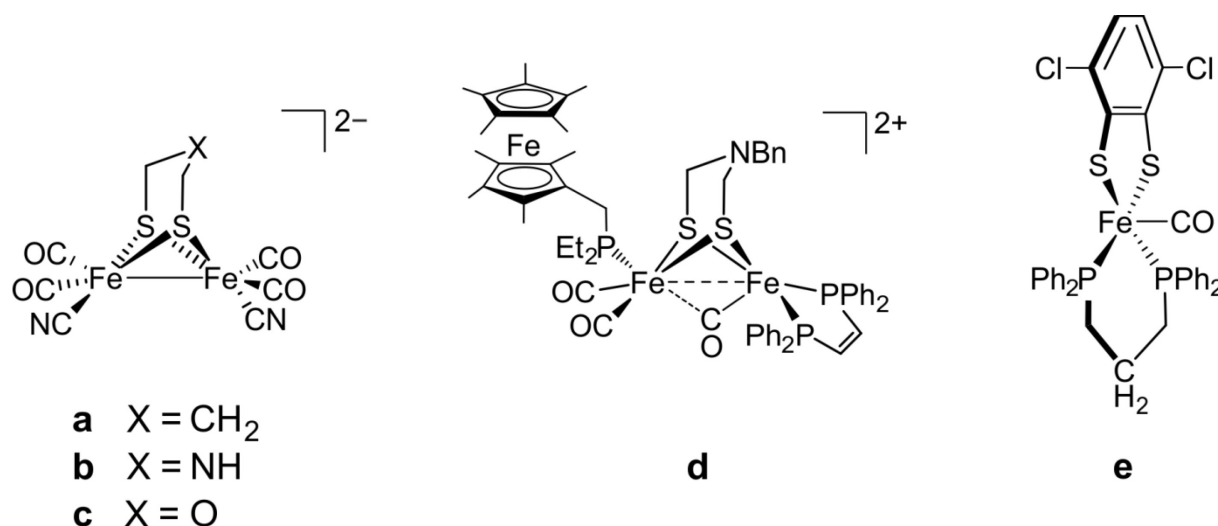


Figure 5. Biomimetic and bioinspired hydrogenase model compounds. Et: ethyl; Ph: phenyl; Bn: benzyl.

1.3.2 Artificial maturation assisted by HydF

As already mentioned, the integration of the H-cluster in the protein pocket occurs in a stepwise manner *in vivo*.^{69,70} The [4Fe-4S]-cluster is formed *in situ* by the standard [FeS]-cluster assembly machinery,^{71,72} whereas the [2Fe]-subsite is assembled by three different maturase proteins called HydE, HydF and HydG (Figure 6).⁷³ In the last decade, some details of the maturation process have been elucidated like the origin of the CO and CN⁻ ligands, which are derived from tyrosine in a HydG-catalyzed reaction.^{74,75} While HydF has been identified as a scaffold protein that transfers the [2Fe]-subsite to the unmaturation

hydrogenase, *i.e.* hydrogenase only containing the [4Fe-4S]-cluster,^{76,77} recent results of the Britt group suggest that HydG transfers an organometallic $\text{Fe}(\text{CO})_2(\text{CN})$ -synthon that forms the [2Fe]-subsite of the H-cluster (Figure 6).⁷⁸

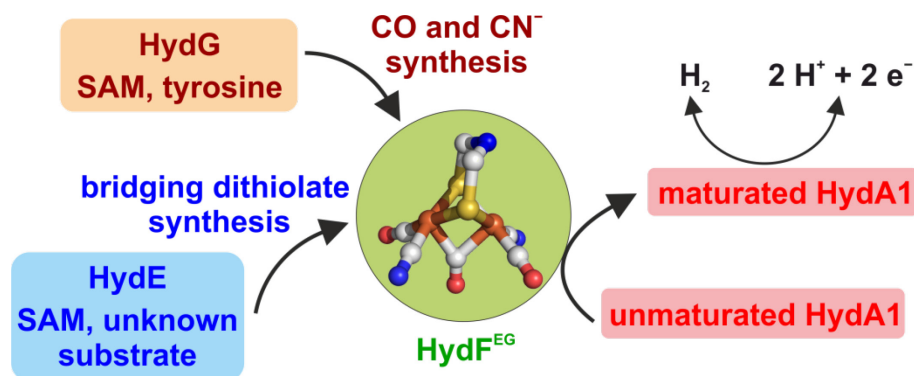


Figure 6. Hypothetical maturation scheme for H-cluster biosynthesis.⁶⁹ SAM: S-adenosyl-L-methionine, HydF^{EG}: maturase protein HydF co-expressed with HydE and HydG.

In 2013, Berggren *et al.* demonstrated that the closest synthetic [FeFe]-hydrogenase [2Fe]-subsite mimics $[\text{Fe}_2((\text{SCH}_2)_2\text{X})(\text{CO})_4(\text{CN})_2]^{2-}$ (chapter 1.3.1, Figure 5a-c) bind to the maturase HydF.⁷⁹ The width of the FTIR bands (see chapter 2.3.2) of the HydF-hybrids is rather large and, therefore indicates conformational freedom of the complex similar to the unbound complex. Importantly, it was shown that mimic-loaded HydF can subsequently deliver the model compounds to unmaturated HydA1. Upon insertion, all three compounds show narrow FTIR bands that are characteristic for the CO and CN vibrational modes in active hydrogenase.⁸⁰ Remarkably, the FTIR spectrum of the mimic $[\text{Fe}_2((\text{SCH}_2)_2\text{NH})(\text{CO})_4(\text{CN})_2]^{2-}$ (Figure 5b) incorporated into unmaturated HydA1 has strong correspondence to native HydA1 and shows full hydrogenase activity.⁷⁹ This provided finally the unequivocal evidence that the bridgehead group has to be an amine, settling a long-lasting debate.^{81,82}

1.3.3 Unassisted artificial maturation

Only a few months after the discovery of the artificial maturation of HydA1 assisted by HydF, during the period in which this thesis was performed, it was demonstrated that the

“middleman” HydF is not needed for the maturation.^{83,84} Upon incubation of $[\text{Fe}_2(\text{adt})(\text{CO})_4(\text{CN})_2]^{2-}$ (adt = azadithiolate = $[(\text{SCH}_2)_2\text{NH}]^{2-}$) with unmaturation HydA1, the model compound is directly incorporated into the enzyme and gives fully active hydrogenase, which is virtually indistinguishable from the native HydA1 as shown by EPR (chapter 2.4.3) and FTIR analysis.⁸⁵ Moreover, the unassisted artificial maturation cannot only be used for the hydrogenase from *Chlamydomonas reinhardtii*, but also for [FeFe]-hydrogenases from the bacteria *Megasphaera elsdenii* and *Clostridium pasteurianum*.⁸³ Additionally, it was shown that artificially matured HydA1 interacts with its natural electron delivery systems, indicating also *in vivo* functionality. Comparing the synthetic mimics and HydA1’s active site (Figure 7, left and right), it is apparent that the mimics contain one CO ligand more than the active site. Indeed, the dissociation of one CO upon the incorporation reaction was observed.⁸³ Figure 7 summarizes the assisted and unassisted maturation. This smart and exclusive procedure is an excellent example of the power of synthetic biology and it was used throughout this work.

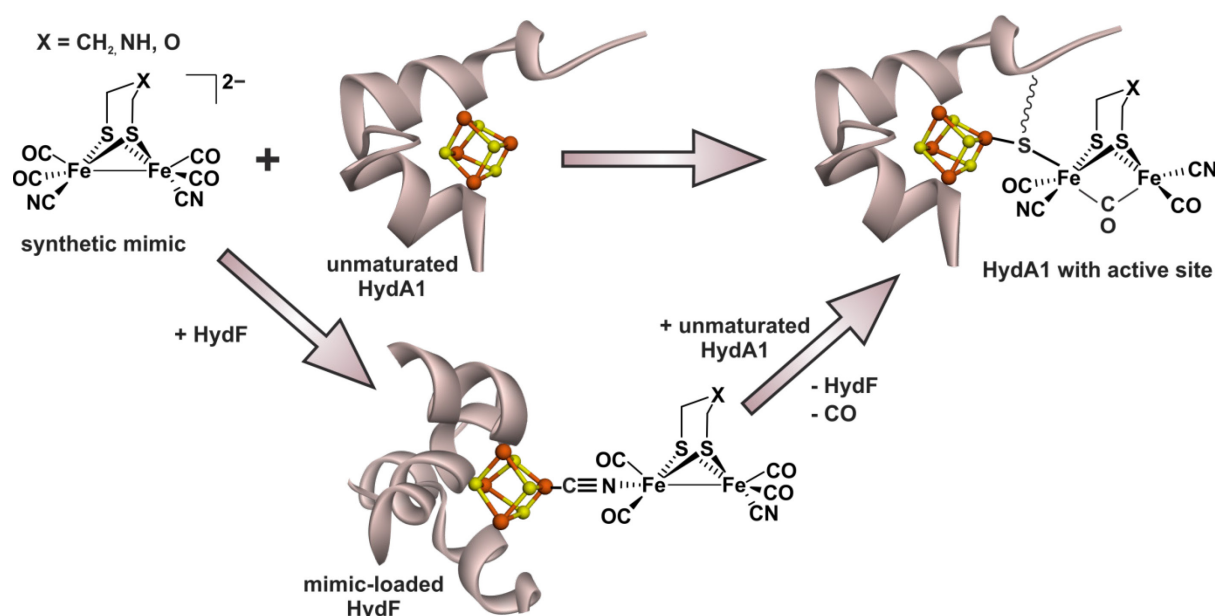


Figure 7. Unassisted (top part) and HydF-assisted (bottom part) maturation of unmaturation HydA1 with synthetic mimics.

1.4 Aim and outline of the research

The unassisted artificial maturation as described in the previous paragraph facilitates the production of large sample quantities: unmaturation HydA1 can be heterologously overexpressed in *Escherichia coli* resulting in very good yields. It is then activated with the synthetic mimic $[\text{Fe}_2(\text{adt})(\text{CO})_4(\text{CN})_2]^{2-}$. These large amounts of active HydA1 were not available before and allow for studies using highly concentrated, voluminous sample-requiring spectroscopic techniques like NMR (nuclear magnetic resonance, paper II and III)^{2,3} and ^{57}Fe -Mössbauer spectroscopy (paper IV)⁴. Moreover, synthetic mimics different from the native one can be tested for incorporation (paper I).¹

The incorporation of various synthetic mimics as presented in paper I gives insight into the functionally relevant parts of the [2Fe]-subsite and the importance of conformational flexibility, which were revealed by activity measurements and determination of the degree of maturation. In paper II and III, the interactions of the natural electron donor PetF with HydA1 and the natural competitor of HydA1, the ferredoxin-NADP⁺-oxidoreductase (FNR), is investigated. Knowledge gained from this work could help to design H₂ producing organisms with an increased H₂ production. Paper IV focusses on gaining insight into the electronic structure of HydA1.

Taken together, all these investigations aim for a better understanding of hydrogenases and their functionality in order to develop an efficient H₂ conversion catalyst for future technological applications.

2 APPLIED METHODS

2.1 Heterologous protein overexpression and purification

Heterologous overexpression is a method widely used in protein biochemistry.⁸⁶ A host organism is thereby used to express a target protein. Often, the well-studied Gram-negative bacterium *Escherichia coli* (*E. coli*) is used as a host.⁸⁷ The gene encoding for the target protein is introduced in *E. coli* on circular deoxyribonucleic acid (DNA), so-called expression vectors or plasmids. Beside the genomic information for the target protein, the plasmid contains restriction enzyme sites (for cloning), genetic information for antibiotic resistance (for selection), a gene regulation system and other specific sites that are depicted in so-called vector maps. Figure 8 shows a simplified vector map of the plasmid pET21b that was used in this work.

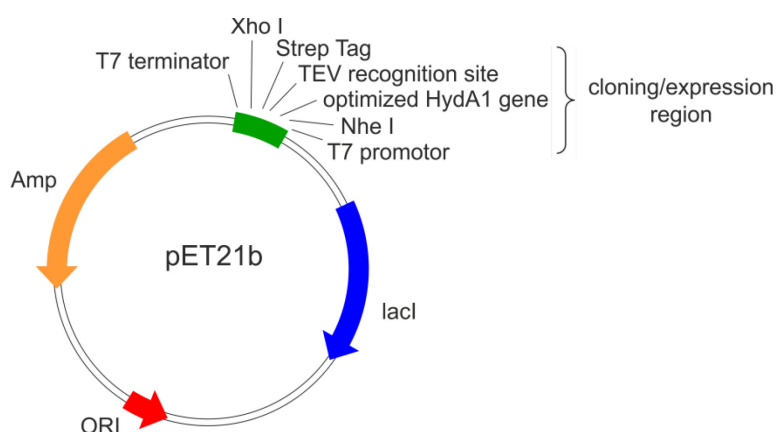


Figure 8. Simplified vector map of pET21b as used in this work: Amp (ampicillin), the antibiotics resistance gene (orange); ORI (origin of replication), DNA sequence that allows the initiation of replication (red); lacI, regulator gene of the *lac*-operon (blue); the cloning/expression region (green). The cloning/expression region contains the T7 promoter and terminator, where the transcription is initiated and stopped, respectively, the restriction enzyme sites Nhe I and Xho I and the gene encoding for the target protein HydA1 with the TEV recognition site and the Strep Tag.

The uptake of the expression vector into the host cell is called transformation. It is often done by a method called calcium chloride transformation, where the cells are treated with Ca^{2+} on ice, making them permeable to plasmid DNA, or by electroporation, using electric pulses that lead to a formation of transient holes in the cell membrane. After the transformation, which means that the host cells are now genetically altered, the cells are grown in a culture medium.

The expression of the target protein starts once an inducer is added. The *lac*-operon is often used for gene regulation. Addition of the inducer isopropyl β -D-1-thiogalactopyranoside (IPTG) and its binding to the *lac* repressor lead to the expression of the target protein. Another gene regulation system, which was also used in this work, is the *tet* operon with anhydrotetracycline as inducer. After protein expression, cell harvesting and breaking, the target protein has to be separated from the host proteins. A widely applied method for protein purification is the affinity chromatography: a specific gene sequence is added to the gene of the target protein that encodes for an affinity tag (Figure 8). This tag is attached to the target protein upon expression. The procedure of protein purification via an affinity tag is shown in Figure 9 using the example of the Strep tag.⁸⁸ The tag can be removed after purification by specific proteolysis. Proteins purified by this method are often obtained at a high degree of purity. If necessary, more purification steps can be applied like, *e.g.*, size exclusion or ion exchange chromatography.

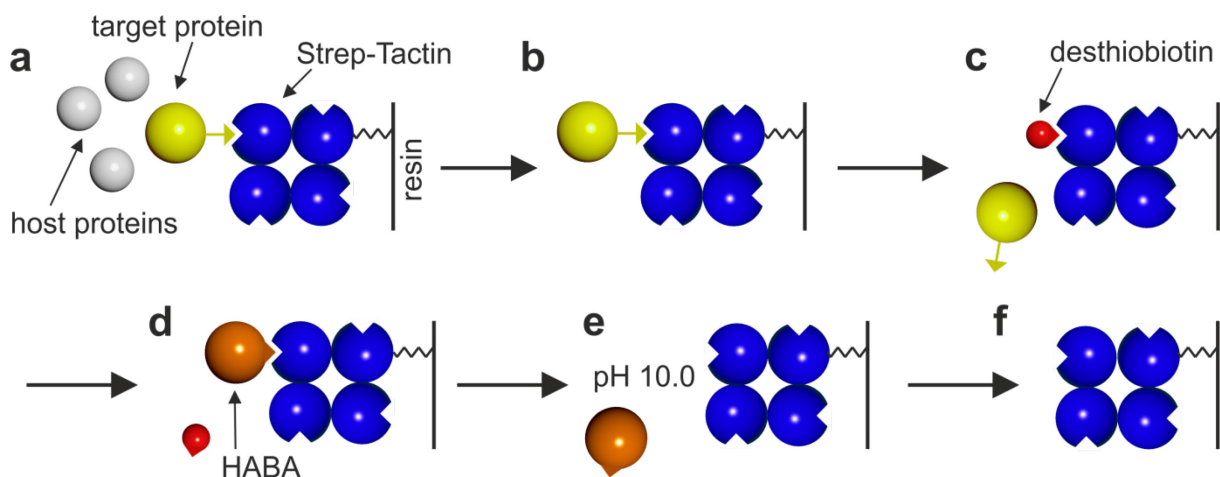


Figure 9. Protein purification using the Strep-Tag. **a.** A solution of protein mixture (*mobile* phase) is added to a *stationary* phase (resin). The target protein (yellow) has a Strep-Tag that binds to Strep-Tactin (blue) of the stationary phase. **b.** All other proteins (gray) are leached out from the stationary phase. **c.** The target protein can be eluted by adding desthiobiotin (red) that binds to the Strep-Tactin. **d.** Desthiobiotin is removed when HABA (2-(4-hydroxyphenyl-azo)benzoic acid, orange) is added. **e.** Changing the pH from 8.0 to 10.0 releases HABA. **f.** The stationary phase is now ready for the next purification run. The figure is adapted from Schmidt *et al.* 2007.⁸⁸

In this study, *E. coli* was used to overexpress HydA1, the [FeFe]-hydrogenase from *C. reinhardtii*. The two organisms have different codon usage, meaning that the occurrence of tRNA (transfer ribonucleic acid) in the translation from the genetic code to the amino acids is different. In order to optimize expression levels, the target gene must be *codon-optimized* for overexpression in *E. coli*. This is crucial for high yields as were needed in this work. Codon-optimized genes are commercially available and produced upon request.

2.2 H₂ conversion activity measurements

[FeFe]-hydrogenases are mainly active in H₂ production, but they also catalyze the reverse reaction, the splitting of H₂.²⁵ The catalytic activities can be quantified.^{46,89} For this purpose, an artificial electron donor/acceptor is needed. Most often, methyl viologen is used. In order to detect H₂ production, the hydrogenase is incubated with methyl viologen and sodium dithionate as electron source. Under these conditions, the hydrogenase produces H₂, which can be detected by gas chromatography. H₂ oxidation is measured indirectly by optical absorption of reduced methyl viologen. In an H₂ saturated buffer, the hydrogenase splits H₂ into protons and electrons, if there is an electron acceptor available. The buffer also contains oxidized, colorless methyl viologen that turns blue upon reduction. The formation of reduced methyl viologen is observed in UV/Vis (ultraviolet-visible) spectroscopy.

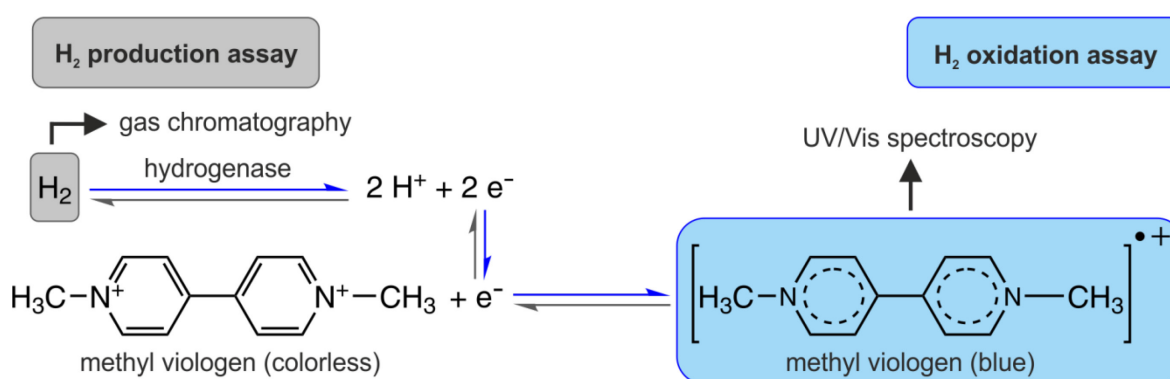


Figure 10. H₂ production and oxidation activity measurements with methyl viologen as electron donor and acceptor, respectively.

2.3 Infrared spectroscopy

2.3.1 Basic concepts

Infrared radiation lies in the electromagnetic spectrum between the visible and the microwave region. It is used in infrared (IR) spectroscopy to study vibrations in molecules. The light is absorbed at specific wavelengths, which are characteristic for specific vibrations of the molecule. The absorption is measured as a function of the wavelength.⁹⁰ Fourier transform infrared spectroscopy (FTIR) is a technique that enables a very efficient recording of the IR spectrum and was used in this work.

There are two basic types of vibrations, stretching (change of the bond length, Figure 11a) and bending (change of the bond angle between two atoms, Figure 11b).

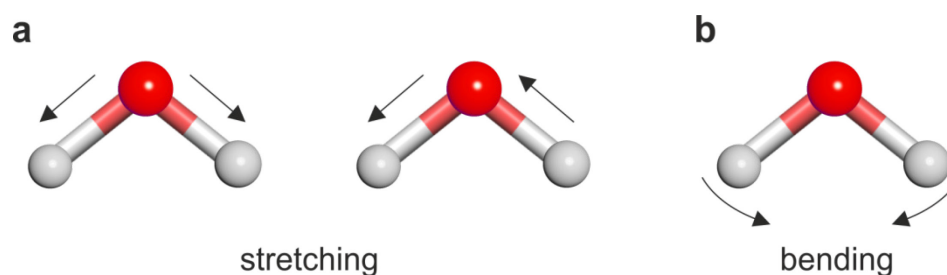


Figure 11. a. Symmetric and antisymmetric stretching vibrations and b. bending vibrations.

The vibration must cause a change in the dipole moment of the molecule in order to be infrared active and observable by IR spectroscopy. Infrared inactive vibrations can often be observed in Raman spectroscopy, which has different selection rules (change in polarizability).⁹¹ Molecular vibrations can be approximated derived from Hooke's law, giving a relation between the frequency of a bond vibration, the bond strength and masses of the atoms.⁹² IR spectra are often reported in wavenumbers, which is the inverse of the wavelength.

2.3.2 Infrared spectroscopy on proteins

In organic chemistry, IR spectroscopy is widely used to identify functional groups in a molecule such as OH, NH, C=O, C≡N and NO₂.⁹³ An IR spectrum of a protein is composed

of many overlapping bands due to the large size of the protein and its chemical structure cannot be deduced from the spectrum. However, changes in the spectrum, for example caused by protonation of side chains, can be detected. Furthermore, the absorption of the amide backbone gives information about the secondary structure of a protein.⁹⁰ In the review of Barth from 2007, the IR spectroscopic applications in protein biochemistry are summarized.⁹⁴ In the research field of hydrogenases, IR spectroscopy is particularly useful, because the unusual CN^- and CO ligands of the active site have specific absorptions between 1800 and 2200 cm^{-1} .^{31,33,41,80,85} They, therefore, do not overlap with any other absorptions of the protein and they are not coupled to backbone vibrations. The CO peaks are very sensitive to any change in the active site of the protein like the oxidation state of the binuclear iron core or the [4Fe-4S]-cluster, protonation, any additional ligands or changes in the ligand sphere. This leads to a specific pattern of the IR spectrum for the different states in the catalytic cycle of hydrogen conversion. Isotope labeling of the CN^- and CO ligands causes shifts in the absorption peaks and is a useful tool to study mechanistic details or the origin of the ligands.^{78,95,96} Figure 12 shows the FTIR spectrum of *C. reinhardtii* HydA1 in the oxidized state, H_{ox} , after subtraction of the broad background signal from the solvent H_2O .

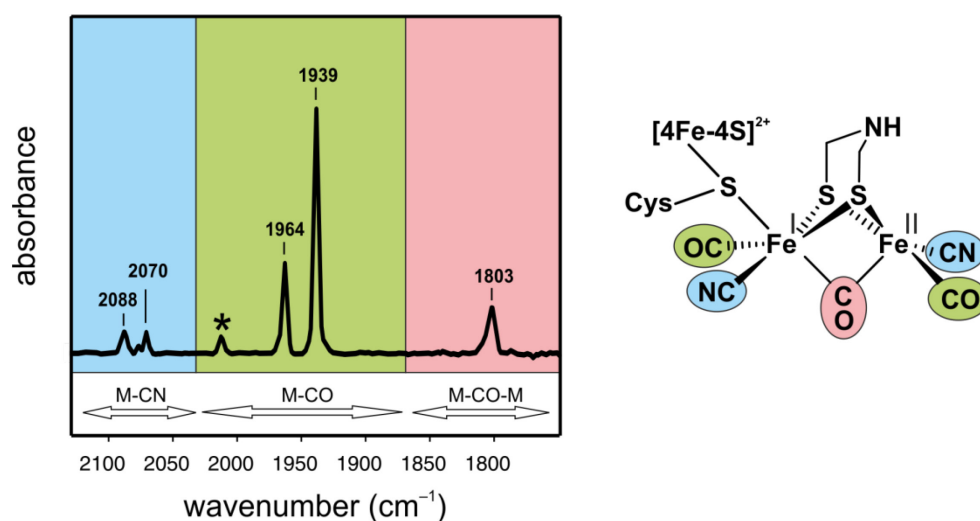


Figure 12. FTIR spectrum of HydA1 in the H_{ox} state and assignment of the respective peaks. The peaks in the blue area arise from CN vibration modes, in the green area from CO vibration modes and in the pink area from vibrations of the bridging CO as indicated in the molecular structure on the right. The asterisk marks a minor contribution of the $\text{H}_{\text{ox}}\text{-CO}$ state. The spectrum is adapted from Adamska-Venkatesh *et al.*, 2014.⁸⁵

In this work, FTIR spectroscopy was used to probe insertion of synthetic complexes into HydA1 and to investigate their structural accommodation within the active site (paper I, chapter 4.1). Quantum chemical calculations of FTIR frequencies gave insight into the corresponding symmetrical and antisymmetrical stretching modes of the CO and CN⁻ ligands.

2.4 Magnetic resonance spectroscopy

2.4.1 Basic concepts

Magnetic resonance spectroscopy is based on the Zeeman effect, *i.e.* the splitting of molecular energy levels in an external magnetic field. This splitting originates from the interaction of the magnetic moment of an atom with the external magnetic field. Nuclear magnetic resonance (NMR) spectroscopy is sensitive to the magnetic moment caused by the nuclear spin, whereas in electron paramagnetic resonance (EPR) spectroscopy, it is the spin transitions of the electron that are observed. In an applied external magnetic field, a spin aligns either parallel or anti-parallel to the magnetic field, giving rise to two distinct energies (Figure 13).

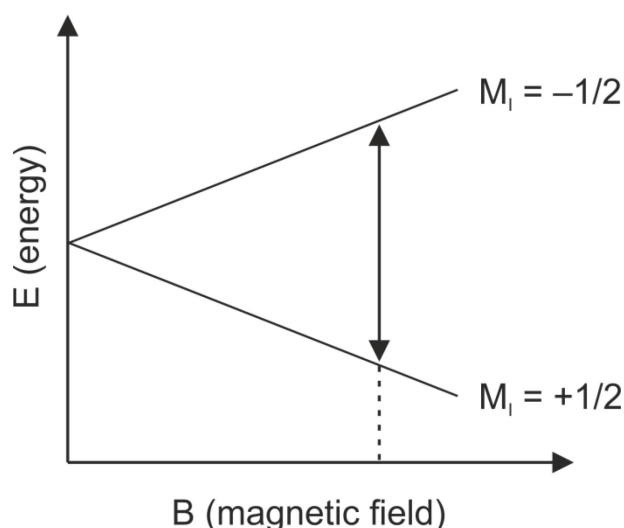


Figure 13. Zeeman splitting for a spin $I = 1/2$ in an applied field with the two states $M_l = +1/2$ and $M_l = -1/2$. The energy splitting is linearly proportional to the magnetic field. By irradiation of the sample with radio frequencies, transitions between the energy state occurs at a certain frequency. This phenomenon is called *resonance*. The frequency at which the resonance condition is obtained

depends on the chemical environment of the nuclei and the paramagnetic center, respectively. As a result, information about the chemical environments can be derived. In NMR spectroscopy, the resonance frequency of a nucleus relative to a standard is called chemical shift δ and is given in ppm.

NMR and EPR spectra are either recorded by continuous wave (CW) or pulse methods. In a CW experiment, the external magnetic field is swept at a constant frequency or *vice versa*, the frequency is swept at a constant magnetic field. The former method is used in EPR spectroscopy, while CW methods in NMR are generally not used anymore because of a poor signal-to-noise ratio. In pulse methods, one or more microwave pulses are applied to the sample in order to perturb the magnetization vector. One can then measure the emitted microwave signal. The measurements can be described by pulse sequences, which are divided into building blocks. Starting with a spin system at thermal equilibrium, the first period is the *preparation*, where the spin system is excited by a single or multiple pulses. This results in a magnetization, which evolves during the *evolution* period. It is followed by a *mixing* period, where magnetization is transferred from one spin to another by one or more pulses. The last period is the *detection*, where the signal is recorded. Figure 14 shows the general pulse sequence of a 2D NMR experiment. The variables t_1 in the evolution period and t_2 in the detection period provide the two axes of the 2D NMR spectrum after Fourier transformation.

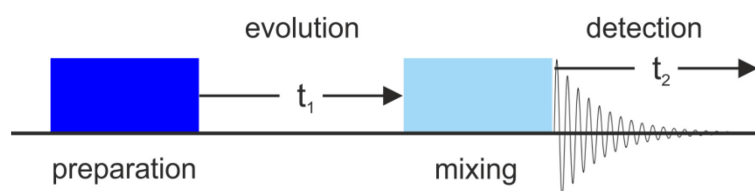


Figure 14. Schematic depiction of a general pulse sequence for a 2D NMR experiment with the four periods preparation, evolution, mixing and detection.

2.4.2 Nuclear magnetic resonance spectroscopy

2.4.2.1 General

Nuclear magnetic resonance (NMR) spectroscopy is the preeminent analytical technique used in organic chemistry. Biomolecular NMR explores the structure and dynamics of proteins, nucleic acids, carbohydrates and protein-ligand complexes. Protein NMR is a rapidly developing field and primarily only hampered by the limitation in protein size that can be studied.⁹⁷

In organic chemistry, the most often used nuclei are ^1H , ^{13}C , ^{19}F and ^{31}P , whereas in protein NMR, they are ^1H , ^{13}C and ^{15}N (all $I = 1/2$). The natural abundance of ^{13}C and ^{15}N is too low for measuring protein NMR spectra and, therefore, has to be enriched. This can be done by growing the cells in minimal media containing $^{15}\text{NH}_4\text{Cl}$ and ^{13}C -glucose. Whereas the ^1H spectrum of a small organic molecule is usually very informative, the ^1H spectrum of a protein contains a large number of partly overlapping signals and normally, only general statements about the secondary/tertiary structure can be made. Hence, higher dimensional (2D or 3D) spectra are often recorded in order to obtain more detailed information.

The investigation of proteins with sizes like that of the [FeFe]-hydrogenase HydA1 (50 kDa) by NMR is in general difficult, because the proteins are tumbling slowly in solution, leading to a fast decay of the NMR signal and a poor signal resolution. Additionally, there is a large number of overlapping signals in the spectrum. Another problem is caused by the active site of the hydrogenase: the paramagnetic iron causes paramagnetic relaxation enhancement (PRE) of residues nearby the active center, their nuclear spins relax fast and their NMR signals become broad or undetectable.

Therefore, in this study, NMR spectroscopy was used to investigate the interactions of the natural electron donor PetF (10 kDa) with the hydrogenase from *Chlamydomonas reinhardtii*, HydA1 (see chapter 4.2 and 4.3, paper II and III). PetF also contains paramagnetic iron in the [2Fe-2S]-cluster that leads to invisible residues nearby the cluster. This problem was

overcome as described in paper III (chapter 4.3) by substitution of paramagnetic iron with diamagnetic gallium(III).

2.4.2.2 2D NMR

Common homonuclear 2D- ^1H experiments in protein NMR are the COSY (correlation spectroscopy), TOCSY (total correlation spectroscopy) and NOESY (nuclear Overhauser and exchange spectroscopy) experiment (Figure 15). A ^1H - ^1H COSY spectrum shows magnetization transfer for protons that are two to three bonds away from each other, whereas in the ^1H - ^1H TOCSY spectrum, all protons from one amino acid are correlated. In a ^1H - ^1H NOESY spectrum, correlations over space up to approximately 5 Å are observed. Therefore, it can give important information about the three dimensional structure of a protein.

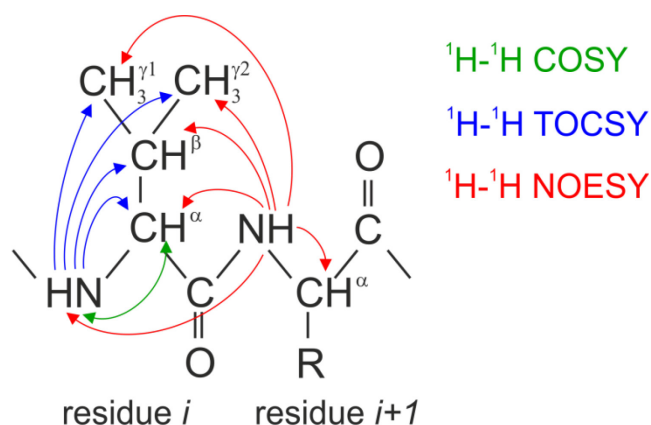


Figure 15. Residues i and $i+1$ of a protein backbone and the magnetization transfer in different 2D- ^1H NMR experiments. In the COSY (green) and TOCSY (blue) experiment magnetization transfer is shown for the amide proton of residue i and in the NOESY (red) experiment for the amide proton of residue $i+1$.

One of the most frequently used heteronuclear 2D protein NMR experiments is the ^1H - ^{15}N HSQC (heteronuclear single quantum coherence) experiment of a ^{15}N -labeled protein.⁹⁰ In this experiment, the resonance frequency of ^{15}N is correlated to the frequency of nitrogen-bound protons. Thereby, the magnetization of the hydrogen nucleus is transferred to the attached ^{15}N nucleus. The chemical shift is evolved on the nitrogen and the magnetization is then transferred back to the hydrogen for detection. In the protein backbone, each amino acid (except for proline) has an amide group and each amide proton gives rise to one single

peak in the ^1H - ^{15}N HSQC experiment. Additionally, nitrogen-connected protons in the side chains of tryptophan, asparagine and glutamine give a signal. In a folded protein, the peaks are usually well-dispersed and most of the individual peaks can be distinguished. A typical ^1H - ^{15}N HSQC spectrum is shown in chapter 4.2, Figure 2.

2.4.2.3 3D NMR

However, for the assignment of the peaks in the ^1H - ^{15}N HSQC spectrum to the respective amino acids in the protein, 3D experiments are needed. In addition to the general pulse sequence shown in Figure 14, they have an additional evolution and mixing period. Combining the pulse sequences for example from a 2D NOESY and a 2D HSQC gives a 3D NOESY-HSQC.

Triple resonance experiments can be recorded with ^{15}N - and ^{13}C -labeled proteins, correlating three different nuclei.⁹⁸ They are very useful because they give relatively simple spectra and provide sequential connectivities between residues. Most of the 3D spectra consist of a ^1H - ^{15}N plane (similar to an HSQC spectrum) expanded with a carbon dimension. Some common triple resonance experiments are HNCA, HN(CO)CA, CBCANH, CBCA(CO)NH, HNCO and HN(CA)CO. This nomenclature indicates key information about the experiment: The nuclei (CB = C^β , CA = C^α , CO = carbonyl carbon, NH/HN = atoms of amide group) are listed in order of their magnetization in the experiment. Nuclei that are used for transfer of the magnetization and of which the resonance frequency is not detected are set in brackets. Figure 16 shows the magnetization transfer in an HNCA experiment for residue i and residue $i-1$ of a protein. Starting from the amide proton, the magnetization is transferred to the amide nitrogen. In the following, a transfer to the C^α nucleus occurs that then goes back the same way to the amide proton. The magnetization from nitrogen is transferred to both C^α of residue i and residue $i-1$. In contrast, the HN(CO)CA gives only connectivities to residue $i-1$. In the HNCO and the HN(CA)CO, the connectivities occur through the carbonyl carbon instead of

C^α . Analysis of different triple resonance experiments in combination makes an assignment of the protein backbone possible.

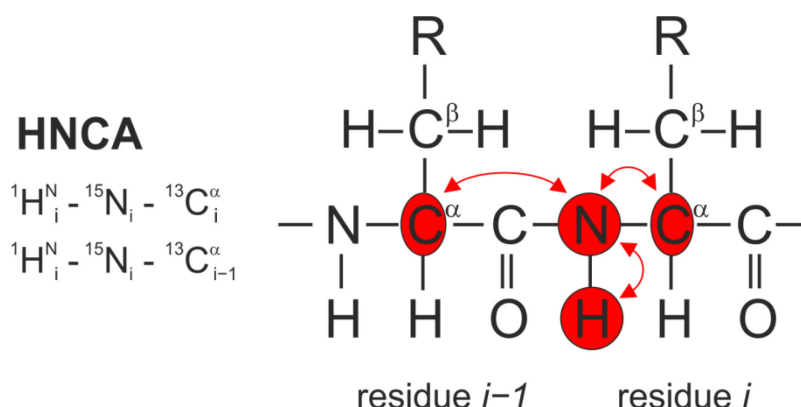


Figure 16. The triple resonance experiment HNCA. The red circles depict the nuclei that are detected. The red arrows indicate the way and direction of the magnetization. On the left is the description of the observed correlations. The figure is adopted from Lottspeich and Zorbas.⁹⁰

2.4.2.4 Applications

An assigned ${}^1\text{H}$ - ${}^{15}\text{N}$ HSQC spectrum can be used to identify amino acids that play a role in complex formation of two molecules. In a titration experiment, an unlabeled molecule is added stepwise to a ${}^{15}\text{N}$ -labeled protein of which ${}^1\text{H}$ - ${}^{15}\text{N}$ HSQC spectra are recorded. Upon complex formation, changes of the peak positions in the ${}^1\text{H}$ - ${}^{15}\text{N}$ HSQC spectrum for some amide protons can be observed. The shifted signals belong to amino acids that interact with the added molecule, thereby changing their chemical environment. Weighted averages of the ${}^1\text{H}$ and ${}^{15}\text{N}$ backbone chemical shift changes $\Delta\delta_{\text{HN}}$ of a particular residue can be calculated according to the equation

$$\Delta\delta_{\text{HN}} = \sqrt{\frac{(\Delta\delta_{\text{H}}^2 + 0.2 \Delta\delta_{\text{N}}^2)}{2}} \quad (3)$$

where $\Delta\delta_{\text{H}}$ is the ${}^1\text{H}$ and $\Delta\delta_{\text{N}}$ the ${}^{15}\text{N}$ chemical shift change. This method was used in chapter 4.2 and 4.3 to investigate the HydA1-PetF complex interface.

Apart from crystallography, NMR is the only method that can solve the structure of a protein and it is, therefore, very powerful. In order to calculate an NMR solution structure, after the identification and assignment of all signals, information about the protein structure need to be

obtained. Thereby, the NOESY experiments are most important, because they provide connectivities through space. The peak intensities of the NOE signals give information about the distances. A COSY spectrum can provide insight in the ϕ angle of the protein backbone. All information about distances and torsion angles are used as input for structure calculation software, where they are converted into energy terms and minimization of the total energy is tried to be achieved. This method was applied to the ferredoxin PetF and an NMR solution structure is presented in paper III, chapter 4.3.

2.4.3 Electron paramagnetic resonance spectroscopy

Electron paramagnetic resonance (EPR) spectroscopy is a technique that is used to study molecules with one or more unpaired electrons. These paramagnetic molecules can be organic radicals or systems that contain transition metals such as manganese, iron, nickel, cobalt or copper. EPR spectra can give insight into electronic structure and the geometrical environment of the paramagnetic center as well as the conformation and dynamics of macromolecules.⁹⁹ As in NMR, irradiation with a frequency, which matches the difference between the energy levels ΔE ; causes resonance. The resonance condition is expressed as

$$\Delta E = h \nu = g \beta B_0 \quad (4)$$

where h is Planck's constant ($6.6 \cdot 10^{-34}$ J·s), ν is the frequency, β is the Bohr magneton and B_0 is the applied magnetic field. The g -factor is dimensionless and describes the proportionality of the resonance energy with respect to the external magnetic field.¹⁰⁰ It is associated with the electronic characteristics of the investigated substance and provides information about the chemical environment and local symmetry of the unpaired electron distribution. The g -value for a free electron is 2.0023.

Protein samples are usually studied in frozen solution, which means that the molecules are immobilized, but randomly oriented. Therefore, the EPR spectrum shows a superposition of sub-spectra of all molecular orientations, each with its own effective g -factor. If the g -values

are dependent on the orientation of the molecule in the external magnetic field, they are described by the effective g -value. In general, a so-called EPR “powder” spectrum is obtained, where the three g -values g_1 , g_2 and g_3 can be recognized as “singularities” in the lineshape. The EPR spectrum can be *axial* (two g -values are identical), *rhombic* (all three g -values are different) or, if there is no g anisotropy, *isotropic*. Figure 17a shows a rhombic spectrum with the three g -values g_1 , g_2 and g_3 .

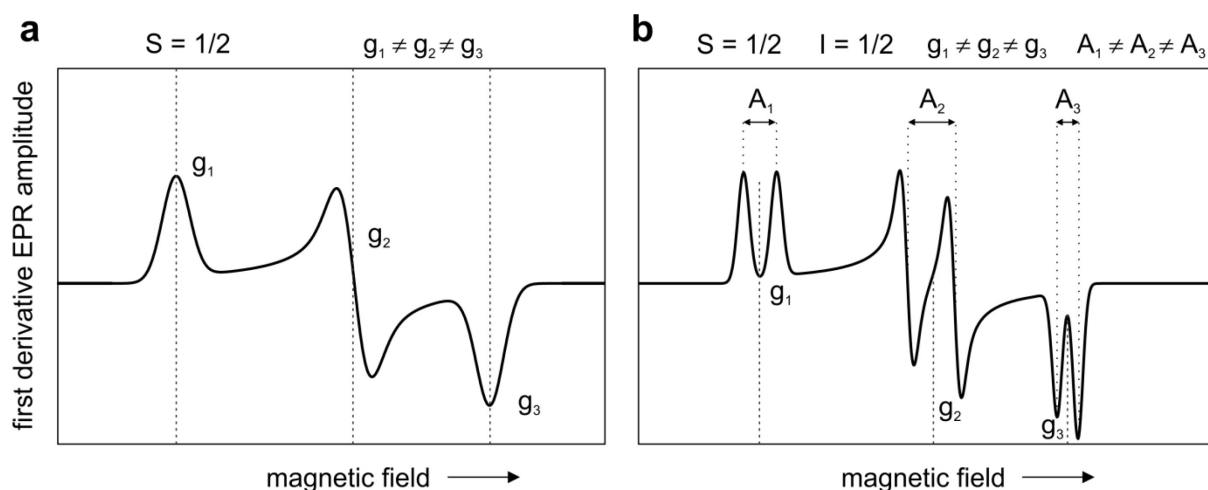


Figure 17. Simulated CW EPR spectra. **a.** Rhombic EPR spectrum ($g_1 \neq g_2 \neq g_3$) without hyperfine splitting. **b.** Rhombic EPR spectrum ($g_1 \neq g_2 \neq g_3$) with hyperfine splitting ($I = 1/2$). In this case, also the A tensor is rhombic and gives different A_1 , A_2 and A_3 .

Additionally to the g -values, also magnetic interactions with an nuclear spin I , leading to a hyperfine splitting of the signals (Figure 17b), can be observed. However, if the hyperfine splitting is small compared to the linewidth, it will not be resolved in a standard EPR experiment. In order to determine small unresolved hyperfine splittings, more advanced EPR techniques like ENDOR (electron nuclear double resonance) and HYSCORE (hyperfine sublevel correlation) have to be applied. These techniques are used in chapter 2.4 (paper IV) to investigate ^{57}Fe hyperfine couplings (nuclear spin $I = 1/2$) of ^{57}Fe -labeled HydA1. Weak hyperfine couplings are usually observed in HYSCORE, whereas stronger hyperfine couplings are better detected in ENDOR spectra. In both methods, the spectra are recorded at a certain field positions that correspond to a set of molecular orientations with respect to the external magnetic field. In ENDOR, the radio frequency is scanned, whereas HYSCORE is a

2D pulse EPR method with variable t_1 and t_2 times as explained for 2D NMR experiments (Figure 14). The hyperfine splitting can provide information about the spin density distribution over a molecule.

In the research field of hydrogenases, EPR has been a powerful tool, because many states of the catalytic cycle are paramagnetic. In HydA1, these include H_{ox} , H_{sred} and H_{ox-CO} .^{7,18} Also the unmaturation hydrogenase with only the [4Fe-4S]-cluster is EPR active in its reduced form. HYSCORE and ENDOR measurements give information about the delocalization of the unpaired electron and the coupling between the [4Fe-4S]-cluster and the [2Fe]-subsite. CW EPR spectra of the H_{ox-CO} state and the unmaturation, reduced form of HydA1 are shown in Figure 18.

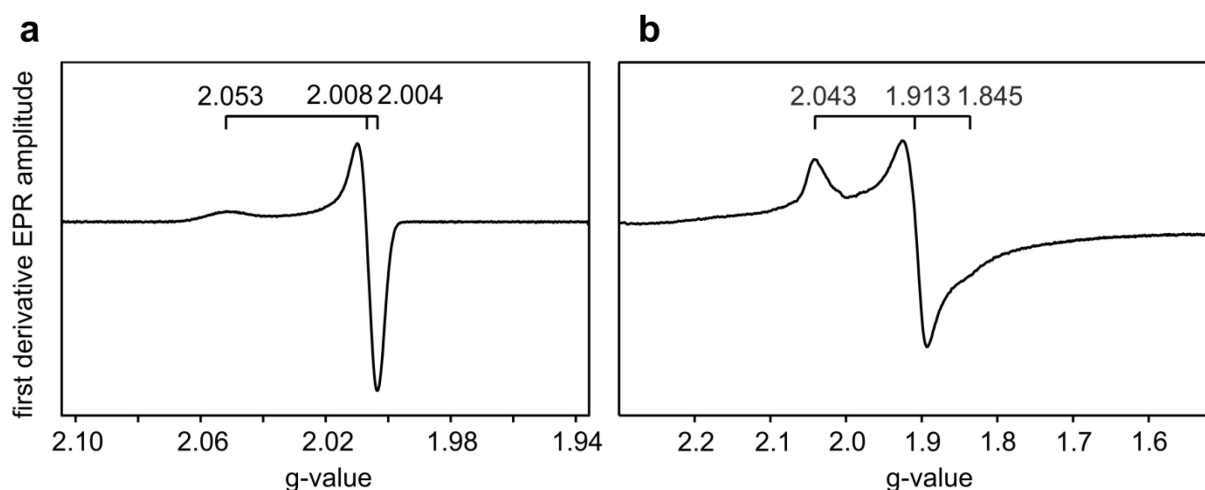


Figure 18. CW EPR spectra. **a.** The almost axial EPR spectrum of the H_{ox-CO} state with the g-values indicated. **b.** EPR spectrum of unmaturation HydA1 containing only the reduced [4Fe-4S]-cluster. The g-values of this rhombic spectrum are characteristic for reduced [4Fe-4S]-clusters.

2.5 Mössbauer spectroscopy

2.5.1 Basic concepts

Mössbauer spectroscopy is a spectroscopic technique based on the Mössbauer effect: the *recoilless resonance absorption and emission of γ -radiation*. It was discovered 1957 by the German scientist Rudolf Mössbauer during his doctoral thesis.⁹⁹ γ -radiation is an electromagnetic radiation (photons) with extremely high energy, produced by the decay of

radioactive nuclides upon transition from a meta-stable higher to a lower energy state. The phenomenon is commonly known as γ -decay. The emission (or absorption) of a photon by a free nucleus in the gas phase or as liquid generally results in recoil of the nucleus, leading to an energy loss of the emitted photon:¹⁰¹

$$E_{\gamma} = E_0 - E_R \quad (5)$$

E_{γ} is the energy of the emitted photon, E_0 the mean nuclear energy (difference between higher and lower energy state) and E_R is the recoil energy. The recoil is caused by the transfer of momentum from the photon upon emission or absorption. The recoil energy can be written as:

$$E_R = \frac{E_0^2}{2Mc^2} \quad (6)$$

where M is the mass of the nucleus and c the speed of light. The recoil effect causes energy separation between the detectable emission and the absorption lines, which is six orders of magnitude larger than the natural width of the γ -lines. Thus, in gases and liquids, they do not overlap and γ -resonance is not possible. Though, as found by Mössbauer, if the nucleus is embedded in a lattice (a crystal), there is a certain finite probability that the lattice as a whole takes the recoil momentum. In this case, M in equation 6 is the mass of the whole lattice and E_R becomes negligibly small.

The recoil can also excite or annihilate a lattice vibration (so-called phonon). In both cases, nuclear γ -resonance becomes impossible. However, because the energy of these phonons is quantized, there is a certain finite probability of a zero-phonon process. This probability factor is known as the Mössbauer-Lamb factor f and denotes the fraction of γ -emission or -absorption occurring without recoil, meaning that γ -resonance becomes possible.¹⁰²

The chemical environment of the Mössbauer nuclei in the γ -absorber (the investigated sample) is distinct from that of the nuclei in the emitter (the source). Therefore, the energy differences of the nuclear ground and excited states are different in the source and the absorber, *i.e.* absorption energies are different from the energy of the emitted γ -rays. As a

consequence, the energy has to be modulated for resonance absorption. This is realized using the Doppler effect by moving the source toward (+v) and away (-v) from the sample, which causes a Doppler shift of the emitted γ -photons proportional to the velocity v. If the emission and absorption line overlap, resonance occurs, which is seen as a reduction in the rate of transmission of γ -rays through the absorber. Due to the Doppler modulation, the energy scale of the Mössbauer spectra is given in mm/s.

2.5.2 ^{57}Fe Mössbauer spectroscopy

Mössbauer spectroscopy is by far most extensively used with the isotope ^{57}Fe , although there are other isotopes that can be studied by Mössbauer spectroscopy (e.g. ^{61}Ni , ^{67}Zn , $^{191,193}\text{Ir}$).¹⁰¹ In ^{57}Fe Mössbauer spectroscopy, ^{57}Co is the source of γ -radiation. It decays to an excited state of ^{57}Fe by electron capture with a half-life of about 270 days. Initially, the 136.5 keV nuclear level of ^{57}Fe ($I = 5/2$) is populated. This excited state decays to the 14.4 keV excited state, which decays further to the ^{57}Fe ground state by emitting a γ -quantum of 14.4 keV (Figure 19).¹⁰³

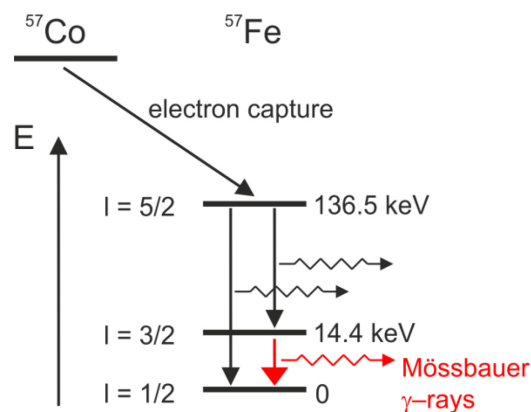


Figure 19. Decay scheme of ^{57}Co to ^{57}Fe and the ^{57}Fe nuclear transitions.

2.5.3 The Mössbauer spectrum

The transmitted γ -rays are detected with a γ -counter (y-axis). They are recorded as function of the Doppler velocity (x-axis), giving rise to the Mössbauer spectrum. A simple Mössbauer spectrum in the absence of magnetic fields, a so-called quadrupole spectrum, is shown in Figure 20a.

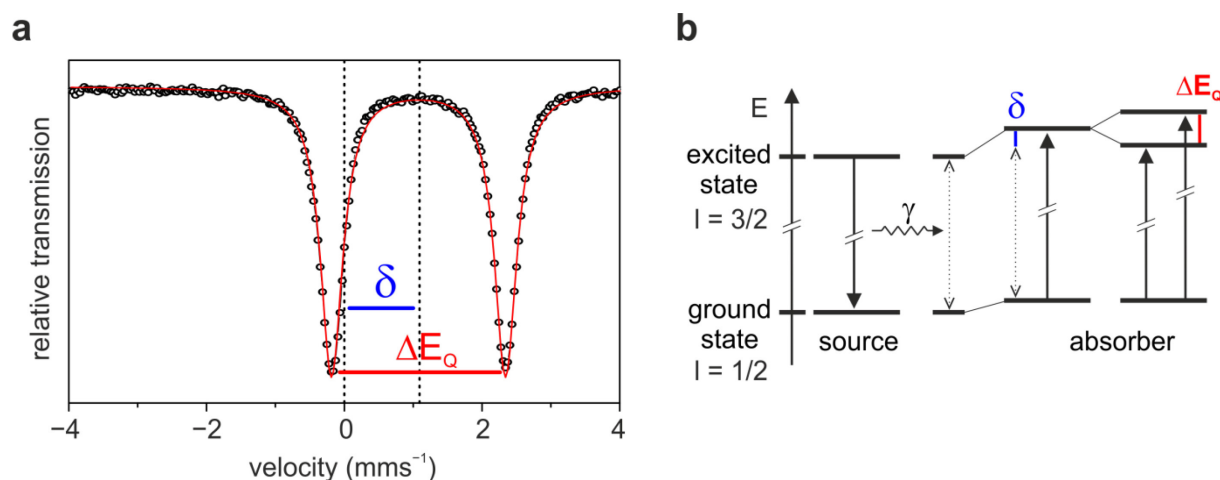


Figure 20. a. Simple Mössbauer spectrum with the isomer shift δ and quadrupole splitting ΔE_Q shown. b. Origin of the isomer shift δ and quadrupole splitting ΔE_Q depicted in the energy level diagram of the absorber.

It is characterized by two parameters, the isomer shift δ and the quadrupole splitting ΔE_Q . Both parameters are given in mm/s. The isomer shift is determined by the average position of the doublet. The quadrupole splitting is given by the separation of the two lines of the doublet. The isomer shift arises from Coulomb interactions between the nucleus and its environment, which is mainly given by s-electrons. It is a product of the charge distribution of the nucleus and the electronic charge density at the nucleus. The electronic densities differ for the source and the absorber because of different chemical composition, which leads to a difference in transition energies from the ground to the excited state (Figure 20b). Therefore, resonance does not appear at Doppler velocity 0, but is shifted by the isomer shift δ . The isomer shift provides information about the oxidation state of the nucleus, the spin state, the number of ligands and their σ -donor and π -acceptor strengths. It is most insightful to interpret the determined parameters in comparison to a similar compound. Some general trends have been obtained from a systematic study of a variety of iron compounds: i) a lower oxidation state leads to a more positive value of the isomer shift, ii) high-spin compounds have a larger isomer shift than low-spin compounds, iii) ionic/hard ligands cause higher isomer shifts than covalent/soft ligands, iv) σ -donating ligands and d_{π} - p_{π} -backdonation of a metal to a ligand results in more negative isomer shifts (s-electron density is increased).¹⁰¹

The quadrupole splitting arises from the splitting of the $I = 3/2$ excited nuclear state (Figure 20b). This state has a non-spherical charge distribution (as compared to the $I = 1/2$ state), producing a quadrupole moment that interacts with an inhomogeneous electric field. This field is generated by a non-cubic charge distribution of the surrounding electrons. The quadrupole moment provides information about the symmetry of the ligand charges around the nucleus and the population of the iron 3d orbital, which is connected to bond properties.¹⁰¹ In addition to the isomer shift and the quadrupole splitting of the Mössbauer spectrum shown in Figure 20a, there can be magnetic hyperfine splitting as a result of interactions between the nucleus and a magnetic field. Such spectra are recorded with an external applied field and paramagnetic properties of a sample can be probed.

In this work, the novel synthesis of ^{57}Fe -labeled $[\text{Fe}_2(\text{adt})(\text{CO})_4(\text{CN})_2]^{2-}$ (Figure 5b) was used to specifically label the binuclear $[\text{2Fe}]$ -subsite of the H-cluster and Mössbauer spectra were recorded. Complementary, the $[\text{4Fe-4S}]$ -cluster was ^{57}Fe -labeled by chemical reconstitution with $^{57}\text{FeCl}_3$ and investigated by Mössbauer spectroscopy. The results are presented in paper IV, chapter 4.4.

3 SUMMARY OF JOURNAL ARTICLES

3.1 Paper I

Hybrid [FeFe]-hydrogenases with modified active sites show remarkable residual enzymatic activity

The unassisted artificial maturation⁸³ as described earlier in chapter 1.3.3 opens new ways to study [FeFe]-hydrogenases. One of them is the insertion of non-native cofactors into the unmaturation form of the hydrogenase. In this study, this procedure has been exploited to test 15 different synthetic iron complexes for their integration into unmaturation HydA1.

By monitoring the behavior of the CO vibration modes (chapter 2.3.2), FTIR spectroscopy was employed to verify if the complex incorporation was successful. Moreover, all complexes inserted into HydA1 were tested for H₂ production and oxidation activity (chapter 2.2). In 2013, Berggren *et al.* demonstrated that variants with a modified bridging dithiolate (propanedithiolate **2a**, oxodithiolate **4**, see Figure 21) integrate into HydA1.⁷⁹ In this work, variants with a thiodithiolate **5**, an *N*-methyldithiolate **3a** and a dimethyldithiolate **6** bridge were incorporated into HydA1. Furthermore, mono-cyanide variants with five CO and one CN⁻ ligand (instead of four CO and two CN⁻ ligands) of the azadithiolate **1b**, propanedithiolate **2b** and *N*-methyldithiolate **3b** analog were shown to bind to unmaturation HydA1. Synthetic models containing no CN⁻ and only CO ligands could not be incorporated. None of the newly synthesized hybrid [FeFe]-hydrogenases showed improved catalytic activity. However, the mono-cyanide variant with an azadithiolate bridge **1b** showed ≈50% of the native enzyme activity. It can, therefore, be inferred that the CN⁻ ligands serve rather for anchoring the [2Fe]-subsite in the protein pocket than being essential for the catalytic activity. The propanedithiolate **2a** and *N*-methyldithiolate **3a** bridgehead analog as well as their mono-cyanide variants **2b** and **3b** showed residual H₂ conversion activity. In all cases, H₂ production and oxidation activities are affected in the same way, giving good evidence that

the catalytic enzyme reaction in both directions relies on the same physical properties of the [2Fe]-subsite.

In summary, one can conclude that the Brønsted base function of the bridgehead and its conformational flexibility are essential for the catalytic activity. The findings also indicate that even small changes in the active site lead to a severe decrease of enzymatic activity. It can, therefore, be assumed that the approach of the incorporation of non-native cofactors into unmaturred HydA1 in order to increase the enzyme activity is only promising when also changing specifically the amino acid surrounding. Nevertheless, interesting insight into functional features of the active site can be gained from studying hybrid [FeFe]-hydrogenases.

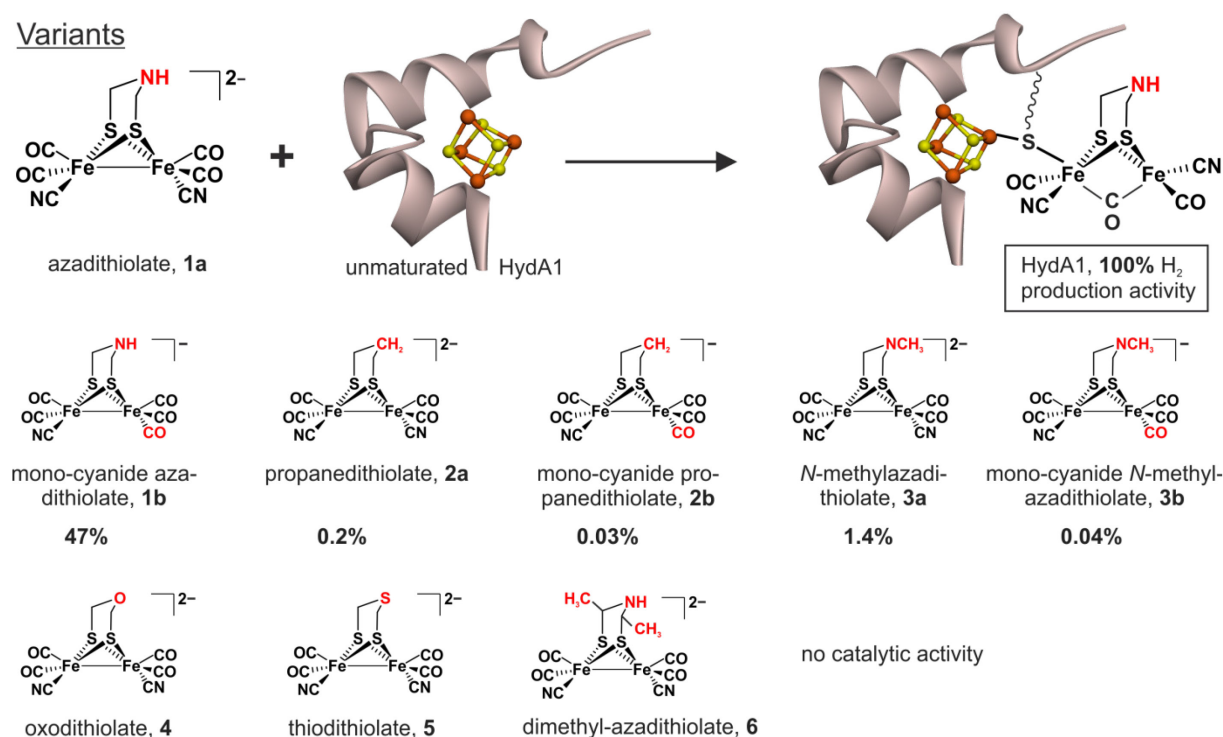


Figure 21. Artificial maturation of $[\text{Fe}_2(\text{adt})(\text{CO})_4(\text{CN})_2]^{2-}$ with unmaturred HydA1. Active hybrid HydA1 is formed having an H₂ production activity identical to that of the native enzyme. It was, therefore, set to 100% activity. Below shown are all variants that could be incorporated into HydA1. The H₂ production activities of HydA1 maturred with these variants are indicated.

3.2 Paper II

Enhancing hydrogen production of microalgae by redirecting electrons from photosystem I to hydrogenase

The results presented in this paper follow a different approach than described in paper I of increasing the catalytic activity of HydA1. It focusses on investigations to improve *in vivo* H₂ production of green algae. Since green algae like *Chlamydomonas reinhardtii* are so far the only known organisms that produce H₂ photosynthetically,¹⁷ they are interesting targets for technological applications.¹⁰⁴ HydA1 receives its electrons for the reduction of protons from the ferredoxin PetF (chapter 1.2.3), which is the electron acceptor of photosystem I. PetF, however, provides electrons to different metabolic pathways.⁴⁸ Most electrons are delivered to the ferredoxin-NADP⁺-oxidoreductase (FNR), which mediates electrons for CO₂ fixation. Down-regulation of this competing process leads to an increased electron delivery to HydA1 and, therefore, higher H₂ production rates.¹⁰⁵

In this study, PetF residues are identified that play a role in PetF/FNR and PetF/HydA1 interaction. This was done by parallel NMR titration experiments of ¹⁵N-labeled PetF supplemented with increasing amounts of FNR or HydA1 and analysis of chemical shift perturbations (chapter 2.4.2.4). Although it was found that most identified PetF residues are involved in complex formation with both proteins, the two aspartate residues D19 and D58 could be identified to be only involved in FNR binding. The identification of these two residues suggests that specific negatively charged amino acids in the binding interface of PetF play a role in the differentiation of the binding partners.

Moreover, D19 and D58 were tested for their potential as targets for improved H₂ production of HydA1. They were, therefore, mutated to alanine (D19A, D58A and the double variant D19A/D58A) and tested in a light-driven H₂ production assays. In the absence of FNR, HydA1 H₂ production rates with all these three PetF mutants as electron donor are not affected, confirming the NMR results that these residues are not important for PetF-HydA1

binding. In a competition assay in the presence of FNR, the H₂ production activity of HydA1 is diminished to 7% compared to the H₂ production activity in the absence of FNR (set to 100%) using wild-type PetF (Figure 22). However, with the variants PetF-D19A and PetF-D58A, the activity is increased 1.5 and 2.5-fold (10% and 19%, respectively). H₂ production of HydA1 with the double variant PetF-D19A/D58A shows a 4-fold increased H₂ production rate (28%), indicating a synergistic enhancement of single effects. Furthermore, combination of the PetF double mutant with mutations of FNR, which were shown before to negatively affect PetF-FNR interactions (K83L, K89L),¹⁰⁶ show an increased HydA1 H₂ production rate of up to 37% (Figure 22).

The variant PetF-D19A/D58A could be used for implementation in H₂ production optimized *C. reinhardtii* strains in order to further increase catalytic activity. This combined metabolic engineering approach can be a step towards the design of H₂-producing organisms for technological applications.

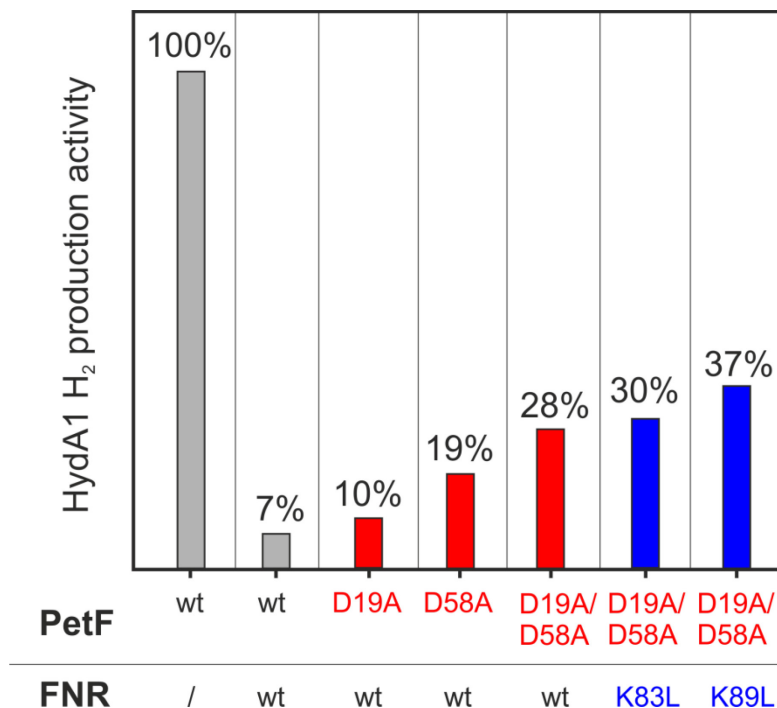


Figure 22. Light-dependent H₂ production activities of HydA1 with wild-type (wt) PetF and wt-FNR as well as with mutants of PetF and FNR as indicated. The activity of HydA1 with wt-PetF in the absence of FNR is set to 100%.

3.3 Paper III

Structural insight into the complex of ferredoxin and [FeFe] hydrogenase from *Chlamydomonas reinhardtii*

Paper III is a follow-up study of paper II. In this work, the complex of the ferredoxin PetF and HydA1 is examined in more detail. Since there is no crystal structure available of *C. reinhardtii* PetF, a PetF NMR solution structure, based on several 3D and 2D NMR experiments, was determined. PetF and HydA1 form a transient electron-transfer complex, for which also no X-ray crystal structure is available. Therefore, a protein-protein docking structure based on the PetF NMR solution structure and the structure of unmaturation HydA1¹⁰⁷ was calculated. This docking model is the basis for the identification of residue substitution targets in order to improve the *in vivo* H₂ production of HydA1.

The binding interface of PetF with HydA1 presented in paper II lacks information about amino acid residues nearby the [2Fe-2S]-cluster of PetF. This is due to paramagnetic relaxation enhancement as described in chapter 2.4.2.1. However, the residues nearby the [2Fe-2S]-cluster are important since some of them reside directly at the interface. The paramagnetic relaxation enhancement was overcome by gallium-substitution of the irons in PetF's [2Fe-2S]-cluster. All residues that were not visible before became detectable and most of them are affected upon HydA1-binding. These new data together with site-directed mutagenesis data^{51,108} were used as input for the docking of PetF to HydA1. The thereby obtained PetF-HydA1 model structure (Figure 23) revealed that PetF-E90 and HydA1-R187 are the residues with the largest number of H-bonds and salt bridges to HydA1 and PetF, respectively. The importance of these residues for the HydA1-PetF complex formation was already demonstrated.^{51,109} Among other charged residues that were identified before, the complex model revealed several amino acids with hydrophobic or polar side-chains that are important for complex formation.

In total, there are three residues that are proposed as possible targets for site-directed mutagenesis to enhance *in vivo* H₂ production: i) PetF-E91A, neighbor of the important E90 residue. This residue is not essential for PetF-HydA1 complex formation as indicated by chemical shift perturbation data. ii) HydA1-R187A. Based on published results for HydA1-R187D, a destabilization of the PetF-HydA1 complex is assumed, but no complete loss of H₂ production. iii) HydA1-T186A, HydA1-R187's neighbor. In analogy to the residues T12 and R13 of cytochrome *c*, one would expect an increased binding affinity of PetF to HydA1.¹¹⁰ A combination of these mutations might result in increased PetF-dependent H₂ production of HydA1.

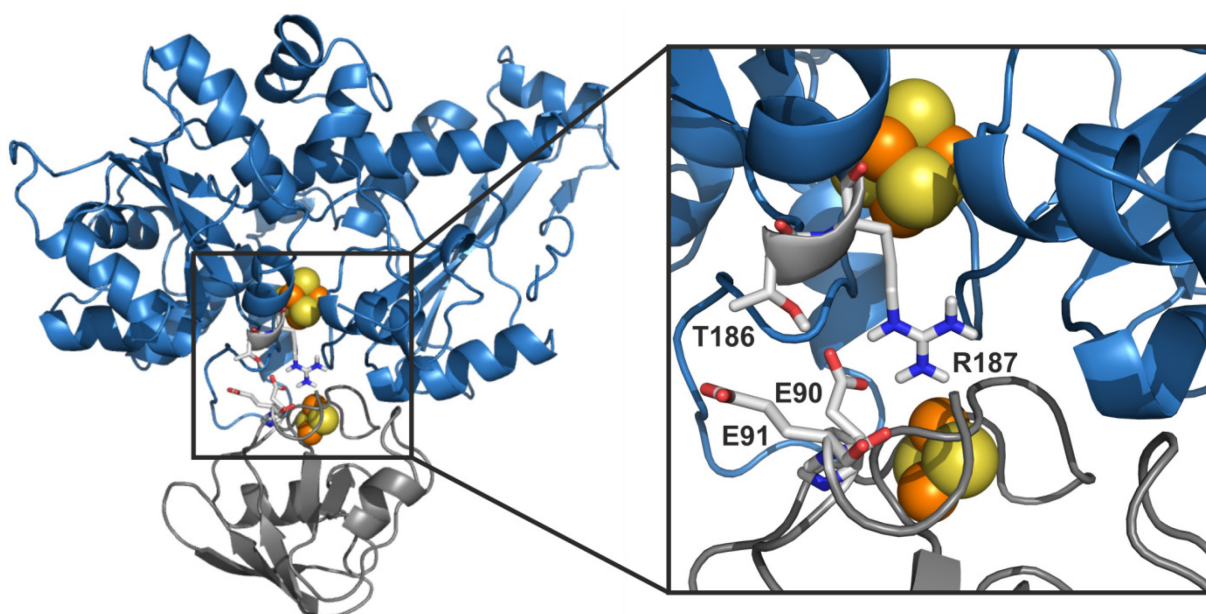


Figure 23. Model of the PetF-HydA1 complex and zoom into the relevant interface region. HydA1 is shown in blue, PetF in gray. The FeS-clusters are displayed as spheres with Fe colored orange and S colored yellow. The HydA1 amino acids T186 and R187 and the PetF residues E90 and E91 (see text) are depicted as sticks.

3.4 Paper IV

Spectroscopic investigations of [FeFe] hydrogenase matured with $[\text{}^{57}\text{Fe}_2(\text{adt})(\text{CN})_2(\text{CO})_4]^{2-}$

Paper IV presents the novel synthesis of $[\text{}^{57}\text{Fe}_2(\text{adt})(\text{CN})_2(\text{CO})_4]^{2-}$ by the Rauchfuss group and spectroscopic investigations of HydA1 matured with $[\text{}^{57}\text{Fe}_2(\text{adt})(\text{CN})_2(\text{CO})_4]^{2-}$ in the CO-inhibited state $\text{H}_{\text{ox}}\text{-CO}$. Via the artificial maturation procedure, HydA1 becomes not only available with modified active sites as described in paper I, but also with isotope labeled versions. This is an extremely helpful tool for detailed spectroscopic investigations⁹⁶ and can shed light on the still not fully understood catalytic mechanism of HydA1.

Finding a route for the synthesis of $[\text{}^{57}\text{Fe}_2(\text{adt})(\text{CN})_2(\text{CO})_4]^{2-}$ is challenging because relevant precursors like $\text{Fe}(\text{CO})_5$ are not available as $^{57}\text{Fe}(\text{CO})_5$. Therefore, $^{57}\text{Fe}(\text{CO})_5$ was avoided as intermediate and $[\text{H}^{57}\text{Fe}(\text{CO})_4]^-$ was used instead. Selective labeling with ^{57}Fe introduces a nucleus that is highly responsive to Mössbauer (see chapter 2.5.2) and nuclear resonance vibrational spectroscopy (NRVS). With a nuclear spin $I = 1/2$, ^{57}Fe is also ideal for investigation by EPR techniques like ENDOR and HYSCORE (chapter 2.4.3).³⁵ So far, there are only very few Mössbauer studies on [FeFe]-hydrogenases due to the difficulty of ^{57}Fe -labeling and the required high amounts of sample. Additionally, Mössbauer analysis has been complicated due to overlapping signals of the [2Fe]-subsite, the [4Fe-4S]-cluster and the accessory [FeS]-clusters.^{36,111,112}

The presented procedure of selective ^{57}Fe labeling of the [2Fe]-subsite solves this problem and provides a clean spectrum of the $[2^{57}\text{Fe}]$ -subsite, clearly showing two non-equivalent iron sites of low-spin iron in a low oxidation state. Furthermore, complementary ^{57}Fe enrichment of the [4Fe-4S]-cluster was realized by reconstitution of the [4Fe-4S]-cluster with $^{57}\text{FeCl}_3$. The selective labeling of the two H-cluster components also greatly simplified the assignment of observed pulse EPR signals. Overall, they confirm previous results from studies of the *Desulfovibrio desulfuricans* [FeFe]-hydrogenase, indicating a strong spin exchange coupling

between the two sub-clusters in the H_{ox} -CO state. NRVS spectra further confirm successful selective ^{57}Fe -labeling of the [2Fe]-subsite. The only previous NRVS spectra of an [FeFe]-hydrogenase suffer from unspecific labeling of [FeS]-clusters. There, the ^{57}Fe -labeling of the hydrogenase was obtained differently through an *in vitro* maturation by the ^{57}Fe -labeled maturases HydE, HydF and HydG.³⁷ The NRVS spectra presented in this works do not show any unspecific labeling.

In summary, the work describes a versatile route to ^{57}Fe -labeled iron carbonyls and the application of $[\text{}^{57}\text{Fe}_2(\text{adt})(\text{CN})_2(\text{CO})_4]^{2-}$ by maturing HydA1. In this study, the ^{57}Fe -labeled non-catalytically active H_{ox} -CO state is presented to demonstrate the successful selective labeling of the [2Fe]-subsite precursor. Investigation of the other labeled states generated by this method may contribute to a better insight into the catalytic mechanism of HydA1.

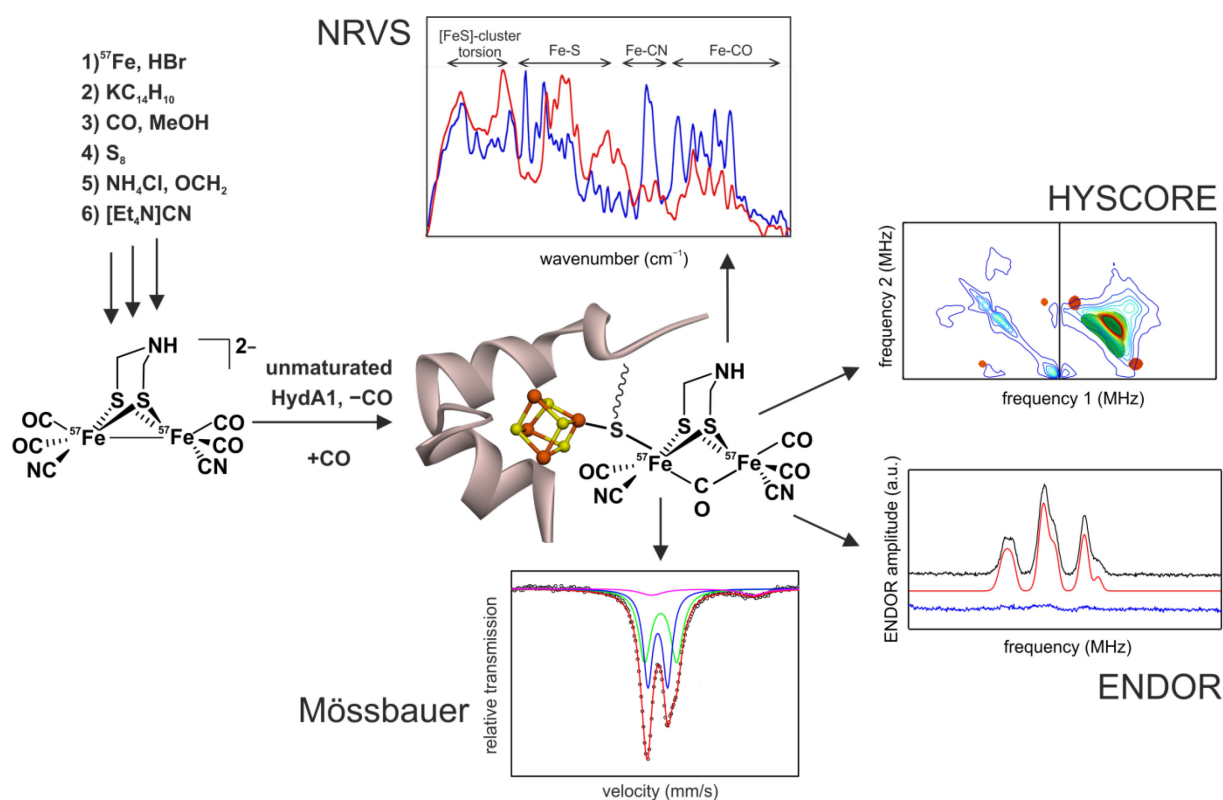


Figure 24. Simplified synthesis scheme of $[\text{}^{57}\text{Fe}_2(\text{adt})(\text{CN})_2(\text{CO})_4]^{2-}$ and the different spectroscopic techniques that can be applied after the insertion of $[\text{}^{57}\text{Fe}_2(\text{adt})(\text{CN})_2(\text{CO})_4]^{2-}$ into HydA1.

4 JOURNAL ARTICLES

4.1 Paper I

Hybrid [FeFe]-hydrogenases with modified active sites show remarkable residual enzymatic activity

Judith F. Siebel, Agnieszka Adamska-Venkatesh, Katharina Weber, Sigrun Rumpel, Edward Reijerse, Wolfgang Lubitz

Reproduced with permission from *Biochemistry* **2015**, *54*, 1474–1483. Copyright © 2015 American Chemical Society.

DOI: 10.1021/bi501391d

Journal name: Biochemistry

Impact factor: 3.015 (in 2014)

Author: first author

Contribution: – 70 %

- I made all biological samples
- I performed all biological analyses/enzyme activity measurements
- I performed the DFT calculations
- I was largely involved in the production of the manuscript

K. Weber performed the synthesis of the model complexes, A. Adamska-Venkatesh made the FTIR measurements and helped with the analysis.

4.1.1 Journal article

BIOCHEMISTRY

including biophysical chemistry & molecular biology

Article

pubs.acs.org/biochemistry

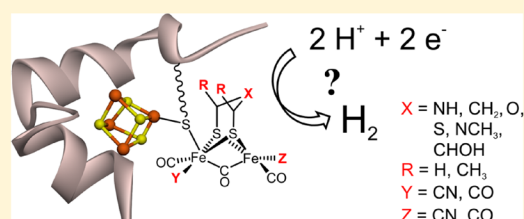
Hybrid [FeFe]-Hydrogenases with Modified Active Sites Show Remarkable Residual Enzymatic Activity

Judith F. Siebel, Agnieszka Adamska-Venkatesh, Katharina Weber, Sigrun Rumpel, Edward Reijerse,* and Wolfgang Lubitz*

Max Planck Institute for Chemical Energy Conversion, Stiftstrasse 34-36, D-45470 Muelheim an der Ruhr, Germany

Supporting Information

ABSTRACT: [FeFe]-hydrogenases are to date the only enzymes for which it has been demonstrated that the native inorganic binuclear cofactor of the active site $\text{Fe}_2(\text{adt})(\text{CO})_3(\text{CN})_2$ (adt = azadithiolate = $[\text{S}-\text{CH}_2-\text{NH}-\text{CH}_2-\text{S}]^{2-}$) can be synthesized on the laboratory bench and subsequently inserted into the unmaturation enzyme to yield fully functional holo-enzyme (Berggren, G. et al. (2013) *Nature* 499, 66–70; Esselborn, J. et al. (2013) *Nat. Chem. Biol.* 9, 607–610). In the current study, we exploit this procedure to introduce non-native cofactors into the enzyme. Mimics of the binuclear subcluster with a modified bridging dithiolate ligand (thiodithiolate, *N*-methylazadithiolate) and three variants containing only one CN^- ligand were inserted into the active site of the enzyme. We investigated the activity of these variants for hydrogen oxidation as well as proton reduction and their structural accommodation within the active site was analyzed using Fourier transform infrared spectroscopy. Interestingly, the monocyanoide variant with the azadithiolate bridge showed ~50% of the native enzyme activity. This would suggest that the CN^- ligands are not essential for catalytic activity, but rather serve to anchor the binuclear subsite inside the protein pocket through hydrogen bonding. The inserted artificial cofactors with a propanedithiolate and an *N*-methylazadithiolate bridge as well as their monocyanoide variants also showed residual activity. However, these activities were less than 1% of the native enzyme. Our findings indicate that even small changes in the dithiolate bridge of the binuclear subsite lead to a rather strong decrease of the catalytic activity. We conclude that both the Brønsted base function and the conformational flexibility of the native azadithiolate amine moiety are essential for the high catalytic activity of the native enzyme.



INTRODUCTION

Hydrogenases are enzymes that catalyze the reversible reaction of molecular hydrogen to electrons and protons: $\text{H}_2 \rightleftharpoons 2 \text{H}^+ + 2 \text{e}^-$.^{1,2} Generally, the activation of hydrogen is difficult due to its strong, nonpolar H–H bond.³ However, in hydrogenases, the reaction takes place at ambient temperature and pressure.^{4–6} The two main classes of these enzymes are the [FeFe]-hydrogenases and [NiFe]-hydrogenases, named according to the metal ions present in their active sites.^{7–10} In general, [FeFe]-hydrogenases are more active in H_2 production.¹¹ Understanding the function of these enzymes will form the basis for a rational design of efficient artificial systems for production of H_2 as a renewable energy carrier for the future.^{12–18}

In [FeFe]-hydrogenases, the catalytic reaction takes place at the so-called H-cluster, a [4Fe-4S]-cluster connected via the thiolate of a cysteine residue to a binuclear [2Fe]-subsite¹⁹ (Figure 1a,b). [FeFe]-hydrogenases from anaerobic bacteria bind several [FeS]-clusters in addition to the H-cluster,^{7,8} whereas in the [FeFe]-hydrogenases of green algae like HydA1 from *Chlamydomonas reinhardtii*, these accessory [FeS]-cluster are absent.^{6,20} In vivo, the [2Fe]-subsite is synthesized and inserted by the hydrogenase maturation proteins HydE, HydF, and HydG.^{21,22} HydG has been recently shown to play a key

role in the maturation process since it produces an {Fe-(CO)₂(CN)} “synthon” that can be regarded as the first precursor to the binuclear subsite.^{23,24} The two Fe atoms of the [2Fe]-subsite are referred to as proximal (Fe_p) and distal (Fe_d) iron relative to the [4Fe-4S]-cluster and are connected via an azadithiolate bridge.⁸ Each Fe is coordinated by a CO and CN^- ligand as well as an additional CO^{25} which can be bridging or terminal depending on the redox state of the H-cluster.²⁶ Fe_p is six-coordinated, whereas Fe_d is five-coordinated leaving an open coordination site where H_2 production and oxidation are proposed to occur.^{27–29} The unusual, small inorganic ligands CO and CN^- are strong field ligands that keep the Fe center in the low-spin state.³⁰

Since the crystal structures of [FeFe]- and [NiFe]-hydrogenase were solved,^{7–9,25,34,35} chemists started to synthesize model compounds that mimic their active sites.^{1,15,16,18} In 1999, three groups separately reported the first [FeFe]-hydrogenase active site model $[\text{Fe}_2(\text{pdt})(\text{CO})_4(\text{CN})_2]^{2-}$ **2a** (pdt = propanedithiolate, Figure 1c).^{36–38} At that time, the nature of the bridgehead atom was not uniquely identified since

Received: November 7, 2014

Revised: January 22, 2015

Published: January 29, 2015

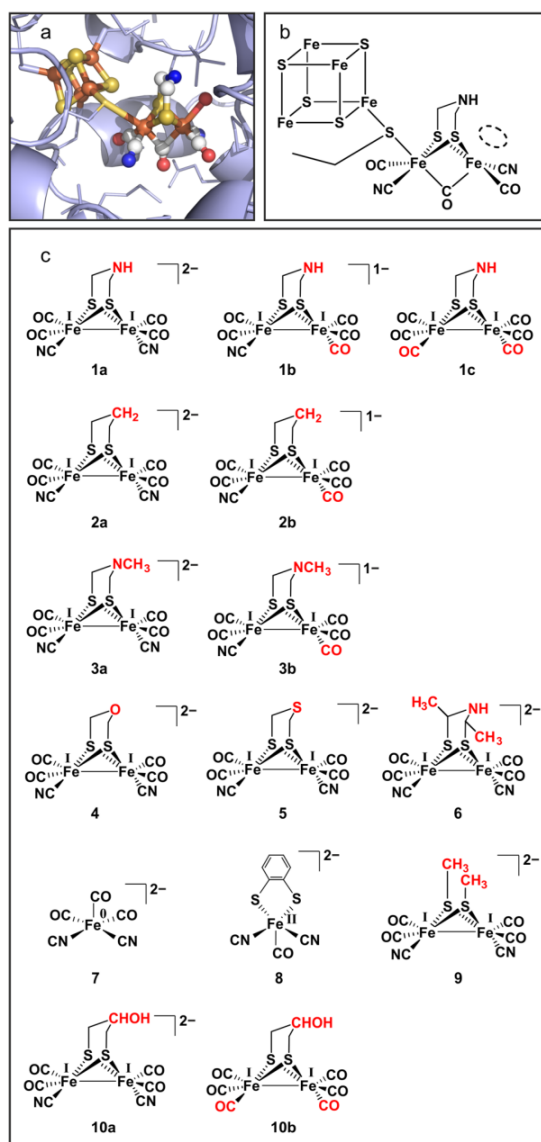


Figure 1. (a) Active site (H-cluster) of *C. reinhardtii* [FeFe]-hydrogenase HydA1 in its protein surrounding. The protein backbone is shown as well as the amino acid residues near the H-cluster. An alignment of the crystal structures of *C. reinhardtii* HydA1 (3LX4³¹) and *Clostridium pasteurianum* (3C8Y³²) was used for the image, generated using the program PYMOL.³³ (b) Schematic structure of the H-cluster with the open coordination site shown as an ellipsoid. (c) Series of all [2Fe]-model compounds that were synthesized and used in the artificial maturation attempts of *C. reinhardtii* HydA1.

C, N, and O could not be distinguished at the available crystallographic resolution. Therefore, additional mimics [Fe₂(adt)(CO)₄(CN)₂]²⁻ **1a** (adt = azadithiolate) and [Fe₂(odt)(CO)₄(CN)₂]²⁻ **4** (odt = oxadithiolate) were synthesized^{39,40} (see Figure 1c). As free complexes in solution **1a**, **2a**, and **4** have a low activity¹ and can therefore be classified as structural rather than functional active site models. A few years later, based on arguments related to the possible catalytic mechanism and a reanalysis of the crystal structure, Nicolet et

al. proposed the nature of the bridgehead atom to be nitrogen.¹⁹ This assignment was later experimentally supported by the magnetic resonance studies of Silakov et al.⁴¹ and Erdem et al.⁴²

Very recently, Berggren et al. demonstrated that **1a**, **2a**, and **4** can be bound to the native maturase HydF, which subsequently delivers the model compound to the unmaturation form of HydA1 that only contains the [4Fe-4S]-cluster but not the [2Fe]-subsite.⁴³ Since only the hybrid enzyme containing mimic **1a** showed full hydrogenase activity, this experiment provided unequivocal evidence for an amine function in the dithiolate bridging ligand.⁴³ Shortly thereafter, Esselborn et al. showed that **1a** can be inserted also directly into unmaturation HydA1⁴⁴ (i.e., unassisted by HydF). The hybrid HydA1-**1a** is fully active and indistinguishable from the native hydrogenase.^{43,44} The electron paramagnetic resonance (EPR) and Fourier transform infrared (FTIR) spectra of HydA1-**1a** showed the same redox states as the native *Chlamydomonas reinhardtii* hydrogenase HydA1.^{43–45} Subsequent FTIR spectroelectrochemical experiments revealed reduction potentials identical to those of the native enzyme.⁴⁵ The FTIR spectra of HydA1-bound **2a** and **4** exhibited vibrational modes from CO, bridging CO, and CN⁻ ligands similar to those of the native H-cluster, but no H₂ production activity was reported.⁴³

In the current study, we investigate a series of model compounds that can be introduced into unmaturation HydA1 (Figure 1c). The central bridgehead atom was replaced by sulfur or the bulkier NCH₃ group (**5** and **3a**, respectively). Furthermore, the free volume of the protein pocket was probed by introducing methyl groups on the adt methylene moieties (**6**). Finally, three variants with only one CN⁻ ligand were synthesized in order to explore the function of the CN⁻ ligands (**1b**, **2b**, and **3b**). The successful insertion of these variants was monitored by FTIR spectroscopy and the new hybrid proteins were tested for their residual H₂ production and oxidation activity using gas chromatography and UV spectroscopy, respectively. None of these variants showed improved hydrogenase activity. Nevertheless, very interesting insight into the conformational and functional features of the active site could be gained by studying the properties of these hybrid hydrogenases.

■ MATERIALS AND METHODS

Preparation of Unmaturation HydA1. The structural gene of *C. reinhardtii* HydA1 was heterologously overexpressed in *E. coli* BL21(DE3)Δ*iscR*⁴⁶ according to a procedure previously described by Kuchenreuther et al.⁴⁷ but without expression of the maturases HydE, HydF, HydX, and HydG. For overexpression, a pET21b expression plasmid containing an *E. coli* codon optimized *C. reinhardtii* HydA1 gene with an N-terminal Strep-tag followed by a TEV (tobacco etch virus) cleavage site (WSHPQFEKSSGRENLYFQ[G]) was used. After purification on a Strep-Tactin Superflow high capacity resin (IBA GmbH), TEV protease was added to unmaturation HydA1 at a ratio of 1:30 (w/w) and incubated overnight at room temperature to cleave the Strep-Tag. The plasmid for expression of the TEV protease was a gift from the Arrowsmith laboratory (University of Toronto). The His₆-tagged TEV protease was removed by addition of Talon metal affinity resin (Clontech, 350 μL column volume Talon beads per mg TEV), incubation for 1 h, and separation of the beads from the protein solution by filtration. Successful TEV-cleavage was confirmed by mass spectrometry (Supporting Information Figure S1a).

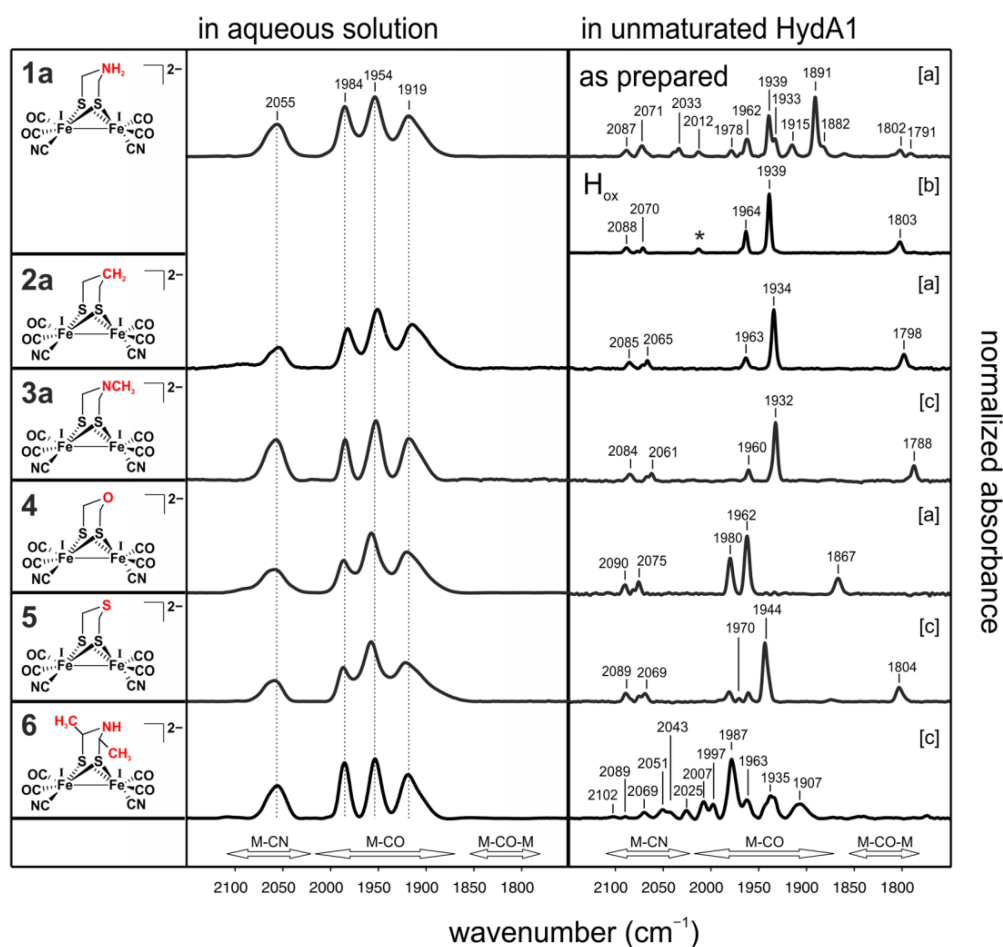


Figure 2. Synthetic complexes **1a**, **2a**, **3a**, **4**, **5**, and **6** (left) and FTIR spectra of those as free complex (middle) and inserted into unmaturation HydA1 (right) as indicated. HydA1-**1a** is shown as-prepared and in the H_{ox} -state. Spectra were measured at 15 °C in 25 mM Tris/HCl, pH 8.0, 25 mM KCl (and 2 mM NaDT in HydA1-x). [a] Ref 43. [b] Ref 45. [c] This work. * peak of CO-inhibited state.

Protein samples (Supporting Information Figure S1b, S1c) were concentrated to 0.5–4 mM in 100 mM Tris/HCl, pH 8.0, 150 mM NaCl, 2.5 mM desthiobiotin, and 2 mM NaDT (sodium dithionite), sealed anaerobically, and stored at –80 °C until use.

Reconstitution with Synthetic Active Site Mimics. All samples were handled under strict anaerobic conditions. For FTIR samples, a concentrated solution of unmaturation HydA1 prepared as described above was diluted in dilution buffer (25 mM Tris/HCl, pH 8.0, 25 mM KCl, and 2 mM NaDT) to reach a concentration of 50–150 μ M. Fivefold excess of either $[Fe_2(xdt)(CO)_4(CN)_2]^{2-}$ (xdt refers to one of the dithiolate bridge variants) or $[Fe_2(xdt)(CO)_5(CN)]^-$, dissolved in DMSO, was added and the mixture was incubated for 1 h at room temperature. Excess of free synthetic complex was removed using PD-10 desalting columns (GE Healthcare). For $[Fe_2(adt)(CO)_5(CN)]^-$ the procedure was slightly different: it was dissolved in acetonitrile, the dilution buffer contained 10 mM NaDT, and protein samples were additionally desalted on a PD-10 column using the dilution buffer supplemented with 10% acetonitrile in order to remove unspecifically bound complex. After desalting, the protein samples were concen-

trated to 0.5–4 mM and used immediately or stored at –80 °C until use.

For activity measurements, a concentrated solution of unmaturation HydA1 was diluted to 1.5–40 μ M. A 10-fold excess of synthetic complex was added and the mixture was incubated for 1 h at room temperature. The samples were used immediately for activity tests. For HydA1-**1b**, the maturation process was performed in the presence of 10 mM NaDT.

FTIR Analysis. FTIR spectra of $[Fe_2(xdt)(CO)_4(CN)_2]^{2-}$ and unmaturation HydA1 matured with any of the synthetic mimic variants (referred to as HydA1-x here) were measured in 25 mM Tris/HCl, pH 8.0, 25 mM KCl, and dilution buffer, respectively. Spectra of $[Fe_2(xdt)(CO)_5(CN)]^-$ were measured in DMSO. All spectra were obtained on a Bruker IFS 66v/s FTIR spectrometer equipped with a Bruker nitrogen cooled MCT (mercury cadmium telluride) detector. The spectra were accumulated in the double-sided, forward–backward mode with 100–1000 scans and a resolution of 2 cm^{-1} at 15 °C. Data processing was facilitated by home-written routines in the MATLAB programming environment.

Hydrogen Production Assay. Hydrogen production was determined according to the procedure described by Winkler et al.⁴⁸ the amount of HydA1-x (1–20 μ L) corresponding to

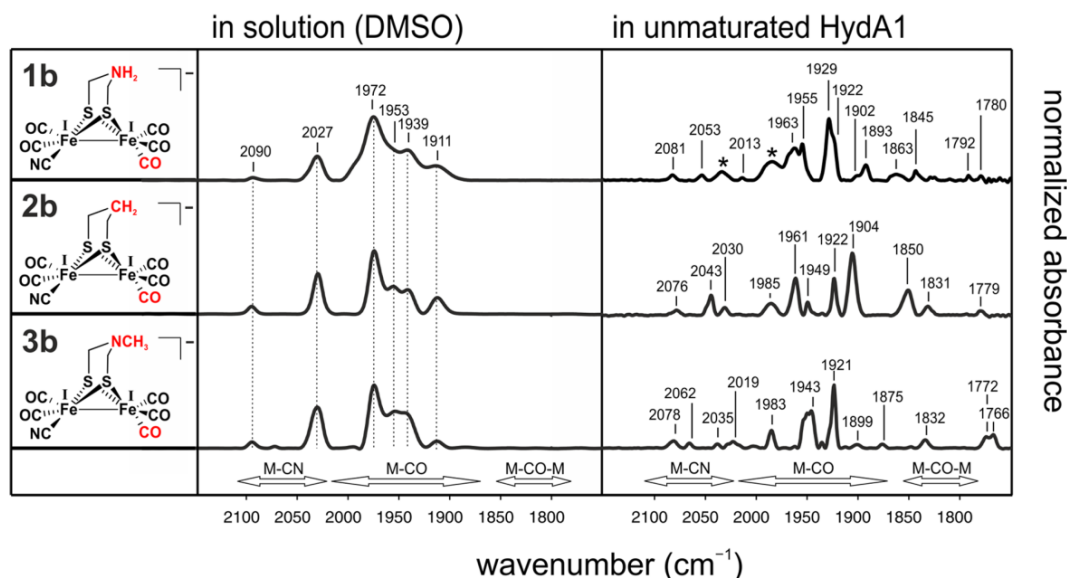


Figure 3. Synthetic complexes **1b**, **2b**, and **3b** (left) and FTIR spectra of those as free complex (middle) and in unmaturation HydA1-bound form (right) as indicated. Spectra of HydA1-x were measured at 15 °C in 25 mM Tris/HCl, pH 8.0, 25 mM KCl, 2 or 10 mM NaDT. The free complexes were measured in DMSO. *peak of the free complex **1b**.

100 ng (HydA1-1a and HydA1-1b) or 10 μ g (all others) was added to a total amount of 400 μ L 100 mM potassium phosphate, pH 6.8, 100 mM NaDT, and 10 mM methyl viologen in a 2 mL vial sealed under anaerobic conditions (Suba-seal septa, 13, Sigma-Aldrich). After flushing with argon for 5 min and incubation at 37 °C for 20 min, a gas chromatogram was recorded on a 6890 Series GC System (Agilent Technologies) using a molecular sieve 5 Å PLOT column by injecting 300 μ L of the headspace gas.

Hydrogen Oxidation Assay. Hydrogen oxidation was measured anaerobically as previously described⁴⁷ with the following modifications: the amount of HydA1-x (1–20 μ L) prepared corresponding to 100 ng (HydA1-1a and HydA1-1b) or 10 μ g (all others) was added to 1 mL 100 mM potassium phosphate, pH 6.8, 10 mM methyl viologen and spectrophotometrically analyzed at 25 °C for 3–30 min depending on the activity (using an Ocean Optics USB2000+XR1-ES, equipped with a DH-MINI Deuterium Tungsten Halogen Source).

Iron Quantification. For iron quantification (see Supporting Information, notes on activity measurements), the samples were prepared as described for FTIR (see above) and used immediately. For each sample, the iron content was determined three times for three different protein concentrations according to the literature procedure.⁴⁹

Synthesis. All reactions were carried out under an inert atmosphere of argon using standard Schlenk-techniques or in a dry argon glovebox (MBraun LabMaster130). Acetonitrile, dichloromethane, diethyl ether, and *n*-hexane were purified by the solvent purification system MBraun MB SPS-800 Auto. THF used was dried over sodium with benzophenone and distilled under argon. The compounds presented in Figure 1c were synthesized corresponding to literature procedures. The dicyanide compounds $[\text{Fe}_2(\text{xdt})(\text{CO})_4(\text{CN})_2]^{2-}$ and $[\text{Fe}_2(\text{SCH}_3)_2(\text{CO})_4(\text{CN})_2]^{2-}$ were synthesized from the corresponding hexacarbonyl compounds $[\text{Fe}_2(\text{xdt})(\text{CO})_6]$ (xdt = adt,³⁹ pdt,^{37,50} odt,^{39,40} dime-adt,⁵¹ NMedt,³⁹ tdt,⁵²

OHpdt⁵³), and $[\text{Fe}_2(\text{SCH}_3)_2(\text{CO})_6]^{54}$ using a standard procedure described in the Supporting Information.^{37,38} Monosubstituted derivatives of the type $[\text{Fe}_2(\text{xdt})(\text{CO})_5(\text{CN})]^-$ were obtained using the decarbonylation agent Me_3NO followed by addition of $[\text{NEt}_4][\text{CN}]^{55}$ (see Supporting Information). The synthesis of **7** and **8** was carried out as reported previously.^{56,57}

RESULTS

Insertion of the Dicyanide Compounds with Different Bridgehead Groups. The CN and CO stretch vibrations as observed in FTIR spectroscopy are very sensitive to changes in the oxidation states of the $[\text{2Fe}]$ -core in the H-cluster. Moreover, slight changes in hydrogen bonding and electrostatic interactions with the surrounding protein pocket are reflected in the FTIR spectra as well. In this work, FTIR was used to check if the complexes are incorporated into unmaturation HydA1 as reported previously for $[\text{Fe}_2(\text{adt})(\text{CO})_4(\text{CN})_2]^{2-}$ **1a**, $[\text{Fe}_2(\text{pdt})(\text{CO})_4(\text{CN})_2]^{2-}$ **2a**, and $[\text{Fe}_2(\text{odt})(\text{CO})_4(\text{CN})_2]^{2-}$ **4**.⁴³ We synthesized three additional complexes with variations in the dithiolate bridge: $[\text{Fe}_2(\text{NMedt})(\text{CO})_4(\text{CN})_2]^{2-}$ **3a** (NMedt = *N*-Methylazadithiolate), an *N*-methyl analogue of adt,³⁹ $[\text{Fe}_2(\text{tdt})(\text{CO})_4(\text{CN})_2]^{2-}$ **5** (tdt = thiodithiolate) with a sulfur atom in the bridgehead,⁵² and $[\text{Fe}_2(\text{dime-adt})(\text{CO})_4(\text{CN})_2]^{2-}$ **6** (dime-adt = dimethyl-azadithiolate) with two methyl groups in the azadithiolate backbone⁵¹ (Figure 1c).

Figure 2 (middle) shows the FTIR spectra of the free model compounds **1a**, **2a**, **3a**, **4**, **5**, and **6**. All six spectra are very similar showing broad bands due to geometrical flexibility of the molecules in solution. The corresponding stretching modes are assigned on the basis of DFT (density functional theory) calculations and are listed in the Supporting Information (Figure S3). The overall pattern is in agreement with previously reported data.⁵⁵ Upon binding to unmaturation HydA1, the respective complex is immobilized in the protein leading to a sharpening of the FTIR bands. This was observed for all

complexes and is indicative of successful insertion (Figure 2, right^{43,45}). It is remarkable that methylation of the bridging amine leading to $[\text{Fe}_2(\text{NMedt})(\text{CO})_4(\text{CN})_2]^{2-}$ **3a** does not impair insertion of the mimic complex. On the other hand, the substantially increased steric demand of $[\text{Fe}_2(\text{dime-adt})(\text{CO})_4(\text{CN})_2]^{2-}$ **6** results in a slight broadening of the FTIR bands as compared to other complexes. The complicated FTIR spectrum suggests the occurrence of multiple species or conformations of the mimic complex which are not properly immobilized inside the protein pocket. The variants HydA1-2a, -3a, -4, and -5 show a simple five peak pattern consistent with one single redox (and conformational) state. The peak patterns of HydA1-2a, -3a, and -5 strongly resemble that of H_{ox} ⁴³ (for the assignment of the corresponding stretching modes of H_{ox} see Supporting Information Figure S4). The FTIR spectrum of HydA1-4 clearly deviates from that of H_{ox} but still reveals an H-cluster-like signature showing the characteristic stretching modes of H_{ox} (Supporting Information Figure S4).

Insertion of the Monocyanide Complexes with Different Bridgehead Groups. To test whether both CN^- ligands of the $[\text{2Fe}]$ -subsite are required for binding to unmaturation HydA1, we synthesized variants of **1a**, **2a**, and **3a** where only one CO ligand is replaced by a CN^- ligand instead of two in the last synthesis step,⁵⁵ namely, $[\text{Fe}_2(\text{adt})(\text{CO})_5(\text{CN})]^-$ **1b**, $[\text{Fe}_2(\text{pdt})(\text{CO})_5(\text{CN})]^-$ **2b**, and $[\text{Fe}_2(\text{NMedt})(\text{CO})_5(\text{CN})]^-$ **3b** (Figure 1c). The FTIR spectra of the monocyanide variants in solution (Figure 3, middle) are in agreement with reported data⁵⁵ and the corresponding stretching modes are shown in Supporting Information Figure S5. As verified by FTIR spectroscopy, **1b**, **2b**, and **3b** can all be inserted into unmaturation HydA1, clearly showing that one CN^- is sufficient for HydA1-binding (Figure 3, right). Surprisingly, **1b** showed some unspecific binding of the complex to unmaturation HydA1. Most of the unspecifically bound complex could be removed by using desalting buffer containing 10% organic solvent (acetonitrile). Nevertheless, some features of the free complex can be seen in the spectrum (Figure 3, right top). The spectra for all HydA1 monocyanide variants are more complex than those for HydA1-2a, -3a, -4, and -5, suggesting the occurrence of multiple redox states and/or conformations. As will be discussed below, the increased structural complexity of the monocyanide H-cluster variants is most likely due to the fact that their precursor complexes are already asymmetric prior to insertion.

Insertion of Mononuclear Iron, All-Carbonyl, and Additional Dicyanide Compounds. Apart from the synthetic compounds already described, several others (Figure 1c) including mononuclear iron and all-carbonyl compounds were incubated with unmaturation HydA1. Except for $[\text{Fe}(\text{CN})_2(\text{CO})_3]^{2-}$ **7**, insertion was unsuccessful. The most common problem is insolubility and instability in water which turned out to be the case for **8**, **1c**, **9**, and **10b** (see Supporting Information). Complex **10a** $[\text{Fe}_2(\text{OHpdt})(\text{CO})_4(\text{CN})_2]^{2-}$ (OHpdt = hydroxo-propanedithiolate) is more polar than **1a**, **2a**, **3a**, **4**, **5**, and **6** and fully soluble in aqueous solution. Nevertheless, insertion into unmaturation HydA1 could not be confirmed using FTIR spectroscopy. After incubation of the mononuclear iron compound **7** and unmaturation HydA1, various peaks could be detected in the FTIR spectrum, indicating successful incorporation (see Supporting Information Figure S6). Based on the complex spectrum, we assume that **7** has multiple binding modes inside the protein.

H_2 Production and Oxidation Activities. The activities of HydA1-x were determined for both H_2 production and oxidation. The activity values were obtained using identical maturation conditions (except for a slightly different buffer in the case of **1b**), but were not corrected for the degree of maturation, i.e., the amount of protein containing the corresponding synthetic mimic (for further details see Supporting Information Figure S2). HydA1-1a and HydA1-1b showed high activity (Figure 4). Also, activities for the much

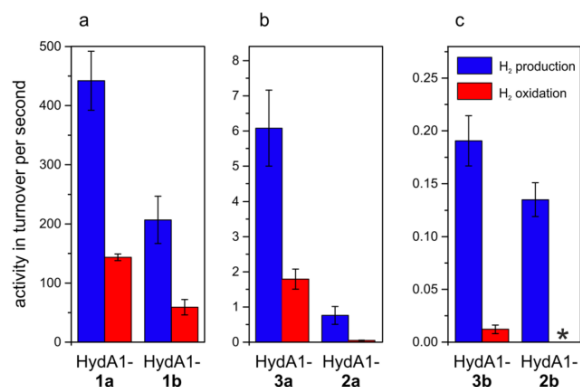


Figure 4. HydA1-x activities given in turnover frequencies (TOF) for H_2 production (blue bars) and oxidation (red bars) under identical maturation conditions. The activity tests were carried out in 100 mM potassium phosphate, pH 6.8, 10 mM methyl viologen with the addition of 100 mM NaDT in the case of H_2 production. It should be noted that the y-axis is different in a–c. Table S1 in the Supporting Information lists all activity values. (a) Activities of HydA1-1a and HydA1-1b. (b) Activities of HydA1-3a and HydA1-2a. (c) Activities of HydA1-3b and HydA1-2b. All samples were measured at least as triplicate from one preparation. For more details see the Supporting Information. *at detection limit.

less active hybrids HydA1-2a and HydA1-3a were observed. HydA1-2b and HydA1-3b showed some residual activity. The H_2 oxidation activity of HydA1-2b is at the detection limit of 0.003 s^{-1} . Activities for HydA1-4, HydA1-5, and HydA1-6 could not be detected. It is remarkable that the HydA1 monocyanide variants consistently show a fraction of the activity of their HydA1 dicyanide parent complexes. Furthermore, both H_2 production and oxidation of the active HydA1-x hybrids are affected in the same way. This suggests that the enzymatic reaction in both directions relies on the same physical properties of the $[\text{2Fe}]$ -subsite. All activity values can be found in the Supporting Information (Table S1).

DISCUSSION

The unassisted insertion of the binuclear subsite precursors into the unmaturation HydA1 protein is a remarkable feat of nature which is not yet fully understood. It is assumed that the protein contains an access channel that directs the precursor toward the active site pocket. In the unmaturation structure of *C. reinhardtii* HydA1 this channel is visible.³¹ It is lined with hydrophilic side-chains that would allow insertion of the water solvated precursor through an entropically driven process.⁵⁸ Once arrived at its destination, the $[\text{2Fe}]$ -precursor must form a covalent bond with the thiolate group of Cys₂₂₅ which coordinates the cubane subcluster. In addition, the precursor must change its coordination sphere and adopt the "rotated

conformation" at the distal iron to accommodate an open coordination site. During this process, also the supernumerary CO ligand must dissociate.⁴⁴ It is likely that the hydrogen bond of the distal CN⁻ ligand to Lys₂₂₈ that is embedded in a strong salt bridge network,⁵⁹ plays a key role in this conformational rearrangement. Apart from the covalent thiolate bridge with Cys₂₂₅, the binuclear part of the H-cluster is only held in position by electrostatic forces and hydrogen bonds via the CN⁻ ligands⁶⁰ (see Figure 5). One can therefore anticipate that

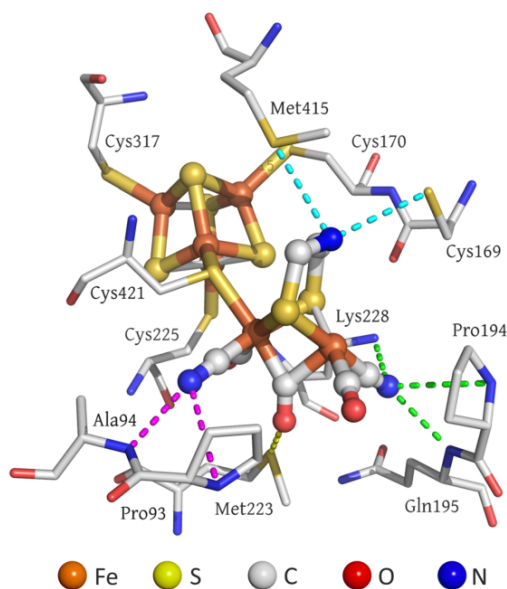


Figure 5. H-cluster in *C. reinhardtii* HydA1 with its protein surrounding. Interactions of the proximal CN⁻ ligand with the protein backbone are shown in pink and of the distal CN⁻ in green. Interactions of the bridging nitrogen with the protein surrounding are depicted in cyan. The interaction of the bridging CO with Met₂₂₃ is shown in yellow. The picture is designed on the basis of the crystal structure of Cpl³² using the program PYMOL.³³

slight changes in the binuclear subcluster ligand sphere as well as the bridgehead group will have a strong effect on the insertion mechanism and the catalytic activity. The series of 15 model complexes (Figure 1c) that are presented in this study cover a wide range of size, charge, polarity, and bridgehead properties that can be used to probe the insertion channel and the protein surrounding of the H-cluster.

Insertion Channel and H-Cluster Protein Pocket. The H-cluster is located in a cavity inside the HydA1 protein. From there, a hydrophilic channel, 8–15 Å wide and about 25 Å deep, leads to the protein surface.³¹ The mononuclear iron compound 7 is significantly smaller than the native [2Fe]-subsite. It can easily pass through the channel and bind to the active site cavity since it has been shown to be inserted into unmaturation HydA1 by FTIR spectroscopy (Supporting Information Figure S6). The spectrum features numerous peaks in the region of CN, CO, and bridging CO, indicating the presence of different states. Compound 7 is small relative to the space provided in the protein pocket and might be able to adopt different orientations since it is not fixed in a certain position like the native [2Fe]-subsite.

In order to find out if the channel and the cavity provide space for a [2Fe]-subsite larger than the native one, we synthesized two [2Fe]-subsite compounds 3a and 6, which have additional steric bulk. 3a has a methyl group on the bridgehead nitrogen, and in 6, two methylene protons are replaced by methyl groups (Figure 1c). The additional methyl groups do not prevent insertion into unmaturation HydA1, clearly showing that the compounds 3a and 6 can pass the channel and bind in the active site cavity. It can be concluded that the H-cluster protein pocket provides more space than needed for the native [2Fe]-subsite. Complex 6 is the bulkiest synthetic compound inserted into HydA1 so far and might be close to the limit in size that we can include in the H-cluster protein pocket. Compound 10a, with its hydroxo-propionate-bridged dithiolate bridge, is sterically less demanding than 3a and 6. However, insertion into unmaturation HydA1 could not be detected. Compound 10a is fully soluble in water as it is more polar than all other compounds discussed in this work. This high polarity might be connected to its unsuccessful insertion. Possibly, the solvation shell is too tightly bound to 10a and cannot be stripped off upon the attempt to enter the channel. Hence, it is too big to pass through the channel and no insertion can occur.

Interactions between the H-Cluster and the Protein Pocket. As already described, the [2Fe]-subsite of the H-cluster forms a covalent bond with a cysteine sulfur which connects it to the [4Fe-4S]-cluster. Apart from that, the strongest interactions of the [2Fe]-subsite with the protein surrounding are H-bonds and other electrostatic interactions (Figure 5).⁶⁰ In order to explore which interactions are necessary for binding, some of the hybrids synthesized lack specific interactions of the [2Fe]-subsite to the nearby amino acids. For example, in HydA1-2a, no H-bond between Cys₁₆₉ and the bridgehead is possible. Also the electrostatic interactions between Met₄₁₅ and the bridgehead are missing. Despite this, 2a can be inserted into unmaturation HydA1. HydA1-2b carries a CO ligand instead of the second CN⁻ ligand. Therefore, there are two different orientations of the [2Fe]-subsite possible with respect to the [4Fe-4S]-cluster. In principle, both orientations can be obtained;⁵⁸ however, the orientation with the distal CN⁻ might be favored due to a strong H-bond to the side chain of Lys₂₂₈.^{41,61} In any case, the interaction of the protein surrounding with one of the CN⁻ ligands is absent. Certainly, this does not prevent binding to unmaturation HydA1. It is therefore apparent that the interactions between nearby amino acids and the CN⁻ ligands are not crucial for the insertion process itself, but they might be important for subsequent stabilization of the [2Fe]-subsite inside the protein pocket.

Structural Effects of the Bridgehead Group. The native binuclear [2Fe]-subsite has an NH group in the bridging dithiolate ligand. In this study, the bridges modified with CH₂, O, S, or NCH₃ are exploited. The FTIR spectra do not differ much depending on the bridgehead (Figure 2, right), matching the results of DFT calculations by Yu et al.⁶² HydA1-2a, -3a, and -5 have a very similar pattern resembling HydA1-1a-H_{ox}. This indicates that all compounds are similarly bound to unmaturation HydA1 in a "rotated conformation" and that the supernumerary CO is dissociated. Presumably, the [2Fe]-subsite is in the redox state Fe^IFe^{II} as suggested for HydA1-2a based on EPR measurements.⁴⁵ Interestingly, the IR frequencies of all peaks of HydA1-4 are shifted to higher energies. This is particularly pronounced for the bridging CO at

1867 cm^{-1} , indicating that the CO has significantly reduced bridging character. However, it is not a terminal ligand on one iron since its frequency is clearly distinct from that of the other CO groups. A shift to higher wavenumber compared to H_{ox} is also observed for the inactive state H_{inact} or H_{trans} of *Desulfovibrio desulfuricans*^{30,63} (see Supporting Information Table S2), where the distal iron carries an additional ligand which was postulated to be a hydroxo group.⁷ Such a ligand might be stabilized by the oxygen bridgehead. Ligand binding to the open coordination site (H_2 , H_2O) or protonation of the bridgehead oxygen in HydA1-4 seems rather unlikely based on calculations⁶² (see also Supporting Information Table S2). We suggest that although the central bridgehead atoms in HydA1-4 (O) and HydA1-5 (S) are isosteric and isoelectronic, it is their interaction with the protein surrounding that gives rise to differences in the spectra. However, HydA1-5 has an additional component in the spectrum (Supporting Information Figure S7), probably indicating a second, minor species that has a similar structure to HydA1-4.

Structural Effects of the Ligand Sphere. HydA1-1b, HydA1-2b, and HydA1-3b contain a CO ligand instead of the second CN^- ligand found in HydA1-1a, -2a, and -3a. The FTIR spectra of HydA1-2b and HydA1-3b are more complex than those for HydA1-2a and -3a (Figures 2 and 3). For all HydA1 monocyanide variants, the two different orientations of the $[2\text{Fe}]$ -subsite with respect to the $[4\text{Fe-4S}]$ -cluster might contribute to the complexity of the spectra. Also, this increased structural complexity of the monocyanide H-cluster variants is likely related to the asymmetric nature of their precursor complexes prior to insertion. The FTIR spectrum of HydA1-1b is also complex but may additionally be explained by the occurrence of a mixture of different catalytically active states. Based on DFT calculations, it seems likely that the spectra of HydA1-2b and HydA1-3b contain signals from the $[2\text{Fe}]$ -subsite in the oxidation states $\text{Fe}^{\text{I}}\text{Fe}^{\text{II}}$ and $\text{Fe}^{\text{I}}\text{Fe}^{\text{I}}$ (Supporting Information Figure S8, Table S3, Figure S9).

HydA1-6 has modifications in the second ligand sphere: the two methylene groups of the dithiolate ligand are modified by one CH_3 group each instead of a proton. This leads to a FTIR spectrum that features various peaks (Figure 2, right bottom). They arise from a mixture of different isoforms and oxidation states (see Supporting Information Figure S10). Changes in the ligand sphere have a strong structural effect on the $[2\text{Fe}]$ -subsite as can be seen from the FTIR spectra.

Catalytic Mechanism and Proton Transfer. In the catalytic cycle, H_2 is reversibly and heterolytically split into protons and electrons. The distal iron of the $[2\text{Fe}]$ -subsite functions as an electron buffer and the protons presumably bind to the bridgehead nitrogen and are transported from there to the surface.⁶⁴ Our experiments revealed, however, that HydA1-2a with a CH_2 group in the bridgehead has some remaining activity, which is decreased by 3 orders of magnitude as compared to HydA1-1a (Figure 4). The catalytic cycle must therefore work differently from that of HydA1-1a, since no protonation of the methylene bridge can occur. More than a decade ago, the bridgehead was suggested to be CH_2 .^{7,8} Therefore, several mechanisms were proposed that did not include protonation of the bridgehead atom.^{65–67} It was instead assumed that one of the sulfurs of the dithiolate bridge is protonated. Basically, one of those functional but, apparently, less efficient mechanisms could occur in HydA1-2a. Also for these mechanisms redox activity of the H-cluster is required. Recently we reported a detailed spectroscopic investigation of

HydA1-2a, where, indeed, two different redox states with a one-electron-oxidation transition were identified.⁴⁵ The low activity of HydA1-2a is probably connected to the lower basicity of the bridging dithiolate group as well as their unfavorable positioning with respect to the proton channel of the enzyme. Supposedly, Cys_{169} is the first amino acid of this chain that is within H-bonding distance of the amine bridge^{60,64} (Figure 5). Clearly, the distance of Cys_{169} to the bridging dithiolates is larger, which considerably slows down proton transfer. For efficient catalysis, it seems, therefore, important that a proton transfer chain is close to the first proton acceptor of the active site.

Following the pendant base paradigm, a decreased activity going from a polar bridgehead (HydA1-1a) to a less polar (HydA1-4 and HydA1-5) and eventually to a nonpolar bridgehead (HydA1-2a) is expected. Experimentally, however, we find that only the nonpolar variant HydA1-2a has residual activity. Apparently, the catalytic mechanism of HydA1-1a depends not only on the correct positioning of the amine group with respect to the proton channel, but also on additional H-bonding and electrostatic interactions of the amine group with residues Cys_{169} and Met_{415} . Supposedly, these interactions are disturbed for HydA1-4 and HydA1-5 resulting in a collapse of the main catalytic mechanism. The question then arises why the mechanism proposed for HydA1-2a does not work for HydA1-4 and HydA1-5. The most likely explanation is the stronger basicity of the dithiolate sulfurs in HydA1-2a than in HydA1-4 and HydA1-5 because of the positive inductive effect of the additional methylene group. This increases the electron density on the thiolate sulfur atoms and favors protonation compared to HydA1-4 and HydA1-5.

HydA1-3a and -6 both have a nitrogen atom in the bridgehead. Its basicity should be approximately the same as for HydA1-1a, because it was shown to be the same within error for the free complexes $[\text{Fe}_2(\text{adt})(\text{CO})_6]$, $[\text{Fe}_2(\text{NMedt})(\text{CO})_6]$, and $[\text{Fe}_2(\text{dime-adt})(\text{CO})_6]$.⁵¹ Nevertheless, the activity of HydA1-3a is decreased and HydA1-6 is inactive. The reason might be that the steric demand of the methyl groups impedes protonation or disturbs the fine-tuned fit in the protein pocket leading to no or lower activity. It is also possible that the protein surrounding changes the basicity of the nitrogen in HydA1-1a, -3a, and -6 in a different way. In HydA1-3a, the methyl group on the nitrogen can be oriented either toward Cys_{170} (equatorial) or toward the open cavity (axial) (Figure 5). The axial position of the methyl group is probably sterically favored. However, in this conformation the lone pair of the bridgehead nitrogen is not accessible for the proton which arises from H_2 splitting at the distal iron site. HydA1-3a is the hybrid with the third highest activity of all semisynthetic hydrogenases, emphasizing the importance of the amine in the bridgehead (see previous section). In contrast, in HydA1-6, the steric bulk of the additional methyl groups and/or the complex stereochemistry eliminate all catalytic ability.

HydA1-1b. Of all the semisynthetic hydrogenases presented here, only HydA1-1b shows activity that is close to the native HydA1 and the hybrid HydA1-1a. Regarding the different key properties identified as crucial for a functional hydrogenase, most of these are given for HydA1-1b: The bridgehead atom is the same as in the native system, the protein pocket has the appropriate size for the synthetic $[2\text{Fe}]$ -subsite, and the proton formed upon H_2 splitting can be accepted by the bridgehead nitrogen followed by transport to the protein surface via the proposed proton transfer channel. The only aspect that is

different in the case of HydA1-1b is the anchoring of the [2Fe]-subsite with the CN⁻ ligands in the protein pocket. This could lead to suboptimal stabilization of the [2Fe]-subsite. The lower activity of HydA1-1b is probably related to the fact that this H-cluster variant can exist in two isomers: one with a distal CN⁻ and one with a proximal CN⁻ ligand. Presumably, only the distal CN⁻ variant is catalytically active, since here the rotated conformation around the distal iron atom is stabilized by the hydrogen bond of the distal CN⁻ to Lys₂₂₈. Furthermore, the reduced negative charge of the [2Fe]-subsite, caused by the missing CN⁻ ligand, might decrease the catalytic activity of the H-cluster. The CN⁻ ligand is a powerful σ -donor ligand whereas CO ligands have a strong π -back-bonding effect. The absence of one CN⁻ ligand and an additional CO ligand likely changes the overall electronic structure of the H-cluster. Presumably, the electron density on the iron center is lowered, which could lead to a less basic amine group.

CONCLUSIONS

A series of modified synthetic binuclear [2Fe]-compounds related to the active center of the native [FeFe]-hydrogenase were introduced into unmaturation HydA1 and tested for their structural and catalytic properties. It was shown that the H₂ production and oxidation activity relies on the same physical and chemical properties of the [2Fe]-subsite. The CN⁻ ligands establish the overall charge of the [2Fe]-subsite. Apart from this, they do not seem to be essential for the catalytic mechanism. Rather, these CN⁻ groups stabilize the H-cluster in the protein pocket through electrostatic and hydrogen bonding interactions. Furthermore, the basicity of the azadithiolate moiety is critical for proton binding and transfer into the binding pocket and, therefore, for the catalytic activity of the H-cluster (the propanedithiolate, oxadithiolate, and thiodithiolate variants are strongly reduced in activity). Also, the conformational flexibility (e.g., flipping of the amine group away from Fe₄) and spatial freedom of the azadithiolate moiety plays an important role in the catalytic mechanism. Introduction of steric bulk (*N*-methylazadithiolate bridge) reduces this flexibility and spatial freedom, significantly impairing catalytic activity. Moreover, the protein pocket around the azadithiolate bridge can accommodate substantial steric bulk. This space is, however, probably needed for adaptive conformational changes of the surrounding protein synchronized with those of the binuclear subsite. This may be the reason the dimethylazadithiolate variant is not comfortably accommodated in HydA1 and does not show any activity. The H-cluster has sufficient flexibility to allow for alternative but less efficient protonation sites and probably also proton transfer pathways as shown for the case of the propanedithiolate variant.

The novel technique of artificial maturation of [FeFe]-hydrogenases^{43,44} introduces many possibilities to engineer semiartificial hydrogenase-derived H₂ producers. However, the introduction of synthetic model compounds into the unmaturation enzyme faces several limitations. First, the protein pocket has defined dimensions and it does not provide space for model compounds of significantly larger size than the native cofactor. On the other hand, small model compounds like mononuclear iron complexes can be easily introduced into the H-cluster pocket, but they seem to have conformations not well tuned to the protein surrounding, which is disadvantageous for catalytic activity. Additionally, the synthetic complex must also be designed in a way that its surface solvation shell is compatible with the cationic protein insertion channel.

Preferably, the mimics should be also water-soluble and stable, although alternative maturation conditions could be developed.

So far, most hydrogenase active site model compounds do not fulfill these conditions. A concerted, knowledge based approach addressing both the protein surrounding as well as the inserted binuclear subcluster precursor might provide a road to improved hydrogenases with respect to activity and oxygen sensitivity. The successful insertion of a series of [2Fe]-subsite variants into native unmaturation HydA1 shown in this work demonstrates the viability of such a strategy.

ASSOCIATED CONTENT

Supporting Information

Protein preparation (Figure S1), notes on activity measurements (Figure S2, Table S1), synthesis of [(NEt₄)₂][Fe₂(pdt)(CO)₄(CN)₂] and [NEt₄][Fe₂(pdt)(CO)₅(CN)], stretching modes of [Fe₂(xdt)(CO)₄(CN)₂]²⁻ (Figure S3), stretching modes of HydA1-H_{ox} (Figure S4), stretching modes of [Fe₂(xdt)(CO)₅(CN)]⁻ (Figure S5), further insertion attempts: mononuclear iron, all-carbonyl and two additional dicyanide compounds (Figure S6), HydA1-2a, 3a, 4, and 5 (Table S2, Figure S7), HydA1 monocyanide variants (Figure S8, Table S3, Figure S9), HydA1-6 (Figure S10). This material is available free of charge via the Internet at <http://pubs.acs.org>.

AUTHOR INFORMATION

Corresponding Authors

*E-mail: edward.reijerse@cec.mpg.de, tel. +49 208 306 3529, fax +49 208 306 3955.

*E-mail: wolfgang.lubitz@cec.mpg.de, tel. +49 208 306 3614, fax +49 208 306 3955.

Funding

This work was supported by the Max-Planck Society and the Deutsche Forschungsgemeinschaft (DIP project LU315/17-1). We also thank the Fonds der Chemischen Industrie for the Doctoral Kekulé Fellowship (K.W.).

Notes

The authors declare no competing financial interest.

ACKNOWLEDGMENTS

We thank Agnes Stoer, Julian Jakobs, Michael Reus, Inge Heise, and Norbert Dickmann for excellent technical assistance. The authors are grateful to Dr. James Birrell for carefully reading the manuscript and his useful suggestions on content and language.

ABBREVIATIONS

adt, azadithiolate; DFT, density functional theory; dime-adt, dimethyl-azadithiolate; DMSO, dimethylsulfoxide; EPR, electron paramagnetic resonance; FTIR, Fourier transform infrared; HydA1-x, HydA1 matured with one of the synthetic mimic variants; odt, oxadithiolate; OHpdt, hydroxo-propanedithiolate; NaDT, sodium dithionite; NMedt, *N*-methylazadithiolate; pdt, propanedithiolate; tdt, thiodithiolate; TEV, tobacco etch virus; THF, tetrahydrofuran; TOF, turnover frequency; Tris, tris(hydroxymethyl)-aminomethane; xdt, one of the dithiolate ligand variants

REFERENCES

- (1) Lubitz, W., Ogata, H., Rüdiger, O., and Reijerse, E. (2014) Hydrogenases. *Chem. Rev.* 114, 4081–4148.

- (2) Vignais, P. M., and Billoud, B. (2007) Occurrence, classification, and biological function of hydrogenases: an overview. *Chem. Rev.* 107, 4206–4272.
- (3) Kubas, G. J. (2007) Fundamentals of H₂ binding and reactivity on transition metals underlying hydrogenase function and H₂ production and storage. *Chem. Rev.* 107, 4152–4205.
- (4) Adams, M. W. W. (1990) The structure and mechanism of iron-hydrogenases. *Biochim. Biophys. Acta: Bioenerg.* 1020, 115–145.
- (5) Hatchikian, E. C., Forget, N., Fernandez, V. M., Williams, R., and Cammack, R. (1992) Further characterization of the [Fe]-hydrogenase from *Desulfovibrio desulfuricans* ATCC 7757. *Eur. J. Biochem.* 209, 357–365.
- (6) Happe, T., and Naber, J. D. (1993) Isolation, characterization and N-terminal amino acid sequence of hydrogenase from the green alga *Chlamydomonas reinhardtii*. *Eur. J. Biochem.* 214, 475–481.
- (7) Nicolet, Y., Piras, C., Legrand, P., Hatchikian, C. E., and Fontecilla-Camps, J. C. (1999) *Desulfovibrio desulfuricans* iron hydrogenase: the structure shows unusual coordination to an active site Fe binuclear center. *Structure* 7, 13–23.
- (8) Peters, J. W., Lanzilotta, W. N., Lemon, B. J., and Seefeldt, L. C. (1998) X-ray crystal structure of the Fe-only hydrogenase (CpI) from *Clostridium pasteurianum* to 1.8 angstrom resolution. *Science* 282, 1853–1858.
- (9) Volbeda, A., Garcin, E., Piras, C., de Lacey, A. L., Fernandez, V. M., Hatchikian, E. C., Frey, M., and Fontecilla-Camps, J. C. (1996) Structure of the [NiFe] hydrogenase active site: evidence for biologically uncommon Fe ligands. *J. Am. Chem. Soc.* 118, 12989–12996.
- (10) Vignais, P. M., Billoud, B., and Meyer, J. (2001) Classification and phylogeny of hydrogenases I. *FEMS Microbiol. Rev.* 25, 455–501.
- (11) Frey, M. (2002) Hydrogenases: hydrogen-activating enzymes. *ChemBioChem* 3, 153–160.
- (12) Artero, V., and Fontecave, M. (2005) Some general principles for designing electrocatalysts with hydrogenase activity. *Coord. Chem. Rev.* 249, 1518–1535.
- (13) Wang, M., Chen, L., and Sun, L. (2012) Recent progress in electrochemical hydrogen production with earth-abundant metal complexes as catalysts. *Energy Environ. Sci.* 5, 6763–6778.
- (14) Darensbourg, M. Y., Lyon, E. J., and Smee, J. J. (2000) The bio-organometallic chemistry of active site iron in hydrogenases. *Coord. Chem. Rev.* 206–207, 533–561.
- (15) Gloaguen, F., and Rauchfuss, T. B. (2009) Small molecule mimics of hydrogenases: hydrides and redox. *Chem. Soc. Rev.* 38, 100–108.
- (16) Tard, C., and Pickett, C. J. (2009) Structural and functional analogues of the active sites of the [Fe]-, [NiFe]-, and [FeFe]-hydrogenases. *Chem. Rev.* 109, 2245–2274.
- (17) Sun, L., Åkermark, B., and Ott, S. (2005) Iron hydrogenase active site mimics in supramolecular systems aiming for light-driven hydrogen production. *Coord. Chem. Rev.* 249, 1653–1663.
- (18) Simmons, T. R., Berggren, G., Bacchi, M., Fontecave, M., and Artero, V. (2014) Mimicking hydrogenases: From biomimetics to artificial enzymes. *Coord. Chem. Rev.* 270–271, 127–150.
- (19) Nicolet, Y., de Lacey, A. L., Vernède, X., Fernandez, V. M., Hatchikian, E. C., and Fontecilla-Camps, J. C. (2001) Crystallographic and FTIR spectroscopic evidence of changes in Fe coordination upon reduction of the active site of the Fe-only hydrogenase from *Desulfovibrio desulfuricans*. *J. Am. Chem. Soc.* 123, 1596–1601.
- (20) Happe, T., and Kaminski, A. (2002) Differential regulation of the Fe-hydrogenase during anaerobic adaptation in the green alga *Chlamydomonas reinhardtii*. *Eur. J. Biochem.* 269, 1022–1032.
- (21) Posewitz, M. C., King, P. W., Smolinski, S. L., Zhang, L., Seibert, M., and Ghirardi, M. L. (2004) Discovery of two novel radical s-adenosylmethionine proteins required for the assembly of an active [Fe] hydrogenase. *J. Biol. Chem.* 279, 25711–25720.
- (22) Shepard, E. M., Mus, F., Betz, J. N., Byer, A. S., Duffus, B. R., Peters, J. W., and Broderick, J. B. (2014) [FeFe]-hydrogenase maturation. *Biochemistry* 53, 4090–4104.
- (23) Kuchenreuther, J. M., Myers, W. K., Stich, T. A., George, S. J., NejatyJahromy, Y., Swartz, J. R., and Britt, R. D. (2013) A radical intermediate in tyrosine scission to the CO and CN⁻ ligands of FeFe hydrogenase. *Science* 342, 472–475.
- (24) Kuchenreuther, J. M., Myers, W. K., Suess, D. L. M., Stich, T. A., Pelmentschikov, V., Shiigi, S. A., Cramer, S. P., Swartz, J. R., Britt, R. D., and George, S. J. (2014) The HydG enzyme generates an Fe(CO)₂(CN) synthon in assembly of the FeFe hydrogenase H-cluster. *Science* 343, 424–427.
- (25) Lemon, B. J., and Peters, J. W. (1999) Binding of exogenously added carbon monoxide at the active site of the iron-only hydrogenase (CpI) from *Clostridium pasteurianum*. *Biochemistry* 38, 12969–12973.
- (26) Silakov, A., Kamp, C., Reijerse, E., Happe, T., and Lubitz, W. (2009) Spectroelectrochemical characterization of the active site of the [FeFe] hydrogenase HydA1 from *Chlamydomonas reinhardtii*. *Biochemistry* 48, 7780–7786.
- (27) Fontecilla-Camps, J. C., Amara, P., Cavazza, C., Nicolet, Y., and Volbeda, A. (2009) Structure–function relationships of anaerobic gas-processing metalloenzymes. *Nature* 460, 814–822.
- (28) Fontecilla-Camps, J. C., Volbeda, A., Cavazza, C., and Nicolet, Y. (2007) Structure/function relationships of [NiFe]- and [FeFe]-hydrogenases. *Chem. Rev.* 107, 4273–4303.
- (29) Lubitz, W., Reijerse, E., and van Gestel, M. (2007) [NiFe] and [FeFe] hydrogenases studied by advanced magnetic resonance techniques. *Chem. Rev.* 107, 4331–4365.
- (30) Pierik, A. J., Hulstein, M., Hagen, W. R., and Albracht, S. P. J. (1998) A low-spin iron with CN and CO as intrinsic ligands forms the core of the active site in [Fe]-hydrogenases. *Eur. J. Biochem.* 258, 572–578.
- (31) Mulder, D. W., Boyd, E. S., Sarma, R., Lange, R. K., Endrizzi, J. A., Broderick, J. B., and Peters, J. W. (2010) Stepwise [FeFe]-hydrogenase H-cluster assembly revealed in the structure of HydA^{ΔEFG}. *Nature* 465, 248–251.
- (32) Pandey, A. S., Harris, T. V., Giles, L. J., Peters, J. W., and Szilagy, R. K. (2008) Dithiomethylether as a ligand in the hydrogenase H-cluster. *J. Am. Chem. Soc.* 130, 4533–4540.
- (33) Schrodinger, L. (2010) The PyMOL Molecular Graphics System, version 1.3r1.
- (34) Volbeda, A., Charon, M.-H., Piras, C., Hatchikian, E. C., Frey, M., and Fontecilla-Camps, J. C. (1995) Crystal structure of the nickel-iron hydrogenase from *Desulfovibrio gigas*. *Nature* 373, 580–587.
- (35) Montet, Y., Amara, P., Volbeda, A., Vernède, X., Hatchikian, E. C., Field, M. J., Frey, M., and Fontecilla-Camps, J. C. (1997) Gas access to the active site of Ni-Fe hydrogenases probed by X-ray crystallography and molecular dynamics. *Nat. Struct. Mol. Biol.* 4, 523–526.
- (36) Le Cloirec, A., C. Davies, S., J. Evans, D., L. Hughes, D., J. Pickett, C., P. Best, S., and Borg, S. (1999) A di-iron dithiolate possessing structural elements of the carbonyl/cyanide sub-site of the H-centre of Fe-only hydrogenase. *Chem. Commun.*, 2285–2286.
- (37) Lyon, E. J., Georgakaki, I. P., Reibenspies, J. H., and Darensbourg, M. Y. (1999) Carbon monoxide and cyanide ligands in a classical organometallic complex model for Fe-only hydrogenase. *Angew. Chem., Int. Ed.* 38, 3178–3180.
- (38) Schmidt, M., Contakes, S. M., and Rauchfuss, T. B. (1999) First generation analogues of the binuclear site in the Fe-only hydrogenases: Fe₂(μ-SR)₂(CO)₄(CN)₂²⁻. *J. Am. Chem. Soc.* 121, 9736–9737.
- (39) Li, H., and Rauchfuss, T. B. (2002) Iron carbonyl sulfides, formaldehyde, and amines condense to give the proposed azadithiolate cofactor of the Fe-only hydrogenases. *J. Am. Chem. Soc.* 124, 726–727.
- (40) Song, L.-C., Yang, Z.-Y., Bian, H.-Z., and Hu, Q.-M. (2004) Novel single and double diiron oxadithiolates as models for the active site of [Fe]-only hydrogenases. *Organometallics* 23, 3082–3084.
- (41) Silakov, A., Wenk, B., Reijerse, E., and Lubitz, W. (2009) ¹⁴N HSCORE investigation of the H-cluster of [FeFe] hydrogenase: evidence for a nitrogen in the dithiol bridge. *Phys. Chem. Chem. Phys.* 11, 6592–6599.
- (42) Erdem, Ö. F., Schwartz, L., Stein, M., Silakov, A., Kaur-Ghumaan, S., Huang, P., Ott, S., Reijerse, E. J., and Lubitz, W. (2011)

A model of the [FeFe] hydrogenase active site with a biologically relevant azadithiolate bridge: a spectroscopic and theoretical investigation. *Angew. Chem., Int. Ed.* 50, 1439–1443.

(43) Berggren, G., Adamska, A., Lambertz, C., Simmons, T. R., Esselborn, J., Atta, M., Gambarelli, S., Mouesca, J. M., Reijerse, E., Lubitz, W., Happe, T., Artero, V., and Fontecave, M. (2013) Biomimetic assembly and activation of FeFe-hydrogenases. *Nature* 499, 66–70.

(44) Esselborn, J., Lambertz, C., Adamska-Venkatesh, A., Simmons, T., Berggren, G., Noth, J., Siebel, J., Hemschemeier, A., Artero, V., Reijerse, E., Fontecave, M., Lubitz, W., and Happe, T. (2013) Spontaneous activation of [FeFe]-hydrogenases by an inorganic [2Fe] active site mimic. *Nat. Chem. Biol.* 9, 607–609.

(45) Adamska-Venkatesh, A., Krawietz, D., Siebel, J., Weber, K., Happe, T., Reijerse, E., and Lubitz, W. (2014) New redox states observed in [FeFe] hydrogenases reveal redox coupling within the H-cluster. *J. Am. Chem. Soc.* 136, 11339–11346.

(46) Akhtar, M., and Jones, P. (2008) Deletion of *iscR* stimulates recombinant clostridial Fe–Fe hydrogenase activity and H₂-accumulation in *Escherichia coli* BL21(DE3). *Appl. Microbiol. Biotechnol.* 78, 853–862.

(47) Kuchenreuther, J. M., Grady-Smith, C. S., Bingham, A. S., George, S. J., Cramer, S. P., and Swartz, J. R. (2010) High-yield expression of heterologous [FeFe] hydrogenases in *Escherichia coli*. *ONE* 5, e15491.

(48) Winkler, M., Hemschemeier, A., Gotor, C., Melis, A., and Happe, T. (2002) [Fe]-hydrogenases in green algae: photofermentation and hydrogen evolution under sulfur deprivation. *Int. J. Hydrogen Energy* 27, 1431–1439.

(49) Fish, W. W. (1988) Rapid colorimetric micromethod for the quantitation of complexed iron in biological samples. *Methods Enzymol.* 158, 357–364.

(50) Winter, A., Zsolnai, L., and Huttner, G. (1982) Dinuclear and trinuclear carbonyliron complexes containing 1,2-dithiolato bridging ligands. *Z. Naturforsch., B: Chem. Sci.* 37, 1430–1436.

(51) Stanley, J. L., Heiden, Z. M., Rauchfuss, T. B., Wilson, S. R., De Gioia, L., and Zampella, G. (2007) Desymmetrized diiron azadithiolato carbonyls: a step toward modeling the iron-only hydrogenases. *Organometallics* 27, 119–125.

(52) Song, L.-C., Yang, Z.-Y., Hua, Y.-J., Wang, H.-T., Liu, Y., and Hu, Q.-M. (2007) Diiron thiadithiolates as active site models for the iron-only hydrogenases: synthesis, structures, and catalytic H₂ production. *Organometallics* 26, 2106–2110.

(53) Song, L.-C., Li, C.-G., Gao, J., Yin, B.-S., Luo, X., Zhang, X.-G., Bao, H.-L., and Hu, Q.-M. (2008) Synthesis, structure, and electrocatalysis of diiron C-functionalized propanedithiolate (PDT) complexes related to the active site of [FeFe]-hydrogenases. *Inorg. Chem.* 47, 4545–4553.

(54) King, R. B. (1962) Organosulfur derivatives of metal carbonyls. I. The isolation of two isomeric products in the reaction of triiron dodecacarbonyl with dimethyl disulfide. *J. Am. Chem. Soc.* 84, 2460–2460.

(55) Gloaguen, F., Lawrence, J. D., Schmidt, M., Wilson, S. R., and Rauchfuss, T. B. (2001) Synthetic and structural studies on [Fe₂(SR)₂(CN)_x(CO)_{6-x}]^{x-} as active site models for Fe-only hydrogenases. *J. Am. Chem. Soc.* 123, 12518–12527.

(56) Kayal, A., and Rauchfuss, T. B. (2003) Protonation studies of the new iron carbonyl cyanide trans-[Fe(CO)₃(CN)₂]²⁻: implications with respect to hydrogenases. *Inorg. Chem.* 42, 5046–5048.

(57) Rauchfuss, T. B., Contakes, S. M., Hsu, S. C. N., Reynolds, M. A., and Wilson, S. R. (2001) The influence of cyanide on the carbonylation of iron(II): synthesis of Fe–SR–CN–CO centers related to the hydrogenase active sites. *J. Am. Chem. Soc.* 123, 6933–6934.

(58) Mulder, D. W., Shepard, E. M., Meuser, J. E., Joshi, N., King, P. W., Posewitz, M. C., Broderick, J. B., and Peters, J. W. (2011) Insights into [FeFe]-hydrogenase structure, mechanism, and maturation. *Structure* 19, 1038–1052.

(59) Finkelman, A. R., Stiebritz, M. T., and Reiher, M. (2014) Inaccessibility of the μ -hydride species in [FeFe] hydrogenases. *Chem. Sci.* 5, 215–221.

(60) Knörzer, P., Silakov, A., Foster, C. E., Armstrong, F. A., Lubitz, W., and Happe, T. (2012) Importance of the protein framework for catalytic activity of [FeFe]-hydrogenases. *J. Biol. Chem.* 287, 1489–1499.

(61) Greco, C., Bruschi, M., Heimdal, J., Fantucci, P., De Gioia, L., and Ryde, U. (2007) Structural insights into the active-ready form of [FeFe]-hydrogenase and mechanistic details of its inhibition by carbon monoxide. *Inorg. Chem.* 46, 7256–7258.

(62) Yu, L., Greco, C., Bruschi, M., Ryde, U., De Gioia, L., and Reiher, M. (2011) Targeting intermediates of FeFe-hydrogenase by CO and CN vibrational signatures. *Inorg. Chem.* 50, 3888–3900.

(63) Roseboom, W., de Lacey, A. L., Fernandez, V. M., Hatchikian, E. C., and Albracht, S. P. J. (2006) The active site of the [FeFe]-hydrogenase from *Desulfovibrio desulfuricans*. II. Redox properties, light sensitivity and CO-ligand exchange as observed by infrared spectroscopy. *J. Biol. Inorg. Chem.* 11, 102–118.

(64) Adamska, A., Silakov, A., Lambertz, C., Rüdiger, O., Happe, T., Reijerse, E., and Lubitz, W. (2012) Identification and characterization of the “super-reduced” state of the H-cluster in [FeFe] hydrogenase: a new building block for the catalytic cycle? *Angew. Chem., Int. Ed.* 51, 11458–11462.

(65) Zhou, T. J., Mo, Y. R., Liu, A. M., Zhou, Z. H., and Tsai, K. R. (2004) Enzymatic mechanism of Fe-only hydrogenase: Density functional study on H-H making/breaking at the diiron cluster with concerted proton and electron transfers. *Inorg. Chem.* 43, 923–930.

(66) Bruschi, M., Fantucci, P., and De Gioia, L. (2002) DFT investigation of structural, electronic, and catalytic properties of diiron complexes related to the [2Fe]_H subcluster of Fe-only hydrogenases. *Inorg. Chem.* 41, 1421–1429.

(67) Bruschi, M., Fantucci, P., and De Gioia, L. (2003) Density functional theory investigation of the active site of [Fe]-hydrogenases: effects of redox state and ligand characteristics on structural, electronic, and reactivity properties of complexes related to the [2Fe]_H subcluster. *Inorg. Chem.* 42, 4773–4781.

4.1.2 Supporting information

Hybrid [FeFe]-hydrogenases with modified active sites show remarkable residual enzymatic activity

Judith F. Siebel, Agnieszka Adamska-Venkatesh, Katharina Weber, Sigrun Rumpel, Edward Reijerse, Wolfgang Lubitz

Protein preparation

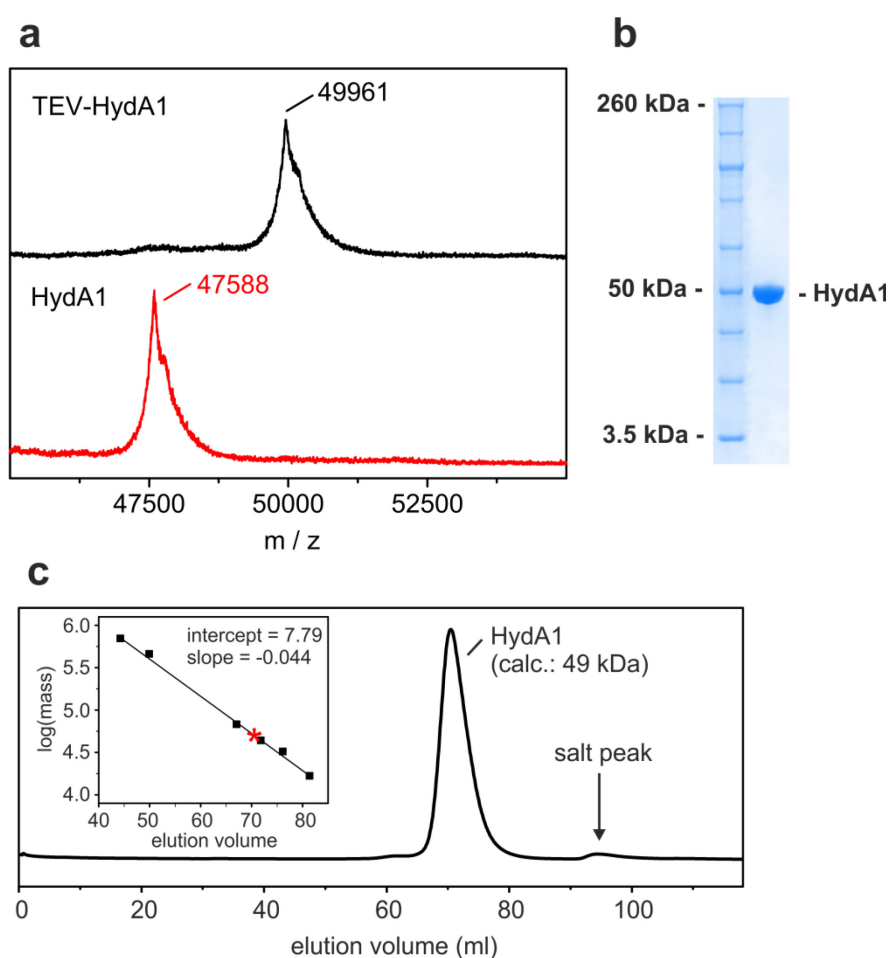


Figure S1. **a)** Mass spectrum of unmaturation HydA1 before and after cleavage of the TEV site. The calculated masses are 49896 Da and 47542 Da, respectively. Spectra were taken on a sina matrix with a Voyager-DE PRO Workstation MALDI-TOF-System (Applied Biosystems). **b)** SDS PAGE of unmaturation HydA1 after one-step purification using affinity chromatography (Strep-tag). Novex Sharp Unstained Protein Standard (Invitrogen) was used as molecular weight marker. **c)** Gel chromatography on a Superdex 16/60 (GE Healthcare) in 50 mM HEPES, pH 7.4, 250 mM NaCl, 2 mM DTT (dithiothreitol) under anaerobic conditions. Unmaturation HydA1 elutes as a single peak after 70.4 ml which corresponds to a mass of 49 kDa, fitting to the actual size of the protein (48 kDa). Inset: Calibration of the Superdex S200 16/60 using thyroglobin (660 kDa), ferritin (440 kDa), albumin (68 kDa), ovalbumin (44 kDa), desoxyribonuclease (31 kDa) and myoglobin (16 kDa) as calibration proteins in 50 mM HEPES, pH 7.4, 250 mM NaCl. Elution of unmaturation HydA1 is shown with a red asterisk.

Notes on activity measurements

HydA1-1a and wild-type HydA1 are known to have an activity of 600–700 $\mu\text{mol H}_2$ per second per mg protein in hydrogen production.^{1, 2} This corresponds to turnover frequency (TOF) of 476–556 turnovers per second (calculated with a protein mass of 47.5 kDa). H_2 oxidation was measured to be $\approx 40\%$ of the H_2 production activity using the same incubation temperature.²

Table S1. H_2 production and oxidation activities

hybrid hydrogenase	H_2 production in s^{-1}	H_2 oxidation in s^{-1}
HydA1-1a	442 ± 50	144 ± 6
HydA1-1b	207 ± 40	59 ± 13
HydA1-3a	6.1 ± 1.1	1.8 ± 0.3
HydA1-2a	0.76 ± 0.25	0.05 ± 0.02
HydA1-3b	0.19 ± 0.02	0.012 ± 0.004
HydA1-2b	0.13 ± 0.02	*

* too close to detection limit of 0.003 s^{-1}

All activities in this study were measured at least three times from one HydA1-x preparation. The reported values are mean values \pm standard deviation. It should be noted that the variations among independently prepared samples are slightly larger than the ones shown. This is mainly caused by the imprecise protein determination of highly diluted samples. Further variations are caused by aging of the protein sample and complex solution as well as inaccuracies in dilution. For exact comparison of activities, ideally the same amount of protein should be used in the measurement, which, however, is not possible for the highly active (HydA1-1a and HydA1-1b) and poorly active (all other) hybrids. Due to the inaccuracy in the activity measurements as outlined above, a direct comparison of absolute numbers is avoided. Therefore, only prominent tendencies in activities which can differ by factor up to 10000 are discussed.

The activity of HydA1-1b is strongly dependent on the maturation conditions. Activation using standard conditions (25 mM Tris/HCl, pH 8.0, 25 mM KCl and 2 mM NaDT, protein concentration of $\approx 5 \mu\text{M}$) leads to large variations in activity which can end up to be a factor of 100 lower than under optimized conditions (25 mM Tris/HCl, pH 8.0, 25 mM KCl and 10 mM NaDT, protein concentration of $\approx 40 \mu\text{M}$). This suggests that during activation in

aqueous buffer HydA1-**1b** is more sensitive to oxidation than HydA1-**1a** and that the insertion reaction is less favored.

All activities in this study were measured after 1 h incubation time (**Figure 4**). Therefore, they do not contain the information on how much of the protein was matured. This was separately tested using iron quantification. Unmatured HydA1 contained 2.3 ± 0.1 iron per protein, corresponding to 55–60 % of protein containing the [4Fe-4S]-cluster. **Figure S2** shows how much of this “competent” fraction was matured with the binuclear [2Fe]-subsite mimic. The degree of maturation varies between 25% and 80%. HydA1-**1a** and HydA1-**1b** both are matured (on average) close to 80%. Therefore the quoted activities need not be corrected. Although there are variations in the degree of maturation (especially low for HydA1-**2a** and high for HydA1-**1a**, HydA1-**1b** and HydA1-**3a**), the overall orders of magnitudes in which the activities of HydA1-**x** are discussed remain unaffected. HydA1-**2a** was shown before to have a low maturation degree using spin counting.³

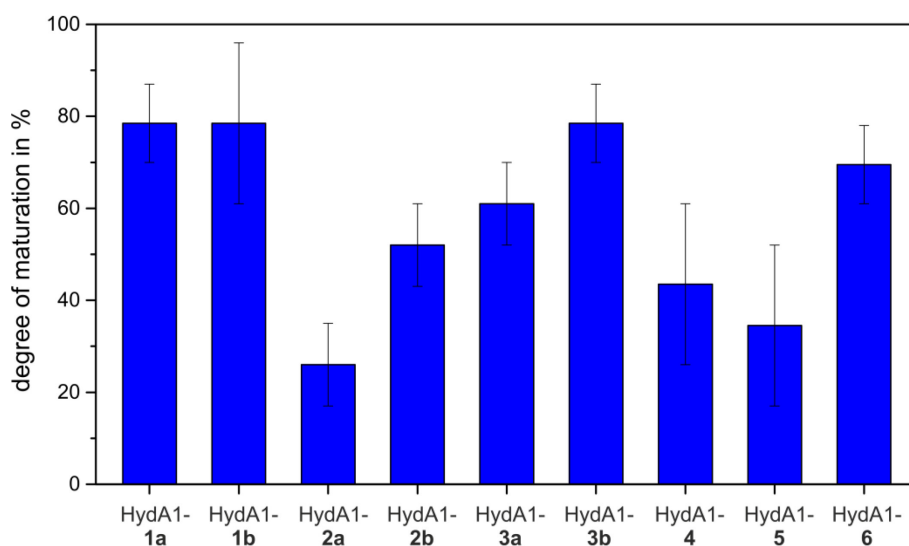


Figure S2. Degree of maturation for all HydA1-**x** after 1 h incubation time of unmaturation HydA1 and 5-fold excess of synthetic complex. Excess complex was removed using PD10 desalting columns (GE Healthcare) as described in *Materials and Methods*. The iron content of each sample was determined in triplicates for three different protein concentrations. The shown values are mean values of all 9 measurements \pm standard deviation.

Synthesis of $[(\text{NEt}_4)_2][\text{Fe}_2(\text{pdt})(\text{CO})_4(\text{CN})_2]$ and $[\text{NEt}_4][\text{Fe}_2(\text{pdt})(\text{CO})_5(\text{CN})]$

The procedure described in the following for **2a** was carried out analogously for **1a**, **3a**, **4**, **5** and **6**.

$[(\text{NEt}_4)_2][\text{Fe}_2(\text{pdt})(\text{CO})_4(\text{CN})_2]$: $[\text{Fe}_2(\text{pdt})(\text{CO})_6]$ (0.11 g, 0.27 mmol) was dissolved in acetonitrile (4 ml) and $[\text{NEt}_4][\text{CN}]$ (0.09 g, 0.56 mmol) was added as a solid at room temperature. After gas evolution stopped, the reaction mixture was stirred for 2 h. The product was precipitated by addition of 8 ml of Et_2O and recrystallized from a dichloromethane solution with *n*-hexane at -40°C . The product was isolated as a deep red crystalline solid (0.13 g, 69%) and verified by $^1\text{H-NMR}$ and FTIR-spectra in agreement with published results.⁴⁻⁶

The procedure described in the following for **2b** was carried out analogously for **1b** and **3b**.

$[\text{NEt}_4][\text{Fe}_2(\text{pdt})(\text{CO})_5(\text{CN})]$: $[\text{Fe}_2(\text{pdt})(\text{CO})_6]$ (0.05 g, 0.13 mmol) was dissolved in acetonitrile (2 ml) and Me_3NO (0.01 g, 0.13 mmol) was added as a solid. The solution was then cooled to -40°C and treated with a solution of $[\text{NEt}_4][\text{CN}]$ (0.02 g, 0.13 mmol) in 1 ml acetonitrile. The reaction mixture was allowed to warm up to room temperature and was stirred for 2 h. The solvent was removed under reduced pressure; the residue was washed with 5 ml Et_2O and then recrystallized from a THF solution with *n*-hexane at -40°C . The product was isolated as a red crystalline solid (0.04 g, 58%) and verified by $^1\text{H-NMR}$ and FTIR spectra in agreement with published results.⁷

Computational methods

All calculations reported in this paper were performed using the ORCA program package (Program Version 3.0.2).⁸ Geometry optimizations and frequency calculations were carried out at DFT level, using the BP86 GGA functional in conjunction with the RI approximation.⁹⁻¹³ The recontracted scalar-relativistic TZVP basis set was used.¹⁴ To fit the BP86/RI/TZVP calculated CN and CO frequencies a calibration according to Yu *et al.*¹⁵ was used: $\nu(\text{CN}_{\text{Scal}}) = 0.990 * \nu(\text{CN}_{\text{Cal}})$; $\nu(\text{CO}_{\text{Scal}}) = 1.023 * \nu(\text{CO}_{\text{Cal}}) - 49$. Calculated models and vibration modes were visualized using the program ChemCraft (Version 1.7).

Stretching modes of $[\text{Fe}_2(\text{xdt})(\text{CO})_4(\text{CN})_2]^{2-}$

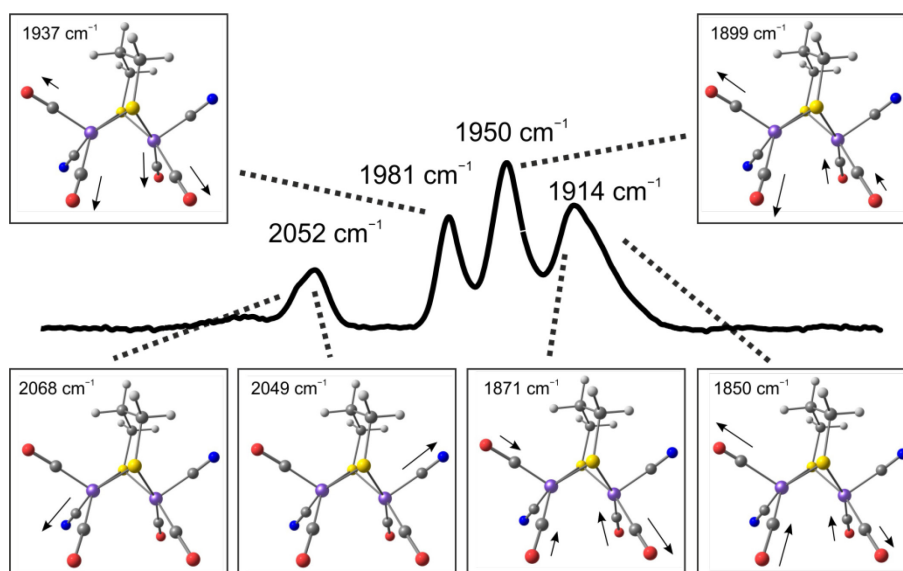


Figure S3. General shape of the FTIR spectrum of $[\text{Fe}_2(\text{xdt})(\text{CO})_4(\text{CN})_2]^{2-}$. Shown here is the measured spectrum of $[\text{Fe}_2(\text{pdt})(\text{CO})_4(\text{CN})_2]^{2-}$ (see also **Figure 2**) and the corresponding symmetrical and antisymmetrical stretching modes of the CO and CN ligands including the calculated wavenumbers. The stretching modes and wavenumbers were calculated for $[\text{Fe}_2(\text{pdt})(\text{CO})_4(\text{CN})_2]^{2-}$ using the ORCA program as described above. These are comparable to $[\text{Fe}_2(\text{adt})(\text{CO})_4(\text{CN})_2]^{2-}$ with a maximum shift of 6 cm^{-1} . The direction of the arrows indicates whether the stretching is in phase or out of phase; the length shows the approximate amplitude of the vibration. As starting structure, the coordinates of the crystal structure from $[(\text{Et}_4\text{N})_2][\text{Fe}_2(\text{pdt})(\text{CO})_4(\text{CN})_2]$ were used⁷ for geometry optimization on DFT level. The cations were removed for the calculation. Stationary points were confirmed to be minima by the absence of imaginary frequencies. The stretching modes of the CN ligands were calculated to be at 2068 cm^{-1} and 2049 cm^{-1} , whereas stretching modes of the CO ligands are between 1937 cm^{-1} and 1850 cm^{-1} and clearly shifted to lower wavenumbers of $\approx 50\text{ cm}^{-1}$ as compared to the measured FTIR spectrum. At 1937 cm^{-1} , all CO ligand stretching vibrations are in phase.

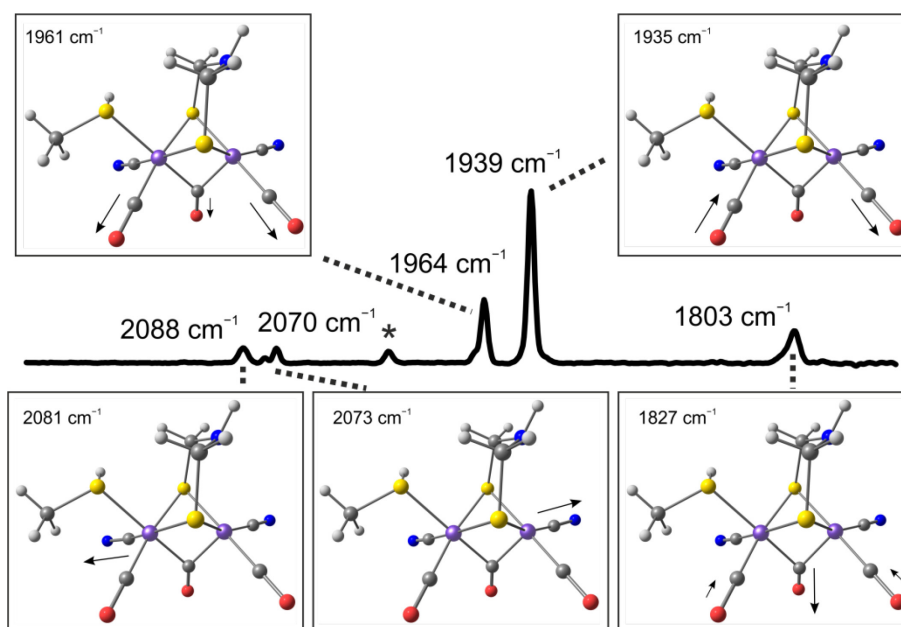
Stretching modes of HydA1-H_{ox}

Figure S4. The FTIR spectrum of HydA1-H_{ox} is taken from Adamska-Venkatesh *et al.*, 2014.¹⁶ The corresponding symmetrical and antisymmetrical stretching modes and wavenumbers of the CO and CN ligands were calculated for $[\text{Fe}_2(\text{adt})(\text{CO})_4(\text{CN})_2]^{2-}$ using the ORCA program for the shown model. The direction of the arrows indicates whether the stretching is in phase, the length shows the approximate size of the elongation. The stretching modes of the CN ligands were calculated to be at 2081 cm⁻¹ and 2073 cm⁻¹. The signal at 1961 cm⁻¹ corresponds to a symmetrical stretching for all CO ligands, whereas the signal at 1935 cm⁻¹ shows antisymmetrical stretching as indicated. The signal at 1827 cm⁻¹ results mainly from the bridging CO ligand.
* peak of CO-inhibited state

Stretching modes of $[\text{Fe}_2(\text{xdt})(\text{CO})_5(\text{CN})]^-$

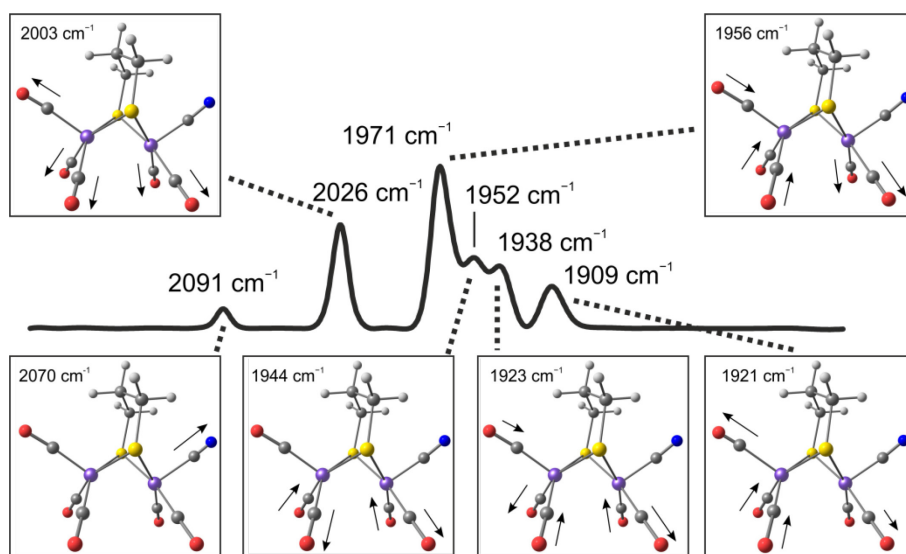


Figure S5. General shape of the FTIR spectrum of $[\text{Fe}_2(\text{xdt})(\text{CO})_5(\text{CN})]^-$. Shown here is the measured spectrum of $[\text{Fe}_2(\text{pdt})(\text{CO})_5(\text{CN})]^-$ (see also **Figure 3**). The corresponding symmetrical and antisymmetrical stretching modes of the CO and CN ligands including the calculated wavenumbers were calculated for $[\text{Fe}_2(\text{pdt})(\text{CO})_5(\text{CN})]^-$ using the ORCA program. They are the same for $[\text{Fe}_2(\text{adt})(\text{CO})_5(\text{CN})]^-$. The direction of the arrows indicates whether the stretching is in phase, the length shows the approximate size of the elongation. As starting structure, the coordinates of optimized structure $[\text{Fe}_2(\text{pdt})(\text{CO})_4(\text{CN})_2]^{2-}$ (**Figure S3**) were used and modified to $[\text{Fe}_2(\text{pdt})(\text{CO})_5(\text{CN})]^-$. Geometry optimization was performed on DFT level. The CN stretching mode was calculated to be at 2070 cm^{-1} ; in addition there are five signals from CO ligand stretching. The signal with highest energy at 2003 cm^{-1} corresponds to a stretching of all CO ligands in phase.

Further insertion attempts: mono-nuclear iron, all-carbonyl and additional di-cyanide compounds

Compound **8** is purple in color and turns black upon water exposure, indicating decomposition. Compound **9** is less polar as compared to all other variants and not fully soluble in DMSO. As a slightly less polar and water mixable solvent acetone was used. However, only a diluted solution of **9** could be made. A mixture of unmaturred HydA1 and **9** turned yellowish-milky, indicating water insolubility. The same phenomenon was observed for a mixture of unmaturred HydA1 and **1c** as well as **10b** dissolved in DMSO.

HydA1-7 did not show any hydrogen production or oxidation activity. **Figure S6** shows the FTIR spectrum of compound **7** in free and HydA1-bound form.

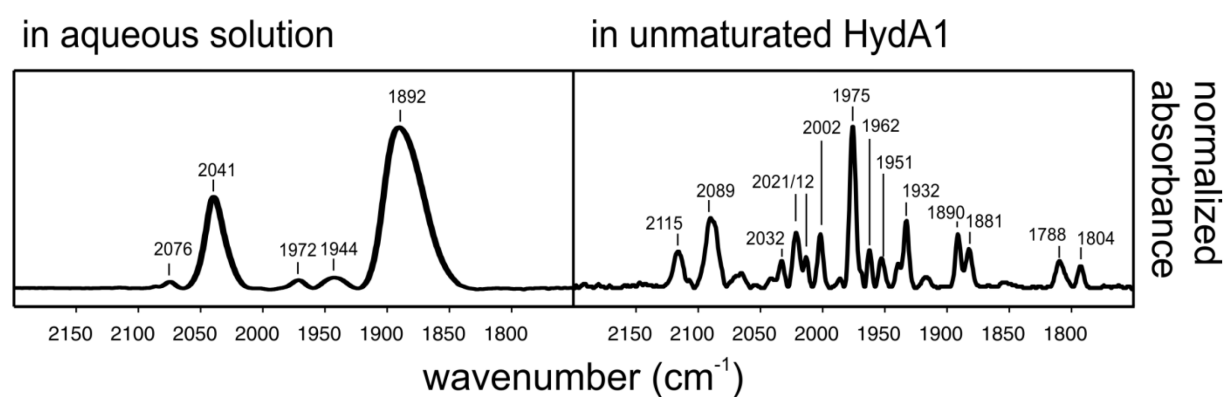


Figure S6. FTIR spectra of $\text{Fe}(\text{CN})_2(\text{CO})_3^{2-}$ in aqueous solution and inserted into unmaturred HydA1. Spectra were measured at 15 °C in 25 mM Tris/HCl, pH 8.0, 25 mM KCl (and 2 mM NaDT in case of HydA1-7). The spectrum on the right is rescaled to the same amplitude.

HydA1-2a, HydA1-3a, HydA1-4 and HydA1-5

Table S2. Vibrational frequencies for *C.r.* HydA1 H_{ox}, HydA1-*x*, *D.d.* H_{trans}, *D.d.* H_{inact} and HydA1-*x*^c.

	$\nu(\text{CN})$ (cm ⁻¹)		$\nu(\text{CO})$ (cm ⁻¹)		$\nu(\mu\text{-CO})$ (cm ⁻¹)	Ref.
<i>C.r.</i> H _{ox}	2083	2070	1964	1940	1800	17
HydA1-2a	2085	2065	1963	1934	1798	18
HydA1-3a	2084	2061	1960	1932	1788	this study
HydA1-5	2089	2069	1971	1944	1804	this study
HydA1-4	2090	2075	1980	1962	1867	18
<i>D.d.</i> H _{trans}	2100	2075	1983	1977	1836	19
<i>D.d.</i> H _{inact}	2106	2087	2007	1983	1848	19
HydA1-1a ^c	2085	2076	1969	1944	1833	15
HydA1-2a ^c	2088	2074	1970	1946	1825	15
HydA1-4 ^c	2091	2083	1980	1953	1838	15
HydA1-4-H ₂ ^c	2104	2087	1983	1955	1835	15
HydA1-4-H ₂ O ^c	2084	2082	1978	1946	1820	15
HydA1-4-H _{eq} ^c	2108	2097	2021	1991	1889	15
HydA1-4-H _{ax} ^c	2113	2006	1994	1978	1872	15

^c = computed

Blue: The FTIR spectra of HydA1-2a, -3a and -5 resemble the H_{ox} state of *C.r.* HydA1.

Yellow: In HydA1-4, especially the vibrational modes of the CO ligands are shifted to higher wavenumbers. This is also seen in H_{trans} and H_{inact} of *D.d.* HydA1.

Green: Computed FTIR spectra. The calculated spectra of HydA1-4 with the ligands H₂ (HydA1-4-H₂^c) and H₂O (HydA1-4-H₂O^c) on the distal iron do not show a big effect on the peak positions. Protonation of the bridgehead oxygen with the proton equatorial (HydA1-4-H_{eq}^c) leads to a shift to higher wavenumbers for all peaks, especially drastic for the CO bands, whereas axial protonation (HydA1-4-H_{ax}^c) leads to a complete change in the peak pattern.¹⁵ From these data, it seems rather unlikely that HydA1-4 as observed in FTIR has an H₂ or H₂O ligand on the distal iron or is protonated on the bridgehead. Compared to HydA1-

$1a^c$ and HydA1-2 a^c , the frequencies of HydA1-4 c are slightly shifted to higher wavenumbers, following the trend observed experimentally.

Looking closely at HydA1-5, there is an additional component in the spectrum similar to the one obtained for HydA1-4, probably indicating a second, very minor species that has a similar structure as HydA1-4 (**Figure S7**).

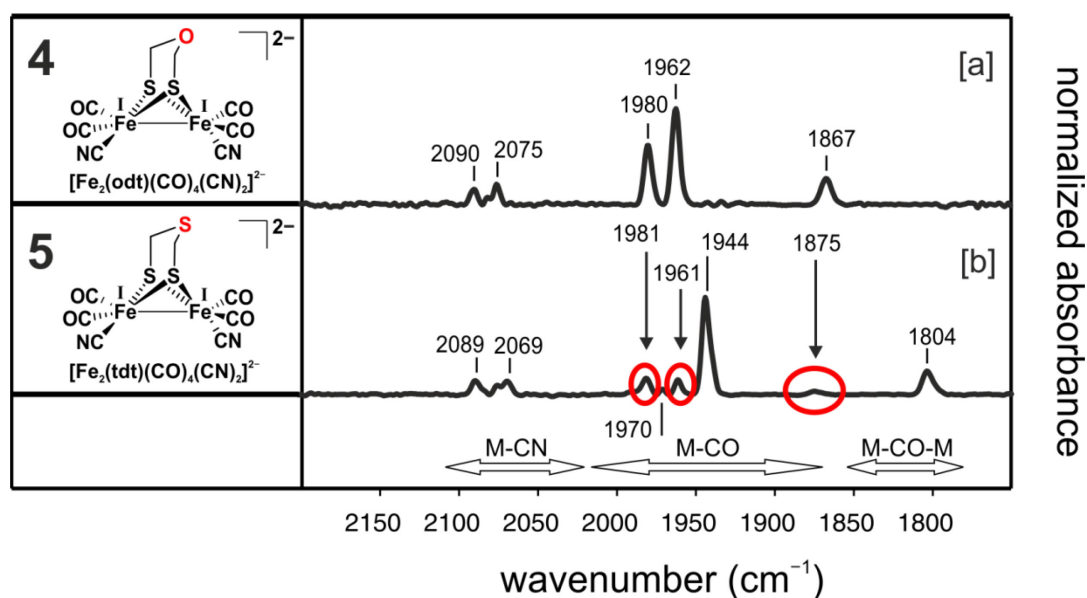


Figure S7. FTIR spectra of HydA1-4 and HydA1-5 as shown in **Figure 2**. Very small peaks in HydA1-5 which resemble the peaks in HydA1-4 are marked in red. They indicate that in the spectrum of HydA1-5, a species similar in structure to HydA1-4 is found.

[a] ¹⁸ [b] this work

HydA1 mono-cyanide variants

The complex FTIR spectra of HydA1-2b and HydA1-3b (**Figure 3**) cannot be explained by the occurrence of multiple redox states due to catalytic activity as for HydA1-1a and HydA1-1b. For all HydA1 mono-cyanide variants, there can be two different orientations with the CN^- ligand on the same side as the [4Fe-4S]-cluster or on the opposite side (**Figure S8**). The position of the CN^- ligand affects the vibrational modes in the FTIR (see **Table S3**). Based on DFT calculations, it seems likely that the spectra of HydA1-2b and HydA1-3b have signals from the binuclear [2Fe]-subsite in the oxidation states $\text{Fe}^{\text{I}}\text{Fe}^{\text{II}}$ and $\text{Fe}^{\text{I}}\text{Fe}^{\text{I}}$ (see below, **Figure S9**). Interactions of the bridgehead with the protein surrounding also have an effect on the CO and CN vibrational modes since the spectra of HydA1-2b and HydA1-3b are not identical.

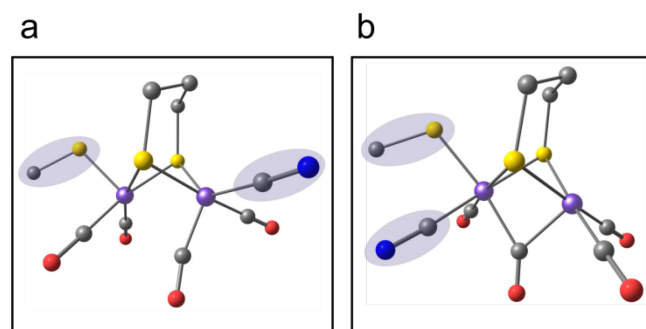


Figure S8. Possible conformations of HydA1 mono-cyanide variants. **a)** The CN^- ligand and the [4Fe-4S]-cluster (here as CH_3SH -group) are on opposite sides. **b)** The [4Fe-4S]-cluster and the CN^- ligand are on the same side.

Geometry optimization has been performed on DFT level for HydA1-2b in the two orientations of the CN^- ligand (**Figure S8**) in the redox states $\text{Fe}^{\text{I}}\text{Fe}^{\text{II}}$ or $\text{Fe}^{\text{I}}\text{Fe}^{\text{I}}$ and the FTIR spectra were predicted (**Table S3**). For comparison, geometry optimization has also been made for HydA1-2a in the redox state $\text{Fe}^{\text{I}}\text{Fe}^{\text{II}}$.

Table S3. Computed vibrational frequencies for HydA1-2a^c and HydA1-2b^c.

HydA1-2a ^c	$\nu(\text{CN})$ (cm ⁻¹)		$\nu(\text{CO})$ (cm ⁻¹)		
Fe ^I Fe ^{II}	2082	2071	1961	1936	1825
HydA1-2b ^c	$\nu(\text{CN})$ (cm ⁻¹)	$\nu(\text{CO})$ (cm ⁻¹)			
Fe ^I Fe ^{II} (o)	2073	2027	1999	1961	1940
Fe ^I Fe ^{II} (s) *	2110	2031	1990	1980	1868 ^[a]
Fe ^I Fe ^I (o)	2089	1969	1941	1905	1895
Fe ^I Fe ^I (s) *	2077	1961	1923	1903	1822 ^[a]

^c = computed

[a] bridging CO

s: CN⁻ ligand and CH₃SH-group point to the same sideo: CN⁻ ligand and CH₃SH-group point to the opposite sides* shown in **Figure S9c** $\nu(\text{CN})$  $\nu(\text{CO})$ shifted to higher wavenumbers compared to HydA1-2a^c $\nu(\text{CO})$ in the same region as HydA1-2a^c $\nu(\text{CO})$ shifted to lower wavenumbers compared to HydA1-2a^c $\nu(\mu\text{-CO})$

As seen in **Figure S9a**, the peaks of FTIR spectra of $[\text{Fe}_2(\text{xdt})(\text{CO})_4(\text{CN})_2]^{2-}$ shift to higher values for $[\text{Fe}_2(\text{xdt})(\text{CO})_5(\text{CN})]^-$ (indicated by arrows, shown for $[\text{Fe}_2(\text{pdt})(\text{CO})_4(\text{CN})_2]^{2-}$ **2**). This is caused by the reduced negative charge of the complex due to the lacking CN⁻ ligand in $[\text{Fe}_2(\text{xdt})(\text{CO})_5(\text{CN})]^-$: the electron density on the irons is lower and less electron density can be donated to the CO ligands via π -back-bonding overall, leading to comparably stronger C \equiv O bonds.

Figure **S9b** shows the experimental FTIR spectra of HydA1-2a and HydA1-2b. In HydA1-2a, the vibrations of the CO ligands are found at 1963 cm⁻¹ and 1934 cm⁻¹ (area shown in pink), whereas in HydA1-2b, we observe peaks above (orange) and below (yellow) that region. Assuming the same structure including a bridging CO as observed, peaks in the orange region can be explained by the general shift to higher wavenumbers from a more to a less electron rich complex as explained above. In this case, the oxidation state must remain constant (*i.e.* Fe^IFe^{II}). Peaks in the yellow region can only be explained by a lowering of the oxidation state, presumably to Fe^IFe^I. The electron for the reduction could come from the reduced [4Fe-4S]-cluster. Compared to di-cyanide variants, the mono-cyanide variants have less electron density on the [2Fe]-subsite and should therefore be easier to reduce. As shown in

our recent paper on HydA1-1a and HydA1-2a³, slight modifications in the [2Fe]-subsite have relatively strong effects on the redox potentials.

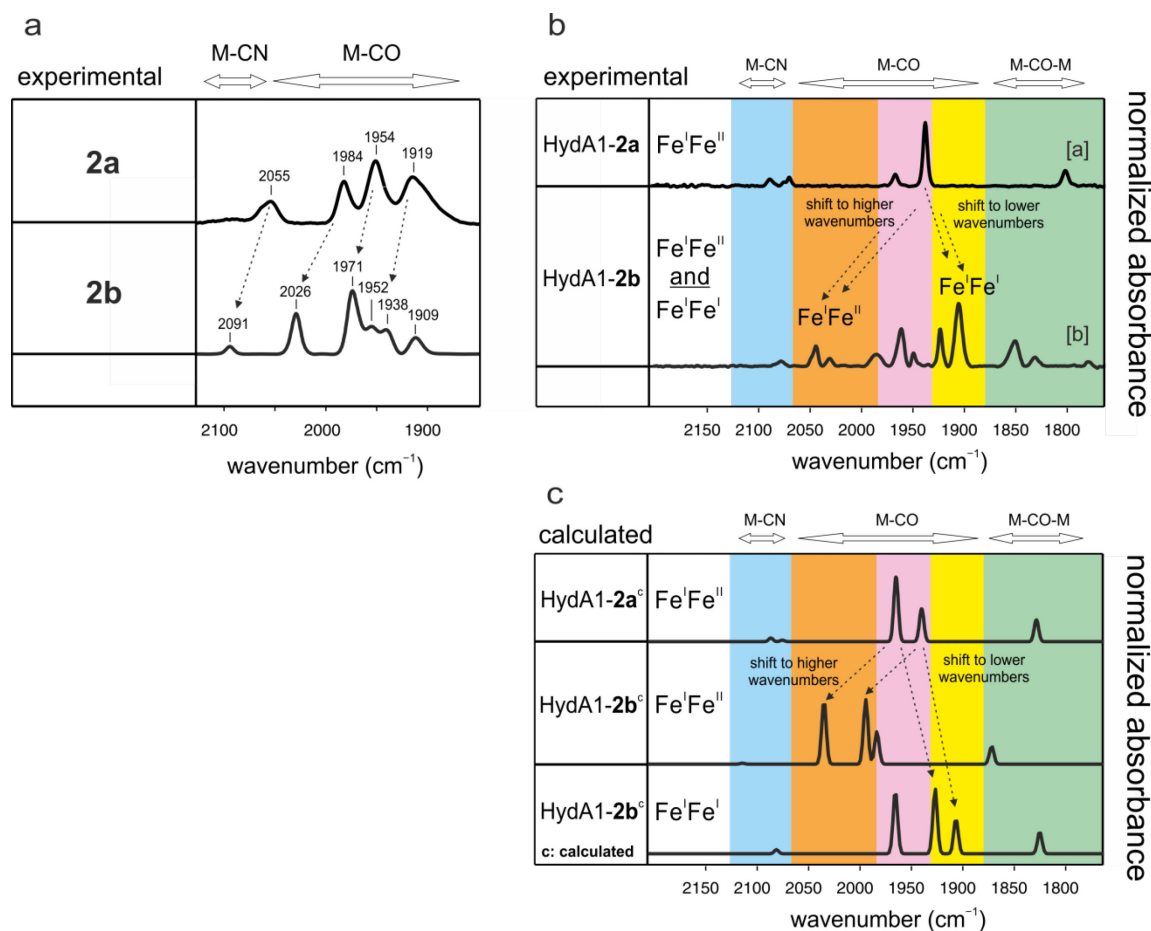


Figure S9. **a**) Spectra of the free complexes $[\text{Fe}_2(\text{pdt})(\text{CO})_4(\text{CN})_2]^{2-}$ and $[\text{Fe}_2(\text{pdt})(\text{CO})_5(\text{CN})]^-$ in solution with shift of frequencies. **b**) Illustration of the origin of the peaks in HydA1-2b. The FTIR spectrum of HydA1-2a is shown on the top and of HydA1-2b at the bottom. **c**) Calculated spectra of HydA1-2a^c in the oxidation state Fe^IFe^{II} (top) and of HydA1-2b^c in the oxidation states Fe^IFe^{II} and Fe^IFe^I. The color coding corresponds to **Table S3**.

[a]¹⁸ [b] this work

Figure S9c shows the calculated spectra HydA1-2a^c, HydA1-2b^c (Fe^IFe^{II}) and HydA1-2b^c (Fe^IFe^I). In HydA1-2b^c (Fe^IFe^{II}), the peaks are shifted to higher wavenumbers (orange region) compared to HydA1-2a^c, whereas the peaks of HydA1-2b^c (Fe^IFe^I) are shifted to lower wavenumbers (yellow region). This confirms the assumption made for the experimental spectrum. Peaks of bridging CO ligands (green area) and peaks in the pink region as seen in the experimental spectrum of HydA1-2b originate from both oxidation states according to DFT calculations (**Table S3**, highlighted in the respective color). It is shown here for HydA1-2b and was chosen as an example for a HydA1 mono-cyanide variant. For the reasons explained above, it seems likely that we observe peaks from the oxidations states Fe^IFe^{II} and Fe^IFe^I in the FTIR spectrum of HydA1-2b and HydA1-3b.

HydA1-6

The FTIR spectrum of the HydA1-6 is very different from HydA1-1a-H_{ox}, HydA1-2a, -3a, -4 and -5. There are various peaks between 2102 cm⁻¹ and 1907 cm⁻¹ and no clear peaks can be observed in the region of the bridging CO (1750–1850 cm⁻¹). Additionally, there are several peaks in the region where none could be observed for HydA1-1a-H_{ox} and HydA1-2a, -3a, -4 and -5 (2051–1987 cm⁻¹ and 1907 cm⁻¹). In summary, this indicates that the electronic structure of HydA1-6 is very different from HydA1-1a-H_{ox} and HydA1-2–5 and that we observe more than one state. This is likely because 6 in contrast to 1–5 has two diastereomers, depending on the orientation of the methyl groups: the *d,l*-isomer (Figure S10a) and the meso-isomer. In the latter the methyl groups can be either diequatorial (Figure S10b) or diaxial (Figure S10c). The additional steric bulk of the methyl groups might also contribute to differences in the electronic structure as compared to HydA1-2–5.

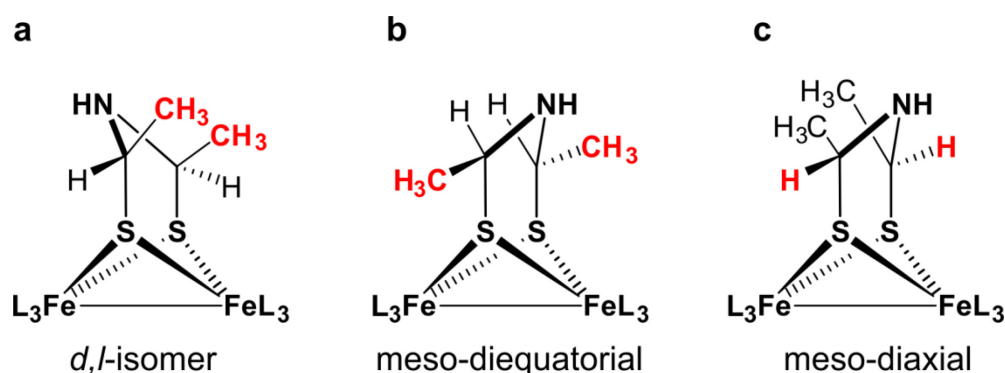


Figure S10. a–c) Isomers of the synthetic complexes $[\text{Fe}_2(\text{dime-adt})(\text{CO})_4(\text{CN})_2]^{2-}$. **a)** The *d,l*-isomer. **b)** The meso-diequatorial diastereomer. **c)** The meso-diaxial diastereomer where the bridge from the meso-diequatorial is flipped.

References

- [1] Esselborn, J., Lambertz, C., Adamska-Venkatesh, A., Simmons, T., Berggren, G., Noth, J., Siebel, J., Hemschemeier, A., Artero, V., Reijerse, E., Fontecave, M., Lubitz, W., and Happe, T. (2013) Spontaneous activation of [FeFe]-hydrogenases by an inorganic [2Fe] active site mimic, *Nat. Chem. Biol.* 9, 607-609.
- [2] Kuchenreuther, J. M., Grady-Smith, C. S., Bingham, A. S., George, S. J., Cramer, S. P., and Swartz, J. R. (2010) High-Yield Expression of Heterologous [FeFe] Hydrogenases in *Escherichia coli*, *ONE* 5, 15491-15491.
- [3] Adamska-Venkatesh, A., Krawietz, D., Siebel, J., Weber, K., Happe, T., Reijerse, E., and Lubitz, W. (2014) New Redox States Observed in [FeFe] Hydrogenases Reveal Redox Coupling Within the H-Cluster, *J. Am. Chem. Soc.* 136, 11339-11346.
- [4] Schmidt, M., Contakes, S. M., and Rauchfuss, T. B. (1999) First Generation Analogues of the Binuclear Site in the Fe-Only Hydrogenases: $\text{Fe}_2(\mu\text{-SR})_2(\text{CO})_4(\text{CN})_2^{2-}$, *J. Am. Chem. Soc.* 121, 9736-9737.
- [5] Lyon, E. J., Georgakaki, I. P., Reibenspies, J. H., and Darensbourg, M. Y. (1999) Monoxide and Cyanide Ligands in a Classical Organometallic Complex Model for Fe-Only Hydrogenase, *Angew. Chem. Int. Edit.* 38, 3178-3180.
- [6] Le Cloirec, A., C. Davies, S., J. Evans, D., L. Hughes, D., J. Pickett, C., P. Best, S., and Borg, S. (1999) A di-iron dithiolate possessing structural elements of the carbonyl/cyanide sub-site of the H-centre of Fe-only hydrogenase, *Chem. Commun.*, 2285-2286.
- [7] Gloaguen, F., Lawrence, J. D., Schmidt, M., Wilson, S. R., and Rauchfuss, T. B. (2001) Synthetic and structural studies on $[\text{Fe}_2(\text{SR})_2(\text{CN})_x(\text{CO})_{6-x}]^{x-}$ as active site models for Fe-only hydrogenases, *J. Am. Chem. Soc.* 123, 12518-12527.
- [8] Neese, F. (2012) The ORCA program system, *Wiley Interdisciplinary Reviews: Comput. Mol. Sci.* 2, 73-78.
- [9] Vahtras, O., Almlöf, J., and Feyereisen, M. W. (1993) Integral approximations for LCAO-SCF calculations, *Chem. Phys. Lett.* 213, 514-518.
- [10] Perdew, J. P. (1986) Density-functional approximation for the correlation energy of the inhomogeneous electron gas, *Physical Review B* 33, 8822-8824.
- [11] Becke, A. D. (1988) Density-functional exchange-energy approximation with correct asymptotic behavior, *Phys. Rev. A* 38, 3098-3100.
- [12] Baerends, E. J., Ellis, D. E., and Ros, P. (1973) Self-consistent molecular Hartree-Fock-Slater calculations I. The computational procedure, *Chem. Phys.* 2, 41-51.

-
- [13] Dunlap, B. I., Connolly, J. W. D., and Sabin, J. R. (1979) On some approximations in applications of $X\alpha$ theory, *J. Chem. Phys.* *71*, 3396-3402.
- [14] Schäfer, A., Huber, C., and Ahlrichs, R. (1994) Fully optimized contracted Gaussian basis sets of triple zeta valence quality for atoms Li to Kr, *J. Chem. Phys.* *100*, 5829-5835.
- [15] Yu, L., Greco, C., Bruschi, M., Ryde, U., De Gioia, L., and Reiheet, M. (2011) Targeting Intermediates of FeFe-Hydrogenase by CO and CN Vibrational Signatures, *Inorg. Chem.* *50*, 3888-3900.
- [16] Adamska-Venkatesh, A., Krawietz, D., Siebel, J., Weber, K., Happe, T., Reijerse, E., and Lubitz, W. (2014) Artificially matured [FeFe] hydrogenase reveals new redox states, *J. Am. Chem. Soc.*
- [17] Silakov, A., Kamp, C., Reijerse, E., Happe, T., and Lubitz, W. (2009) Spectroelectrochemical Characterization of the Active Site of the [FeFe] Hydrogenase HydA1 from *Chlamydomonas reinhardtii*, *Biochemistry* *48*, 7780-7786.
- [18] Berggren, G., Adamska, A., Lambertz, C., Simmons, T. R., Esselborn, J., Atta, M., Gambarelli, S., Mouesca, J. M., Reijerse, E., Lubitz, W., Happe, T., Artero, V., and Fontecave, M. (2013) Biomimetic assembly and activation of FeFe-hydrogenases, *Nature* *499*, 66-70.
- [19] Roseboom, W., Lacey, A., Fernandez, V., Hatchikian, E. C., and Albracht, S. J. (2006) The active site of the [FeFe]-hydrogenase from *Desulfovibrio desulfuricans*. II. Redox properties, light sensitivity and CO-ligand exchange as observed by infrared spectroscopy, *J. Biol. Inorg. Chem.* *11*, 102-118.

4.2 Paper II

Enhancing hydrogen production of microalgae by redirecting electrons from photosystem I to hydrogenase

Sigrun Rumpel, Judith F. Siebel, Christophe Farès, Jifu Duan, Edward Reijerse, Thomas Happe, Wolfgang Lubitz, Martin Winkler

Energy Environ. Sci. **2014**, 7, 3296–3301 - Reproduced by permission of The Royal Society of Chemistry.

DOI: 10.1039/C4EE01444H

Journal name: Energy & Environmental Science

Impact factor: 20.523 (in 2014)

Author: second author

Contribution: – 20 %

- I established protein preparations
- I made all biological samples for NMR experiments
- I contributed to the preparation of the manuscript

S. Rumpel measured and analyzed the NMR data, J. Duan and M. Winkler performed the biological sample preparations for the activity measurements and their analyses.

4.2.1 Journal article

Energy &
Environmental
Science

COMMUNICATION

View Article Online
View Journal | View IssueCite this: *Energy Environ. Sci.*, 2014, 7, 3296Received 9th May 2014
Accepted 29th July 2014

DOI: 10.1039/c4ee01444h

www.rsc.org/ees

Enhancing hydrogen production of microalgae by redirecting electrons from photosystem I to hydrogenase†

Sigrun Rumpel,^{*a} Judith F. Siebel,^a Christophe Farès,^b Jifu Duan,^c Edward Reijerse,^a Thomas Happe,^c Wolfgang Lubitz^a and Martin Winkler^{*c}

Photohydrogen generation in microalgae is catalysed by hydrogenases, which receive electrons from photosystem I via the ferredoxin PETF. The dominant acceptor of photosynthetic electrons is, however, ferredoxin-NADP⁺-oxidoreductase (FNR). By utilizing targeted ferredoxin and FNR variants in a light-dependent competition assay, electrons can be redirected to the hydrogenase yielding a five-fold enhanced hydrogen evolution activity.

Introduction

Dihydrogen (H₂) has the highest mass energy density of all known fuel types and as it can be generated from and converted back into water, it is one of the most attractive energy carriers to appease both the world's climate and energy crisis.^{1,2} The solar-driven bio-H₂ production by microalgae like *Chlamydomonas (C.) reinhardtii* complements chemical technologies for solar fuel generation.³ Upon sulfur or nitrogen depletion *C. reinhardtii* switches to anaerobic growth conditions.⁴⁻⁶ As a consequence of anaerobiosis, the [FeFe]-hydrogenase HYDA1 is expressed.⁷ It receives electrons from photosystem I (PSI) via the plant-type photosynthetic electron transport ferredoxin (PETF) for catalysing the reversible reduction of protons to H₂.^{8,9} Under normal growth conditions PETF provides photosynthetic electrons for a variety of different metabolic pathways such as the assimilation of nitrate, sulfate and ammonia, as well as the reductive regeneration of glutathione.¹⁰ Most of its electrons are, however, used for CO₂ fixation mediated by the PETF-dependent ferredoxin-NADP⁺-oxidoreductase (FNR) (Fig. 1).¹¹

While [FeFe]-hydrogenases can achieve very high turnover rates of up to 10⁴ molecules H₂ per second *in vitro*,¹² H₂

Broader context

The most urgent challenge of our time is to replace the dwindling resources of fossil fuels by sustainable non-polluting alternatives. Hydrogen is a promising energy vector and can be utilized as a regenerative carrier of emission-free energy especially when produced biologically. Unicellular green algae like *Chlamydomonas reinhardtii* are known to produce hydrogen light-dependently. Their highly efficient [FeFe]-hydrogenase (HYDA1) catalyzes the reversible reduction of protons and electrons to dihydrogen. However, evolutionary and physiological constraints severely restrict the hydrogen yield of algae. An important key to achieve an economically viable biohydrogen production is the understanding and modulation of the photosynthetic electron flow via the ferredoxin PETF to HYDA1 which is limited by its competition with enzymes of other metabolic pathways. The most important alternative electron transfer pathway results in NADPH production by the ferredoxin-NADP⁺-oxidoreductase (FNR). Here, we were able to identify targets for manipulating the common redox-partner binding site of PETF to selectively shift the bias of PETF from FNR towards HYDA1. Indeed, genetic modifications of the identified residues result in an enhanced light-driven hydrogen production and might lead to the design of an economically competitive hydrogen producing organism.

evolution is strongly limited *in vivo* by the O₂ sensitivity of the hydrogenase¹³ and the availability of reduced PETF.¹⁴ The latter issue has been addressed in several studies demonstrating that through down-regulation of competing processes the electron flow of photosynthetic electrons can be redirected towards the hydrogenase HYDA1 inducing enhanced H₂ photoproduction.¹⁵⁻¹⁸ Very recently it has been shown that a knock-down of FNR expression in *C. reinhardtii* leads to a 2.5-fold higher H₂ production activity under sulfur deprivation.¹⁹ In another drastic approach Yacoby *et al.* were able to increase H₂ photoproduction using a PETF/HYDA1 fusion protein thus enforcing the bias of PETF to switch from FNR to HYDA1.²⁰

However, for stable photosynthetic growth a certain level of FNR activity has to be conserved and independent PETF is mandatory to dissipate at least a minor fraction of electrons to other essential redox pathways. In the long run a more subtle approach will be favored to develop a healthy growing algal

^aMax-Planck-Institut für Chemische Energiekonversion, Stiftstrasse 34-36, 45470 Mülheim an der Ruhr, Germany. E-mail: sigrun.rumpel@cec.mpg.de

^bMax-Planck-Institut für Kohlenforschung, Kaiser-Wilhelm-Platz 1, 45470 Mülheim an der Ruhr, Germany

^cLehrstuhl für Biochemie der Pflanzen, Fakultät für Biologie und Biotechnologie, Ruhr-Universität Bochum, AG Photobiotechnologie, 44801 Bochum, Germany. E-mail: martin.winkler-2@rub.de

† Electronic supplementary information (ESI) available: Experimental details and additional figures. See DOI: 10.1039/c4ee01444h

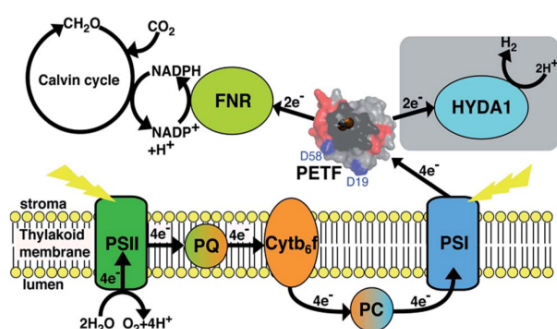


Fig. 1 Scheme showing competing electron transfer pathways in the chloroplast of the microalga *C. reinhardtii* leading either to H₂ or NADPH production. The surface presentation of PETF is shown with the residues closer than 7 Å to the [2Fe–2S]-cluster in dark grey. PETF residues affected by HYDA1-binding are coloured red (cf. Fig. 3). Residues D19 and D58 (see text) are in blue. H₂ production by HYDA1 requires anaerobic conditions (grey box). PSI and PSII, photosystems I and II, respectively; PQ, plastoquinone pool; PC, plastocyanin; Cyt, cytochrome.

strain with a strong but not self-destructive solitary focus on H₂ production.

In the current study, we follow a new approach at the molecular level aiming to reduce the PETF affinity for FNR without affecting its interaction with HYDA1. Both interactions are driven by Coulomb forces between conserved acidic PETF residues near the [2Fe–2S]-cluster with corresponding basic residues on HYDA1 and FNR. Many of the contact sites for the PETF/FNR interaction have already been identified using mutagenesis²¹ and NMR-titration studies.^{22,23} The PETF/HYDA1 interaction has also been investigated based on mutagenesis studies.⁹ These investigations were, however, not specifically aimed at a differentiation between the PETF/HYDA1 and PETF/FNR contacts.

Results and discussion

To distinguish between contacts of PETF to HYDA1 and FNR, we conducted parallel NMR titrations of ¹⁵N-labeled PETF with increasing amounts of HYDA1 or FNR and monitored the magnitude of the chemical shift changes ($\Delta\delta_{\text{HN}}$) of the backbone amide resonances of PETF using ¹H–¹⁵N-TROSY-HSQC experiments (Fig. 2, see further details in the ESI†).²⁴

In our study, the largest NMR chemical shift perturbations upon complex formation with HYDA1 and FNR were observed for the backbone amides of residues 23–28, 58–67 and 89–94 and, indeed, most identified PETF residues are involved in complex formations with both proteins (Fig. 3).

In addition, these residues are similar to the FNR-binding interfaces of highly homologous PETF molecules from other species (Table S1 in the ESI†)^{21,22} and protrude to three directions from the [2Fe–2S]-cluster which is located close to one side of the molecular surface of PETF.²⁵ Overall, the observed chemical shift perturbations are small suggesting multiple orientations of the proteins in the complex, which have also

been described for other electron transfer complexes like myoglobin/cytochrome b₅ (ref. 26), cytochrome c/cytochrome b₅ (ref. 27) and superoxide reductase/rubredoxin.²⁸ Importantly, when comparing the chemical shift changes for PETF/HYDA1 and PETF/FNR the two aspartate residues D19 and D58 can be identified as being only affected upon FNR-binding (Fig. 2 and 3). The other residues, that are only significantly affected when FNR, but not when HYDA1 binds to PETF, are either not solvent accessible (Val54, Gln56, and Thr87) or marginally affected in reduced PETF (Tyr1, Tyr21, and Asp55) (for further details see ESI, Fig. S1–S3†). The chemical shift changes indicate D58 as a part of the PETF-binding interface for FNR and as an immediate neighbour of the PETF-binding interface for HYDA1 (Fig. 3). Remarkably, D19 does not belong to the residues surrounding the [2Fe–2S]-cluster (Fig. 1). A possible explanation for its importance is provided by the X-ray structure of the homologous PETF/FNR complex from *maize leaf*.²² In this structure, D19 is about 12 Å away from the apparent N-terminal FNR residue, however, this structure is 18 and 13 amino acids shorter at the N-terminus compared to the native FNR of *maize leaf* and *C. reinhardtii*, respectively. These missing N-terminal residues might form an embracing loop with PETF and interact with D19 (Fig. S4 in the ESI†). The identification of D19 and D58 of PETF as being solely important for the PETF/FNR and not for the PETF/HYDA1 complex suggests the differentiation between individual binding partners as a so far unknown function of the negatively charged residues of plant-type ferredoxins.

To investigate the potential use of D19 and D58 of PETF for improving bio-H₂ production their importance for differentiating between FNR and HYDA1 was confirmed by mutagenesis to alanine. The resulting three PETF variants (PETF-D19A, -D58A and -D19A/D58A) were examined in a light-driven H₂ production assay in the absence and presence of FNR for their efficiency to donate electrons to HYDA1. This assay is a simplification of an earlier described reconstitution system⁹ on the basis of proflavine (PF) as a photosensitizer substituting PSL. The original upstream electron transfer compounds 2,6-dichlorophenolindophenol and plastocyanin were omitted and instead of ascorbate a low concentration of EDTA was used as a sacrificial electron donor. To assess H₂ production by HYDA1 in direct competition with NADPH-production by FNR, equimolar concentrations of HYDA1 and FNR were used. The FNR co-substrate NADP⁺ was further included alongside with the enzyme nitrate reductase (NAR) from *Aspergillus niger*²⁹ to ensure a constant co-substrate recycling (Fig. 4).

In the absence of FNR, the measured light-dependent HYDA1-activity remains almost unchanged for mutant-PETF when compared to wild type (wt)-PETF (Fig. 5). However, in the presence of FNR the H₂ production level of HYDA1 with wt-PETF is diminished to only 7% (Fig. 5) due to the significantly lower affinity of PETF for HYDA1 (21–35 μM)^{9,30} than for FNR (2.6–6.6 μM).³¹ This HYDA1-activity is the control level of the competition assay, in which PETF-D19A exhibits about 1.5-fold and PETF-D58A about 2.5-fold increased H₂ production (Fig. 5). Importantly, H₂ production with PETF-D19A/D58A is 4-fold increased indicating a synergistic enhancement of the single effects (Fig. 5). These results confirm the role of the acidic PETF

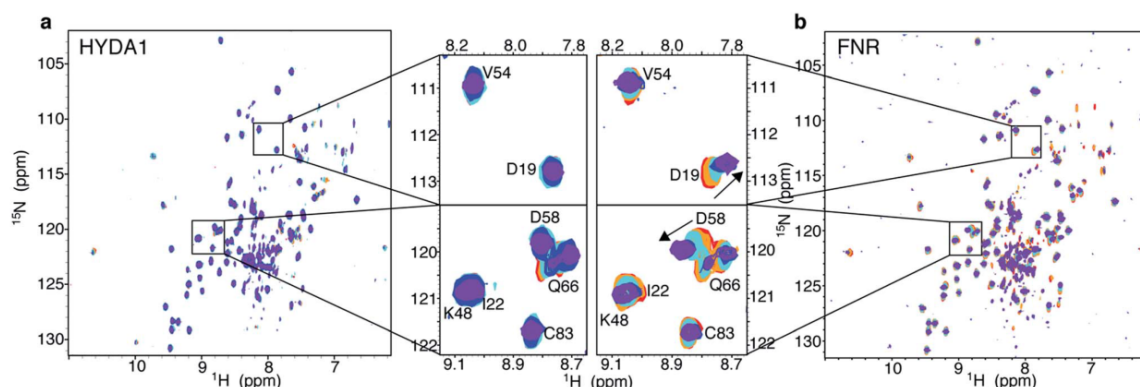


Fig. 2 NMR-titration analysis of the interaction of PETF with HYDA1 and FNR. Overlay of ^1H - ^{15}N TROSY-HSQC spectra of PETF with HYDA1 (a) and FNR (b) at ratios of 1 : 0 (red), 1 : 1 (orange), 1 : 5 (cyan), 1 : 10 (blue) and 1 : 15 (violet). Backbone amide signals for residues 35–45 and 73–76 were not observed in the NMR-spectra due to a distance of <7 Å to the paramagnetic $[2\text{Fe}-2\text{S}]$ -cluster.

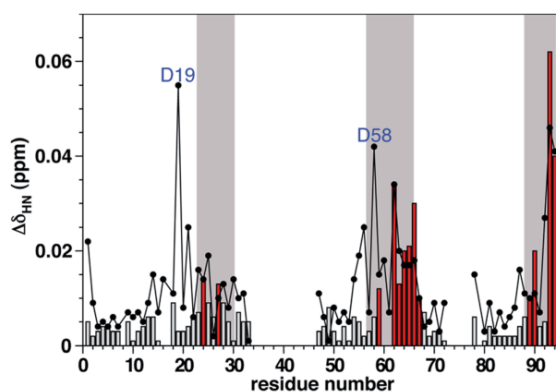


Fig. 3 NMR chemical shift perturbation of PETF upon complex formation with HYDA1 and FNR. Average backbone amide chemical shift changes ($\Delta\delta_{\text{HN}}$) for free and bound PETF at a 15-fold excess of HYDA1 (bars) and FNR (black line) were calculated according to the equation $\Delta\delta_{\text{HN}} = [(\Delta\delta_{\text{H}})^2 + 0.2\Delta\delta_{\text{N}}^2]/2^{1/2}$ and plotted versus the residue number. The red bars indicate PETF residues with $\Delta\delta_{\text{HN}} \geq 0.01$ ppm upon HYDA1-binding. A grey background highlights the PETF regions known to bind to FNR (Table S1 in the ESI †) which exhibit also the largest chemical shift changes upon complex formation with HYDA1 and FNR.

residues D19 and D58 for distinguishing HYDA1 and FNR. The high homology between plant-type $[2\text{Fe}-2\text{S}]$ -ferredoxins from different origins (Fig. S5 in the ESI †) further suggests a general importance of residues D19 and D58 to direct electrons towards FNR. Apart from that, PETF-D19A/D58A promises to be valuable for the bioengineering of an efficient H_2 production pathway.

The profound shift of electron transfer away from FNR towards HYDA1 is even more pronounced when FNR variants are used that exhibit a decreased PETF-dependent catalytic efficiency.³¹ The two FNR variants which have been earlier described to be affected either in the PETF affinity (FNR-K83L) or in the PETF-dependent maximum reaction rate (FNR-K89L) were assayed in comparison to wt-PETF (Fig. 5). FNR-K83L and

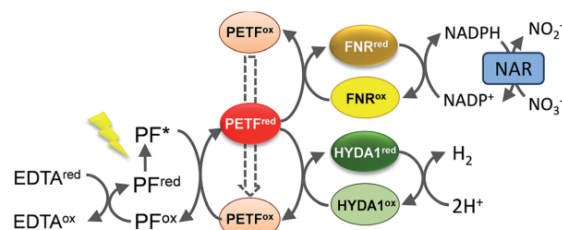


Fig. 4 Schematic illustration of the electron transfer pathway of the light-dependent H_2 production assay to investigate the competition between HYDA1 and FNR for reduced PETF. PF = proflavin; NAR = nitrate reductase; red = reduced; ox = oxidized.

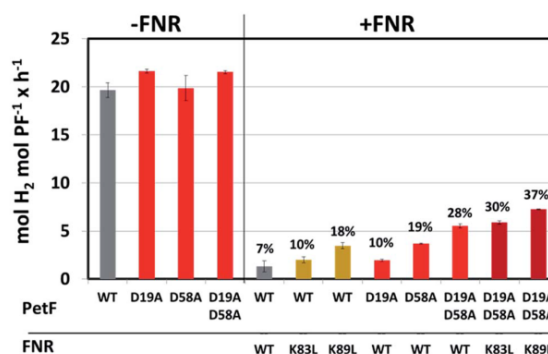


Fig. 5 Rates of light-dependent H_2 production determined for HYDA1 with wt- or mutant-PETF in the absence (-FNR) and in the presence of wt- or mutant-FNR (+FNR). The indicated 7% HYDA1-activity in the presence of FNR refers to 100% HYDA1-activity in the absence of FNR. The error bars depict the standard deviation of 4 independent measurements.

-K89L allow for H_2 production rates about 1.5- and more than 2.5-fold higher than the control level, resembling the effects of PETF mutagenesis. Importantly, H_2 production is increased

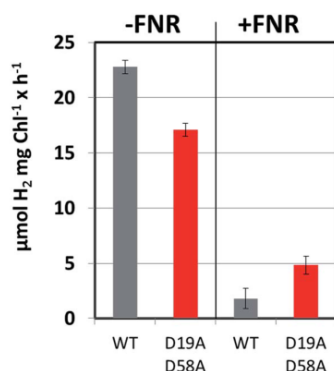


Fig. 6 PSI-dependent H₂ photoproduction rates of HYDA1 with wt-PETF and PETF-D19A/D58A in the absence (–FNR) and presence of FNR (+FNR). The error bars depict the standard deviation of 3–4 independent measurements.

about 5-fold compared to the control level when performing the assay with FNR-K89L and PETF-D19A/D58A (Fig. 5). This almost additive effect demonstrates that the electron transfer hierarchy can be most effectively shifted by addressing both, FNR and PETF.

We also examined PETF-D19A/D58A in the light-dependent H₂ production assay with PSI, which is the native electron donor for PETF and hence mimics more closely the *in vivo* situation in *C. reinhardtii*. In this PSI-dependent assay, light-driven H₂ production is slightly decreased for PETF-D19A/D58A in the absence of FNR (Fig. 6) indicating that at least one exchange mildly affects the interaction with PSI. Nevertheless, the H₂ production activity in the presence of FNR is increased about 3-fold for PETF-D19A/D58A compared to wt-PETF (Fig. 6) reproducing the result of the proflavin-dependent assay.

Our knowledge-based variant PETF-D19A/D58A may be used in addition to or as part of a PETF/HYDA1 fusion protein as published by Yacoby *et al.*²⁰ to achieve the best H₂ production capacities. Furthermore, an implementation of these modifications within a *C. reinhardtii* strain like *Stm6* with about a 5-fold higher H₂ evolution yield¹⁶ is a promising strategy to increase the efficiency of microalgal H₂ production beyond the 5% light energy-to-H₂ conversion efficiency which is expected to be required for commercial use.³²

Conclusions

Conserved PETF aspartic acid residues D19 and D58 are crucial for the differential recognition of FNR and HYDA1 as an electron transfer binding partner. Mutation of these residues to alanine suppresses FNR binding and redirects PETF electron flow towards Hyda1 thus enhancing *in vivo* hydrogen production. It can be anticipated that also in other metabolic pathways highly conserved acidic ferredoxin residues are relevant for molecular recognition of their binding partners. The effects of PETF and FNR genetic modifications are additive, *i.e.* the interaction efficiency of PETF for FNR can be further reduced by

employing the targeted FNR variants K83L and K89L in combination with the PETF-D19A/D58A variant. This combined metabolic engineering approach opens new avenues for the design of H₂-producing organisms with an increased photo-fermentative H₂ production.

Materials and methods

Protein preparation

All FeS-cluster containing proteins were heterologously expressed in *Escherichia coli* BL21(DE3)ΔiscR.³³ Recombinant HYDA1 holoprotein and PETF from *C. reinhardtii* were expressed and prepared as described earlier.^{9,34} Site directed exchanges were introduced following the QuikChange procedure described for the site-directed mutagenesis kit from Stratagene (Agilent Technologies). Introduced mutations were confirmed by DNA sequencing (3130x Genetic Analyzer, Applied Biosystems). The *fur* cDNA of *C. reinhardtii* was amplified excluding the N-terminal sequence part that covers the chloroplast transit peptide³⁵ and cloned behind the Strep-tag II sequence of the expression vector pASK-IBA7 (IBA GmbH, Goettingen). FNR was expressed in *E. coli* BL21(DE3)pLysS using lysogeny broth (LB) medium and purified analogously to PETF. Protein purity was verified *via* SDS-PAGE and Coomassie staining (Fig. S6†).

Samples for NMR spectroscopy were expressed using *E. coli* codon optimized genes of *C. reinhardtii* PETF and HYDA1 inserted into pET21b. The expression plasmid for PETF contained a C-terminal TEV cleavage site preceded by a Strep-tag II and the expression plasmid for HYDA1 contained an N-terminal TEV cleavage site followed by a Strep-tag II. To prepare ¹⁵N- and ¹³C/¹⁵N-labeled samples, *E. coli* cells were grown in M9-based minimal medium containing ¹⁵NH₄Cl and/or ¹³C₆-glucose. For purification, following affinity chromatography, the protein was incubated with TEV protease at a ratio of 1 : 1 (w/w) overnight at room temperature to remove the Strep-tag. The plasmid for expressing TEV protease was a gift of the Arrowsmith laboratory. The His6-tagged TEV protease was removed with Talon beads (Clontech) and PETF was further purified by gel filtration using a Superdex 75 16/60 (GE Healthcare). Recombinant apo-HYDA1 was activated by addition of [Fe₂(CO)₄(CN)₂][(SCH₂)₂NH]²⁻.

NMR spectroscopy

NMR samples contained 0.1–1 mM PETF in 50 mM potassium phosphate pH 6.8, 50 mM NaCl and 10% D₂O (v/v). All NMR experiments were performed at 298 K on a Bruker AVANCE 600 spectrometer equipped with a cryogenic probehead. The 3D spectra employed a non-uniform sampling scheme in the indirect dimension and were reconstructed by the multi-dimensional decomposition software MDDNMR³⁶ interfaced with the MDDGUI³⁷ and NMRPipe/NMRDraw.³⁸ Backbone assignments were obtained using standard triple resonance experiments.³⁹ All spectra were analyzed using Sparky (T. D. Goddard and D. G. Kneller, University of California, San Francisco).

NMR titration experiments

PETF complex formation with HYDA1 and FNR was monitored by carrying out a series of 2D ^1H - ^{15}N -TROSY-HSQC experiments of a 100 μM ^{15}N -labeled PETF solution with a binding partner at a molar ratio of 1 : 0, 1 : 1, 1 : 2, 1 : 5, 1 : 10 and 1 : 15. Weighted averages of the ^1H and ^{15}N backbone chemical shift changes of a particular residue were calculated according to the equation $\Delta\delta_{\text{HN}} = [(\Delta\delta_{\text{H}}^2 + 0.2\Delta\delta_{\text{N}}^2)/2]^{1/2}$.

Measurement of light-driven hydrogen production and competition assay

To determine the light-driven H_2 production, 50 nM HYDA1 was combined with wild type (wt) or mutant forms of 20 μM PETF. The total volume of 200 μl contained 40 mM EDTA as a sacrificial electron donor and 200 μM proflavine (acridine-3,6-diamine) as a photosensitizer in 100 mM potassium phosphate pH 6.8, supplemented with 1 mM sodium dithionite and 3 mM NaNO_3 .

To determine the H_2 production efficiency of HYDA1 under competitive conditions, 50 nM FNR and 2 mM NADP^+ were added. For stabilizing the level of NADP^+ and thus the competitive efficiency of the FNR during the H_2 production period, 0.36 U of nitrate reductase (NAR) from *Aspergillus niger* (Sigma-Aldrich) was further included. Compound concentrations were adjusted for optimal H_2 production efficiency (Fig. S7†).

PSI-dependent H_2 photoproduction was measured as described earlier.³⁰ The assay comprised 5 mM sodium ascorbate, 0.6 mM DCPIP (2,6-dichlorophenol-indophenol), 30 μM plastocyanin, 20 μM PETF, 50 nM HYDA1 in 20 mM Tris pH 7.4, 20 mM MgCl_2 , 0.03% β -DM, 1 mM sodium dithionite and 3 mM NaNO_3 . PSI was added corresponding to the amount of 5 μg chlorophyll (Chl). For determining the PSI-dependent HYDA1-activity under competitive conditions 50 nM FNR, 2 mM NADP^+ and 0.036 U NAR were added.

All reaction samples were prepared under anoxic conditions in 2 ml Eppendorf tubes and sealed with Suba-Seal stoppers (size 13, Sigma-Aldrich). After sparging the reaction mixture with argon for 5 min, the reaction tubes were light-exposed ($1200 \mu\text{mol photons m}^{-2} \text{s}^{-1}$) under constant shaking at 37 °C. H_2 production was determined after 30 min by analyzing 400 μl of the headspace *via* gas chromatography (GC-2010, Shimadzu).

Acknowledgements

We thank Katharina Weber for providing $[\text{Fe}_2(\text{CO})_4(\text{CN})_2][(\text{SCH}_2)_2\text{NH}]^{2-}$. This work was supported by the Max Planck Society and the Bundesministerium für Bildung und Forschung (BMBF) (Bio-H2) (to T.H. and W.L.). T.H. and M.W. gratefully acknowledge support from the Deutsche Forschungsgemeinschaft (HA 255/2-1) and the Volkswagen Foundation (LigH2t).

Notes and references

- 1 J. Hetland and G. Mulder, *Int. J. Hydrogen Energy*, 2007, **32**, 736–747.

- 2 M. Ball and M. Wietschel, *Int. J. Hydrogen Energy*, 2009, **34**, 615–627.
- 3 A. Volgusheva, S. Styring and F. Mamedov, *Proc. Natl. Acad. Sci. U. S. A.*, 2013, **110**, 7223–7228.
- 4 A. Melis and T. Happe, *Plant Physiol.*, 2001, **127**, 740–748.
- 5 A. Melis, L. Zhang, M. Forestier, M. L. Ghirardi and M. Seibert, *Plant Physiol.*, 2000, **122**, 127–136.
- 6 G. Philipps, T. Happe and A. Hemschemeier, *Planta*, 2012, **235**, 729–745.
- 7 M. Pape, C. Lambertz, T. Happe and A. Hemschemeier, *Plant Physiol.*, 2012, **159**, 1700–1712.
- 8 S. T. Stripp and T. Happe, *Dalton Trans.*, 2009, 9960–9969.
- 9 M. Winkler, S. Kuhlger, M. Hippler and T. Happe, *J. Biol. Chem.*, 2009, **284**, 36620–36627.
- 10 M. Winkler, A. Hemschemeier, J. Jacobs, S. Stripp and T. Happe, *Eur. J. Cell Biol.*, 2010, **89**, 998–1004.
- 11 N. Carrillo and E. A. Ceccarelli, *Eur. J. Biochem.*, 2003, **270**, 1900–1915.
- 12 W. Lubitz, H. Ogata, O. Rüdiger and E. Reijerse, *Chem. Rev.*, 2014, **114**, 4081–4148.
- 13 S. T. Stripp, G. Goldet, C. Brandmayr, O. Sanganas, K. A. Vincent, M. Haumann, F. A. Armstrong and T. Happe, *Proc. Natl. Acad. Sci. U. S. A.*, 2009, **106**, 17331–17336.
- 14 M. Winkler, S. Kawelke and T. Happe, *Bioresour. Technol.*, 2011, **102**, 8493–8500.
- 15 C. M. Agapakis, D. C. Ducat, P. M. Boyle, E. H. Wintermute, J. C. Way and P. A. Silver, *J. Biol. Eng.*, 2010, **4**, 3.
- 16 O. Kruse, J. Rupprecht, K. P. Bader, S. Thomas-Hall, P. M. Schenk, G. Finazzi and B. Hankamer, *J. Biol. Chem.*, 2005, **280**, 34170–34177.
- 17 T. Rühle, A. Hemschemeier, A. Melis and T. Happe, *BMC Plant Biol.*, 2008, **8**, 107.
- 18 D. Tolleter, B. Ghysels, J. Alric, D. Petroustos, I. Tolstygina, D. Krawietz, T. Happe, P. Auroy, J. M. Adriano, A. Beyly, S. Cuine, J. Plet, I. M. Reiter, B. Genty, L. Cournac, M. Hippler and G. Peltier, *Plant Cell*, 2011, **23**, 2619–2630.
- 19 Y. Sun, M. Chen, H. Yang, J. Zhang, T. Kuang and F. Huang, *Int. J. Hydrogen Energy*, 2013, **38**, 16029–16037.
- 20 I. Yacoby, S. Pochekailov, H. Toporik, M. L. Ghirardi, P. W. King and S. Zhang, *Proc. Natl. Acad. Sci. U. S. A.*, 2011, **108**, 9396–9401.
- 21 T. Mayoral, M. Martinez-Julvez, I. Perez-Dorado, J. Sanz-Aparicio, C. Gomez-Moreno, M. Medina and J. A. Hermoso, *Proteins*, 2005, **59**, 592–602.
- 22 G. Kurisu, M. Kusunoki, E. Katoh, T. Yamazaki, K. Teshima, Y. Onda, Y. Kimata-Arigo and T. Hase, *Nat. Struct. Biol.*, 2001, **8**, 117–121.
- 23 P. N. Palma, B. Lagoutte, L. Krippahl, J. J. G. Moura and F. Guerlesquin, *FEBS Lett.*, 2005, **579**, 4585–4590.
- 24 K. Pervushin, R. Riek, G. Wider and K. Wüthrich, *Proc. Natl. Acad. Sci. U. S. A.*, 1997, **94**, 12366–12371.
- 25 K. Fukuyama, *Photosynth. Res.*, 2004, **81**, 289–301.
- 26 J. A. R. Worrall, Y. Liu, P. B. Crowley, J. M. Nocek, B. M. Hoffman and M. Ubbink, *Biochemistry*, 2002, **41**, 11721–11730.

[View Article Online](#)

Communication

Energy & Environmental Science

- 27 A. N. Volkov, D. Ferrari, J. A. R. Worrall, A. M. J. J. Bonvin and M. Ubbink, *Protein Sci.*, 2005, **14**, 799–811.
- 28 R. M. Almeida, P. Turano, I. Moura, J. J. Moura and S. R. Pauleta, *ChemBioChem*, 2013, **14**, 1858–1866.
- 29 B. Dziedzic, J. Mazanowska-Gajdowicz, A. Walczewska, A. Sarniak and D. Nowak, *Clin. Chim. Acta*, 2003, **335**, 65–74.
- 30 T. Happe and J. D. Naber, *Eur. J. Biochem.*, 1993, **214**, 475–481.
- 31 P. Decottignies, V. Flesch, C. Gerard-Hirne and P. Le Marechal, *Plant Physiol. Biochem.*, 2003, **41**, 637–642.
- 32 E. Stephens, I. L. Ross, Z. King, J. H. Mussgnug, O. Kruse, C. Posten, M. A. Borowitzka and B. Hankamer, *Nat. Biotechnol.*, 2010, **28**, 126–128.
- 33 M. K. Akhtar and P. R. Jones, *Appl. Microbiol. Biotechnol.*, 2008, **78**, 853–862.
- 34 J. Esselborn, C. Lambert, A. Adamska-Venkatesh, T. Simmons, G. Berggren, J. Noth, J. Siebel, A. Hemschemeier, V. Artero, E. Reijerse, M. Fontecave, W. Lubitz and T. Happe, *Nat. Chem. Biol.*, 2013, **9**, 607–609.
- 35 P. Decottignies, P. Lemarechal, J. P. Jacquot, J. M. Schmitter and P. Gadal, *Arch. Biochem. Biophys.*, 1995, **316**, 249–259.
- 36 A. Gutmanas, P. Jarvoll, V. Y. Orekhov and M. Billeter, *J. Biomol. NMR*, 2002, **24**, 191–201.
- 37 A. Lemak, A. Gutmanas, S. Chitayat, M. Karra, C. Fares, M. Sunnerhagen and C. H. Arrowsmith, *J. Biomol. NMR*, 2011, **49**, 27–38.
- 38 F. Delaglio, S. Grzesiek, G. W. Vuister, G. Zhu, J. Pfeifer and A. Bax, *J. Biomol. NMR*, 1995, **6**, 277–293.
- 39 A. Bax and S. Grzesiek, *Acc. Chem. Res.*, 1993, **26**, 131–138.

4.2.2 Supporting information

Enhancing hydrogen production of microalgae by redirecting electrons from photosystem I to hydrogenase

Sigrun Rumpel, Judith F. Siebel, Christophe Farès, Jifu Duan, Edward Reijerse, Thomas Happe, Wolfgang Lubitz, Martin Winkler

Abbreviations

PETF^{ox}: oxidized PETF

PETF^{red}: reduced PETF

S1 Materials and Methods

Protein preparation

All FeS-cluster containing proteins were heterologously expressed in *E. coli* BL21(DE3) $\Delta iscR$.¹ Recombinant HYDA1 holoprotein and PETF from *C. reinhardtii* were expressed and prepared as described earlier.^{2,3} Site directed exchanges were introduced following the QuikChange procedure described for the site-directed mutagenesis kit from Stratagene (Agilent Technologies). Introduced mutations were confirmed by DNA sequencing (3130x Genetic Analyzer, Applied Biosystems). The *fnr* cDNA of *C. reinhardtii* was amplified excluding the N-terminal sequence part that covers the chloroplast transit peptide⁴ and cloned behind the Strep-tag II sequence of expression vector pASK-IBA7 (IBA GmbH, Goettingen). FNR was expressed in *E. coli* BL21(DE3)pLysS using lysogeny broth (LB) medium and purified analogously to PETF. Protein purity was verified via SDS-PAGE and Coomassie staining (**Fig. S6**).

Samples for NMR spectroscopy were expressed using *E. coli* codon optimized genes of *C. reinhardtii* PETF and HYDA1 inserted into pET21b. The expression plasmid for PETF contained a C-terminal TEV cleavage site preceded by a Strep-tag II and the expression plasmid for HYDA1 contained a N-terminal TEV cleavage site followed by a Strep-tag II. To prepare ¹⁵N- and ¹³C/¹⁵N-labeled samples, *E. coli* cells were grown in M9-based minimal medium containing ¹⁵NH₄Cl and/or ¹³C₆-glucose. For purification, following affinity

chromatography, the protein was incubated with TEV protease at a ratio of 1:1 (w/w) overnight at room temperature to remove the Strep-tag. The plasmid for expressing TEV protease was a gift of the Arrowsmith lab. The His₆-tagged TEV protease was removed with Talon beads (Clontech) and PETF was further purified by gel filtration using a Superdex 75 16/60 (GE Healthcare). Recombinant apo-HYDA1 was activated by adding of $[\text{Fe}_2(\text{CO})_4(\text{CN})_2[(\text{SCH}_2)_2\text{NH}]]^{2-}$.

NMR spectroscopy

NMR samples contained 0.1-1 mM PETF in 50 mM potassium phosphate pH 6.8, 50 mM NaCl and 10% D₂O (v/v). All NMR experiments were acquired at 298 K on a Bruker AVANCE 600 spectrometer equipped with a cryogenic probehead. The 3D spectra employed a non-uniform sampling scheme in the indirect dimension and were reconstructed by the multi-dimensional decomposition software MDDNMR⁵ interfaced with the MDDGUI⁶ and NMRPipe/NMRDraw.⁷ Backbone assignments were obtained using standard triple resonance experiments.⁸ All spectra were analyzed using Sparky (T. D. Goddard and D. G. Kneller, University of California, San Francisco).

NMR titration experiments

PETF complex formation with HYDA1 and FNR was monitored by recording a series of 2D ¹H-¹⁵N-TROSY-HSQC experiments of a 100 μM ¹⁵N-labeled PETF solution with binding partner at a molar ratio of 1:0, 1:1, 1:2, 1:5, 1:10 and 1:15. Weighted averages of the ¹H and ¹⁵N backbone chemical shift changes of a particular residue were calculated according to the equation $\Delta\delta_{\text{HN}} = [(\Delta\delta_{\text{H}}^2 + 0.2\Delta\delta_{\text{N}}^2)/2]^{1/2}$.

Measurement of light-driven hydrogen production and competition assay

To determine the light-driven H₂ production, 50 nM HYDA1 was combined with wild type (wt) or mutant forms of 20 μM PETF. The total volume of 200 μl contained 40 mM EDTA (ethylenediaminetetraacetic acid) as sacrificial electron donor and 200 μM proflavine (acridine-3,6-diamine) as a photosensitizer in 100 mM potassium phosphate pH 6.8, supplemented with 1 mM sodium dithionite and 3 mM NaNO₃.

To determine the H₂-production efficiency of HYDA1 under competitive conditions, 50 nM FNR and 2 mM NADP⁺ were added. For stabilizing the level of NADP⁺ and thus the competitive efficiency of the FNR during the H₂-production period, 0.36 U of nitrate

reductase from *Aspergillus niger* (Sigma-Aldrich) was further included. Compound concentrations were adjusted for optimal H₂-production efficiency (Fig. S7).

PSI-dependent H₂-photoproduction was measured as described earlier.² The assay comprised 5 mM sodium ascorbate, 0.6 mM DCPIP (2,6-Dichlorophenol-indophenol), 30 μM plastocyanin, 20 μM PETF, 50 nM HYDA1 in 20 mM Tris pH 7.4, 20 mM MgCl₂, 0.03% β-DM, 1 mM sodium dithionite and 3 mM NaNO₃. PSI was added corresponding to the amount of 5 μg chlorophyll (Chl). For determining the PSI-dependent HYDA1-activity under competitive conditions 50 nM FNR, 2 mM NADP⁺ and 0.036 U nitrate reductase were added. All reaction samples were prepared under anoxic conditions in 2 ml Eppendorf tubes and sealed with Suba-Seal stoppers (size 13, Sigma-Aldrich). After sparging the reaction mixture with argon for 5 min, the reaction tubes were light-exposed (1200 μmol photons m⁻² s⁻¹) under constant shaking at 37 °C. H₂-production was determined after 30 min by analyzing 400 μl of the head-space via gas chromatography (GC-2010, Shimadzu).

S2 Identification of PetF-residues involved in complex formation with Hyda1

Titration experiments were performed with both PETF^{ox} and PETF^{red} as well as fully active HYDA1 and apo-HYDA1 containing only the [4Fe-4S]-part of the H-cluster (Fig. 1 in the main text and Figs. S1-S3).^{3,9} Since, not unexpectedly, the titration of PETF^{red} with active HYDA1 was virtually identical to that of apo-HYDA1 (Fig. S1), only the apo-HYDA1 results are discussed in the main text. Both PETF^{red} and PETF^{ox} titrations with HYDA1 and FNR confirmed the previously identified binding surfaces (Table S1). Interestingly, Δδ_{HN} for PETF^{red} were increased about 4-fold compared to PETF^{ox} and almost unchanged at a 3-times lower excess of HYDA1 (Fig. 1 in the main text and Fig. S2b) indicating a higher affinity of PETF^{red} than PETF^{ox} for HYDA1. For PETF^{red}, the additionally significant Δδ_{HN} for residues 47-49, 71 and 78 are probably secondary effects due to a conformational change in the neighboring regions (35-45 and 73-76) that coordinate the [2Fe-2S]-cluster. This conformational change is most likely related to electron transfer from PETF^{red} to HYDA1. Surprisingly, the larger difference in the observed Δδ_{HN} for D19 and D58 is more pronounced for PETF^{ox} than for PETF^{red} although PETF^{red} forms the reactive electron transfer complex (Fig. S3).

Table S1. Summary of the largest chemical shift perturbations of PETF upon FNR and HYDA1 addition and shortest intermolecular distance for the PETF/FNR complex structure 1GAQ. PETF residues identified as important for protein binding are labeled by gray background.

$\Delta\delta_{\text{HN}}$ (ppm) upon HYDA1-binding	PETF		PETF/FNR complex ^a	
	residue	$\Delta\delta_{\text{HN}}$ (ppm) upon FNR-binding	residue(s) closest to the PETF residue	minimum distance (Å)
0.003	D19	0.055	E19 ^c	11.9
0.004	Y21	0.025	K153	5.4
0.007	L23 ³	0.016	E154	6.1
0.014	D24 ²	0.014	E154	6.5
0.009	A25 ¹⁰	0.019	K301	6.9
0.013	E27 ²	0.01	K301, K304	3.4, 3.1
0.009	E28 ²	0.013	K301, R305	1.7, 3.8
0.005	A29 ¹⁰	0.008	K301	3.8
0.001	G30 ^{10,11}	0.014	K301, F297	4.2, 5
0.007	L31	0.01	K301	6.3
0.005	D32	0.011	F297	3.8
0.006	V54	0.014	K35	13.8
0.005	D55	0.019	K33	10.4
0.002	Q56	0.025	K33	7.2
0.003	S57 ¹⁰	0.007	K33	4.5
0.006	D58 ^{2,10}	0.042	N30, K33, K153	3.1, 3.4, 4.9
0.012	Q59 ¹⁰	0.015	K35, K33	2.8, 3.8
disappeared	S60 ²	disappeared	N30, K33, P34	2.5, 3.2, 2.3
disappeared	F61 ²	disappeared	V92	2.2
0.034	L62 ^{10,11}	0.034	K91, K35	4.3, 4.9
0.013	D63 ^{2,10}	0.02	K91	2
0.02	D64 ¹⁰	0.017	K88	2.6
0.021	A65 ¹⁰	0.017	K88	5.1
0.03	Q66	0.018	K91	2.9
0.006	Y78	0.015	K153	8.3
0.006	H88 ³	0.011	K275	7.8
0.01	Q89 ³	0.01	K275	10.2
0.02	E90 ²	0.011	K88, K91	7.2, 7.2
0.004	E91 ²	0.007	K88	7.2
0.005	A92	0.027	R93, Y120	7.6, 7.2
0.062	L93	0.046	K85	4.9
0.04	Y94 ^{10,11}	0.041	N86	5.8

^abased on the X-ray structure for the PETF/FNR complex from *maize leaf* (1GAQ).

^bE19 is the N-terminal residue of FNR in 1GAQ. 18 N-terminal residues are missing in the X-ray structure.

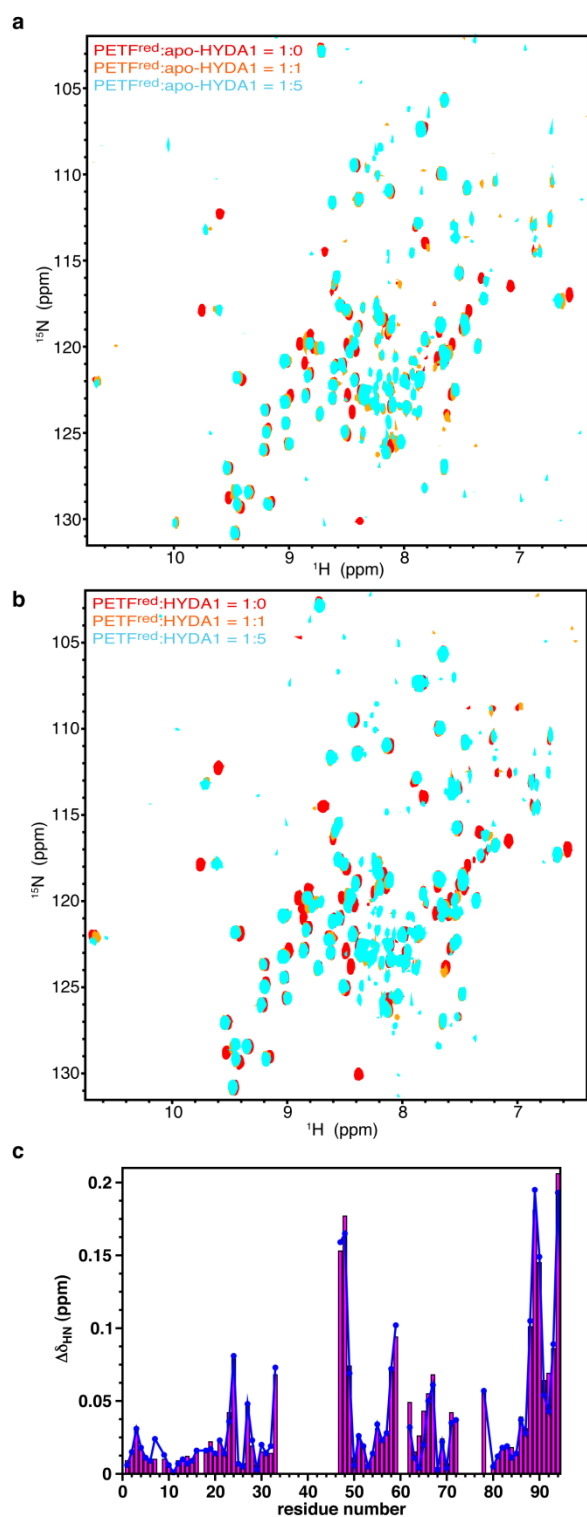


Figure S1. (a,b) Overlay of ^1H - ^{15}N TROSY-HSQC spectra of PETF^{red} with binding partner at ratios of 1:0 (red), 1:1 (orange) and 1:5 (cyan) shown for PETF^{red} :apo-HYDA1 (a) and PETF^{red} : active HYDA1 (b). (c) Weighted averages of the ^1H and ^{15}N backbone chemical shift changes plotted versus the residue number at a 5-fold excess of apo-HYDA1 (blue line) and active HYDA1 (magenta bars) upon binding to PETF^{red} .

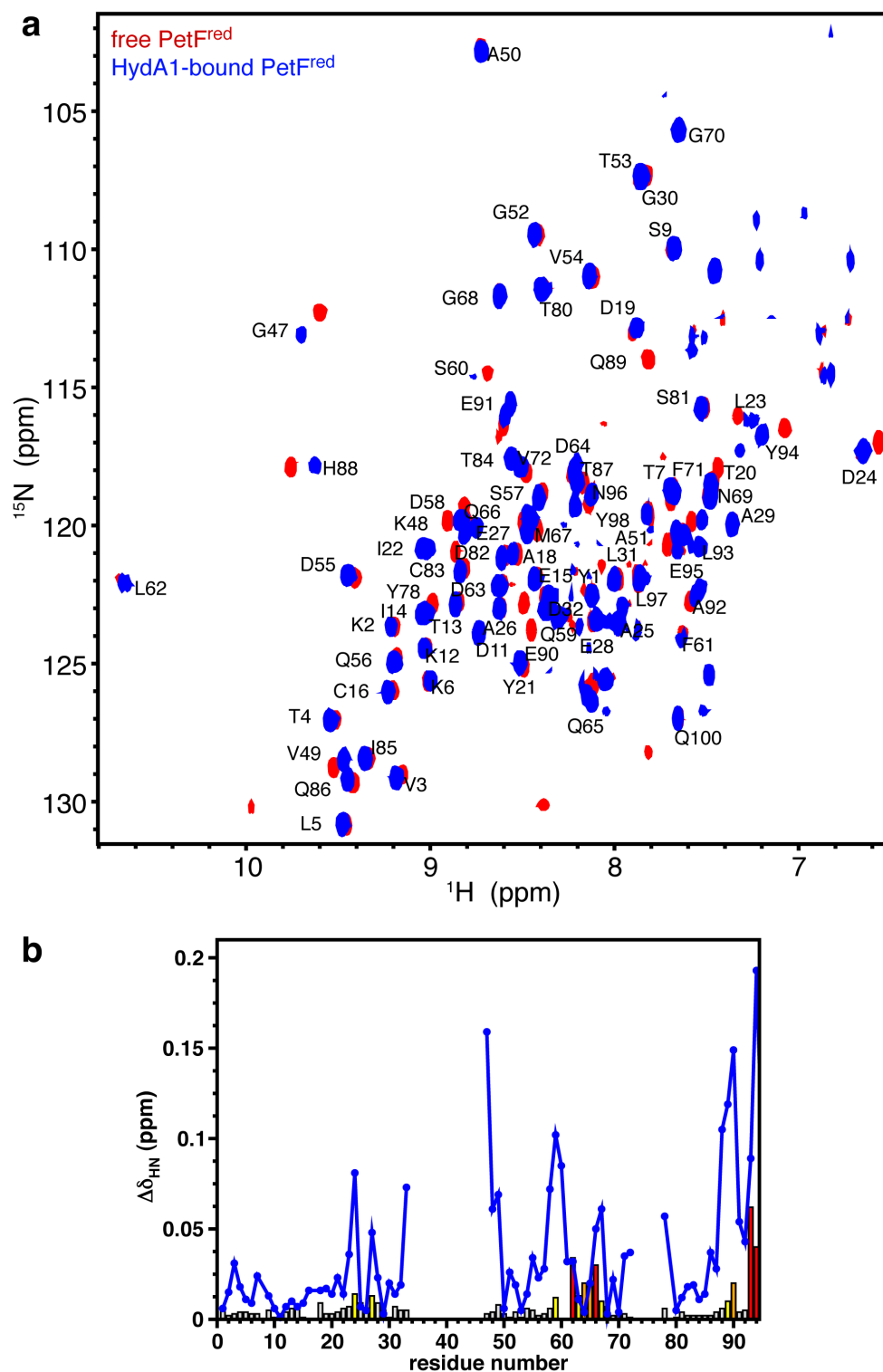


Figure S2. (a) Overlay of ^1H - ^{15}N TROSY-HSQC spectra of ^{15}N -labeled PETF^{red} in the absence (red) and presence (blue) of HYDA1 at a 1:1 molar ratio. (b) Amide backbone chemical shift changes of PETF^{ox} and PETF^{red} upon HYDA1-binding. Weighted averages of the ^1H and ^{15}N backbone chemical shift changes plotted versus the residue number at a 15-fold excess of HYDA1 for PETF^{ox} (bars) and a 5-fold excess of HYDA1 for PETF^{red} (blue line). The coloured bars correspond to **Fig. 3**.

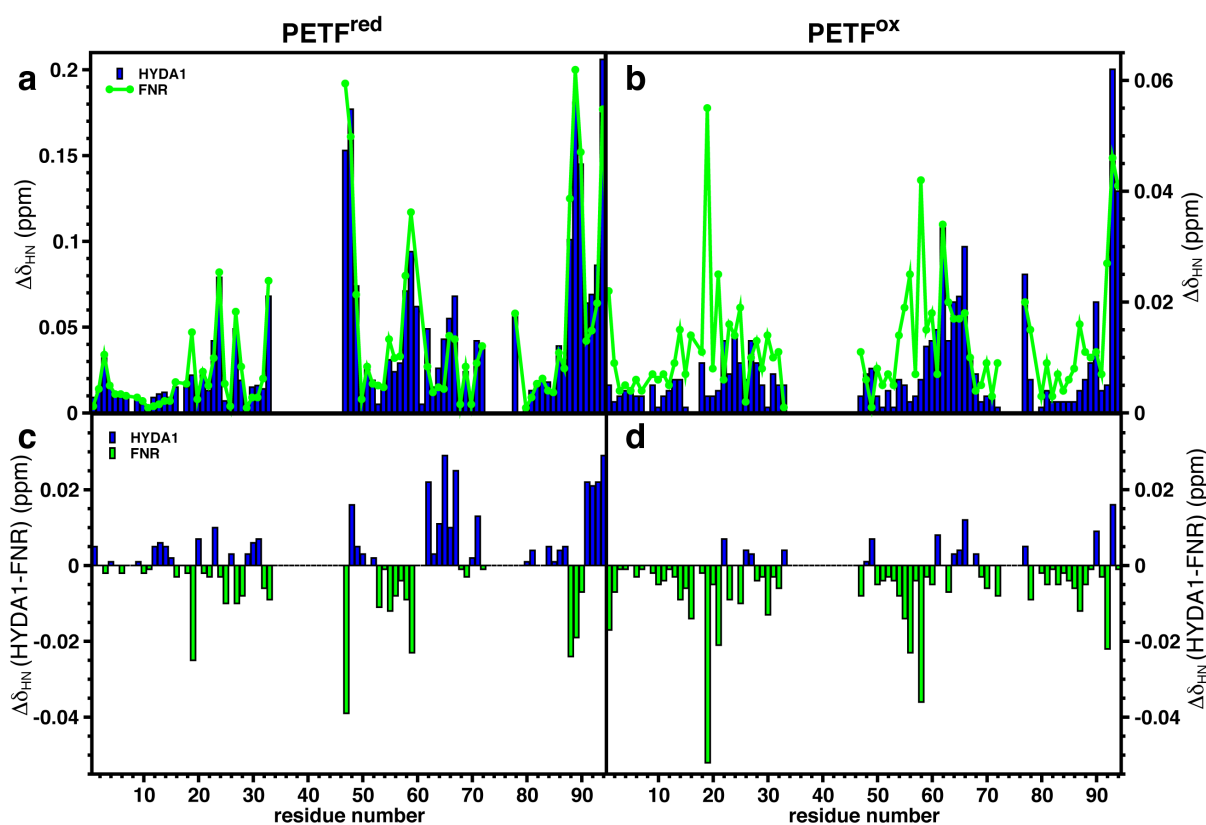


Figure S3. Differences between HYDA1- and FNR-binding to PETF^{red} and PETF^{ox}. Weighted averages of the amide backbone ¹H and ¹⁵N chemical shift changes ($\Delta\delta_{\text{HN}}$) upon protein binding are plotted versus the residue number for PETF^{red} (a,c) and for PETF^{ox} (b,d). (a,b) Chemical shift changes between free and bound PETF are calculated for a 5- and 15-fold excess of binding partner, respectively. Bars indicating the results for HYDA1 are colored blue and green lines indicate results obtained with FNR. (c,d) Differences of the average chemical shift changes for FNR- and HYDA1-binding were determined as $\Delta\delta_{\text{HN}}(\text{HYDA1})-\Delta\delta_{\text{HN}}(\text{FNR})$ and residues with larger chemical shift changes for HYDA1 are shown as blue bars and as green bars for FNR.

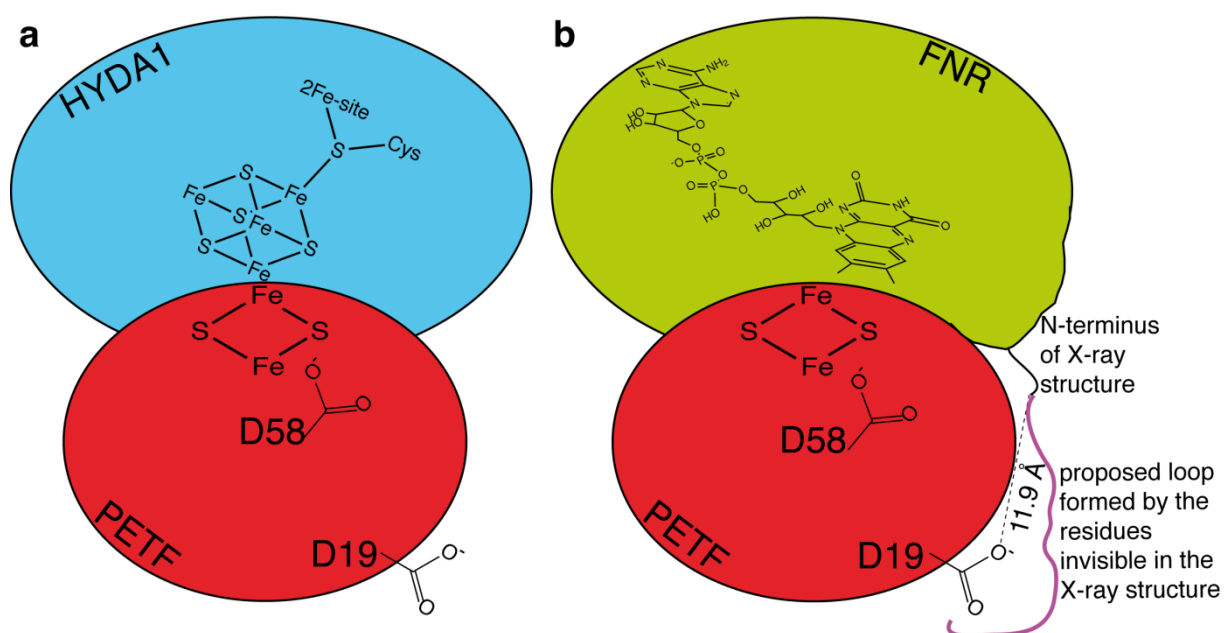


Figure S4. Schematic representation of the PETF/HYDA1 (a) and the PETF/FNR complex (b).

```

                D19                                D58
PETFCr  YKVTL--KTPSGDKTIECPADTYILDAEEEAGLDLPYSRAGACSSCAGKVAAGTVDQSDQSFLLDDAQMGNGFVLTQVAYPTSDCTIQTHQEEALY-
FDX Vc  YKVTF--KTPSGDKVVEVADDVYLLDAEEEAGMDLPYSCRAGACSSCAGKIVSGTVDQSDQSFLLDDKQMEAGFVLTQVAYATSDLVILTNQEEGLY-
FDX Cf  YKVTL--KTPSGEETIECPEDTYILDAEEEAGLDLPYSCRAGACSSCAGKVESGEVDQSDQSFLLDDAQMGKGFVLTQVAYPTSDVTILTHQEEALY-
FDX Ds  YMVTL--KTPSGEQKVEVSPDSYILDAEEEAGVDLPYSCRAGSCSSCAGKVESGTVDQSDQSFLLDDQMDSGFVLTQVAYATSDCTIVTHQEEENLY-
FDX At  YKVKFI--TPEGEQEVECEEDVYVLDAAEEEAGLDLPYSCRAGSCSSCAGKVVSIGSDQSDQSFLLDDEQMSEGYVLTQVAYPTSDVVIETHKKEEAIM-
FDX Zm  YNVKLI--TPEGEVELQVPDDVYILDQAEEDGIDLDPYSCRAGSCSSCAGKVVSIGSDQSDQSYLDDGQIADGWVLTCHAYPTSDVVIETHKKEELTGA
FDX Ps  YKVKLV--TPDGTQEFECPSDYYILDHAAEEVIGIDLDPYSCRAGSCSSCAGKVVGGEVDQSDQSFLLDDEQIEAGFVLTQVAYPTSDVVIETHKKEEDLTA-
FDX S   YTVKLI--TPDGESSIECSDDTYILDAEEEAGLDLPYSCRAGACSTCAGKITAGSVQSDQSFLLDDQIEAGYVLTQVAYPTSDCTIETHKKEEDLY-
FDX N   FKVTLINEAEGTKHEIEVPDDEYILDAAEEQGYDLPFSCRAGACSTCAGKLVSGTVDQSDQSFLLDDQIEAGYVLTQVAYPTSDVVIQTHKKEEDLY-
FDX Te  YKVTLV-RPDGSETTIDVPEDEYILDVAEEQGLDLPFSRAGACSTCAGKLEGEVDQSDQSFLLDDQIEKGFVLTQVAYPRSDCKILTQNEEELY--
    
```

Figure S5. Sequence alignment of different plant-type ferredoxins. PETF sequences of different photosynthetic organisms are compared comprising representative species from algae, higher plants and cyanobacteria. N-terminal sequences parts have been trimmed in reference to the sequence homology to mature PETFCr excluding the chloroplast transit peptide. Positions D19 and D58 of PETFCr which promote selective recognition of FNR are indicated by a red background color. A yellow background marks cysteine residues that participate in the ligation of the [2Fe-2S]-cluster. Other parts with strict sequence conservation are indicated by a gray background color. PETFCr: ferredoxin I of *C. reinhardtii* (protein ID: XP_001692808), FDX Vc: ferredoxin I of *Volvox carteri f. nagariensis* (protein ID: XP_002958725), FDX Cf: Ferredoxin of *Chlorella fusca* (protein ID: P56408), FDX Ds: ferredoxin I of *Dunaliella salina* (protein ID: P00239), FDX At: ferredoxin I of *Arabidopsis thaliana* (protein ID: NP_172565), FDX Zm: ferredoxin 1 of *Zea mays* (protein ID: NP_001105345), FDX Ps: ferredoxin I of *Pisum sativum* (protein ID: P09911), FDX S: ferredoxin I of *Synechocystis* sp. PCC 6803 (protein ID: NP_442127), FDX N: ferredoxin I of *Nostoc* sp. PCC 7120 (protein ID: NP_488188), FDX Te : ferredoxin I of *Thermosynechococcus elongatus* BP-1 (protein ID: NP_681799).

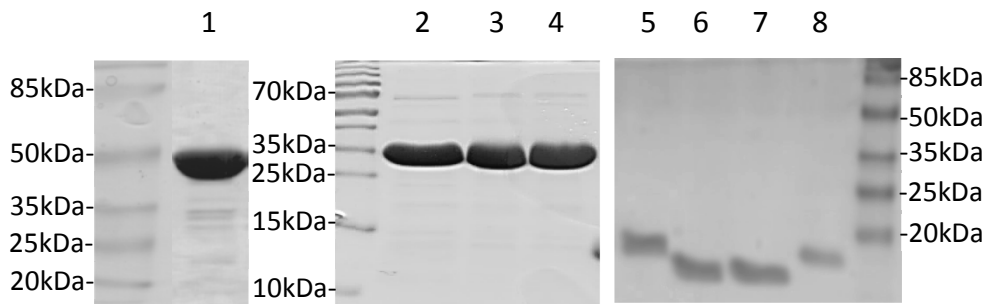


Figure S6. Analysis of purified proteins by SDS-PAGE visualized by Coomassie staining. 1: 30 µg HYDA1; 2: 25 µg FNR-wt; 3: 25 µg FNR-K83L; 4: 25 µg FNR-K89L; 5: 7 µg PETF-wt; 6: 7 µg PETF-D58A; 7: 7 µg PETF-D19A/D58A; 8: 5 µg PETF-D19A.

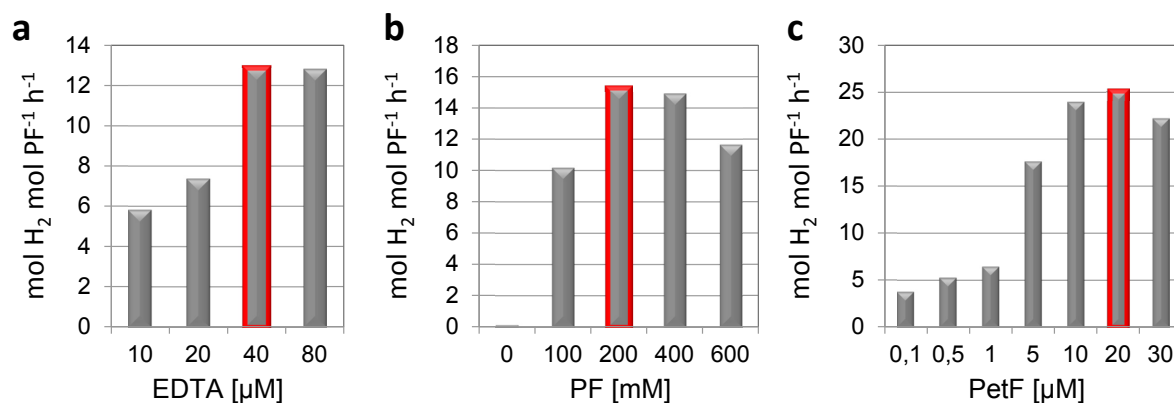


Figure S7. Adjustment of compound concentrations of the proflavine dependent *in vitro* assay for light driven H₂-production. Test series with increasing concentrations of EDTA, PF and PETF were screened for the highest yield of photoproduced H₂. The indicated concentrations (red framed bars) were chosen as standard system parameters for all PF-dependent measurements.

References

- [1] M. K. Akhtar and P. R. Jones, *Appl. Microbiol. Biotechnol.*, 2008, **78**, 853-862.
- [2] M. Winkler, S. Kuhlert, M. Hippler and T. Happe, *J. Biol. Chem.*, 2009, **284**, 36620-36627.
- [3] J. Esselborn, C. Lambertz, A. Adamska-Venkatesh, T. Simmons, G. Berggren, J. Noth, J. Siebel, A. Hemschemeier, V. Artero, E. Reijerse, M. Fontecave, W. Lubitz and T. Happe, *Nat. Chem. Biol.*, 2013, **9**, 607-609.
- [4] P. Decottignies, P. Lemarechal, J. P. Jacquot, J. M. Schmitter and P. Gadal, *Arch. Biochem. Biophys.*, 1995, **316**, 249-259.
- [5] A. Gutmanas, P. Jarvoll, V. Y. Orekhov and M. Billeter, *J. Biomol. NMR*, 2002, **24**, 191-201.
- [6] A. Lemak, A. Gutmanas, S. Chitayat, M. Karra, C. Fares, M. Sunnerhagen and C. H. Arrowsmith, *J. Biomol. NMR*, 2011, **49**, 27-38.
- [7] F. Delaglio, S. Grzesiek, G. W. Vuister, G. Zhu, J. Pfeifer and A. Bax, *J. Biomol. NMR*, 1995, **6**, 277-293.
- [8] A. Bax and S. Grzesiek, *Acc. Chem. Res.*, 1993, **26**, 131-138.
- [9] D. W. Mulder, E. S. Boyd, R. Sarma, R. K. Lange, J. A. Endrizzi, J. B. Broderick and J. W. Peters, *Nature*, 2010, **465**, 248-251.
- [10] G. Kurisu, M. Kusunoki, E. Katoh, T. Yamazaki, K. Teshima, Y. Onda, Y. Kimata-Arigo and T. Hase, *Nat. Struct. Biol.*, 2001, **8**, 117-121.
- [11] P. N. Palma B. Lagoutte, L. Krippahl, J. J. G. Moura and F. Guerlesquin, *FEBS Lett.*, 2005, **579**, 4585-4590.

4.3 Paper III

Structural insight into the complex of ferredoxin and [FeFe] hydrogenase from *Chlamydomonas reinhardtii*

Sigrun Rumpel, Judith F. Siebel, Mamou Diallo, Christophe Farès, Edward J. Reijerse,
Wolfgang Lubitz

Reproduced with the permission from ChemBioChem **2015**, accepted manuscript.

License number: 3651771256687, © 2015 Wiley-VCH Verlag GmbH & Co. KGaA,
Weinheim

DOI: 10.1002/cbic.201500130

Journal name: ChemBioChem

Impact factor: 3.088 (in 2014)

Author: second author

Contribution: – 35 %

– I established the Gallium-substitution reaction

– I made all biological samples

– I analyzed the chemical shift data of the Ga-PetF titrated with
HydA1

– I was involved in the production of the manuscript

S. Rumpel performed the NMR measurements and the analyses, calculated the NMR solution and complex structure.

4.3.1 Journal article



DOI: 10.1002/cbic.201500130

CHEMBIOCHEM
Full Papers

Structural Insight into the Complex of Ferredoxin and [FeFe] Hydrogenase from *Chlamydomonas reinhardtii*

Sigrun Rumpel,^{*,[a]} Judith F. Siebel,^[a] Mamou Diallo,^[a] Christophe Farès,^[b] Edward J. Reijerse,^[a] and Wolfgang Lubitz^{*,[a]}

The transfer of photosynthetic electrons by the ferredoxin PetF to the [FeFe] hydrogenase HydA1 in the microalga *Chlamydomonas reinhardtii* is a key step in hydrogen production. Electron delivery requires a specific interaction between PetF and HydA1. However, because of the transient nature of the electron-transfer complex, a crystal structure remains elusive. Therefore, we performed protein–protein docking based on

new experimental data from a solution NMR spectroscopy investigation of native and gallium-substituted PetF. This provides valuable information about residues crucial for complex formation and electron transfer. The derived complex model might help to pinpoint residue substitution targets for improved hydrogen production.

Introduction

Protein–protein interactions are fundamental to all biological processes and result in static or transient complexes. In order to allow a high turnover rate, the protein complexes involved in electron transfer (ET) reactions are typically highly specific and short-lived.^[1] The initial encounter of the complex is dominated by electrostatic interactions, and the complex is subsequently stabilized by hydrophobic contacts to produce the highly specific and productive ET complex.^[2]

The ET complex formation between the photosynthetic electron transfer ferredoxin (PetF) and the hydrogenase HydA1 from the microalga *Chlamydomonas reinhardtii* is an important step in the mechanism of biological hydrogen production. It is of particular interest as the use of solar energy to photosynthetically generate electrons for hydrogen production by direct proton reduction is unique to microalgae.^[3] PetF transfers electrons from photosystem I to HydA1, and HydA1 catalyzes the reversible reaction of protons and electrons to hydrogen. Because of the transient character of the PetF/HydA1 complex, its structural characterization by diffraction methods remains elusive. However, the interaction between PetF and hydrogenase has been modeled in silico based on homology models of the free proteins.^[4] These studies highlight the dominant electrostatic contributions to the interaction, which are of

central importance for the formation of an initial encounter complex.^[1]

PetF is a member of the family of plant-type ferredoxins, which contain a [2Fe–2S] cluster and have molecular weights of about 10 kDa. This family is characterized by a low redox potential, high acidity, and high sequence similarity.^[5] The two irons are tetrahedrally coordinated and antiferromagnetically coupled. In the oxidized state, both irons are Fe^{II}. Upon one-electron uptake, the iron close to the protein surface is reduced, thereby resulting in a mixed valence Fe^{II}/Fe^{III} state.^[6] The three dimensional solution and crystal structures of plant-type ferredoxins from several organisms have been solved,^[7] but the experimental 3D structure of PetF from *C. reinhardtii* is unknown. Plant-type ferredoxins are of central importance as they form an ET complex with many proteins to deliver the photosynthetically derived electrons to various metabolic pathways.^[7]

HydA1 belongs to the family of [FeFe] hydrogenases. These enzymes are outstanding catalysts for hydrogen evolution because of their low overpotentials and high turnover rates of up to 10⁴ s⁻¹.^[8] Their active site is referred to as the “H-cluster” and contains a [4Fe–4S] cluster, which is linked by a bridging thiolate of a coordinating cysteine to a unique [FeFe] subcluster. It is assumed to be the catalytically active center. The crystal structure of unmaturation HydA1 containing only the [4Fe–4S] cluster has been reported.^[9] The HydA1 surface that covers the entrance to the invaginated H-cluster binding site is framed by 14 basic amino acids, which are highly conserved.^[10] Among these residues, R56, K139, K356, K357, K393, and R187 play a role in the complex formation with PetF, as demonstrated by site-directed mutagenesis studies.^[4b,11] These positively charged side chains can be initially recognized by several negatively charged residues of PetF.

For PetF from different organisms, the binding interface with nitrite reductase,^[12] ferredoxin NADP⁺ oxidoreductase

[a] Dr. S. Rumpel, J. F. Siebel, M. Diallo, Dr. E. J. Reijerse, Prof. W. Lubitz
Department for Biophysical Chemistry
Max-Planck-Institut für Chemische Energiekonversion
Stiftstrasse 34–36, 45470 Mülheim an der Ruhr (Germany)
E-mail: wolfgang.lubitz@cec.mpg.de
sigrun.rumpel@cec.mpg.de

[b] Dr. C. Farès
NMR Department, Max-Planck-Institut für Kohlenforschung
Kaiser-Wilhelm-Platz 1, 45470 Mülheim an der Ruhr (Germany)

Supporting information for this article is available on the WWW under <http://dx.doi.org/10.1002/cbic.201500130>.

(FNR),^[13] and ferredoxin thioredoxin reductase^[14] has been identified by NMR-titration experiments. Our recent NMR study identified the binding interface of PetF with HydA1 from *C. reinhardtii*.^[15] Apart from the study of the interaction with ferredoxin thioredoxin reductase,^[14] none of these NMR spectroscopic investigations provided information about the important residues coordinating and surrounding the [2Fe–2S] cluster. Because of the proximity of these residues to the cluster, their nuclear spins relax quickly, and their NMR signals become broad or undetectable. This paramagnetic relaxation enhancement (PRE) can be avoided by substitution of the paramagnetic iron with diamagnetic gallium(III).^[16]

Here, we report the solution NMR structure of oxidized PetF from *C. reinhardtii* as well as the entire binding interface of its Ga-substituted analogue with HydA1. These data were used to construct the first model of the PetF/HydA1 complex based on experimental structures of the free proteins and experimental restraints defining the complex interface.

Results and Discussion

Solution structure and dynamics of PetF

The solution NMR structure of the oxidized ferredoxin PetF from *C. reinhardtii* (Figure 1), subsequently used in the model complex structure with HydA1, was solved based on 1716 inter-proton distances and 148 dihedral angle restraints (Table S1 in the Supporting Information). To avoid mistakes during the initial stages of the network anchoring of the structure calculation, the X-ray coordinates of the homologous ferredoxin from the related algal species *Chlorella fusca* (PDB ID: 1AWD) with 89% sequence identity (Figure S1) have been used as a starting structure and were combined with manually assigned medium- and long-range distances from ¹⁵N- and ¹³C-edited NOEs. Thereby, convergence was ensured in the absence of distance restraints for residues 35–46 and 73–76, in-

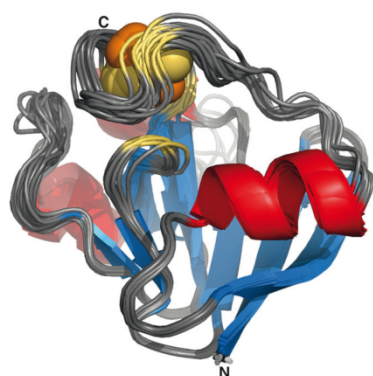


Figure 1. Solution NMR structure of residues 1 to 94 of oxidized PetF from *C. reinhardtii*. Ensemble of 15 lowest-energy solution-NMR structures after refinement in explicit solvent. The β -strands and α -helices are shown in blue and red, respectively. The [2Fe–2S] cluster is displayed as spheres. Fe is colored orange and S as well as the [2Fe–2S] cluster-ligating cysteines are colored yellow.

cluding all cysteines coordinating the [2Fe–2S] cluster. These 16 residues are less than 7 Å away from the two paramagnetic Fe^{III} ions in the low-temperature diamagnetic iron–sulfur cluster, and are thus invisible in the NMR spectra due to PRE.

PetF is composed of three α -helices and seven β -strands (Figures 1 and S3), and the structural characteristics have been described in detail elsewhere.^[17] The root-mean-square deviation (RMSD) values within the ensemble of NMR structures and to the X-ray structure (PDB ID: 1AWD) and an analysis of the flexible regions by backbone amide heteronuclear NOEs are presented in Figures S2 and S3.

Gallium-substituted PetF

In order to detect all PetF residues by NMR spectroscopy, including those in the vicinity of the [2Fe–2S] cluster, the cofactor was removed, and the protein was reconstituted in the presence of Na₂S and Ga(NO₃)₃ (Figure S4). Successful refolding of the resulting Ga^{III}-substituted PetF (Ga-PetF) was confirmed by comparison of the ¹⁵N,¹H HSQC spectra of native and Ga-PetF (Figure 2).

Both spectra are well dispersed, with backbone proton resonances between 6 and 11 ppm, indicative of a well-folded protein. Also, most of the resonances observed for PetF and Ga-PetF match very well, thus confirming that the secondary structure and overall protein fold are conserved upon Ga substitution (Figure 2). Because of the strong paramagnetic effect of the Fe^{III} ions in the iron–sulfur cluster of PetF, residues 35–46 and 73–76 were not assigned and S60 as well as F61 could only be detected in some NMR spectra. In Ga-PetF, all these 18 residues can be readily observed, as they are now in the vicinity of the diamagnetic Ga^{III}.

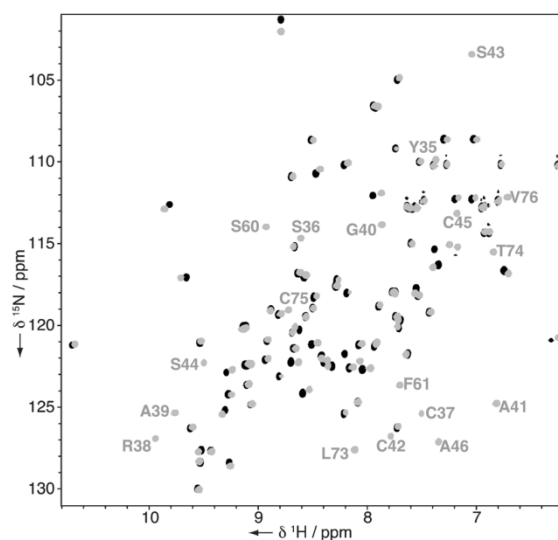


Figure 2. Overlay of the ¹⁵N,¹H HSQC spectra of native, oxidized PetF (black) and Ga-PetF (gray). Assignments of the peaks observed only for the Ga^{III}-substituted protein are indicated. Figure S5 displays the same overlay with the signals of Ga-PetF colored red.

For complete assignment of the ^1H and ^{15}N backbone amide resonances of Ga-PetF, a 3D $^{15}\text{N},^1\text{H}$ NOESY-HSQC was used. In this spectrum, all sequential NOE connectivities and almost all expected long-range NOEs based on the 3D structure of PetF are present. Based on this single experiment, the unambiguous assignment of all new resonances and confirmation of all "old" ^1H and ^{15}N amide backbone resonances was accomplished. The newly revealed peaks are labeled with residue letters and numbers in Figure 2.

Complete interaction interface of PetF with HydA1

Recently, the binding interface of PetF with HydA1 was investigated. Residues 23–28 of helix α_1 , 58–67 of helix α_2 and the preceding loop, as well as 89–94 of the C-terminal helix were identified as involved in complex formation.^[15] These three regions surround the residues coordinating the [2Fe–2S] cluster on the surface of PetF (Figure 3B). Furthermore, they coincide with flexible regions I, III, and IV, identified by steady-state heteronuclear $^{15}\text{N},^1\text{H}$ NOE values (Figure S3), thus supporting the proposed importance of the flexible regions of PetF for promoting specific protein–protein interactions.^[18]

Upon stepwise addition of HydA1 to ^{15}N -labeled Ga-PetF, chemical-shift changes for all backbone amide ^1H and ^{15}N resonances ($\Delta\delta_{\text{HN}}$) are observed. The changes for the detectable

resonances in the native PetF are identical within the experimental error (triangles in Figure 3A). For the newly observed residues 35–46 forming the long iron–sulfur cluster coordinating loop, the chemical-shift perturbations upon HydA1 binding were largest with a maximum $\Delta\delta_{\text{HN}}$ value of 0.16 ppm detected for C37. In contrast, the chemical shifts of residues 73–76 constituting the short iron–sulfur cluster-coordinating loop only detected for Ga-PetF are not affected. Residues S60 and F61 in the middle of region III are significantly shifted and even disappear in the $^{15}\text{N},^1\text{H}$ HSQC spectra of PetF in the presence of excess HydA1. This disappearance can be attributed to line broadening as a result of the decreased relaxation time of HydA1-bound PetF compared to free PetF, and intermolecular paramagnetic effects originating from the [4Fe–4S] cluster of HydA1. In principle, these intermolecular paramagnetic effects, which include pseudo contact shifts and PRE, can be used to provide additional restraints for modeling protein–protein complexes.^[15] However, a completely diamagnetic analogue of the PetF/HydA1 complex for the reference spectrum is unfortunately not available. Moreover, the electron spin density cannot be localized at one position due to the presence of several antiferromagnetically coupled irons.^[19] Therefore, determination of reliable intermolecular distance restraints caused by paramagnetic effects originating from the intrinsic iron–sulfur clusters of the PetF/HydA1 complex would be at best very challenging.

Overall, the chemical-shift perturbations for PetF upon HydA1-binding are small (Figure 3A), because of the high degree of dynamics in the complex thus leading to averaging of the shifts. This has been observed for several other ET complexes, where smaller chemical-shift perturbations correlate with larger populations of the encounter complex compared to the specific complex.^[1]

HADDOCK model of the PetF/HydA1 complex

In order to reveal the pattern of possible intermolecular contacts responsible for PetF/HydA1 complex formation, we generated a model structure of the PetF/HydA1 complex with the software HADDOCK.^[20] The docking was guided by data from the chemical-shift perturbations and site-directed mutagenesis studies (Table S2). The solution NMR structure of oxidized PetF reported here and the X-ray structure of unmaturing HydA1 (which contains only the [4Fe–4S] cluster) were used as starting structures.^[9] Conformational differences between this unmaturing HydA1 and active HydA1 with the complete H-cluster are expected to be negligible for the residues involved in PetF binding. This assumption is supported by the small interface RMSD of 1 Å (residues 131–190 and 350–394) between unmaturing HydA1 and the homologous [FeFe] hydrogenase Cpl containing the intact H-cluster.^[21]

The preferred model for the specific PetF/HydA1 complex was selected from the four lowest-energy structures of the best HADDOCK cluster (Figure 4C and S6 and Table S3), based on the smallest distance between the reducible Fe of PetF^[6] and the closest Fe of HydA1 (Figure 4A). At 11.1 Å, this distance is well below the maximum distance for efficient ET^[22]

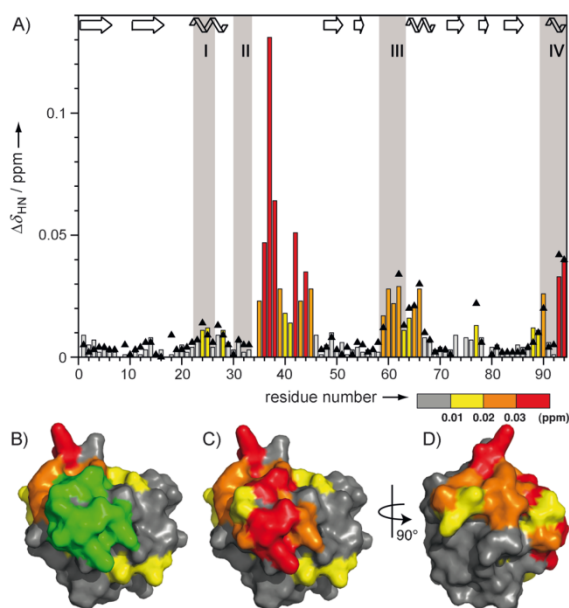


Figure 3. A) Weighted averages of backbone amide chemical-shift changes plotted against the residue number for ^{15}N Ga-PetF with a tenfold excess of HydA1 (bars). Black triangles indicate the corresponding chemical-shift perturbations for PetF at a tenfold excess of HydA1 containing only the [4Fe–4S] cluster. B) Surface representation of the 3D mean structure of PetF (rotated by -45° about the x-axis relative to Figure 1). Undetected residues in proximity to the [2Fe–2S] cluster are shown in green; chemical-shift changes upon HydA1 titration are colored according to A). C) As B) but for Ga-PetF, for which no paramagnetic effect is present. D) As C) but y-rotated by 90° .

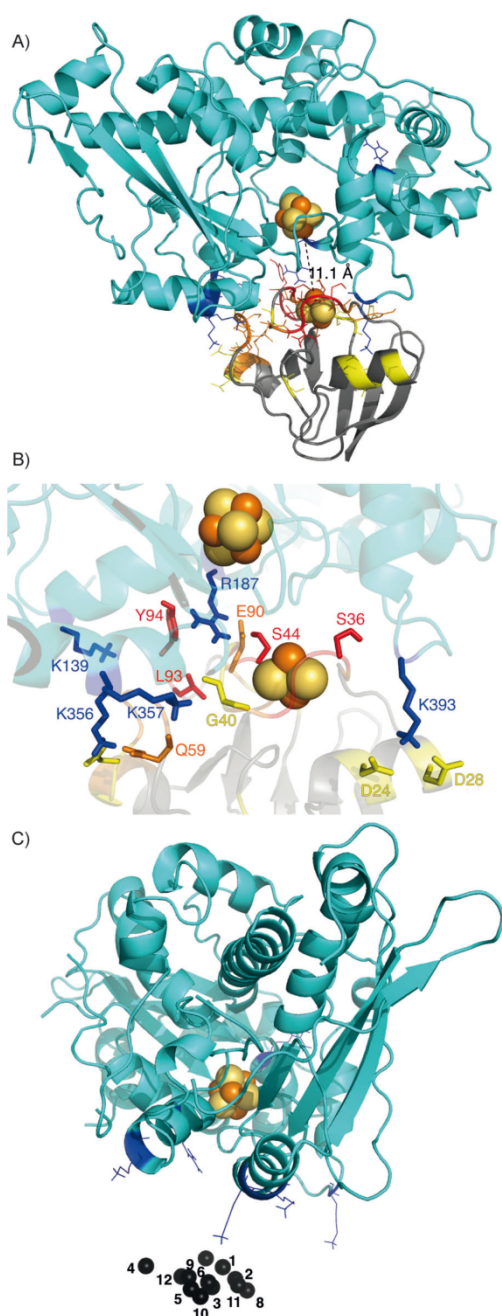


Figure 4. Best HADDOCK model of the PetF/HydA1 complex structure. HydA1 (cyan) contains only the [4Fe-4S] cluster; PetF is shown in gray. Side chains of residues defined as ambiguous interface restraints for protein-protein docking are shown in blue for HydA1 and are colored as in Figure 3 for PetF. The Fe-S clusters are displayed as spheres (Fe orange, S yellow). The orientation of the complex is: A) as in Figure 1, B) rotated 30° about the y-axis, C) rotated 90° about the y-axis and -10° about the x-axis. C) Centers of mass of PetF from each HADDOCK cluster (black spheres) superimposed onto the ribbon representation of HydA1. The centers of mass were calculated for the four best structures of each cluster (cluster numbering in column 1 of Table S3).

and fits very well with the distance between all Fe-S clusters in [FeFe] hydrogenases (~11 Å).^[8]

The docking solutions found in HADDOCK clusters 1–12 (Figure S6 and Table S3) represent multiple orientations of PetF and HydA1 in a dynamic complex (Figure 4C). These conformations are reflected qualitatively by the small chemical-shift changes (Figure 3A) that result from averaging over all orientations. All HADDOCK clusters might contribute to different extents to the encounter state and to efficient ET. Correspondingly, the shortest intermolecular Fe-Fe distance among the best four structures of all HADDOCK clusters is 9.3 Å, which is found for a complex of cluster 7.

PetF helix $\alpha 1$ was chosen to compare the orientation of PetF and HydA1 in the model to that in the model of Winkler et al.^[4b] When HydA1 in the previous model complex is superimposed onto HydA1 of the newly proposed complex structure, this helix is rotated by about 32°. The important HydA1 interface residue R187^[11] forms several possible H-bond and salt-bridge contacts with PetF in our model. In the complex of Winkler et al., the shortest distance from R187 to PetF is 8.5 Å.^[4b] The most important intermolecular interactions in our PetF/HydA1 model are summarized in Table 1 and are discussed below.

Table 1. Summary of PetF and HydA1 residues in the PetF/HydA1 complex structure with a distance less than 3 Å to the interaction partner.^[a]

PetF residue	HydA1 residue	Interaction
D24, E28 (r)	K393	sc-sc
E27 (g)	K393	sc-sc
D32 (g)	R389	sc-sc
C37 (r)	P378	sc-bb
A39 (o)	K357	bb-sc
G40 (y)	G351, L352, L352	bb-bb
A41 (y)	G351, L352, L352	bb-bb
A41 (y)	P378	bb-sc
C42 (r)	A376	sc-bb
C42 (r)	P378	sc-sc
D58 (g)	K357	sc-sc
Q59 (o)	K356	bb-sc, sc-sc
Q59 (o)	G353	bb-bb
S60 (o)	K356	bb-sc
S60 (o)	G353	sc-bb
D63 (y)	K356	bb-sc
E90 (o)	R187, T186	sc-sc
Y94 (r)	K139	bb-sc
Y94 (r)	R187	sc-sc
Y94 (r)	G132	sc-bb
[2Fe-2S]	P378	Fe1-sc

[a] Chemical-shift perturbations according to Figure 3 (r=red, g=gray, o=orange, y=yellow); sc=side chain, bb=backbone. E90 of PetF and R187 of HydA1, which are at present identified as the most important residues for complex formation, are indicated in bold.

Charged residues at the PetF/HydA1 interface

E90 is the PetF residue with the largest number of possible H-bonds and salt bridges to HydA1. Most importantly, its side chain is close to the side chain of R187, which is the HydA1 residue with the largest number of H-bonds and salt bridges

to PetF (Figure 4 and Table S4). The hydroxy group of the adjacent T186 has contacts with the side chain of PetF E90. The importance of R187 and E90 has already been demonstrated for the variants HydA1-R187W and HydA1-R187D,^[11] as well as for PetF-E90Q and PetF-E90K.^[4b] For the variants HydA1-R187W and -R187D, the PetF-dependent hydrogen production is decreased about 20- and 100-fold, whereas the catalytic activity with methyl viologen as electron donor is unchanged and about sixfold increased, respectively.^[11] Mutations of PetF E90 drastically change the redox potential by about +70 mV,^[23] and PetF-E90Q leads to a decreased hydrogen production.^[4b]

Consistent with the pronounced $\Delta\delta_{\text{HN}}$ upon HydA1 addition (Figure 3A), the carbonyl oxygen and tyrosyl side chain of Y94 of PetF are close to the ϵ -amino group of K139 and the guanidinium group of R187 of HydA1, respectively (Figure 4B and S7B). Furthermore, the significant perturbation of the backbone amide resonances of residues 59–66 upon HydA1 binding indicates the importance of this region for complex formation. This is reflected by the distances smaller than 3 Å between the carbonyl oxygens of Q59 and S60 and the δ -protons of K356 of HydA1. In addition, the side-chain amide group of Q59 and the carboxyl group of D63 of PetF are within H-bonding distance of the ϵ -amino groups of K356 of HydA1 (Figures 4B and S7A). The side chain of K357 of HydA1 is in proximity to the side chain of D58 and the backbone of A39 of PetF (Table S4).

In agreement with the significant chemical-shift perturbations of PetF D24 and E28, their side chains are within H-bonding distance of the side chain of HydA1 K393 (Figure 4B). The side chains of K393 and R389 of HydA1 have H-bond contacts with the side chains of E27 and D32 of PetF, respectively (Table S4). These contacts support the importance of acidic PetF side chains and basic HydA1 side chains for formation of the optimal ET complex. Most of these residues have also been identified by site-directed mutagenesis.^[4b,11]

Hydrophobic and polar residues at the PetF/HydA1 interface

Our model points not only to residues of HydA1 and PetF with charged side chains as important for complex formation, but also several residues with hydrophobic and polar side chains. These residues are mainly close to the cysteines coordinating the [4Fe–4S] cluster of HydA1 (C130, C185, C377, and C381) and in the long [2Fe–2S] cluster-coordinating loop of PetF (residues 35–46). Accordingly, all PetF residues of this loop are significantly affected upon HydA1 binding (Figure 3A).

HydA1 G132 forms an H-bond with the hydroxy group of PetF Y94. This HydA1 residue is adjacent to highly conserved residues, including C130. The variant HydA1-G132D was reported to yield four-fold increased hydrogen production in combination with mutation N227S.^[24] The hydrophobic residues G351, L352, and G353 of HydA1 exhibit many contacts with PetF residues 40–43. These include backbone–backbone H-bond interactions between the three HydA1 residues and G40 as well as A41 of PetF. In addition, G353 is within H-bonding distance of the backbone of Q59 and the side chain of S60 of

PetF. The carbonyl oxygen of A376 might form an H-bond with H β of C42 of PetF.

P378 is adjacent to C377, which coordinates the [4Fe–4S] cluster. Importantly, there are several distances smaller than 3 Å between P378 and A41, as well as C37 and C42, which coordinate the [2Fe–2S] cluster. Moreover, the highly conserved P378 is only 2.8 Å from the reducible iron of the [2Fe–2S] cluster (Table S4). Thus, P378 probably plays a crucial role in the stability of HydA1 as well as in its complex with PetF.

Mutations targeted to enhanced hydrogen production

Predicting the effect of mutations on complex formation is extremely challenging, as protein–protein interaction networks are very intricate. For the PetF/HydA1 complex, E90 of PetF and R187 of HydA1 are at the center of the interface with their respective binding partners, in agreement with mutagenesis studies.^[4b,11] Substitution of R187 by an oppositely charged amino acid abrogates PetF-dependent hydrogen production on the one hand, but on the other hand leads to a sixfold increase in methyl-viologen-dependent hydrogen production.^[11]

To the best of our knowledge, there is only one study that provides a framework to predict the outcome of point mutations at the center of the interface of an ET complex. In this study, the interface of cytochrome *c* with cytochrome *c* peroxidase was investigated.^[25] Cytochrome *c* residues T12 and R13 are in the middle of the interface. Mutation to R13A led to destabilization of the complex, whereas T12A increased the binding to cytochrome *c* peroxidase.^[25] Similarly, the two HydA1 amino acids T186 and R187 are at the center of the HydA1–PetF interface (Figure 4). Therefore, complex formation between HydA1 and PetF may be modulated by alanine substitution at T186 and R187. As for cytochrome *c* R13A, we propose destabilization of the complex by R187A, but not a complete loss of hydrogen production activity, as observed for HydA1-R187D. It is also important to test the substitution T186A of HydA1 to investigate whether binding to PetF and PetF-dependent hydrogen production are enhanced.

For PetF, we suggest an exchange of E91 (neighbor of E90) to alanine, as the chemical-shift perturbation data indicate that this residue is nonessential for PetF/HydA1 complex formation (Figure 3A). Also, residue 91 of the ferredoxin from *C. fusca* is alanine, and a change of this residue does not change PetF's redox potential.^[23] Presumably a combination of these modifications may result in increased PetF-dependent hydrogen production by HydA1, possibly even when HydA1 competes with other proteins.^[15]

Conclusion

Our recent NMR titration study identified PetF residues that interact with the [FeFe] hydrogenase HydA1 from *C. reinhardtii*.^[15] However, for the ¹H and ¹⁵N amide resonances of PetF residues in proximity of the [2Fe–2S] cluster, the signals are broadened beyond detection due to PRE caused by the two Fe^{III} ions.

In this work, substitution of gallium for iron in PetF renders all backbone amide resonances visible and allows determination of the complete interaction interface of PetF with HydA1. For HydA1, no backbone assignment is currently available, and a strategy for ^{13}C - and ^{15}N -labeling remains to be established. Therefore, identification of HydA1 residues interacting with PetF were based on published results from site-directed mutagenesis. These data were used in combination with the new solution NMR structure of PetF and the X-ray structure of HydA1 containing only the [4Fe-4S] cluster to derive the first knowledge-guided model structure of the PetF/HydA1 complex. With the shortest distance from HydA1 to D19 of PetF of 11.5 Å, our complex model confirms that the recently identified residue D19 is dispensable for PetF binding to HydA1.^[15]

In our model, PetF and HydA1 form a transient electrostatic ET complex, with the shortest intermolecular Fe-Fe distance of 11.1 Å. Analysis of the key determinants for complex formation between PetF and HydA1 and comparison with the available literature enabled us to propose HydA1-R187A, HydA1-T186A, and PetF-E91A as promising targets for site-directed mutagenesis aimed at enhancing *in vivo* hydrogen production.

Experimental Section

Protein preparation and Ga substitution of PetF: ^{15}N -PetF and HydA1 protein samples were prepared as described previously.^[15] For gallium substitution in PetF, the protein was precipitated by addition of hydrochloric acid and resolubilized as previously described^[16a] with the following differences: the aerobically purified protein sample was buffer exchanged into oxygen-free Tris-HCl (100 mM, pH 8.0) in an anaerobic chamber (Coy Laboratories Products) on a NAP5 column (GE Healthcare); $\text{Ga}(\text{NO}_3)_3$ was used instead of GaCl_3 , and the reconstituted protein was separated from excess reagents on a PD10 column (GE Healthcare) and eluted with Tris-HCl (50 mM, pH 8.0) or potassium phosphate (55 mM, pH 6.8) and NaCl (55 mM). Complete removal was confirmed by the absence of the characteristic absorption maxima of the [2Fe-2S] cluster of PetF at 330, 422, and 465 nm (Cary 60, Agilent; Figure S4). Ga-PetF migrated identically to wild-type PetF on an 18% native PAGE gel,^[25] thus indicating successful refolding.

Protein concentration was determined by measuring the absorption at 280 nm with an extinction coefficient of $\epsilon_{280} = 9315 \text{ cm}^{-1} \text{ M}^{-1}$ determined by using the ExPASy ProtParam tool (web.expasy.org/protparam/).

NMR spectroscopy: NMR samples contained PetF (0.1–1 mM) in potassium phosphate (50 mM, pH 6.8) with NaCl (50 mM) and D_2O (10%, *v/v*). All NMR data were acquired at 298 K on an AVANCE 600 spectrometer (Bruker) equipped with a cryogenic probe. The 3D spectra employed a non-uniform sampling scheme in the indirect dimension and were reconstructed by the multidimensional decomposition software MDDNMR^[27] interfaced with MDDGUJ^[28] and NMRPipe/NMRDraw.^[29] Backbone assignments were obtained using standard triple-resonance experiments.^[30] Aliphatic side-chain assignments were obtained from ^{13}C -edited 3D HCCH, CCONH, and HCCONH TOCSY spectra. Aromatic side chains were assigned from a 2D $(\text{H}\beta)\text{C}\beta(\text{C}\gamma\text{C}\delta)\text{H}\delta$ and a 2D $(\text{H}\beta)\text{C}\beta(\text{C}\gamma\text{C}\delta\text{C}\epsilon)\text{H}\epsilon$ experiment.^[31] For structure determination, a ^{15}N - and a ^{13}C -edited 3D NOESY-HSQC with a mixing time of 120 ms were measured. All spectra were analyzed with Sparky (T. D. Goddard and D. G. Kneller, University of California, San Francisco).

Steady-state heteronuclear $^{15}\text{N},^1\text{H}$ NOE values were calculated as the intensity ratios from $^{15}\text{N},^1\text{H}$ correlation peaks from a pair of spectra acquired in an interleaved manner with and without ^1H presaturation during the recycle delay (5 s).^[32]

NMR solution structure determination: Assigned chemical-shift data have been deposited in the BioMagResBank (www.bmrb.wisc.edu) under accession number 19622. These assigned resonances and dihedral angle restraints were used as input for combined automated NOE assignment and structure calculation with ARIA2.3^[33] and CNS.^[34] Dihedral angles were predicted from chemical shifts with TALOS^[35] and derived from the X-ray structure of ferredoxin (PDB ID: 1AWD) from the related algal species *C. fusca* for residues 35–46 and 73–76 broadened out due to the paramagnetic [2Fe-2S] cluster. This X-ray structure was also used as the start structure together with 67 manually assigned medium- and long-range distances from the ^{15}N - and ^{13}C -edited NOEs. After refinement in explicit solvent, the 15 lowest-energy structures were analyzed with MOLMOL^[36] and PROCHECK.^[37] The 15-structure bundle has been deposited with the Protein Data Bank (ID: 2MH7). Structure diagrams were prepared by using PyMOL (www.pymol.org/).

HydA1 titration: PetF/HydA1 complex formation was monitored by recording a series of 2D $^1\text{H},^{15}\text{N}$ TROSY-HSQC experiments with ^{15}N -labeled Ga-PetF (83 μM) and HydA1 (42, 82, 168, 438, and 876 μM). Weighted averages of the ^1H and ^{15}N backbone chemical-shift changes of a particular residue were calculated according to the equation $\Delta\delta_{\text{HN}} = [(\Delta\delta_{\text{H}}^2 + 0.2\Delta\delta_{\text{N}}^2)/2]^{1/2}$.

Docking model of the PetF/HydA1 complex structure: A model of the PetF/HydA1 complex was obtained by using HADDOCK.^[20,38] The X-ray structure of HydA1 containing only the [4Fe-4S] cluster (PDB ID: 3LX4) served as the starting structure. For PetF, the ensemble of the ten lowest-energy solution-NMR structures (PDB ID: 2MH7) was used (Figure 1). Topologies and parameters for the [4Fe-4S] and [2Fe-2S] clusters were added to the CNS parameter and topology files used by HADDOCK. Ambiguous interaction restraints (AIRs) were generated as previously described^[38] and based on site-directed mutagenesis for HydA1^[4b,11] and chemical-shift perturbation data for PetF. Residues used to generate the AIRs are summarized in Table S2. In addition, unambiguous restraints were specified for all cysteines coordinating the Fe-S clusters as 2.3 Å (+0.05 Å and -0.1 Å). Initially, 1000 rigid-body solutions were generated, and the 200 lowest-energy structures were used for semi-flexible simulated annealing and the final water refinement. The cluster analysis was performed with the 3.5 Å cut-off criterion. Analysis and clustering of the HADDOCK results is summarized in Table S3, and an overview of the HADDOCK clusters is shown in Figures 4C and S6. The coordinates of the best four structures of HADDOCK cluster 1 have been submitted to the Protein Data Bank (ID: 2N0S).

Acknowledgements

We thank Julian Jakobs and Agnes Stoer for support in protein preparation and Martin Winkler for useful discussions. This work was supported by the Max Planck Society and the Deutsche Forschungsgemeinschaft (DIP project LU315/17-1).

Keywords: electron transfer · hydrogenases · NMR spectroscopy · photosynthesis · protein-protein interactions

- [1] Q. Bashir, S. Scanu, M. Ubbink, *FEBS J.* **2011**, *278*, 1391–1400.
- [2] J. Schilder, M. Ubbink, *Curr. Opin. Struct. Biol.* **2013**, *23*, 911–918.
- [3] A. Hemschemeier, A. Melis, T. Happe, *Photosynth. Res.* **2009**, *102*, 523–540.
- [4] a) C. H. Chang, P. W. King, M. L. Ghirardi, K. Kim, *Biophys. J.* **2007**, *93*, 3034–3045; b) M. Winkler, S. Kuhlert, M. Hippler, T. Happe, *J. Biol. Chem.* **2009**, *284*, 36620–36627; c) H. Long, C. H. Chang, P. W. King, M. L. Ghirardi, K. Kim, *Biophys. J.* **2008**, *95*, 3753–3766; d) H. Long, P. W. King, M. L. Ghirardi, K. Kim, *J. Phys. Chem. A* **2009**, *113*, 4060–4067.
- [5] G. Hanke, P. Mulo, *Plant Cell Environ.* **2013**, *36*, 1071–1084.
- [6] L. B. Dugad, G. N. La Mar, L. Banci, I. Bertini, *Biochemistry* **1990**, *29*, 2263–2271.
- [7] K. Fukuyama, *Photosynth. Res.* **2004**, *81*, 289–301.
- [8] W. Lubitz, H. Ogata, O. Rüdiger, E. Reijerse, *Chem. Rev.* **2014**, *114*, 4081–4148.
- [9] D. W. Mulder, E. S. Boyd, R. Sarma, R. K. Lange, J. A. Endrizzi, J. B. Broderick, J. W. Peters, *Nature* **2010**, *465*, 248–251.
- [10] M. Winkler, J. Esselborn, T. Happe, *Biochim. Biophys. Acta* **2013**, *1827*, 974–985.
- [11] K. Sybirna, P. Ezanno, C. Baffert, C. Léger, H. Bottin, *Int. J. Hydrogen Energy* **2013**, *38*, 2998–3002.
- [12] Y. Sakakibara, H. Kimura, A. Iwamura, T. Saitoh, T. Ikegami, G. Kurisu, T. Hase, *J. Biochem.* **2012**, *151*, 483–492.
- [13] a) G. Kurisu, M. Kusunoki, E. Katoh, T. Yamazaki, K. Teshima, Y. Onda, Y. Kimata-Arigo, T. Hase, *Nat. Struct. Biol.* **2001**, *8*, 117–121; b) P. N. Palma, B. Lagoutte, L. Krippahl, J. J. G. Moura, F. Guerlesquin, *FEBS Lett.* **2005**, *579*, 4585–4590.
- [14] X. Xu, S.-K. Kim, P. Schürmann, M. Hirasawa, J. N. Tripathy, J. Smith, D. B. Knaff, M. Ubbink, *FEBS Lett.* **2006**, *580*, 6714–6720.
- [15] S. Rumpel, J. F. Siebel, C. Farès, J. Duan, E. Reijerse, T. Happe, W. Lubitz, M. Winkler, *Energy Environ. Sci.* **2014**, *7*, 3296–3301.
- [16] a) E. Vo, H. C. Wang, J. P. Germanas, *J. Am. Chem. Soc.* **1997**, *119*, 1934–1940; b) S. Kazanis, T. C. Pochapsky, T. M. Barnhart, J. E. Penner-Hahn, U. A. Mirza, B. T. Chait, *J. Am. Chem. Soc.* **1995**, *117*, 6625–6626.
- [17] M. T. Bes, E. Parisini, L. A. Inda, L. M. Saraiva, M. L. Peleato, G. M. Sheldrick, *Structure* **1999**, *7*, 1201–1211.
- [18] H. Kameda, K. Hirabayashi, K. Wada, K. Fukuyama, *PLoS One* **2011**, *6*, e21947.
- [19] A. Silakov, E. J. Reijerse, W. Lubitz, *Eur. J. Inorg. Chem.* **2011**, 1056–1066.
- [20] S. J. de Vries, A. D. J. van Dijk, M. Krzeminski, M. van Dijk, A. Thureau, V. Hsu, T. Wassenaar, A. M. J. J. Bonvin, *Proteins* **2007**, *69*, 726–733.
- [21] A. S. Pandey, T. V. Harris, L. J. Giles, J. W. Peters, R. K. Szilagy, *J. Am. Chem. Soc.* **2008**, *130*, 4533–4540.
- [22] H. B. Gray, J. R. Winkler, *Proc. Natl. Acad. Sci. USA* **2005**, *102*, 3534–3539.
- [23] M. I. García-Sánchez, A. Díaz-Quintana, C. Gotor, J.-P. Jacquot, M. A. De la Rosa, J. M. Vega, *J. Biol. Inorg. Chem.* **2000**, *5*, 713–719.
- [24] J. A. Stapleton, J. R. Swartz, *PLoS One* **2010**, *5*, e10554.
- [25] A. N. Volkov, Q. Bashir, J. A. R. Worrall, G. M. Ullmann, M. Ubbink, *J. Am. Chem. Soc.* **2010**, *132*, 11487–11495.
- [26] T. Ahn, S.-K. Yim, H.-I. Choi, C.-H. Yun, *Anal. Biochem.* **2001**, *291*, 300–303.
- [27] A. Gutmanas, P. Jarvoll, V. Y. Orekhov, M. Billeter, *J. Biomol. NMR* **2002**, *24*, 191–201.
- [28] A. Lemak, A. Gutmanas, S. Chitayat, M. Karra, C. Farès, M. Sunnerhagen, C. H. Arrowsmith, *J. Biomol. NMR* **2011**, *49*, 27–38.
- [29] F. Delaglio, S. Grzesiek, G. W. Vuister, G. Zhu, J. Pfeifer, A. Bax, *J. Biomol. NMR* **1995**, *6*, 277–293.
- [30] A. Bax, S. Grzesiek, *Acc. Chem. Res.* **1993**, *26*, 131–138.
- [31] T. Yamazaki, J. D. Forman-Kay, L. E. Kay, *J. Am. Chem. Soc.* **1993**, *115*, 11054–11055.
- [32] N. A. Farrow, R. Muhandiram, A. U. Singer, S. M. Pascal, C. M. Kay, G. Gish, S. E. Shoelson, T. Pawson, J. D. Forman-Kay, L. E. Kay, *Biochemistry* **1994**, *33*, 5984–6003.
- [33] W. Rieping, M. Habeck, B. Bardiaux, A. Bernard, T. E. Malliavin, M. Nilges, *Bioinformatics* **2007**, *23*, 381–382.
- [34] A. T. Brünger, P. D. Adams, G. M. Clore, W. L. DeLano, P. Gros, R. W. Grosse-Kunstleve, J.-S. Jiang, J. Kuszewski, M. Nilges, N. S. Pannu, R. J. Read, L. M. Rice, T. Simonson, G. L. Warren, *Acta Crystallogr. Sect. D* **1998**, *54*, 905–921.
- [35] G. Cornilescu, F. Delaglio, A. Bax, *J. Biomol. NMR* **1999**, *13*, 289–302.
- [36] R. Koradi, M. Billeter, K. Wüthrich, *J. Mol. Graph.* **1996**, *14*, 51.
- [37] R. A. Laskowski, J. A. C. Rullmann, M. W. MacArthur, R. Kaptein, J. M. Thornton, *J. Biomol. NMR* **1996**, *8*, 477–486.
- [38] C. Dominguez, R. Boelens, A. M. J. J. Bonvin, *J. Am. Chem. Soc.* **2003**, *125*, 1731–1737.

Manuscript received: March 12, 2015

Accepted article published: May 25, 2015

Final article published: ■ ■ ■, 0000

4.3.2 Supporting information

Structural insight into the complex of ferredoxin and [FeFe] hydrogenase from *Chlamydomonas reinhardtii*

Sigrun Rumpel, Judith F. Siebel, Mamou Diallo, Christophe Farès, Edward J. Reijerse, Wolfgang Lubitz

Solution structure and dynamics of PetF

Table S1. NMR and refinement statistics for oxidized PetF.

	Oxidized PetF
NMR distance and dihedral constraints	
Distance constraints	
Total NOE	1412
Intra-residue	574
Inter-residue	838
Sequential ($ i - j = 1$)	288
Medium-range ($ i - j < 4$)	158
Long-range ($ i - j > 5$)	392
Hydrogen bonds	5
Total dihedral angle restraints	148
ϕ	74
ψ	74
Structure statistics	
Violations (mean and s.d.)	
Distance constraints (Å)	0.061 ± 0.006
Dihedral angle constraints (°)	1.143 ± 0.057
Max. dihedral angle violation (°)	2.333
Max. distance constraint violation (Å)	1.239
Deviations from idealized geometry	
Bond lengths (Å)	0.0054 ± 0.0016
Bond angles (°)	0.674 ± 0.020
Improper (°)	1.862 ± 0.077
Average pairwise r.m.s. deviation** (Å)	
Heavy	0.60 ± 0.13
Backbone	1.16 ± 0.16
Ramachandran plot statistics	
Residues in most-favored region (%)	73.9
Residues in additionally allowed region (%)	23.9
Residues in generously allowed region (%)	2.3
Residues in disfavored region (%)	0

**Pairwise r.m.s. deviation was calculated among 15 refined structures for residues 1-94.

```

1      10      20      30      40      50      60      70      80      90
Cr YKVTLKTPSGDKTIECPADTYILDAAEEAGLDLPYSCRAGACSSCAGKVAAGTVDQSDQSFLLDDAQMNGFVLTVCVAYPTSDCTIQTHQEELY
Cf YKVTLKTPSGEETIECPEDTYILDAAEEAGLDLPYSCRAGACSSCAGKVESGEVDQSDQSFLLDDAQMKGKGFVLTVCVAYPTSDVTILTHQEELY
*****:***** ***** ***** *****:***** ***** ***** ***** *****

```

Figure S1. Sequence alignment of residues 1 to 94 of PetF from *C. reinhardtii* (Cr) and of the ferredoxin of *Chlorella fusca* (Cf) with the pdb-code 1AWD. Cysteines ligating the [2Fe-2S] cluster are highlighted by a yellow background. The line below the two ferredoxin sequences indicates identical residues by * and conserved residues by .

Highest root-mean-square deviation (RMSD) values within the ensemble of NMR structures were found for residues 35 to 46 and 73 to 76 (regions lacking experimental restraints) as well as for the C-terminus (Figure 1). Those regions show also the highest RMSD to the X-ray structure 1AWD, which has an average backbone RMSD (residues 1-94) to the mean NMR-structure of 1.71 Å. Differences within the NMR ensemble and with respect to the X-ray structure are in the same range with the exception of residues 26 to 32, which precede the long iron-sulfur cluster coordinating loop (Figure S2).

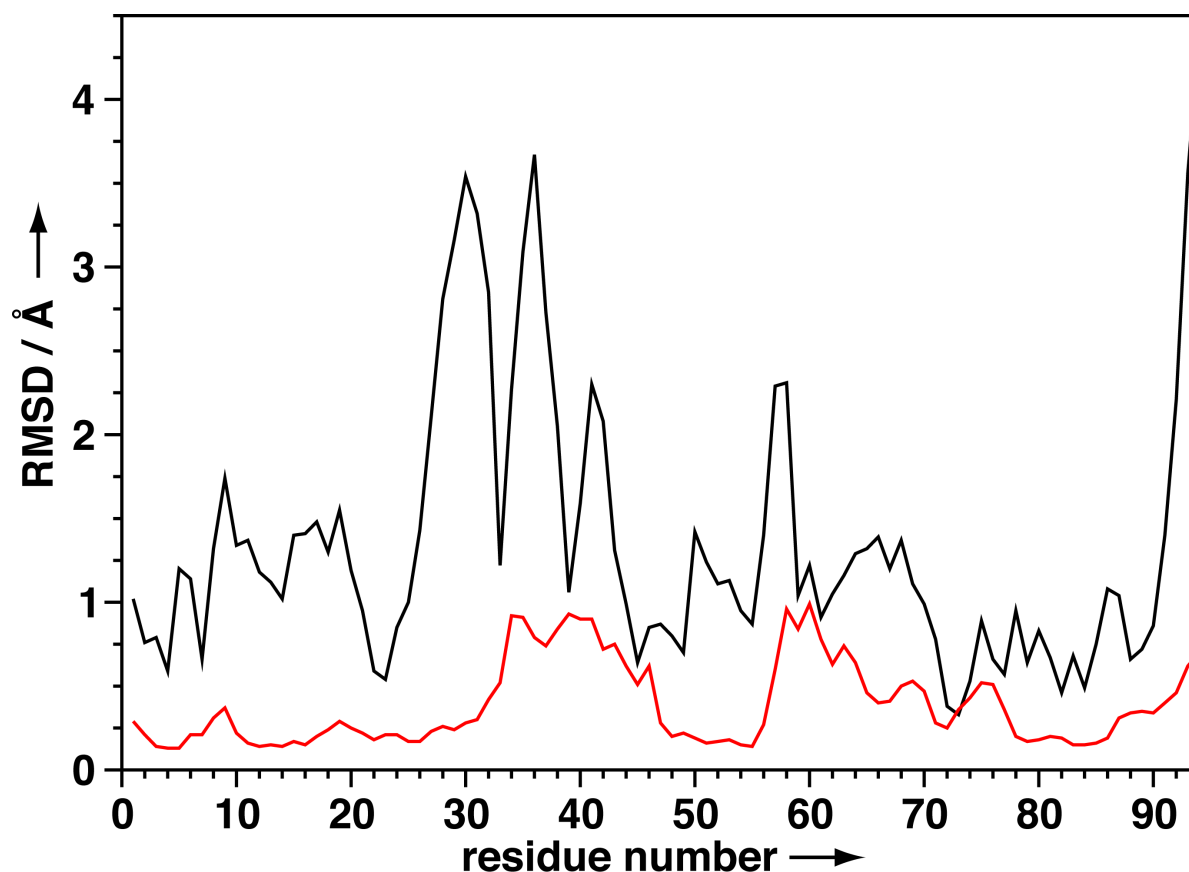


Figure S2. Backbone RMSD per residue within the ensemble of 10 solution NMR structures (red line) and between mean solution NMR structure and the X-ray structure 1AWD of the related ferredoxin from the green alga *Chlorella fusca* (black line).

Most residues of PetF exhibit steady-state ^{15}N - ^1H -NOE values above 0.75 that indicate a lack of internal motions on the nanosecond timescale (Figure S3). However, there are four flexible regions as indicated by NOE values below 0.75: (I) residues 23-26 of helix $\alpha 1$, (II) residues 31-33 of the loop following helix $\alpha 1$, (III) residues 59-63 of the loop preceding helix $\alpha 2$ and (IV) the C-terminal helix $\alpha 4$ (residues 90-94). These four regions surround the $[2\text{Fe-2S}]$ cluster protruding in three directions. A detailed analysis of the B-factors of the X-ray structures of plant-type ferredoxins has revealed the same regions as flexible and important for protein-protein complex formation. This study also revealed residues 7 to 10 connecting the first two β -strands as an additional flexible region.¹ However, this loop is located at the opposite site of the $[2\text{Fe-2S}]$ cluster and thus unlikely to be important for the recognition of HydA1 and other PetF-dependent enzymes.

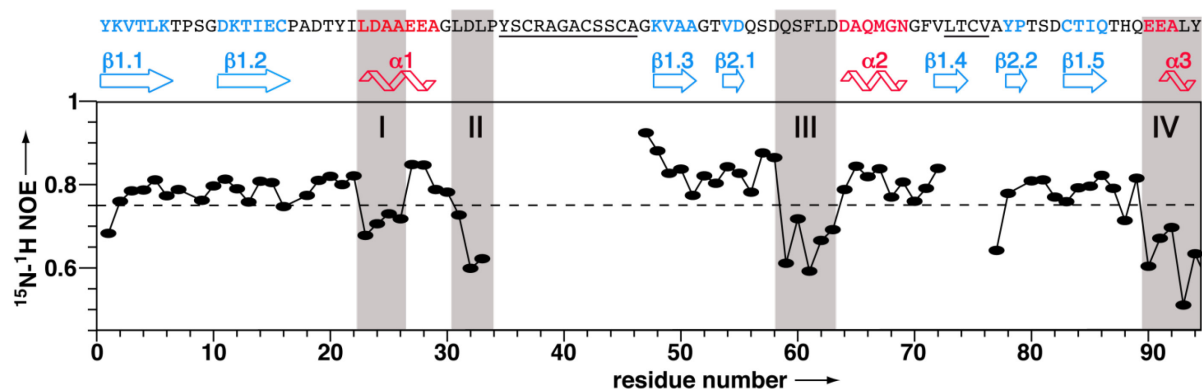


Figure S3. ^{15}N - ^1H steady-state heteronuclear NOE of oxidized PetF plotted against the residue number with the native amino acid sequence of PetF indicated above the plot. The heteronuclear NOE value of 0.75 is indicated by the dashed line. Flexible regions I-IV with heteronuclear NOE values below 0.75 are shaded in gray. Residues 35-46 and 73-76 close to the $[2\text{Fe-2S}]$ cluster are invisible in the NMR-spectra and are underlined in the amino acid sequence.

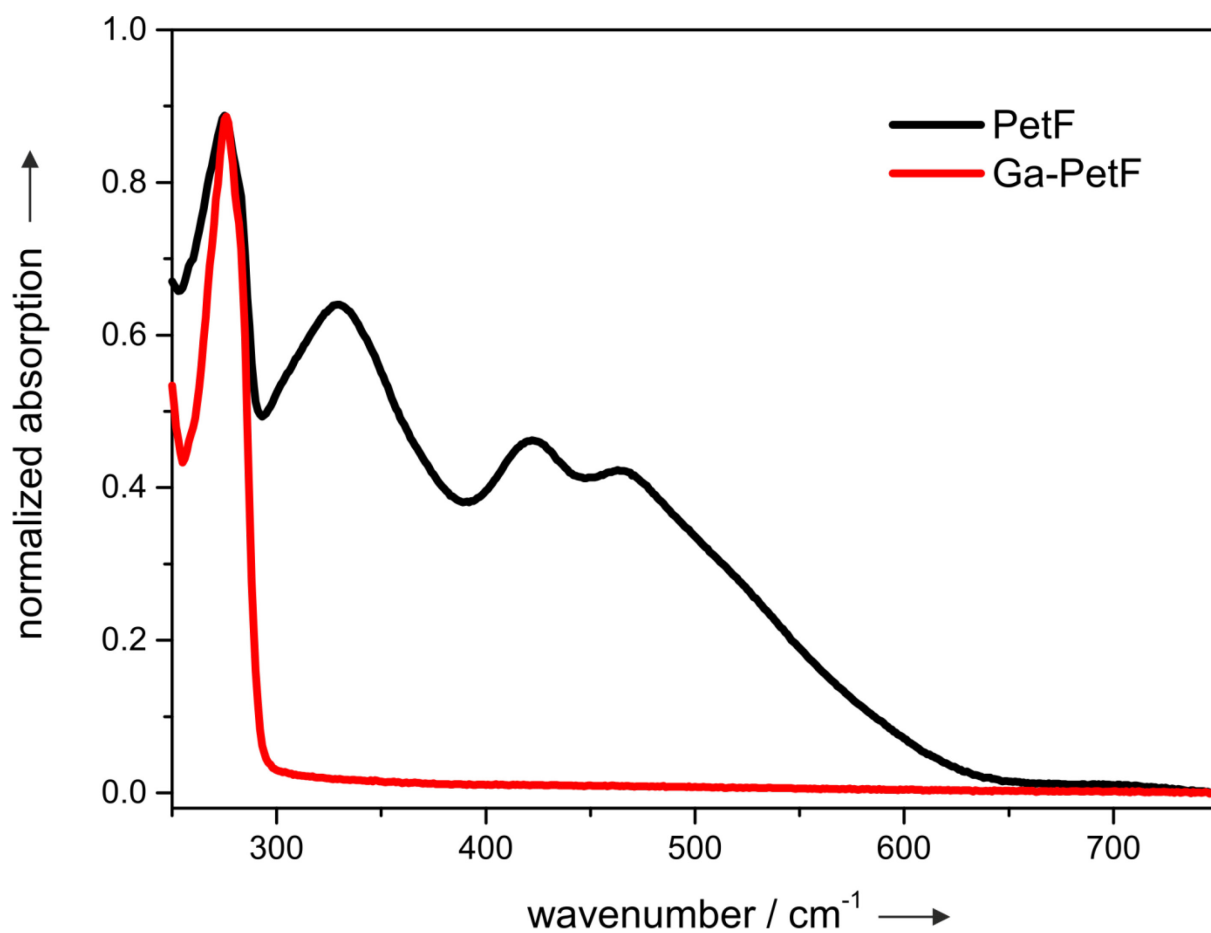
Gallium-substituted PetF

Figure S4. Absorption spectra of [2Fe-2S] PetF (black line) and Ga-PetF (red line). The characteristic absorption maxima of [2Fe-2S] ferredoxin at 330 nm, 422 nm and 465 nm disappear upon gallium substitution, confirming the absence of the [2Fe-2S] cluster. The spectra are normalized to the same absorption maximum at 276 nm.

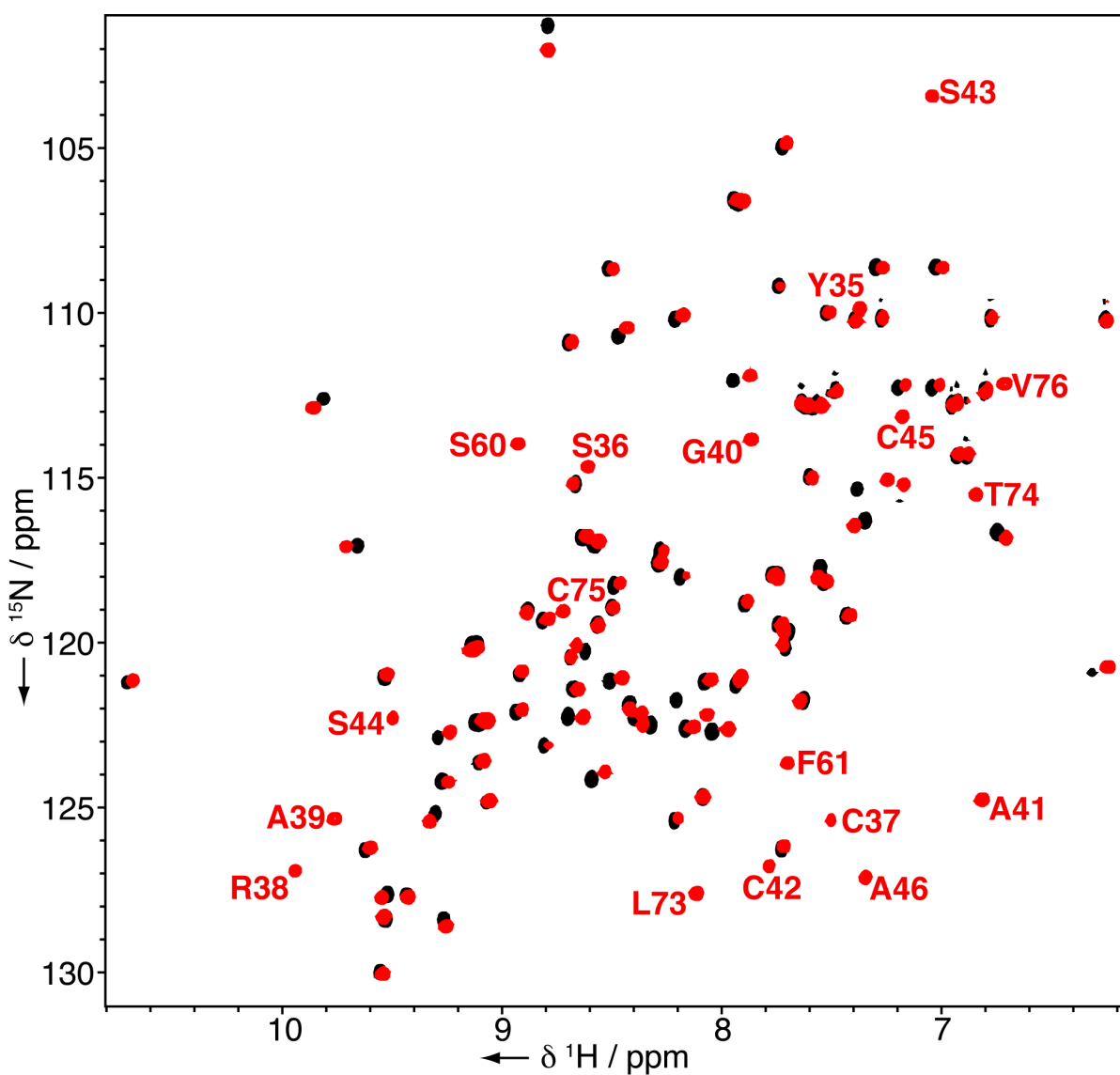


Figure S5. Overlay of the ^{15}N - ^1H HSQC spectra of native, oxidized PetF (black) and Ga-PetF (red). Assignments of the peaks observed only for the Ga(III)-substituted protein are indicated. This figure is identical to Figure 2 except for the color of Ga-PetF.

HADDOCK model of the PetF/HydA1 complex

Table S2. Active and passive residues used in the definition of the ambiguous distance restraints (AIRs). Solvent accessible residues experimentally identified as involved in the interaction are termed “active” and solvent accessible residues neighboring active residues are termed “passive”.

PetF

Active residues ^a	D24, A25, E28, Y35-C45, Q59-66, H88-E90, L93-Y94
Passive residues ^c	E27, P34, A46, D58, M67, E91-A92

HydA1

Active residues ^b	R56, K139, R187, K356-K357, K393
Passive residues ^c	S140, T186, T360, D392, A394

^aDerived from the average chemical shift perturbation observed for Ga(III) substituted PetF when titrated with HydA1.

^bDetermined by site-directed mutagenesis.²

^cDefined according to the HADDOCK protocol.³

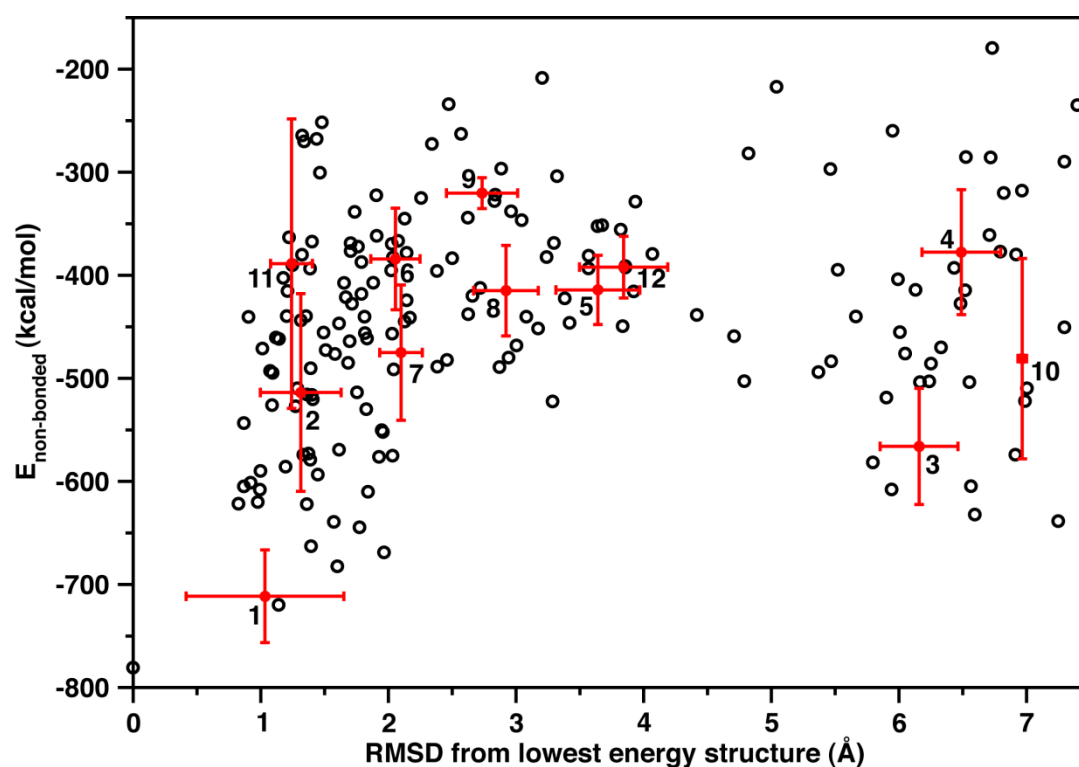


Figure S6. Intermolecular non-bonded energy of the 200 HADDOCK solutions for the PetF/HydA1 complex as a function of the backbone RMSD from the lowest energy structure for the docked structures. The cluster averages are indicated by red circles with error bars, which represent the standard deviation from the mean for the four lowest-energy structures of each cluster. The numbering of clusters corresponds to column 1 of Table S3.

Table S3. Structural statistics of the four best docking structures of each cluster. The clusters are sorted according to an increasing HADDOCK score and the best cluster is highlighted in bold.

	N ^a	HAD-DOCK score	E _{inter} ^b	E _{nb} ^c	E _{vdw} ^d	E _{elec} ^e	E _{AIR} ^f	BSA ^g	Fe-Fe distance ^h
1	56	-91.94	-505.27	-711.4	-47.66	-663.74	206.13	1923.08	11.6
3	11	-65.99	-352.33	-566	-41.55	-524.45	213.67	1711.55	18.6
7	5	-62.33	-226.57	-474.97	-58.65	-416.32	248.4	2016.17	11.1
2	15	-46.47	-277.27	-513.71	-33.18	-480.54	236.44	1651.27	11.9
8	5	-29.75	-193.16	-414.93	-40.34	-374.59	221.77	1616.49	16
5	6	-29.71	-206.13	-414.25	-36.1	378.15	208.12	1331.98	18.2
4	8	-26.37	-205.69	-377.62	-27.89	-349.74	171.93	1224.86	13.5
6	6	-24.48	-168.93	-384.14	-42.24	-341.89	215.21	1477.05	12.9
10	4	-22.62	-234.58	-480.85	-33.09	-447.76	246.27	1416.70	21.9
11	4	-14.54	-174.36	-388.77	-28.90	-359.8	214.4	1391.55	12.6
12	4	-10.88	-161.07	-392.12	-31.96	-360.16	231.05	1244.28	11
9	5	-0.72	-139.73	320.29	-26.71	-293.58	180.56	1387.22	16.5

^aNumber of structures per cluster

^bE_{inter} (kcal/mol) – intermolecular total energy (E_{vdw}+E_{elec}+E_{AIR})

^cE_{nb} (kcal/mol) – intermolecular non-bonded energy

^dE_{vdw} (kcal/mol) – intermolecular van der Waals energy

^eE_{elec} (kcal/mol) – intermolecular electrostatic energy

^fE_{AIR} (kcal/mol) – ambiguous intermolecular restraints (AIRs) energy

^gBSA (Å²) – buried surface area

^hFe-Fe distance (Å) – average intermolecular distance from Fe1 of PetF to the closest Fe of HydA1

Table S4. Possible intermolecular H-bond and salt bridge contacts with distances smaller than 3 Å of the PetF/HydA1 complex structure model. Contacts between R187 of HydA1 and E90 of PetF are highlighted bold and by a gray background.

HydA1			PetF			distance (Å)
residue #	residue type	atom 1	residue #	residue type	atom 2	
132	GLY	HA1	94	TYR	OH	2.72
139	LYS	HZ3	94	TYR	O	2.99
186	THR	HG1	90	GLU	OE2	1.7
186	THR	OG1	90	GLU	HE2	2.23
187	ARG	HD2	94	TYR	OH	2.59
187	ARG	HE	90	GLU	OE1	2.37
187	ARG	HE	90	GLU	OE2	1.89
187	ARG	HH11	94	TYR	OH	2.03
187	ARG	HH12	43	SER	OG	2.66
187	ARG	NH2	43	SER	OG	2.84
187	ARG	NH2	90	GLU	OE1	2.63
187	ARG	HH21	90	GLU	OE1	1.64
187	ARG	HH22	43	SER	OG	1.85
187	ARG	NE	90	GLU	HE2	2.44
187	ARG	NH1	94	TYR	OH	2.85
187	ARG	NH2	43	SER	OG	2.84
187	ARG	NH2	90	GLU	OE1	2.63
285	ASP	OD1	39	ALA	HB2	2.69
351	GLY	HA1	41	ALA	O	2.88
352	LEU	HD12	43	SER	OG	2.6
352	LEU	N	41	ALA	O	2.81
352	LEU	N	41	ALA	O	2.81
352	LEU	HN	41	ALA	O	2.03
353	GLY	HN	41	ALA	O	2.54
353	GLY	HA1	59	GLN	O	2.9
353	GLY	HA2	40	GLY	O	2.46
353	GLY	HA2	60	SER	OG	3
356	LYS	HD2	60	SER	O	2.48
356	LYS	HD3	59	GLN	O	2.65
356	LYS	NZ	59	GLN	HE22	2.94
356	LYS	NZ	59	GLN	OE1	2.69
356	LYS	NZ	63	ASP	HD2	1.7
356	LYS	NZ	63	ASP	OD2	2.63
356	LYS	HZ1	59	GLN	OE1	2.99
356	LYS	HZ1	63	ASP	OD1	2.87
356	LYS	HZ1	63	ASP	OD2	1.68
356	LYS	HZ2	63	ASP	OD1	2.84
356	LYS	HZ2	63	ASP	OD2	2.89
356	LYS	HZ3	59	GLN	OE1	1.72
357	LYS	HD3	58	ASP	OD2	2.38
357	LYS	HZ2	58	ASP	OD1	1.73
357	LYS	HZ2	58	ASP	OD2	2

357	LYS	HZ3	39	ALA	O	2.18
357	LYS	HZ3	58	ASP	OD1	2.82
357	LYS	NZ	58	ASP	OD1	2.67
357	LYS	NZ	58	ASP	OD2	2.89
376	ALA	O	42	CYS	HB3	2.95
378	PRO	HB3	Cluster	[2Fe-2S]	Fe1	2.83
378	PRO	HB3	37	CYS	SG	2.42
389	ARG	HD2	32	ASP	OD2	2.84
389	ARG	HD3	32	ASP	OD1	2.62
389	ARG	HG3	32	ASP	OD2	2.88
390	SER	O	35	TYR	HH	2.81
392	ASP	HN	35	TYR	OH	2.62
392	ASP	O	35	TYR	HE1	2.87
393	LYS	HA	35	TYR	O	2.81
393	LYS	N	35	TYR	HE1	2.6
393	LYS	HD3	27	GLU	OE1	2.65
393	LYS	HE2	27	GLU	OE2	2.61
393	LYS	HZ1	28	GLU	OE2	1.82
393	LYS	NZ	28	GLU	OE2	2.84
393	LYS	HZ2	27	GLU	OE1	1.58
393	LYS	HZ2	27	GLU	OE2	2.42
393	LYS	HZ3	24	ASP	OD1	2.86
393	LYS	HZ3	24	ASP	OD2	2.73
393	LYS	NZ	27	GLU	HE2	2.44
393	LYS	NZ	27	GLU	OE1	2.61
393	LYS	NZ	28	GLU	HE2	2.67
393	LYS	O	36	SER	HA	2.36
393	LYS	O	36	SER	HG	2.52
396	THR	HG1	36	SER	OG	2.45

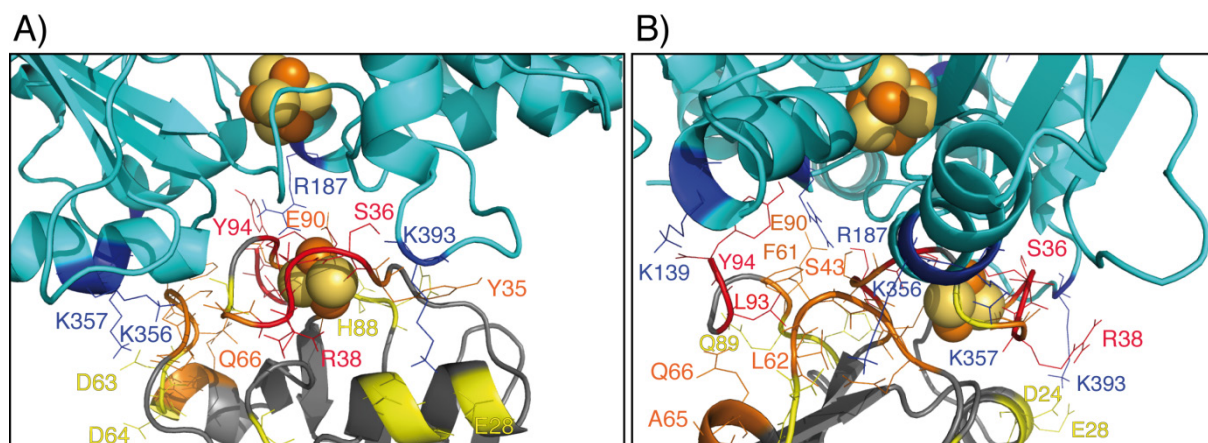


Figure S7. Zoom in of the best HADDOCK model of the PetF/HydA1 complex structure presented in Figure 4. The ribbon representation of HydA1 and PetF is shown in cyan and grey, respectively. Side chains of residues defined as ambiguous interface restraints for protein-protein docking are shown in blue for HydA1 and as in Figure 3 and 4 for PetF. The FeS-clusters are displayed as spheres with Fe colored orange and S colored yellow. The orientation of the complex corresponds to Figure 1 in (A) and is rotated 90° about its y- and -10° about its x-axis in (B).

References

- [1] H. Kameda, K. Hirabayashi, K. Wada, K. Fukuyama, *PLoS One* **2011**, *6*, e21947.
- [2] a) M. Winkler, S. Kuhlert, M. Hippler, T. Happe, *J. Biol. Chem.* **2009**, *284*, 36620-36627; b) K. Sybirna, P. Ezanno, C. Baffert, C. Léger, H. Bottin, *Int. J. Hydrogen Energy* **2013**, *38*, 2998-3002.
- [3] C. Dominguez, R. Boelens, A. M. J. J. Bonvin, *J. Am. Chem. Soc.* **2003**, *125*, 1731-1737.

4.4 Paper IV

Spectroscopic investigations of [FeFe] hydrogenase matured with $[\text{}^{57}\text{Fe}_2(\text{adt})(\text{CN})_2(\text{CO})_4]^{2-}$

Ryan Gilbert-Wilson, Judith F. Siebel, Agnieszka Adamska-Venkatesh, Cindy C. Pham,
Edward Reijerse, Hongxin Wang, Stephen P. Cramer, Wolfgang Lubitz, Thomas B.
Rauchfuss

Reproduced with permission from *J. Am. Chem. Soc.* **2015**, accepted manuscript. Copyright ©
2015 American Chemical Society.

DOI: 10.1021/jacs.5b03270

Journal name: Journal of the American Chemical Society
Impact factor: 12.113 (in 2014)
Author: joint first authors (shared equally with R. Gilbert-Wilson)
Contribution: – 35 %
– I established the reconstitution reaction
– I made all biological samples
– I analyzed the Mössbauer spectra
– I was involved in the production of the manuscript

R. Gilbert-Wilson performed the synthetic work leading to the ^{57}Fe labeled complex,
A. Adamska-Venkatesh performed the EPR measurements and analyses, C. Pham and
H. Wang made the NRVS measurements and analyses.

4.4.1 Journal article

Spectroscopic Investigations of [FeFe] Hydrogenase Maturated with $[^{57}\text{Fe}_2(\text{adt})(\text{CN})_2(\text{CO})_4]^{2-}$

Ryan Gilbert-Wilson,^{#,†} Judith F. Siebel,^{#,‡} Agnieszka Adamska-Venkatesh,[‡] Cindy C. Pham,[§] Edward Reijerse,[‡] Hongxin Wang,^{§,||} Stephen P. Cramer,^{*,§,||} Wolfgang Lubitz,^{*,‡} and Thomas B. Rauchfuss^{*,†}

[†]School of Chemical Sciences, University of Illinois at Urbana–Champaign, Urbana, Illinois 61801, United States

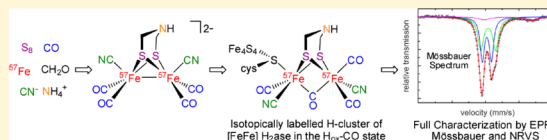
[‡]Max-Planck-Institut für Chemische Energiekonversion, Stiftstrasse 34-36, 45470 Mülheim an der Ruhr, Germany

[§]Department of Chemistry, University of California, Davis, California 95616, United States

^{||}Physical Biosciences Division, Lawrence Berkeley National Laboratory, Berkeley, California 94720, United States

S Supporting Information

ABSTRACT: The preparation and spectroscopic characterization of a CO-inhibited [FeFe] hydrogenase with a selectively ^{57}Fe -labeled binuclear subsite is described. The precursor $[^{57}\text{Fe}_2(\text{adt})(\text{CN})_2(\text{CO})_4]^{2-}$ was synthesized from the ^{57}Fe metal, S_8 , CO, $(\text{NEt}_4)\text{CN}$, NH_4Cl , and CH_2O . $(\text{Et}_4\text{N})_2[^{57}\text{Fe}_2(\text{adt})(\text{CN})_2(\text{CO})_4]$ was then used for the maturation of the [FeFe] hydrogenase HydA1 from *Chlamydomonas reinhardtii*, to yield the enzyme selectively labeled at the $[2\text{Fe}]_{\text{H}}$ subcluster. Complementary ^{57}Fe enrichment of the $[4\text{Fe-4S}]_{\text{H}}$ cluster was realized by reconstitution with $^{57}\text{FeCl}_3$ and Na_2S . The $\text{H}_{\text{ox}}\text{-CO}$ state of $[2^{57}\text{Fe}]_{\text{H}}$ and $[4^{57}\text{Fe-4S}]_{\text{H}}$ HydA1 was characterized by Mössbauer, HYSCORE, ENDOR, and nuclear resonance vibrational spectroscopy.



INTRODUCTION

Since their crystallographic identification, the hydrogenases (H_2 ases) represent perfect paradigms for bioinspired energy transformations. Utilizing only base metals and operating at near thermodynamic potentials, these enzymes promote reactions at extraordinary rates, in the case of [FeFe] H_2 ases thousands of turnover per second.¹ Further motivating this theme are the practical implications of the H_2/H^+ redox reaction, which is the basis for fuel cells.

Many [FeFe] H_2 ases have been studied, but the algal H_2 ase from *Chlamydomonas reinhardtii*, HydA1,² has received particular attention.³ The *C. reinhardtii* protein is ideal for studies on biosynthesis⁴ and spectroscopy because it represents a “minimal architecture” enzyme containing only the active site.⁵ In contrast, most [FeFe] H_2 ases feature multiple accessory [Fe–S] clusters. The active site of all [FeFe] H_2 ases is the “H-cluster”, consisting of a $[4\text{Fe-4S}]_{\text{H}}$ cluster appended via a bridging cysteinyl thiolate to a diiron subunit called $[2\text{Fe}]_{\text{H}}$.⁶ In $[2\text{Fe}]_{\text{H}}$, a diiron center is bound to CO, CN^- , and azadithiolate ($\text{adt}^{2-} = [(\text{SCH}_2)_2\text{NH}]^{2-}$) ligands (Figure 1).⁷

Recent work has shown that functional HydA1 enzyme can be produced through incubation of unmaturation HydA1 containing only the $[4\text{Fe-4S}]_{\text{H}}$ subcluster, with a synthetic active site mimic $(\text{Et}_4\text{N})_2[^{57}\text{Fe}_2(\text{adt})(\text{CN})_2(\text{CO})_4]$.⁸ This innovation exploits the fact that the active site is attached to the protein through few covalent bonds. Via this artificial maturation, the enzyme is now available with wide variety of chemically and isotopically labeled versions^{9,10} of the $[2\text{Fe}]_{\text{H}}$

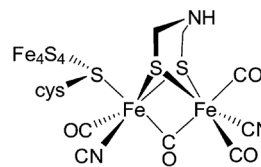
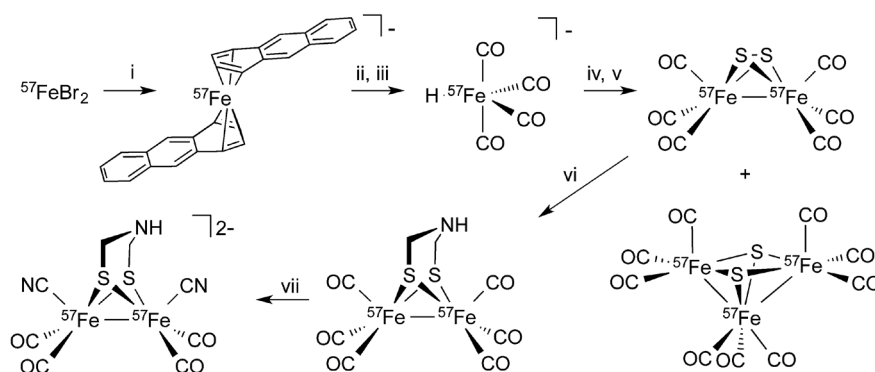


Figure 1. H-cluster of HydA1 in the $\text{H}_{\text{ox}}\text{-CO}$ state.

subunit on a scale and at a pace that would not be readily achieved by in vitro maturation routes.^{11,12} This “artificial maturation” allows a detailed characterization of individual active site states and the catalytic mechanism through a variety of spectroscopic techniques.⁹

The artificial maturation route in principle should allow the selective labeling of the $[2\text{Fe}]_{\text{H}}$ subunit with ^{57}Fe , a nucleus highly responsive to Mössbauer and nuclear resonance vibrational spectroscopies (NRVS). With a nuclear spin $I = 1/2$, ^{57}Fe is also ideal for the suite of EPR techniques that provide exquisite insights into Fe-based enzymes.¹³ ^{57}Fe -labeling of the $[2\text{Fe}]_{\text{H}}$ subunit however poses a significant synthetic challenge because salts of $[^{57}\text{Fe}_2(\text{adt})(\text{CN})_2(\text{CO})_4]^{2-}$ are prepared by multistep sequences starting from reagents that would only be awkwardly and inefficiently labeled with ^{57}Fe . In this report these challenges are surmounted, as established by the preparation of HydA1 with a selectively ^{57}Fe -labeled $[2\text{Fe}]_{\text{H}}$

Received: March 29, 2015

Scheme 1. Synthesis of $[^{57}\text{Fe}_2(\text{adt})(\text{CN})_2(\text{CO})_4]^{2-}$ 

^a(i) 4 $\text{KCl}_{14}\text{H}_{10}$, (ii) CO , (iii) MeOH , (iv) S_8 , (v) H^+ , (vi) CH_2O , NH_4^+ , (vii) $(\text{NEt}_4)\text{CN}$.

site. The $\text{H}_{\text{ox}}\text{-CO}$ state of HydA1 (Figure 1) can be obtained as a pure state and was therefore chosen to demonstrate the selective labeling. Using $(\text{Et}_4\text{N})_2[^{57}\text{Fe}_2(\text{adt})(\text{CN})_2(\text{CO})_4]$ as precursor the $[2\text{Fe}]_{\text{H}}$ subsite in $\text{H}_{\text{ox}}\text{-CO}$ was labeled using artificial maturation. In a complementary experiment the $[4\text{Fe-4S}]$ subcluster in $\text{H}_{\text{ox}}\text{-CO}$ was labeled using FeS reconstitution. The two ^{57}Fe labeled versions of $\text{H}_{\text{ox}}\text{-CO}$ were studied using Mössbauer, electron nuclear double resonance (ENDOR), hyperfine sublevel correlation (HYSCORE) as well as nuclear resonance vibrational (NRVS) spectroscopy.

RESULTS AND DISCUSSION

Synthesis and Characterization of $[^{57}\text{Fe}_2(\text{adt})(\text{CN})_2(\text{CO})_4]^{2-}$. The precursor to the target $[^{57}\text{Fe}_2(\text{adt})(\text{CN})_2(\text{CO})_4]^{2-}$ is $^{57}\text{Fe}_2(\text{adt})(\text{CO})_6$, which undergoes dicyanation nearly quantitatively.¹⁴ Synthesis of the diiron hexacarbonyl, however, poses challenges because it is derived via a series of inefficient reactions from precursors that are not readily labeled with ^{57}Fe . Low yielding routes to unlabeled $\text{Fe}_2(\text{adt})(\text{CO})_6$ are tolerated¹⁴ because the relevant reagents, e.g., $\text{Fe}(\text{CO})_5$, are inexpensive and the early steps in the preparation can be conducted on a multigram scale. The industrial method for production of $\text{Fe}(\text{CO})_5$ involves the direct carbonylation of Fe metal at high temperatures and pressures, e.g., 175 atm at 150 °C.¹⁵ Such reactions require specialized autoclaves,¹⁶ which are not suited for producing small amounts of $^{57}\text{Fe}(\text{CO})_5$. A variety of laboratory syntheses of $^{57}\text{Fe}(\text{CO})_5$ have been described, but they suffer from low yields and difficult separations even when using specialized equipment.¹⁷

The above considerations led to a focus on routes that avoid the intermediacy of $\text{Fe}(\text{CO})_5$. Retrosynthetic analysis reminds one that $\text{Fe}_2\text{S}_2(\text{CO})_6$, the immediate precursor to $\text{Fe}_2(\text{adt})(\text{CO})_6$ is formed from the $[\text{HFe}(\text{CO})_4]^-$ anion, *not* the pentacarbonyl. Thus, syntheses of $[\text{H}^{57}\text{Fe}(\text{CO})_4]^-$ from $^{57}\text{FeX}_2$ are of interest. Literature methods¹⁸ for generating $[\text{HFe}(\text{CO})_4]^-$ from iron halides proved low-yielding in our hands. Relevant to possible routes to $[\text{H}^{57}\text{Fe}(\text{CO})_4]^-$ is the fact that it is easily derived from $[\text{Fe}(\text{CO})_4]^{2-}$ by protonation. The anion $[\text{Fe}(\text{anthracene})_2]^-$, prepared by Ellis and co-workers in 61% yield from FeBr_2 , carbonylates at ambient pressures.¹⁹ The product, obtained in 81% isolated yield, is $[\text{K}(\text{18-crown-6})_2]_2[\text{Fe}_2(\text{CO})_8]$. Unfortunately, attempts to convert this salt into $\text{Fe}_2\text{S}_2(\text{CO})_6$ were unfruitful. Treatment of $[\text{K}(\text{18-crown-6})_2]_2[\text{Fe}_2(\text{CO})_8]$ with S_2Cl_2 or S_8 gave complex mixtures including $[\text{Fe}_2\text{S}_2(\text{S}_5)_2]^{2-}$ and intractable solids but no $\text{Fe}_2\text{S}_2(\text{CO})_6$. A successful method for the direct synthesis of $\text{Fe}_2\text{S}_2(\text{CO})_6$ was inspired by details in the PhD thesis of W. W. Brennessel of the Ellis group, who describes the synthesis of $\text{K}_2\text{Fe}(\text{CO})_4$ from FeBr_2 in ~50% yield.²⁰ His method involves treatment of FeBr_2 in THF with *four* equivalents of potassium anthracene at low temperature, followed by carbonylation at 1 atm. The Fe(-II) derivative is proposed to form via reduction of $\text{K}_2\text{Fe}_2(\text{CO})_8$ by the fourth equivalent of $\text{K}(\text{anthracene})$. This reaction was reproduced. Treatment of the resulting $\text{K}_2\text{Fe}(\text{CO})_4$ with methanol efficiently afforded $\text{KHF}(\text{CO})_4$ ²¹ which reacted with elemental sulfur to give $\text{Fe}_2\text{S}_2(\text{CO})_6$ after standard workup.²¹ In this way, starting from 500 mg of ^{57}Fe , we prepared 180 mg of $^{57}\text{Fe}_2\text{S}_2(\text{CO})_6$ (11.8% from ^{57}Fe metal) together with 60.8 mg (4.5% yield) of $^{57}\text{Fe}_2\text{S}_2(\text{CO})_9$ (Scheme 1). Repeat synthesis using the same procedure resulted in the yield of $^{57}\text{Fe}_2\text{S}_2(\text{CO})_6$ improving to 371 mg (24.4% from ^{57}Fe metal). The ^{13}C NMR spectra of $^{57}\text{Fe}_2\text{S}_2(\text{CO})_6$ and $^{57}\text{Fe}_2\text{S}_2(\text{CO})_9$ gives $^1J(^{57}\text{Fe},^{13}\text{C}) = 28.3$ and 26.3 Hz, respectively. The most problematic step in the synthesis is the conversion of $\text{KHF}(\text{CO})_4$ into $\text{Fe}_2\text{S}_2(\text{CO})_6$, which we estimate proceeded in 30% yield.

Conversion of $^{57}\text{Fe}_2\text{S}_2(\text{CO})_6$ to $[^{57}\text{Fe}_2(\text{adt})(\text{CN})_2(\text{CO})_4]^{2-}$ requires two steps, which have been described previously for the unlabeled versions of these complexes.²² The first of these steps is the conversion of $^{57}\text{Fe}_2\text{S}_2(\text{CO})_6$ to $^{57}\text{Fe}_2(\text{adt})(\text{CO})_6$. This conversion was achieved by reduction of $^{57}\text{Fe}_2\text{S}_2(\text{CO})_6$ with LiBEt_3H to give $^{57}\text{Fe}_2(\text{SLi})_2(\text{CO})_6$, followed by protonation to $^{57}\text{Fe}_2(\text{SH})_2(\text{CO})_6$ and subsequent adt bridge formation through reaction with a mixture of ammonia and formaldehyde to yield $^{57}\text{Fe}_2(\text{adt})(\text{CO})_6$. Conversion of $^{57}\text{Fe}_2(\text{adt})(\text{CO})_6$ to $[^{57}\text{Fe}_2(\text{adt})(\text{CN})_2(\text{CO})_4]^{2-}$ was achieved by reaction with 2 equiv of $(\text{NEt}_4)\text{CN}$. The isotopic purity of the anion $[^{57}\text{Fe}_2(\text{adt})(\text{CN})_2(\text{CO})_4]^{2-}$ was established by negative ion ESI mass spectrometry (see Supporting Information (SI), Figure S1).

Selective Labeling of HydA1. The insertion of $[^{57}\text{Fe}_2(\text{adt})(\text{CN})_2(\text{CO})_4]^{2-}$ into unmaturation HydA1 was monitored by Fourier transform infrared spectroscopy (FT-IR). The precursor undergoes substantial rearrangement upon incorporation into unmaturation HydA1 (Figure S2A and S2B, SI). One CO ligand migrates to the bridging position and the CN^- groups shift from apical to basal sites. Furthermore, in a

major desymmetrizing event, one of the two previously equivalent Fe sites binds to cysteinyl sulfur, which links the $[2\text{Fe}]_{\text{H}}$ and $[4\text{Fe-4S}]_{\text{H}}$ clusters. Under the usual reductive maturation conditions one terminal CO ligand of the distal Fe dissociates affording an open coordination site where substrate and inhibitors can bind. After oxidation with thionin (Figure S2C, SI) and flushing with CO, a pure $\text{H}_{\text{ox}}\text{-CO}$ state is created (Figure S2D, SI). In the $\text{H}_{\text{ox}}\text{-CO}$ state, the $[2\text{Fe}]_{\text{H}}$ subunit is in a delocalized mixed valence Fe(II)Fe(I) configuration.

In order to realize complementary ^{57}Fe enrichment, in a separate experiment the $[4\text{Fe-4S}]_{\text{H}}$ cluster was ^{57}Fe -labeled as described in the Experimental Section. In a first step, unfolding and thereby loss of the unlabeled $[4\text{Fe-4S}]_{\text{H}}$ cluster was observed by subsequent loss of the brownish color of the solution. The $[4\text{Fe-4S}]_{\text{H}}$ cluster was reconstituted with $^{57}\text{FeCl}_3$ and Na_2S , accompanied by recovery of the brownish color. Successful reconstitution was confirmed by activity measurements, UV-vis and EPR spectroscopy (see SI for detailed information).

EPR Characterization. The selective labeling of the two components of the H-cluster with ^{57}Fe greatly simplifies the assignment of the observed pulse EPR signals (see Figure 2). For the hybrid in which the $[2\text{Fe}]_{\text{H}}$ subcluster is labeled, two spectral features in the HYSCORE spectra can be observed (Figure 2B,C). The correlation ridges in the right-hand section of the spectra (positive frequencies) are assigned to a weakly coupled ^{57}Fe nucleus while the ones in the left-hand section (negative frequencies) originate from a strongly coupled ^{57}Fe nucleus. These signals can both be simulated with axial hyperfine tensors (see Table S1 in the SI). Their A_{iso} values are 4.4 and 1.3 MHz, respectively, suggesting that one iron in the $[2\text{Fe}]_{\text{H}}$ subsite has ~ 4 times more spin density than the other. According to the spin-exchange model describing the electronic structure of $\text{H}_{\text{ox}}\text{-CO}$ (see below), the proximal iron in $[2\text{Fe}]_{\text{H}}$ has the largest spin density. The obtained hyperfine parameters are in agreement with previously reported EPR data on the $[\text{FeFe}] \text{H}_2$ ases from *Desulfovibrio desulfuricans* (DdH).¹³ Earlier Mössbauer studies on the $[\text{FeFe}] \text{H}_2$ ases from *Desulfovibrio vulgaris* Hildenborough (DvH) and *Clostridium pasteurianum* (CpI) provided the first estimates for the hyperfine ^{57}Fe interactions in the $[2\text{Fe}]_{\text{H}}$ subsite.^{23,25} These measurements, however, suffered from overlapping signals from the accessory $[4\text{Fe-4S}]_{\text{H}}$ clusters and are therefore less accurate (see Table S1). The complete hyperfine tensor information on Fe1 and Fe2 as obtained from HYSCORE (Table S1) accurately defines the electronic structure of the binuclear subsite and can be used to validate quantum chemical calculations on the H-cluster properties.

As described above, it is also possible to selectively label the $[4\text{Fe-4S}]_{\text{H}}$ subcluster with ^{57}Fe . For this sample in the $\text{H}_{\text{ox}}\text{-CO}$ state, no signal in the HYSCORE spectra was observed. In the ENDOR spectra between 10–20 MHz signals from strongly coupled Fe nuclei are observed. As it is shown in Figure 2A, these signals are not observed when only the $[2\text{Fe}]_{\text{H}}$ subcluster is labeled. This unequivocally confirms that these signals originate from the $[4\text{Fe-4S}]_{\text{H}}$ subcluster. As presented in Figure 3, these signals can be simulated with four distinct anisotropic hyperfine interactions corresponding to the four Fe centers in the $[4\text{Fe-4S}]_{\text{H}}$ subcluster (hyperfine interaction parameters are listed in Table S1). In earlier Mössbauer studies on CpI, these relatively large hyperfine interactions of the formally diamagnetic $[4\text{Fe-4S}]_{\text{H}}$ subcluster were interpreted as originating from spin density induced by a substantial exchange

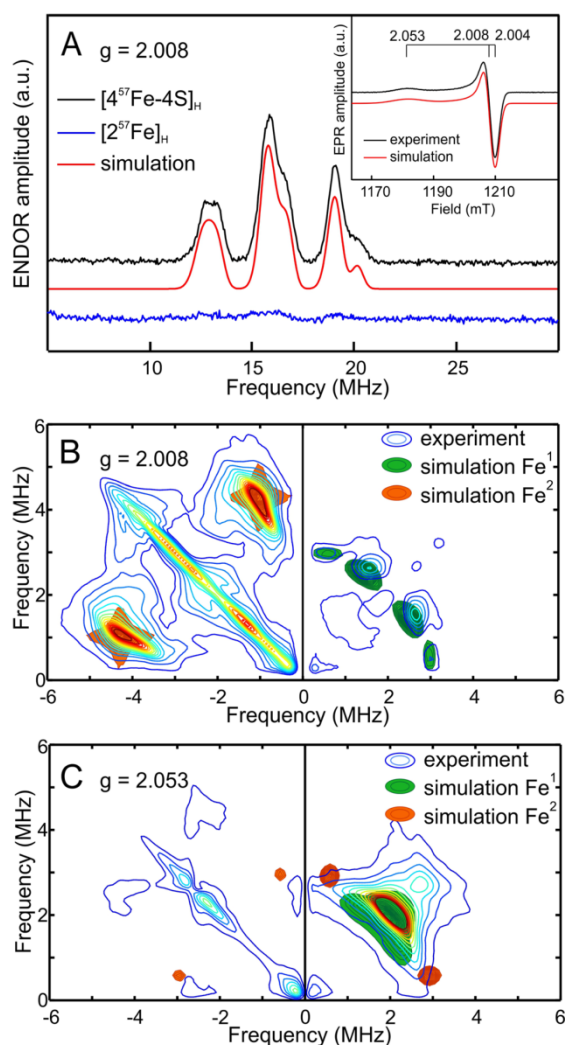


Figure 2. Q-band ^{57}Fe ENDOR and HYSCORE spectra (20 K) of selectively labeled HydA1 $\text{H}_{\text{ox}}\text{-CO}$ recorded at field positions indicated in the EPR spectrum (inset); for experimental parameters see SI. (A) Davies ENDOR of $\text{H}_{\text{ox}}\text{-CO}$ ^{57}Fe labeled at $[4\text{Fe-4S}]_{\text{H}}$ (black) or $[2\text{Fe}]_{\text{H}}$ (blue); simulations are indicated in red. (B) and (C) HYSCORE spectra recorded for $\text{H}_{\text{ox}}\text{-CO}$ ^{57}Fe labeled at $[2\text{Fe}]_{\text{H}}$ at $g = 2.008$ and $g = 2.053$ respectively; for all simulation parameters see Table S1.

coupling between the two subclusters.²³ The four hyperfine interactions were predicted to be divided in two groups representing the two $S = 9/2$ Fe(II)Fe(III) pairs which are mutually antiferromagnetically coupled to effective spin $S = 0$. Later ENDOR studies on DdH confirmed this analysis and showed that the hyperfine interaction of the two groups have opposite signs.¹³ The current data on HydA1 are fully in line with these studies. The two groups are defined by pair 1 with $A_{\text{iso}} = 33.2$ MHz (brown) and 30.0 MHz (orange), pair 2 $A_{\text{iso}} = 28.0$ MHz (blue) and 27.6 MHz (green).

Mössbauer Characterization. The selective ^{57}Fe -labeling of the $[2\text{Fe}]_{\text{H}}$ site enables the investigation of this specific subsite by Mössbauer spectroscopy. Previous Mössbauer

C

DOI: 10.1021/jacs.5b03270
J. Am. Chem. Soc. XXXX, XXX, XXX–XXX

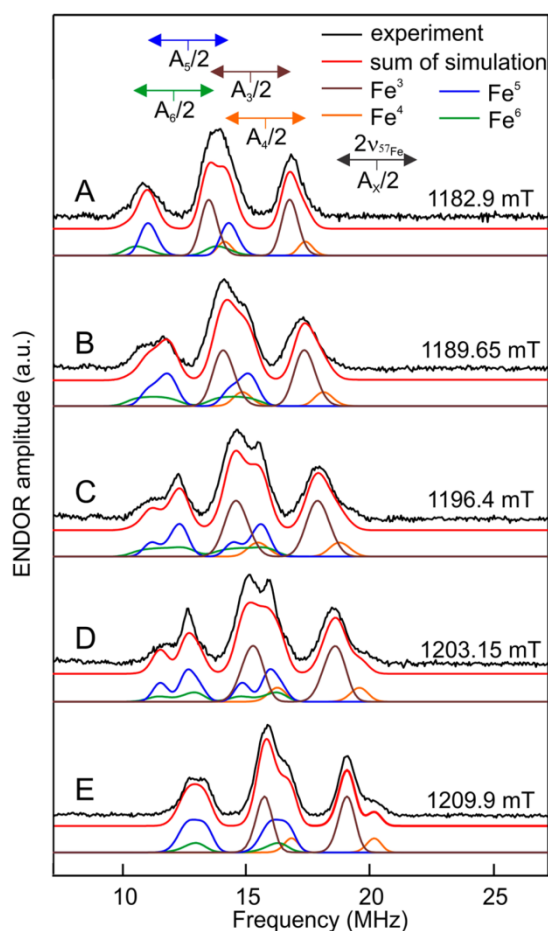


Figure 3. Q-band Davies ENDOR spectra and simulations of H_{ox} -CO HydA1 selectively labeled with ^{57}Fe at the $[4\text{Fe-4S}]_H$ cluster. Spectra were recorded with an RF pulse of $45 \mu\text{s}$, shot repetition time $800 \mu\text{s}$, microwave frequency 33.93396 GHz , temperature 20 K at field positions: (A) $1182.9 \text{ mT} \approx g_1$, (B) 1189.65 mT , (C) 1196.4 mT , (D) 1203.15 mT , (E) $1209.9 \text{ mT} \approx g_2$. The black line represents experimental data and the red line the sum of the simulations. The colored lines below each experimental spectrum are the components of the simulation corresponding to the four hyperfine couplings: brown Fe^3 , orange Fe^4 , blue Fe^5 , green Fe^6 (see Table S1).

studies on the active $[\text{FeFe}] \text{H}_2\text{ases}$ $\text{CpI}^{23,24}$ and DvH^{25} are complicated by the presence of accessory $[4\text{Fe-4S}]$ clusters in addition to the H-cluster. Using our approach of selective labeling, the Mössbauer spectra are simplified and Mössbauer parameters can be obtained without the cosimulation of other ^{57}Fe -components. Additionally, this method enables high concentrations of the sample and therefore high-quality spectra. The Mössbauer spectrum of the $[4^{57}\text{Fe-4S}]_H$ cluster from HydA1 matured with unlabeled $[\text{Fe}_2(\text{adt})(\text{CN})_2(\text{CO})_4]^{2-}$ in the H_{ox} -CO state is shown in Figure 4A. The counterpart spectrum, the ^{57}Fe -labeled $[2\text{Fe}]_H$ site in the H_{ox} -CO state, is presented in Figure 4B. Both spectra are quite simple and can be simulated with relatively few components. Figure 4C displays a superimposition of the simulated spectra 4A and 4B. It clearly shows the overlap between the signals from the

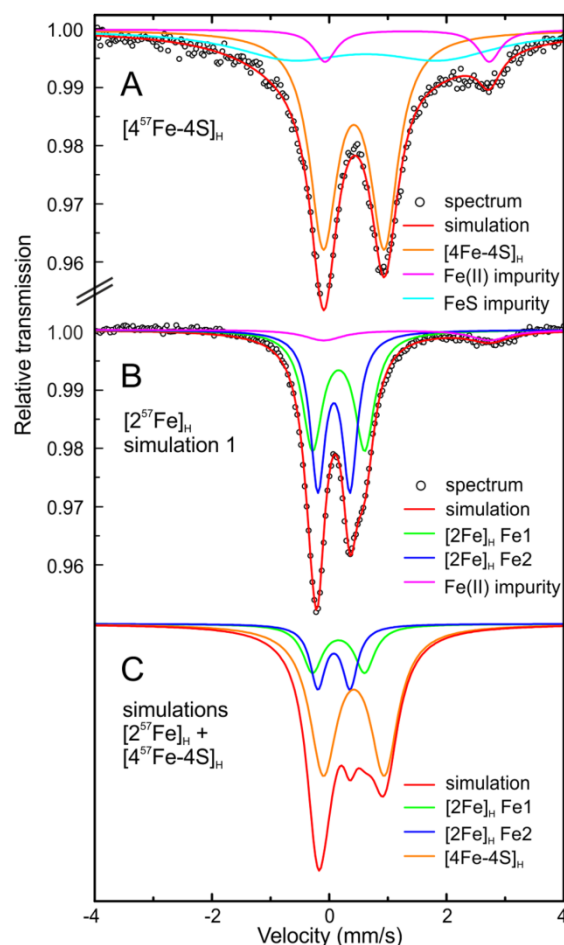


Figure 4. (A) Mössbauer spectrum and simulations of H_{ox} -CO HydA1 selectively labeled with ^{57}Fe at the $[4\text{Fe-4S}]_H$ subcluster. (B) Mössbauer spectrum and simulations of H_{ox} -CO HydA1 selectively labeled with ^{57}Fe at the $[2\text{Fe}]_H$ subcluster. (C) Superimposition of the simulations of the ^{57}Fe -labeled $[2\text{Fe}]_H$ subunit and the $[4\text{Fe-4S}]_H$ cluster, ratio 0.5:1. All spectra were measured at 160 K in zero magnetic field.

$[4\text{Fe-4S}]_H$ cluster and the $[2\text{Fe}]_H$ site, which would require 9 parameters for its simulation (apart from the background contributions).

The isomer shift ($\delta = 0.42 \text{ mm/s}$) and the quadrupole splitting ($\Delta E_Q = 1.04 \text{ mm/s}$) found for the $[4^{57}\text{Fe-4S}]_H$ cluster are typical for oxidized $[4\text{Fe-4S}]$ clusters.²⁶ The spectrum of the ^{57}Fe -labeled $[2\text{Fe}]_H$ site can be analyzed assuming two nonequivalent Fe sites. A small amount of an Fe(II) impurity is apparent as well. The data can be fitted assuming a slight nonequivalence either more pronounced in the quadrupole splitting (simulation 1, Figure 4B) or in the isomer shift (simulation 2, Figure S5). Simulation 1 (Figure 4B) is slightly favored. Taking into account the different ligands coordinating the two irons one would expect clear differences in quadrupole splitting whereas the isomer shift is relatively insensitive to electron density differences for low valence iron centers.²⁷ Simulation 1 is characterized by the isomer shifts $\delta 1(1) = 0.16 \text{ mm/s}$, $\delta 1(2) = 0.08 \text{ mm/s}$ and quadrupole splittings of

D

DOI: 10.1021/jacs.5b03270
J. Am. Chem. Soc. XXXX, XXX, XXX-XXX

$\Delta E_{Q1}(1) = 0.89$ mm/s, $\Delta E_{Q1}(2) = 0.55$ mm/s. The parameters of all simulations can be found in Table S2 in the SI. The fitted Mössbauer parameters are not identical to those obtained previously by Pereira et al. for DvH ($\delta 1(1) = 0.17$ mm/s, $\delta 1(2) = 0.13$ mm/s and $\Delta E_{Q1}(1) = 0.70$ mm/s, $\Delta E_{Q1}(2) = 0.65$ mm/s, see also Table S2), but lie in the same range that is consistent with low-spin iron in a low oxidation state. The slight differences between the parameters obtained in this work and those by Pereira et al. could originate from the lower accuracy in the latter study caused by the overlapping F-cluster signals but it is also possible that the H-cluster of [FeFe] H_2 ases in different organisms (DvH vs HydA1) slightly different electronic structures. To verify this, DvH could be matured using the method described here to obtain a Mössbauer spectrum from the selectively labeled $[2Fe]_H$ site. This would also pave the way to study in detail the elusive “inactive” oxidation states in DvH H_{ox} -air and H_{trans} as well as the “regular” active oxidation states H_{ox} and H_{red} .

NRVS Characterization. The $[^{57}Fe]_H$ -HydA1 H_{ox} -CO sample was also analyzed by nuclear resonance vibrational spectroscopy (NRVS). This technique is exclusively responsive to vibrations affecting the ^{57}Fe site. Previous attempts to record NRVS spectra of [FeFe] H_2 ase (CpI)¹¹ were hampered by signals from other ^{57}Fe labeled components, and not purely originating from the $[2Fe]_H$ subcluster (see Figure 6). In this study, NRVS spectra of $(Et_4N)_2[^{57}Fe_2(adt)(CN)_2(CO)_4]^{2-}$ and $[^{57}Fe]_H$ HydA1 H_{ox} -CO were obtained (Figure 5). The NRVS

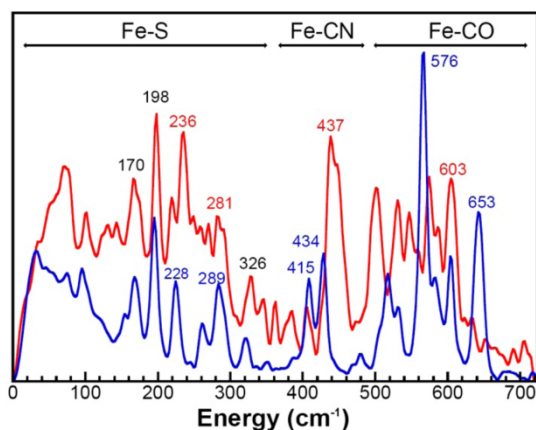


Figure 5. NRVS spectrum of $[^{57}Fe]_H$ HydA1 H_{ox} -CO (red) and the precursor $[^{57}Fe_2(adt)(CN)_2(CO)_4]^{2-}$ (blue). The peaks labeled in black are the same energy ± 2 cm^{-1} in both spectra.

spectrum of the precursor displays intense bands in the regions assigned to Fe-CO stretching and Fe-C-O bending (six bands between 490 and 650 cm^{-1}) and the Fe-CN region (two bands between 400 and 500 cm^{-1}).^{28,29} Comparing the spectrum of the precursor to that for the HydA1 H_{ox} -CO spectrum, one can clearly see that the Fe-C bands are strongly affected, with Fe-CO modes being (on average) red-shifted and Fe-CN modes being blue-shifted. The Fe-CO/-CN shift is consistent with major changes in the primary coordination sphere of the Fe centers upon insertion into the enzyme and conversion to H_{ox} -CO.

The notable band at 653 cm^{-1} is assigned as having significant contributions from a diequatorial $Fe(CO)_2$ stretch—

bend by comparison with assignments of previous model complexes.^{29–31} This band is absent in the $[^{57}Fe]_H$ HydA1 H_{ox} -CO spectrum as there are no longer two CO ligands in the basal positions of either iron center.³¹ The high intensity of the Fe-CO band at 576 cm^{-1} in the $[^{57}Fe_2(adt)(CN)_2(CO)_4]^{2-}$ spectrum is due to the high symmetry of this complex.

When comparing the low energy portion of the two spectra, it is clear that the bands at 170, 198, and 326 cm^{-1} are largely unmoved and there are only minor shifts for other bands in the Fe-S region. This is an indication that there is little change in the Fe-S geometry upon incorporation of the precursor into the enzyme. A common feature of the NRVS of $[4Fe-4S]$ clusters are bands due to Fe-S bending and breathing at 150 cm^{-1} .³⁰ The absence of any strong band at 150 cm^{-1} demonstrates that there is no significant ^{57}Fe incorporation into the $[4Fe-4S]_H$ cluster, verifying the results from the Mössbauer spectroscopy. Further discussion of bands and their assignments can be found in the Supporting Information.

The benefits of the selective labeling by the artificial maturation process are illustrated also by the NRVS measurements. The previously reported NRVS spectrum was recorded on CpI, which was only partially labeled by incubation/activation of the ^{56}Fe -labeled inactive apo protein with ^{57}Fe -enriched maturation proteins (Figure 6).¹¹ The CpI spectrum

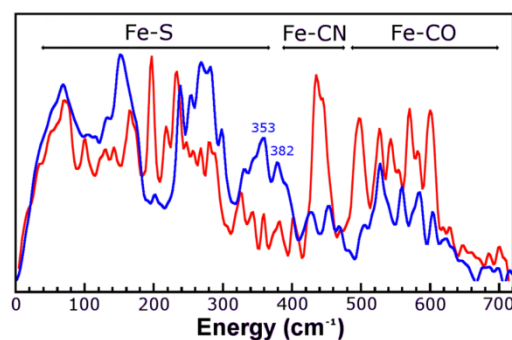


Figure 6. NRVS spectrum of HydA1 H_{ox} -CO of this work (red) and CpI from previous NRVS on hydrogenase (mixed states, blue).¹¹ The assignments are not pure vibrational modes.

has characteristic features at 353 and 382 cm^{-1} in the Fe-S region (300–400 cm^{-1}) assigned to Fe-S bands of oxidized $[4Fe-4S]^{2+}$ clusters. These bands are indicative of unselective labeling of a $[4Fe-4S]$ cluster. For the $[^{57}Fe]_H$ HydA1 H_{ox} -CO spectrum, only low intensity features are present in this region. Selective labeling is also evident in a notable increase in the intensity of the Fe-CN and Fe-CO signals in the 400–600 cm^{-1} region.

CONCLUSIONS

In summary, the work demonstrates the selective ^{57}Fe -labeling of the HydA1 enzyme at both the $[2Fe]_H$ subunit and the subcluster $[4Fe-4S]_H$. The route to ^{57}Fe -labeled iron carbonyls is described using only conventional Schlenk techniques. The method is clearly adaptable to labeling of other derivatives, perhaps other hydrogenases, and their synthetic analogues.³² Focusing on the protein prepared in the H_{ox} -CO state, all spectroscopic measurements confirm the selectivity of the labeling.

E

DOI: 10.1021/jacs.5b03270
J. Am. Chem. Soc. XXXX, XXX, XXX–XXX

The ^{57}Fe hyperfine interactions from the $[2\text{Fe}]_{\text{H}}$ and $[4\text{Fe-4S}]_{\text{H}}$ subclusters in HydA1 obtained from HYSCORE and ENDOR spectroscopies are consistent with those obtained earlier from the H-cluster of the H_2 ase DdH although slight species dependent variations were observed. The overall electronic structures of $\text{H}_{\text{ox}}\text{-CO}$ of DdH and HydA1 seem therefore virtually identical. The Mössbauer parameters from the $[2\text{Fe}]_{\text{H}}$ subsite in HydA1 revealed an intrinsic ambiguity (i.e., two equivalent combinations of isomer shift and quadrupole splitting) that was not detected in earlier studies on DvH.

NRVS analysis demonstrated that through this selective ^{57}Fe labeling the intensity of signals from the key $[2\text{Fe}]_{\text{H}}$ subunit can be improved significantly. This improvement opens up the possibility of new modes involving the bridging CO, hydrides, or Fe–Fe interactions being identified. This future effort would require suitable isotopic labeling experiments of other atoms of the $[2\text{Fe}]_{\text{H}}$ subunit and complementary simulations. These labeling experiments are facilitated by the frugal use of common reagents in this synthetic method, which allows easy substitution for their isotopically labeled counterparts $^{34}\text{S}_8$, ^{13}CO , and $^{13}\text{CN}^-$.³³ Such isotope labeling of atoms bound directly to ^{57}Fe will facilitate assignment of the NRVS spectrum of catalytically significant states.

Further work is underway to spectroscopically characterize the “active” states of the enzyme, specifically H_{ox} , H_{red} , and H_{red} . Through selective labeling the overlapping ^{57}Fe ENDOR spectra of the two subclusters in H_{ox} ^{13,34} can now be disentangled. The effects of, e.g., the bridging CO ligand and the exchange coupling to the $[4\text{Fe-4S}]_{\text{H}}$ subcluster can now for the first time be studied on selectively labeled H-clusters. In addition, also “inactive” precursors $[\text{Fe}_2(\text{pdt})(\text{CN})_2(\text{CO})_4]^{2-}$ (pdt^{2-} = propanedithiolate = $[(\text{SCH}_2)_2\text{CH}_2]^{2-}$) and $[\text{Fe}_2(\text{odt})(\text{CN})_2(\text{CO})_4]^{2-}$ (odt^{2-} = oxadithiolate = $[(\text{SCH}_2)_2\text{O}]^{2-}$) will be studied in ^{57}Fe labeled form as a product of this work. Although largely inactive, these variants show “trapped” intermediates that may be related to the catalytic cycle.³⁵

EXPERIMENTAL SECTION

General Considerations. Unless otherwise indicated, reactions were conducted using standard Schlenk techniques or in a glovebox under an N_2 atmosphere at room temperature with stirring. Synthesis of $^{57}\text{FeBr}_2$ from ^{57}Fe ,³⁶ $^{57}\text{Fe}_2(\text{adt})(\text{CO})_6$ from $^{57}\text{Fe}_2\text{S}_2(\text{CO})_6$,³⁷ and $(\text{Et}_4\text{N})_2[\text{Fe}_2(\text{adt})(\text{CN})_2(\text{CO})_4]$ from $^{57}\text{Fe}_2(\text{adt})(\text{CO})_6$,¹⁴ were achieved by modification of literature procedures for the equivalent unlabeled complexes. Details can be found in the Supporting Information.

Synthesis of $^{57}\text{Fe}_2\text{S}_2(\text{CO})_6$. A potassium anthracene solution was prepared by stirring thinly sliced potassium metal (1.41 g, 36.2 mmol) and anthracene (6.44 g, 36.1 mmol) in THF (120 mL) overnight using a glass covered stir bar to give a deep blue solution of potassium anthracene. In a separate flask $^{57}\text{FeBr}_2$ (1.82 g, 8.40 mmol) was also stirred overnight in THF (100 mL) giving a suspension of yellow solid in a pale orange solution. Both solutions were chilled to -77°C , and the $^{57}\text{FeBr}_2$ solution was cannula transferred into the potassium anthracene solution over a period of 10 min. The solution was allowed to warm to room temperature over a period of 5 h, resulting in a color change from blue to very dark red/brown indicating the formation of $\text{K}[\text{Fe}(\text{anthracene})_2]$. The solution was then filtered through Celite (the solution contains very fine particles that easily block glass frits and even block up Celite if too much pressure is applied). The volume of the filtrate was reduced to ~ 150 mL under a vacuum. The solution was cooled to -77°C , and the headspace was replaced by an atmosphere of CO. The solution was then allowed to warm to room temperature

over a period of 10 h under a constant 1.05 atm of CO. Once warmed to room temperature the solution is a dark color with a significant amount of pale precipitate. All solvent was removed to give a brown solid containing the desired $\text{K}_2\text{Fe}(\text{CO})_4$. This solid was cooled to -77°C , and treated with MeOH (50 mL) added over the course of 20 min. The initially brown/green solution changed to dark red as the mixture was warmed to room temperature over the course of an hour, indicating the formation of $\text{KHF}(\text{CO})_4$. The solution was filtered through Celite, and any remaining solid was washed with MeOH. The volume of the solution was reduced to ~ 10 mL, with the aim of keeping as much of the red color in solution, not coprecipitating with the colorless solids, which precipitate upon this volume reduction. The solution was cooled to 0°C , and solid potassium hydroxide (1.30 g, 23.2 mmol) was added against a positive pressure of argon, followed by the addition of degassed water (15 mL). After 5 min of stirring at 0°C , elemental sulfur (1.29 g, 40.2 mmol) was added directly against a flow of argon. The mixture was stirred at 0°C for 1.5 h before degassed water (20 mL) and hexane (50 mL) were added. Solid NH_4Cl (3.22 g, 60.2 mmol) was added against a flow of argon, and a needle with attached bubbler was attached to the flask and the solution stirred for 16 h. Subsequent steps were performed in air. Stirring was ceased and the red hexane layer was decanted and reserved. The remaining aqueous solution was extract with hexane (4×20 mL) until no red color remained in the hexane layer, with the extracts then added to the previously reserved solution. The solution was passed through a short silica plug (2 cm) and the filtrate then evaporated on a rotary evaporator ($\text{Fe}_2\text{S}_2(\text{CO})_6$ readily sublimates under oil pump vacuum at room temperature). An extract of the resulting red oil in hexane (3 mL) was chromatographed on a silica gel column (2 cm \times 30 cm), eluting with hexane. The first orange band was identified as $^{57}\text{Fe}_2\text{S}_2(\text{CO})_6$ (180 mg, 0.520 mmol, 12.4% from $^{57}\text{FeBr}_2$) and the second dark red band as $^{57}\text{Fe}_3\text{S}_2(\text{CO})_9$ (60.8 mg, 4.5% from $^{57}\text{FeBr}_2$). The preparation was repeated with improved handling giving an improved yield of $^{57}\text{Fe}_2\text{S}_2(\text{CO})_6$ (371 mg, 1.07 mmol, 25.4% from $^{57}\text{FeBr}_2$) and a small amount of $^{57}\text{Fe}_3\text{S}_2(\text{CO})_9$ (15 mg, 0.031 mmol, 1.1% from $^{57}\text{FeBr}_2$). $^{57}\text{Fe}_2\text{S}_2(\text{CO})_6$: IR (pentane): $\nu_{\text{C}=\text{O}}$ = 2085 (m), 2045 (s), 2008 (s), 1993 (w); ^{13}C NMR (600 MHz, d_6 -Toluene): δ 208.66 (d, $J_{\text{C}-\text{Fe}}$ = 28.3 Hz, CO); $^{57}\text{Fe}_3\text{S}_2(\text{CO})_9$: IR (pentane): $\nu_{\text{C}=\text{O}}$ = 2063 (s), 2045 (s), 2024(s), 2008 (m), 1988 (w); ^{13}C NMR (600 MHz, d_6 -Toluene): δ 209.23 (d, $J_{\text{C}-\text{Fe}}$ = 26.3 Hz, CO). MS ESI- (m/z) 515.6 ($(\text{Et}_4\text{N})[\text{Fe}_2(\text{adt})(\text{CN})_2(\text{CO})_4]^-$) IR (acetonitrile): $\nu_{\text{C}=\text{N}}$ = 2075 (m) $\nu_{\text{C}=\text{O}}$ = 1968 (s), 1924 (s), 1891 (s), 1873 (sh).

Preparation of ^{57}Fe -Labeled HydA1. All samples were handled strictly anaerobically. All buffers were carefully degassed. Unmaturated HydA1 was prepared as described by Kuchenreuther et al.³⁸ In order to selectively label the $[4\text{Fe-4S}]_{\text{H}}$ cluster with ^{57}Fe , unmaturated HydA1 was treated with 6 M guanidinium chloride in 100 mM Tris/HCl pH, 8.0, 20 mM EDTA to have a final concentration of 100–200 μM protein. After 30 min of incubation, samples were buffer exchanged into 100 mM Tris/HCl, pH 8.0, 150 mM NaCl using PD10 desalting columns (GE Healthcare). For the reconstitution reaction, a protocol similar to literature procedures was used.³⁹ $^{57}\text{FeCl}_3$ was prepared from ^{57}Fe powder by dissolving in concentrated hydrochloric acid, evaporation of the solvent and resolubilizing in distilled water. The protein solution (50–70 μM) was incubated with 5 mM DDT for 5 min and slightly stirred. 10-fold excess of $^{57}\text{FeCl}_3$ solution was added stepwise to the reaction mixture within 20 min. Thereafter, 10-fold excess of an aqueous solution of Na_2S was added stepwise. The reaction mixture turned from reddish (after addition of $^{57}\text{FeCl}_3$) to a brownish color typical for unaturated HydA1. After removing excess of ions using PD10 desalting columns, samples were concentrated and kept frozen until use.

In order to selectively label unaturated HydA1 on the $[2\text{Fe}]_{\text{H}}$ subcluster, it was incubated with a 2-fold excess of $(\text{Et}_4\text{N})_2[\text{Fe}_2(\text{adt})(\text{CN})_2(\text{CO})_4]$ following recent protocols.^{8,10} In order to obtain the $\text{H}_{\text{ox}}\text{-CO}$ inhibited state, samples were first oxidized with thionine and then flushed with CO for 20 min (Figure S2, SI). The redox states of all samples were verified using FT-IR spectroscopy.

EPR Analysis. Field swept Q-band EPR spectra were recorded in the pulsed mode using FID detection after a 1 μs $\pi/2$ excitation pulse.

F

DOI: 10.1021/jacs.5b03270
J. Am. Chem. Soc. XXXX, XXX, XXX–XXX

After a pseudomodulation transformation, the spectra obtained in this way are comparable to those using CW EPR.⁴⁰

Electron nuclear double resonance (ENDOR) was used to study the ⁵⁷Fe hyperfine interactions. In this investigation the Davies ENDOR sequence was used: $[\pi]-t_{d1}-[RF]-t_{d2}-[\pi/2]-\tau-[\pi]-\tau-(ESE)$.^{41,42} The excitation of nuclear spin transitions is detectable through an increase in the inverted ESE intensity. The microwave preparation pulse was set to 140 ns, whereas the length of the radiofrequency (RF) pulse was 45 μ s and the shot repetition time 0.8 ms.

Q-band hyperfine sublevel correlation spectroscopy (HYSCORE) experiments were performed using the standard HYSCORE pulse sequence: $[\pi/2]-\tau-[\pi/2]-t_1-[\pi]-t_2-[\pi/2]-\tau-(ESE)$.^{42,43} The length of the microwave $[\pi/2]$ and $[\pi]$ pulses was adjusted to the maximum available microwave power (3 W). The delay between the first two pulses (τ) was 352 ns. The starting t_1 and t_2 delays in all measurements were 100 ns and were changed by a step of 16 ns. To suppress the effect of unwanted echoes, a four step phase cycling of the microwave pulses was used.

Q-band experiments were performed on a Bruker ELEXYS E580 spectrometer with a SuperQ-FT microwave bridge and a home-built resonator described earlier.⁴⁴ Cryogenic temperatures (20 K) were obtained by an Oxford CF935 flow cryostat. ENDOR experiments were performed using the random (stochastic) acquisition technique and making use of a 300W ENI 300 L RF amplifier. A Trilithic H4LE35-3-AA-R high-power low pass filter (cut off frequency around 35 MHz) was used to suppress the "harmonics" of the ¹H ENDOR signals.

All the simulations were performed in an EasySpin based program written in the MATLAB environment.⁴⁵ ENDOR spectra were simulated using the "salt" routine and the frequency domain calculations of HYSCORE spectra were simulated using the "saffron" routine. Signals corresponding to the different nuclei were simulated separately in order to reduce computing time.

Mössbauer Analysis. Mössbauer spectra were recorded on a conventional spectrometer with alternating constant acceleration of the γ -source. The sample temperature was maintained constant in an Oxford Instruments Variox cryostat. Isomer shifts are quoted relative to iron metal at 300 K. Mössbauer spectra were collected for frozen aqueous solution samples (1–2 mM, 650 μ L) at 160 K and fitted using the program MFIT (written by Eckhard Bill, Max Planck Institute for Chemical Energy Conversion) with Lorentzian doublets.

NRVS. Nuclear resonance vibrational spectroscopy (NRVS) of $[2^{57}\text{Fe}]_{\text{H}} \text{HydA1 H}_{\text{ox}}\text{-CO}$ and the precursor $(\text{Et}_4\text{N})_2[\text{Fe}_2(\text{adt})(\text{CN})_2(\text{CO})_4]$ were measured with a coldfinger helium cryostat maintained at 10 K. The real sample temperatures were obtained by the imbalance of the spectra and ranged from 40–60 K. NRVS measurement was performed at Spring-8, BL09XU and BL19LXU using C beam mode. A high heat load LN₂-cooled Si(1,1,1) double crystal monochromators followed by a high resolution monochromators of Ge(4,2,2) and two Si(9,7,5) were used to achieve a 0.8 meV energy resolution. The delayed nuclear and K α fluorescence were measured with a 2 \times 2 APD array, and processed with the associated electronics.

■ ASSOCIATED CONTENT

📄 Supporting Information

Spectra and preparative details. The Supporting Information is available free of charge on the ACS Publications website at DOI: 10.1021/jacs.5b03270.

■ AUTHOR INFORMATION

Corresponding Authors

*spjcramer@ucdavis.edu
*wolfgang.lubitz@cec.mpg.de
*rauchfuz@illinois.edu

Author Contributions

#R.G.-W. and J.F.S. contributed equally to this work.

Notes

The authors declare no competing financial interest.

■ ACKNOWLEDGMENTS

We thank Annika Gurowski and Agnes Stoer for their excellent technical assistance, Eckhard Bill and Bernd Mienert for their help with the Mössbauer spectroscopy, and Lars Lauterbach, Leland Gee, Yoshitaka Yoda and Kenji Tamasaku for their expertise in NRVS. This project was supported by the National Institutes of Health (GM061153, GM-65440), the Max-Planck Society, the Deutsche Forschungsgemeinschaft (DIP project LU315/17–1), and US Department of Education (CFDA-84.200A). The NRVS experiments were performed at SPRING-8 BL09XU (JASRI proposed no.2014B1032) and BL19LXU (RIKEN proposal no 20140033).

■ REFERENCES

- (1) Frey, M. *ChemBioChem* **2002**, *3*, 153.
- (2) Happe, T.; Naber, J. D. *Eur. J. Biochem.* **1993**, *214*, 475.
- (3) Swanson, K. D.; Ratzloff, M. W.; Mulder, D. W.; Artz, J. H.; Ghose, S.; Hoffman, A.; White, S.; Zadovornyy, O. A.; Broderick, J. B.; Bothner, B.; King, P. W.; Peters, J. W. *J. Am. Chem. Soc.* **2015**, *137*, 1809. Mulder, D. W.; Ratzloff, M. W.; Bruschi, M.; Greco, C.; Koonce, E.; Peters, J. W.; King, P. W. *J. Am. Chem. Soc.* **2014**, *136*, 15394. Knörzer, P.; Silakov, A.; Foster, C. E.; Armstrong, F. A.; Lubitz, W.; Happe, T. *J. Biol. Chem.* **2012**, *287*, 1489.
- (4) Peters, J. W.; Broderick, J. B. *Annu. Rev. Biochem.* **2012**, *81*, 429. Shepard, E. M.; Mus, F.; Betz, J. N.; Byer, A. S.; Duffus, B. R.; Peters, J. W.; Broderick, J. B. *Biochemistry* **2014**, *53*, 4090.
- (5) Happe, T.; Kaminski, A. *Eur. J. Biochem.* **2002**, *269*, 1022. Mulder, D. W.; Boyd, E. S.; Sarma, R.; Lange, R. K.; Endrizzi, J. A.; Broderick, J. B.; Peters, J. W. *Nature* **2010**, *465*, 248.
- (6) Nicolet, Y.; de Lacey, A. L.; Vernede, X.; Fernandez, V. M.; Hatchikian, E. C.; Fontecilla-Camps, J. C. *J. Am. Chem. Soc.* **2001**, *123*, 1596.
- (7) Lemon, B. J.; Peters, J. W. *Biochemistry* **1999**, *38*, 12969. Berggren, G.; Adamska, A.; Lambert, C.; Simmons, T. R.; Esselborn, J.; Atta, M.; Gambarelli, S.; Mouesca, J. M.; Reijerse, E.; Lubitz, W.; Happe, T.; Artero, V.; Fontecave, M. *Nature* **2013**, *499*, 66.
- (8) Esselborn, J.; Lambert, C.; Adamska-Venkatesh, A.; Simmons, T.; Berggren, G.; Noth, J.; Siebel, J.; Hemschemeier, A.; Artero, V.; Reijerse, E.; Fontecave, M.; Lubitz, W.; Happe, T. *Nat. Chem. Biol.* **2013**, *9*, 607.
- (9) Adamska-Venkatesh, A.; Simmons, T. R.; Siebel, J. F.; Artero, V.; Fontecave, M.; Reijerse, E.; Lubitz, W. *Phys. Chem. Chem. Phys.* **2015**, *17*, 5421.
- (10) Siebel, J. F.; Adamska-Venkatesh, A.; Weber, K.; Rumpel, S.; Reijerse, E.; Lubitz, W. *Biochemistry* **2015**, *54*, 1474.
- (11) Kuchenreuther, J. M.; Guo, Y.; Wang, H.; Myers, W. K.; George, S. J.; Boyke, C. A.; Yoda, Y.; Alp, E. E.; Zhao, J.; Britt, R. D.; Swartz, J. R.; Cramer, S. P. *Biochemistry* **2012**, *52*, 818.
- (12) Kuchenreuther, J. M.; George, S. J.; Grady-Smith, C. S.; Cramer, S. P.; Swartz, J. R. *PLoS One* **2011**, *6*, e20346.
- (13) Silakov, A.; Reijerse, E. J.; Albracht, S. P. J.; Hatchikian, E. C.; Lubitz, W. *J. Am. Chem. Soc.* **2007**, *129*, 11447.
- (14) Li, H.; Rauchfuss, T. B. *J. Am. Chem. Soc.* **2002**, *124*, 726.
- (15) Wildermuth, E.; Stark, H.; Friedrich, G.; Ebenhöch, F. L.; Kühborth, B.; Silver, J.; Rituper, R. In *Ullmann's Encyclopedia of Industrial Chemistry*; Wiley-VCH Verlag GmbH & Co. KGaA: Weinheim, 2000.
- (16) Seel, F. In *Handbook of Preparative Inorganic Chemistry*, 2nd ed.; Brauer, G., Ed.; Academic Press: New York, 1965; p 1741.
- (17) Bernard, B.; Daniels, L.; Hance, R.; Hutchinson, B. *Synth. React. Inorg. Met.-Org. Chem.* **1980**, *10*, 1.
- (18) Rameshkumar, C.; Periasamy, M. *Organometallics* **2000**, *19*, 2400. Devasagayaraj, A.; Periasamy, M. *Transition Metal Chem.* **1991**, *16*, 503.

G

DOI: 10.1021/jacs.5b03270
J. Am. Chem. Soc. XXXX, XXX, XXX–XXX

- (19) Brennessel, W. W.; Jilek, R. E.; Ellis, J. E. *Angew. Chem., Int. Ed.* **2007**, *46*, 6132.
- (20) Brennessel, W. W. PhD. Dissertation, University of Minnesota, 2009.
- (21) Brandt, P. F.; Lesch, D. A.; Stafford, P. R.; Rauchfuss, T. B. *Inorg. Synth.* **1997**, *31*, 112.
- (22) Mack, A. E.; Rauchfuss, T. B. *Inorg. Synth.* **2011**, *35*, 142.
- (23) Popescu, C. V.; Münck, E. *J. Am. Chem. Soc.* **1999**, *121*, 7877.
- (24) Rusnak, F. M.; Adams, M. W. W.; Mortenson, L. E.; Münck, E. *J. Biol. Chem.* **1987**, *262*, 38.
- (25) Pereira, A. S.; Tavares, P.; Moura, I.; Moura, J. J. G.; Huynh, B. H. *J. Am. Chem. Soc.* **2001**, *123*, 2771.
- (26) Middleton, P.; Dickson, D. P. E.; Johnson, C. E.; Rush, J. D. *Eur. J. Biochem.* **1978**, *88*, 135. Antonkine, M. L.; Koay, M. S.; Epel, B.; Breitenstein, C.; Gupta, O.; Gärtner, W.; Bill, E.; Lubitz, W. *Biochim. Biophys. Acta* **2009**, *1787*, 995. Beinert, H.; Holm, R. H.; Münck, E. *Science* **1997**, *277*, 653.
- (27) Güttlich, P.; Bill, E.; Trautwein, A. X. *Mössbauer Spectroscopy and Transition Metal Chemistry*; Springer: Berlin, 2011.
- (28) Kamali, S.; Wang, H.; Mitra, D.; Ogata, H.; Lubitz, W.; Manor, B. C.; Rauchfuss, T. B.; Byrne, D.; Bonnefoy, V.; Jenney, F. E.; Adams, M. W. W.; Yoda, Y.; Alp, E.; Zhao, J.; Cramer, S. P. *Angew. Chem., Int. Ed.* **2013**, *52*, 724.
- (29) Galinato, M. G. I.; Whaley, C. M.; Lehnert, N. *Inorg. Chem.* **2010**, *49*, 3201.
- (30) Kuchenreuther, J. M.; Guo, Y.; Wang, H.; Myers, W. K.; George, S. J.; Boyke, C. A.; Yoda, Y.; Alp, E. E.; Zhao, J.; Britt, R. D.; Swartz, J. R.; Cramer, S. P. *Biochemistry* **2013**, *52*, 818.
- (31) Guo, Y.; Wang, H.; Xiao, Y.; Vogt, S.; Thauer, R. K.; Shima, S.; Volkens, P. I.; Rauchfuss, T. B.; Pelmeshnikov, V.; Case, D. A.; Alp, E. E.; Sturhahn, W.; Yoda, Y.; Cramer, S. P. *Inorg. Chem.* **2008**, *47*, 3969.
- (32) Tard, C.; Pickett, C. J. *Chem. Rev.* **2009**, *109*, 2245.
- (33) Gloaguen, F.; Lawrence, J. D.; Schmidt, M.; Wilson, S. R.; Rauchfuss, T. B. *J. Am. Chem. Soc.* **2001**, *123*, 12518.
- (34) Kuchenreuther, J. M.; Myers, W. K.; Suess, D. L. M.; Stich, T. A.; Pelmeshnikov, V.; Shiigi, S. A.; Cramer, S. P.; Swartz, J. R.; Britt, R. D.; George, S. J. *Science* **2014**, *343*, 424.
- (35) Adamska-Venkatesh, A.; Krawietz, D.; Siebel, J.; Weber, K.; Happe, T.; Reijerse, E.; Lubitz, W. *J. Am. Chem. Soc.* **2014**, *136*, 11339.
- (36) Winter, G.; Thompson, D. W.; Loehe, J. R. In *Inorganic Synthesis*; John Wiley & Sons, Inc.: Hoboken, NJ, 2007; p 99.
- (37) Stanley, J. L.; Rauchfuss, T. B.; Wilson, S. R. *Organometallics* **2007**, *26*, 1907.
- (38) Kuchenreuther, J. M.; Grady-Smith, C. S.; Bingham, A. S.; George, S. J.; Cramer, S. P.; Swartz, J. R. *PLoS One* **2010**, *5*, e15491.
- (39) Rubach, J. K.; Brazzolotto, X.; Gaillard, J.; Fontecave, M. *FEBS Lett.* **2005**, *579*, 5055. Mulder, D. W.; Ortillo, D. O.; Gardenghi, D. J.; Naumov, A. V.; Ruebush, S. S.; Szilagy, R. K.; Huynh, B.; Broderick, J. B.; Peters, J. W. *Biochemistry* **2009**, *48*, 6240.
- (40) Hyde, J. S.; Pasenkiewicz-Gierula, M.; Jesmanowicz, A.; Antholine, W. E. *Appl. Magn. Reson.* **1990**, *1*, 483.
- (41) Davies, E. R. *Phys. Lett. A* **1974**, *47*, 1.
- (42) Schweiger, A.; Jeschke, G. *Principles of Pulse Electron Paramagnetic Resonance*; Oxford University Press: Oxford, 2001.
- (43) Höfer, P.; Grupp, A.; Nebenführ, H.; Mehring, M. *Chem. Phys. Lett.* **1986**, *132*, 279. Shane, J. J.; Höfer, P.; Reijerse, E. J.; de Boer, E. J. *Magn. Reson.* **1992**, *99*, 596.
- (44) Reijerse, E.; Lendzian, F.; Isaacson, R.; Lubitz, W. *J. Magn. Reson.* **2012**, *214*, 237.
- (45) Stoll, S.; Schweiger, A. *J. Magn. Reson.* **2006**, *178*, 42.

4.4.2 Supporting information

Spectroscopic investigations of [FeFe] hydrogenase matured with $[\text{}^{57}\text{Fe}_2(\text{adt})(\text{CN})_2(\text{CO})_4]^{2-}$

Ryan Gilbert-Wilson, Judith F. Siebel, Agnieszka Adamska-Venkatesh, Cindy C. Pham, Edward Reijerse, Hongxin Wang, Stephen P. Cramer, Wolfgang Lubitz, Thomas B. Rauchfuss

Experimental details

General considerations. Unless otherwise indicated, reactions were conducted using standard Schlenk techniques or in a glovebox under an N_2 atmosphere at room temperature with stirring. Elemental sulfur, 37% solution of formaldehyde, potassium metal, anthracene, tetraethyl ammonium cyanide and ammonium chloride were obtained from Aldrich and used as received. Cylinders of carbon monoxide were obtained from SJ Smith and used as received. ^{57}Fe metal powder was purchased from Isoflex and used as received. ^{13}C (150.6 MHz) spectra were acquired in a Varian UNITY Inova 600. ESI-MS data for compounds were acquired using a Waters Micromass Quattro II spectrometer.

Synthesis of $^{57}\text{FeBr}_2$: $^{57}\text{FeBr}_2$ was synthesized by modification of a literature procedure for FeBr_2 synthesis.¹ ^{57}Fe metal (501 mg, 8.80 mmol) and a small stirrer bar were transferred to a Schlenk flask under an argon atmosphere. A septa and a needle with attached bubbler were attached to the flask. Fresh concentrated hydrobromic acid (48%, 2.5 mL) was then transferred to the flask by syringe resulting in hydrogen evolution. Once hydrogen evolution had slowed the septa was replaced with a glass stopper and the flask was heated to 80 °C with stirring for 2 hours. The solution was then allowed to cool to room temperature and methanol (5 mL) was added. The solvents were then removed under vacuum. The remaining white/yellow solid was heated at 100 °C under a vacuum of 10 torr for 4 hours, with the end point identified as the point when a piece of dry ice applied to the side of the flask did not condense any methanol. Note: Previous tests with FeBr_2 indicated increased temperatures or stronger vacuum led to sublimation of FeBr_2 out of the flask into the attached trap. The flask was allowed to cool to room temperature under vacuum and then moved to the glovebox where the pale yellow solid was collected to yield $^{57}\text{FeBr}_2$ (1.82 g, 8.40 mmol, 95% yield).

Synthesis of $^{57}\text{Fe}_2\text{S}_2(\text{CO})_6$: Description in the main text.

Synthesis of $^{57}\text{Fe}_2(\text{adt})(\text{CO})_6$: $^{57}\text{Fe}_2(\text{adt})(\text{CO})_6$ was synthesized by modification of a literature procedure for $\text{Fe}_2(\text{adt})(\text{CO})_6$ synthesis.²

(a) Aminomethylation reagent. Aminomethylation reagent was prepared fresh before use. Ammonium carbonate (450 mg, 4.68 mmol) was placed under an argon atmosphere, followed by the addition of THF (6 mL). The resulting suspension was stirred and heated to 60 °C, at which point a septa and needle with bubbler were attached to the flask and a 37% solution of formaldehyde was added (5.0 mL, 67 mmol) resulting in significant gas evolution. The resulting clear solution was stirred at 60 °C and then allowed to cool to room temperature.

(b) $^{57}\text{Fe}_2(\text{adt})(\text{CO})_6$. $^{57}\text{Fe}_2\text{S}_2(\text{CO})_6$ (180 mg, 0.524 mmol) in THF (10 mL) was cooled to -77 °C. 1.07 mL of a 1 M solution of LiBEt_3H (1.07 mmol) was then added dropwise, inducing a color change to brown and eventually green. The solution was then allowed to warm to -40 °C and stirred at -40 °C causing a color change to brown/red. The solution was then cooled back to -77 °C and CF_3COOH (85 μL , 1.14 mmol) was added dropwise over a period of 10 minutes resulting in a color change to a lighter red. The solution was then allowed to warm to room temperature and was then cannula transferred into the aminomethylation solution which had been pre-chilled to 0 °C, causing a color change to darker red. The solution was allowed to slowly warm to room temperature and stirred for 12 hours. The solvent was then removed under vacuum to leave a red and white residue. The flask was refilled with argon and dichloromethane (10 mL) was added. From this point manipulations were performed in air. The mixture was sonicated and the red solution decanted. The residue was extracted again with dichloromethane (2 x 10 mL) and all extracts were combined and filtered through celite. The solution was then evaporated under reduced pressure to leave a bright red residue, which was subsequently extracted with a 4:1 mixture of hexane:dichloromethane (3 x 2 mL) and chromatographed on a 2 x 30 cm silica gel column. Elution with hexanes gave an orange first band which was identified by IR spectroscopy as $^{57}\text{Fe}_2\text{S}_2(\text{CO})_6$ (5 mg). Increasing the polarity to 4:1 hexane:dichloromethane gave elution of a red second band which remains unidentified. A further slow shift in the polarity to an eventual concentration of 1:1 hexane:dichloromethane led to elution of a bright red third band which consisted of $^{57}\text{Fe}_2(\text{adt})(\text{CO})_6$ (58.0 mg, 0.149 mmol, 28% yield). IR (pentane): $\nu_{\text{C}=\text{O}}$ = 2076 (s), 2036 (s), 2008 (s), 1990 (s), 1980 (m); ^{13}C NMR (600 MHz, d_8 -Toluene, 60 °C): δ 208.03 (d, $J_{\text{C-Fe}}$ = 26.4 Hz, CO); 45.25 (s, CH_2).

Synthesis of $(\text{Et}_4\text{N})_2[{}^{57}\text{Fe}_2(\text{adt})(\text{CN})_2(\text{CO})_4]$: $(\text{Et}_4\text{N})_2[{}^{57}\text{Fe}_2(\text{adt})(\text{CN})_2(\text{CO})_4]$ was synthesized by modification of a literature procedure for $(\text{Et}_4\text{N})_2[\text{Fe}_2(\text{adt})(\text{CN})_2(\text{CO})_4]$.³ $[\text{NEt}_4][\text{CN}]$ (26.2 mg, 0.168 mmol) was dissolved in acetonitrile (1.5 mL) under a glove box atmosphere. A solution of ${}^{57}\text{Fe}_2(\text{adt})(\text{CO})_6$ (32.6 mg, 0.084 mmol) in acetonitrile (1.5 mL) was then added to the flask with stirring leading to a small amount of CO evolution, once this ceased the flask was sealed and allowed to stir for 10 hours. The solvent was removed under vacuum to give a bright red solid. THF (2 mL) was then added and the mixture thoroughly agitated. The red solid was then collected and washed again with THF (2 mL) and pentane (2 x 3 mL) before drying to yield $(\text{Et}_4\text{N})_2[{}^{57}\text{Fe}_2(\text{adt})(\text{CN})_2(\text{CO})_4]$ (50.1 mg, 0.078 mmol, 93% yield). MS ESI- (m/z) 515.6 ($(\text{Et}_4\text{N})[{}^{57}\text{Fe}_2(\text{adt})(\text{CN})_2(\text{CO})_4]^-$) IR (acetonitrile): $\nu_{\text{C}\equiv\text{N}} = 2075$ (m) $\nu_{\text{C}=\text{O}} = 1968$ (s), 1924 (s), 1891 (s), 1873 (sh).

Mass spectrometry

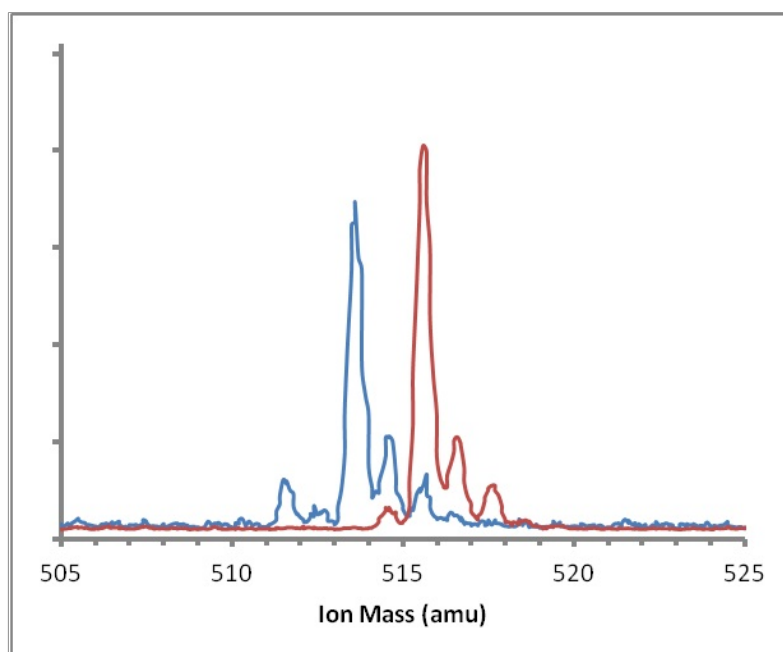


Figure S1. Negative ion mass spectrometry plot of the $(\text{Et}_4\text{N})[\text{Fe}_2(\text{adt})(\text{CN})_2(\text{CO})_4]^-$ (blue) and $(\text{Et}_4\text{N})[{}^{57}\text{Fe}_2(\text{adt})(\text{CN})_2(\text{CO})_4]^-$ (red) ions overlaid.

Negative ion ESI mass spectrometry was used to confirm the successful incorporation of ${}^{57}\text{Fe}$ into $(\text{Et}_4\text{N})_2[{}^{57}\text{Fe}_2(\text{adt})(\text{CN})_2(\text{CO})_4]$. This was achieved through a comparison with the unlabeled cluster $(\text{Et}_4\text{N})_2[\text{Fe}_2(\text{adt})(\text{CN})_2(\text{CO})_4]$. The major ion detected was the tetraethylamine-cluster ion pair with a single negative charge. As can be observed in Figure S1 there is a clear 2 mass unit shift for the labeled cluster vs. the unlabeled cluster,

demonstrating the shift from a sample containing largely ^{56}Fe versus the labeled spectra which contains ^{57}Fe almost exclusively.

^{13}C NMR of ^{57}Fe clusters

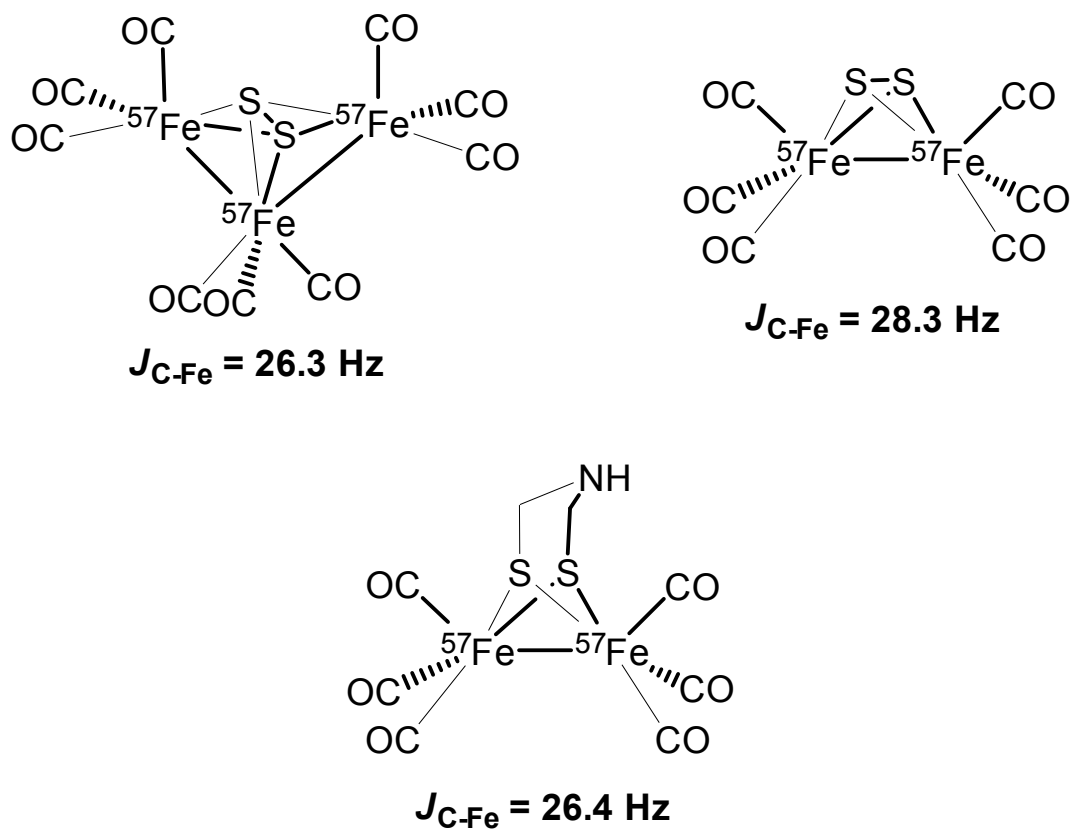


Chart S1. Iron sulfur carbonyl clusters synthesized with $J_{\text{C-Fe}}$ coupling constants.

H_{ox}-CO state preparation

FTIR spectroscopy was used to follow the preparation of the H_{ox}-CO state of HydA1. FTIR measurements were carried out using a Bruker IFS 66v/s FTIR spectrometer equipped with a nitrogen cooled Bruker mercury cadmium telluride (MCT) detector. The spectra were accumulated in the double-sided, forward-backward mode with 1000 scans (14 min) and a resolution of 2 cm⁻¹ at 15 °C. Data processing was facilitated by home written routines in the MATLAB™ programming environment.

The FTIR spectrum obtained from freshly matured HydA1 with [⁵⁷Fe₂(adt)(CN)₂(CO)₄]²⁻ exhibits a mixture of signals originating from all active and CO inhibited redox states (Figure S2B). Upon oxidation of HydA1 with thionine (ratio 1:1) only a mixture of H_{ox} and H_{ox}-CO states is present (Figure S2C) that allows generating a pure H_{ox}-CO state after flushing the sample for 20 minutes with CO gas (Figure S2D).

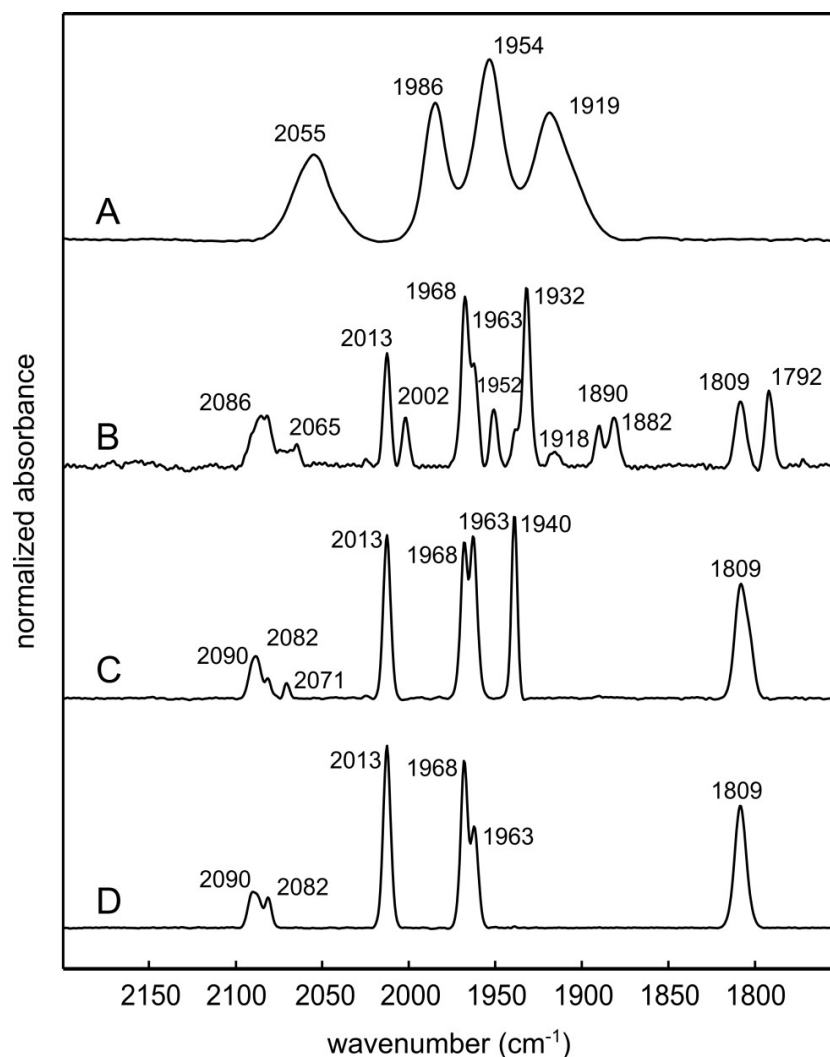


Figure S2. Normalized FTIR spectra recorded for the (Et₄N)₂[⁵⁷Fe₂(adt)(CN)₂(CO)₄] precursor (A) and HydA1 selectively labeled with ⁵⁷Fe at the [2Fe]_H subunit of the H-cluster (B-D) recorded at 15 °C. (B) as obtained from maturation, (C) oxidized with thionine, (D) oxidized with thionine and flushed with CO gas.

Selective ^{57}Fe -labeling of the $[4\text{Fe-4S}]_{\text{H}}$ cluster

For activity measurements, $[\text{Fe}_2(\text{adt})(\text{CN})_2(\text{CO})_4]^{2-}$ was added to reconstituted unmaturred HydA1 as described earlier.⁴ Reconstituted HydA1 matured with $[\text{Fe}_2(\text{adt})(\text{CN})_2(\text{CO})_4]^{2-}$ showed an H_2 oxidation activity of $136 \pm 2 \text{ s}^{-1}$ as observed before for as-isolated HydA1 matured with $[\text{Fe}_2(\text{adt})(\text{CN})_2(\text{CO})_4]^{2-}$.⁴ Figure S3 shows the UV spectrum of as-isolated unmaturred HydA1 before any treatment (blue) and after unfolding (green). Unfolding leads to absence of the broad absorption shoulder from 300–550 nm, clearly showing the absence of any $[4\text{Fe-4S}]_{\text{H}}$ cluster. After reconstitution with $^{57}\text{FeCl}_3$ and Na_2S followed by desalting, the absorption of the $[4\text{Fe-4S}]_{\text{H}}$ cluster is re-established (red). As shown in the Figure S4 the EPR signal of as-isolated unmaturred HydA1 in the presence of sodium dithionate (blue) is characterized by the same g -values as reconstituted unmaturred HydA1 (red) under the same conditions.

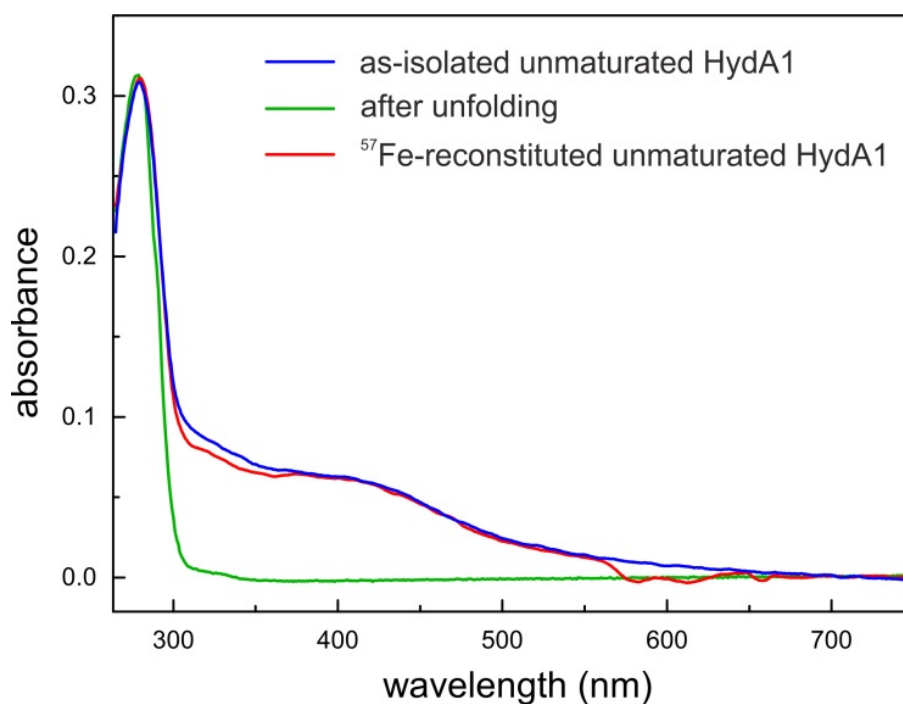


Figure S3. UV spectrum of as-isolated unmaturred HydA1 (blue), after treatment with 6 M guanidium chloride (green) and ^{57}Fe -reconstituted unmaturred HydA1 (red). The spectra were measured in 100 mM Tris/HCl, pH 8.0 and 150 mM NaCl at room temperature using an Ocean Optics USB2000+XR1-ES, equipped with a DH-MINI Deuterium Tungsten Halogen Source.

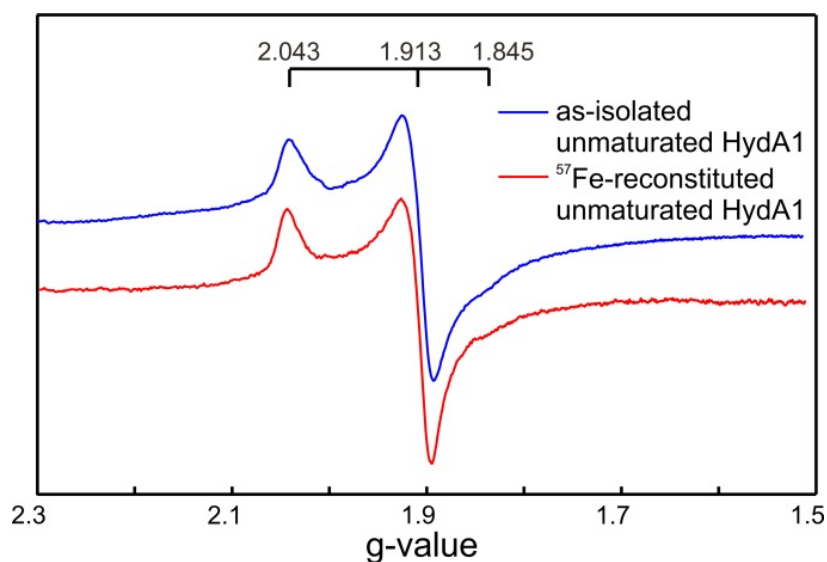


Figure S4. X-band CW EPR spectra of as-isolated unmaturation HydA1 (blue) and reconstituted unmaturation HydA1 (both reduced with 10 mM sodium dithionite). The experimental conditions are as following: 40 dB attenuation, ν_{mw} 9.65 GHz, time constant 40.96 ms, conversion time 81.92 ms, modulation amplitude 0.5 mT, modulation frequency 100 kHz, temperature 10 K.

EPR spectroscopy

Table S1. Principal values of the ^{57}Fe hyperfine tensor of the H-cluster of [FeFe] hydrogenase in the $\text{H}_{\text{ox}}\text{-CO}$ state

	A_1 (MHz)	A_2 (MHz)	A_3 (MHz)	$ A_{\text{iso}} $ (MHz)	α (°)	β (°)	γ (°)	Ref.
Fe^1	2.2	5.5	5.5	4.4 ± 0.3	0	0	0	this work
Fe^2	-1.7	2.8	2.8	1.3 ± 0.3	0	30	90	
Fe^3	29.9	35.1	25.1	30.0 ± 0.2	8	0	0	
Fe^4	31.2	37.3	31.2	33.2 ± 0.2	0	0	0	
Fe^5	28.6	24.7	30.8	28.0 ± 0.2	110	0	0	
Fe^6	23.5	29.6	29.8	27.6 ± 0.2	20	0	0	
Fe_p	-2.2	-4.5	-5.3	4.0 ± 0.1	110	25	44	DdH ⁵
Fe_d	-1.7	+2.1	+2.1	0.8 ± 0.1	0	30	90	
Fe^3	-30.4	-35.0	-35.4	33.6 ± 0.15	90	185	0	
Fe^4	-30.7	-38.4	-34.5	34.5 ± 0.2	90	5	0	
Fe^5	+30.3	+21.8	+27.8	26.7 ± 0.2	6	110	0	
Fe^6	+30.2	+23.8	+26.7	27.0 ± 0.2	76	-93	0	
Fe^1	-6.85	-6.85	-6.85	6.85 ± 2				<i>D. vulgaris</i> ⁶
Fe^2	0	0	0	0				
Pair ¹	-30.95	-38.35	-32.19	33.8 ± 2.7				
Pair ²	+27.94	+29.45	+31.50	29.6 ± 1.35				
Fe^1+Fe^2				(-9.5)				CpI ⁷
Pair1				+25.3				
Pair2				-28.3				

In this work the signs of the hyperfine couplings were not determined. Rows indicated in blue present values assigned to the $[2\text{Fe}]_{\text{H}}$ cluster and in green to the $[4\text{Fe-4S}]_{\text{H}}$ cluster. The most important parameter for comparison $|A_{\text{iso}}|$ is marked in orange.

Mössbauer spectroscopy

When compared to simulation 1 (Figure 4B), simulation 2 (Figure S5) has more similar quadrupole splitting ($\Delta E_Q2(1) = 0.77$ mm/s, $\Delta E_Q2(2) = 0.60$ mm/s) while the difference in isomer shifts ($\delta2(1) = 0.21$ mm/s, $\delta2(2) = 0.04$ mm/s) is larger.

Table S2. Mössbauer parameters

spectrum	component	δ (mm/s)	ΔE_Q (mm/s)	linewidth (mm/s)	relative intensity (%)
Figure 4A. [4^{57}Fe-4S] _H H_{ox}-CO	[4Fe-4S] _H	0.42	1.04	0.57	64
	Fe(II) impurity	1.33	2.80	0.46	8
	FeS impurity	0.60	2.55	2.39	28
Figure 4B. [2^{57}Fe] _H H_{ox}-CO simulation 1	[2Fe] _H Fe1	0.16	0.89	0.41	46
	[2Fe] _H Fe2	0.08	0.55	0.31	46
	Fe(II) impurity	1.32	2.83	0.81	8
Figure S5. [2^{57}Fe] _H H_{ox}-CO simulation 2	[2Fe] _H Fe1	0.21	0.77	0.40	45
	[2Fe] _H Fe2	0.04	0.60	0.31	45
	Fe(II) impurity	1.15	3.18	0.71	10
Figure 4C. simulations [2^{57}Fe] _H + [4^{57}Fe-4S] _H H_{ox}-CO	[2Fe] _H Fe1	0.16	0.89	0.41	16
	[2Fe] _H Fe2	0.08	0.55	0.31	16
	[4Fe-4S] _H	0.42	1.04	0.57	68
Pereira et al.⁶ [4^{57}Fe-4S] _H + [2^{57}Fe] _H H_{ox}-CO	[4Fe-4S] _H 1	0.44	0.95		
	[4Fe-4S] _H 2	0.41	0.98		
	[2Fe] _H Fe1	0.17	0.70		
	[2Fe] _H Fe2	0.13	0.65		

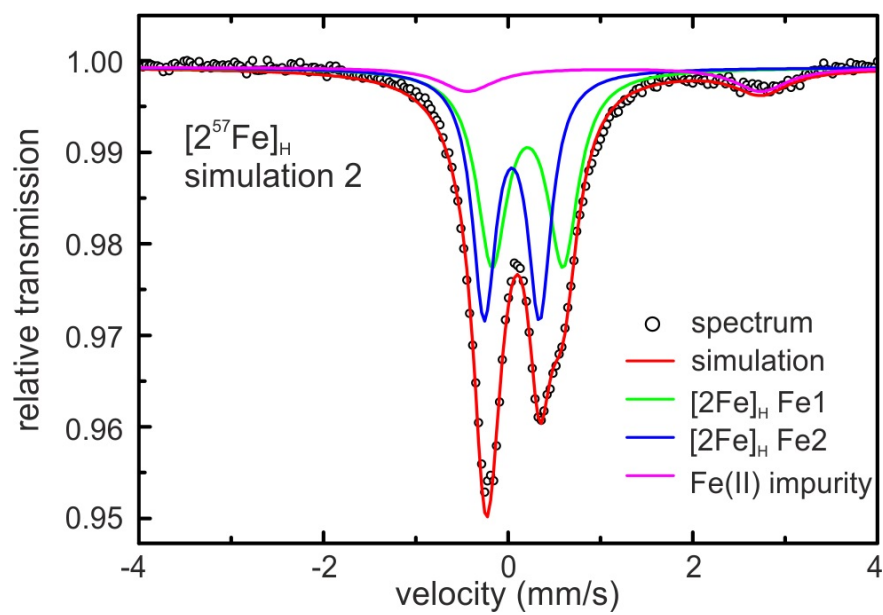


Figure S5. Mössbauer spectrum and simulation of $\text{H}_{\text{ox}}\text{-CO HydA1}$ selectively labeled with ^{57}Fe at the $[2\text{Fe}]_{\text{H}}$ subunit measured at 160 K. Shown here is the second possible simulation 2. Simulation 1 is shown in Figure 4B in the main text.

Nuclear resonance vibrational spectroscopy (NRVS)

NRVS spectra are used to identify the vibrational modes associated with all ^{57}Fe sites. Fe-CN modes are generally found in the 400–500 cm^{-1} region of a NRVS spectrum. The NRVS spectrum for $(\text{Et}_4\text{N})_2[^{57}\text{Fe}_2(\text{adt})(\text{CN})_2(\text{CO})_4]$ displays two clear features in this region at 415 and 434 cm^{-1} , and the NRVS spectrum of $[2^{57}\text{Fe}]_{\text{H}}$ HydA1 $\text{H}_{\text{ox}}\text{-CO}$ displays two features at 437 and 446 cm^{-1} . These features are assigned as Fe-CN modes and are the contributions from Fe-CN stretches and Fe-C-N bends. The clear blue shift of the Fe-CN modes upon incorporation of the precursor into the enzyme is indicative of either a strengthened Fe-CN bond, which increases the Fe-CN stretch energy, or a contribution from a higher energy Fe-C-N bend. As the $\nu_{\text{C}\equiv\text{N}}$ for $(\text{Et}_4\text{N})_2[^{57}\text{Fe}_2(\text{adt})(\text{CN})_2(\text{CO})_4]$ (2055 cm^{-1}) is lower in energy than the $\nu_{\text{C}\equiv\text{N}}$ for $\text{H}_{\text{ox}}\text{-CO}$ (2090 and 2082 cm^{-1} , see Figure S2) the Fe-CN bond should be weaker when incorporated into the enzyme. This would be consistent with the one electron oxidation upon insertion resulting in less π back-bonding from the metal into the π^* orbitals of the cyanide ligand. The higher Fe-CN mode energy must therefore be assigned to an increase in the energy of the Fe-C-N bends upon enzyme incorporation. The known hydrogen bonding of the cyanide ligands to the conserved lysine and serine residues in the enzyme active site (Lys358 and Ser232 in the $[\text{FeFe}]$ -hydrogenase from *Clostridium pasteurianum*, CpI)⁸ would explain this restriction and hence the energy increase in the Fe-CN modes.

Fe-CO modes are generally found in the 490–650 cm^{-1} region of an NRVS spectrum. The NRVS spectrum for $(\text{Et}_4\text{N})_2[^{57}\text{Fe}_2(\text{adt})(\text{CN})_2(\text{CO})_4]$ displays six peaks in the region of 490–650 cm^{-1} (at 516, 532, 576, 582, 603 and 653 cm^{-1} respectively). Fe-CO modes are at higher energy than the Fe-CN modes. This is as a result of strong π back-bonding from the iron to the π^* orbital of the carbonyl ligand resulting in the Fe-CO having a more linear symmetry and hence higher energy.⁹ The NRVS spectrum of $[2^{57}\text{Fe}]_{\text{H}}$ HydA1 $\text{H}_{\text{ox}}\text{-CO}$ displays seven features in this region at 500, 530, 548, 557, 574, 587 and 603 cm^{-1} . It is notable that the Fe-CO modes are (on average) red shifted upon incorporation of the precursor into the enzyme. This is consistent with a one electron oxidation of the $[2\text{Fe}]_{\text{H}}$ subcluster, which results in less π back-bonding from the metal into the π^* orbitals of the carbonyl ligand. It should also be noted that the redox change also causes a change in structure and symmetry of the molecule, thus causing the Fe-CO modes to red shift in the $\text{H}_{\text{ox}}\text{-CO}$ spectra. This was also observed in *Pyrococcus furiosus* D14C ferredoxin.¹⁰ Thus, the lines in the 500–600 cm^{-1} region correspond to symmetric and asymmetric stretching modes. The small features in the spectra at 557 and 587 cm^{-1} are representative of the in-plane and out-of-plane bending modes.

Fe-Fe (stretching and bending) bonds have previously been observed between 200–300 cm^{-1} for Fe-Fe model complexes, and $(\text{Et}_4\text{N})_2[^{57}\text{Fe}_2(\text{adt})(\text{CN})_2(\text{CO})_4]$ has a notable feature at 195 cm^{-1} . This feature is also observed in the $[^{57}\text{Fe}]_{\text{H}}$ HydA1 $\text{H}_{\text{ox}}\text{-CO}$ enzyme at 197 cm^{-1} .¹⁰ Features below 100 cm^{-1} are indicative of the Fe-S cluster torsional modes.¹¹

References

- [1] Winter, G.; Thompson, D. W.; Loehe, J. R., Iron(II) Halides. In *Inorg. Syn.*, John Wiley & Sons, Inc.: New York, **2007**; pp 99-104.
- [2] Stanley, J. L.; Rauchfuss, T. B.; Wilson, S. R., *Organometallics* **2007**, *26*, 1907-1911.
- [3] Li, H.; Rauchfuss, T. B., *J. Am. Chem. Soc.* **2002**, *124*, 726-727.
- [4] Siebel, J. F.; Adamska-Venkatesh, A.; Weber, K.; Rumpel, S.; Reijerse, E.; Lubitz, W., *Biochemistry* **2015**, *54*, 1474-1483.
- [5] Silakov, A.; Reijerse, E. J.; Albracht, S. P. J.; Hatchikian, E. C.; Lubitz, W., *J. Am. Chem. Soc.* **2007**, *129*, 11447-11458.
- [6] Pereira, A. S.; Tavares, P.; Moura, I.; Moura, J. J. G.; Huynh, B. H., *J. Am. Chem. Soc.* **2001**, *123*, 2771-2782.
- [7] Popescu, C. V.; Münck, E., *J. Am. Chem. Soc.* **1999**, *121*, 7877-7884.
- [8] Knörzer, P.; Silakov, A.; Foster, C. E.; Armstrong, F. A.; Lubitz, W.; Happe, T., *J. Biol. Chem.* **2012**, *287*, 1489-1499.
- [9] Kuchenreuther, J. M.; Guo, Y.; Wang, H.; Myers, W. K.; George, S. J.; Boyke, C. A.; Yoda, Y.; Alp, E. E.; Zhao, J.; Britt, R. D.; Swartz, J. R.; Cramer, S. P., *Biochemistry* **2012**, *52*, 818-826.
- [10] Mitra, D.; Pelmeshnikov, V.; Guo, Y.; Case, D. A.; Wang, H.; Dong, W.; Tan, M.-L.; Ichiye, T.; Jenney, F. E.; Adams, M. W. W.; Yoda, Y.; Zhao, J.; Cramer, S. P., *Biochemistry* **2011**, *50*, 5220-5235.
- [11] Cramer, S.; Xiao, Y.; Wang, H.; Guo, Y.; Smith, M., *Hyperfine Interact* **2006**, *170*, 45-54.

5 CONCLUSIONS & OUTLOOK

In this work, the heterologous protein overexpression in *E. coli* of the hydrogenase HydA1 and its natural electron donor PetF from *Chlamydomonas reinhardtii* were established and optimized for high yields. In the following, the proteins were investigated by different spectroscopic and biological methods.

The concept of the direct artificial maturation,⁸³ which was discovered in the period of this thesis, opens new possibilities to study [FeFe]-hydrogenases. For example, the incorporation of non-native cofactors into unmaturation HydA1 has been probed and the catalytic activity of the resulting artificial hydrogenases was determined with the aim to better understand the function of HydA1 (paper I).¹ In this work, 15 different synthetic iron complexes were tested for incorporation of which 10 could be successfully inserted. It could clearly be shown that small changes in the active site, e.g. substitution of one single atom, lead to a dramatic decrease of the catalytic H₂ conversion activity. It is concluded that by changing the binuclear [2Fe]-subsite, the perfect interplay between the cofactor and the protein surrounding is disrupted. Since the enzymes have developed and evolved over millions of years, this result is not surprising. Hence, engineering of the [2Fe]-subsite alone is not a promising approach for improving hydrogenase activity. Clearly, a concerted strategy changing the cofactor in combination with alterations of the amino acid surrounding is necessary.

The direct artificial maturation also opens the possibility to produce native-like HydA1 specifically isotope-labeled. The power of the method is shown in paper IV:⁴ incorporation of [⁵⁷Fe₂(adt)(CN)₂(CO)₄]²⁻ into unmaturation HydA1 introduces ⁵⁷Fe into the protein. The labeling allows investigations at the central nuclei by various spectroscopic techniques like Mössbauer, NRVs, ENDOR and HYSCORE. Furthermore, the second H-cluster component, the [4Fe-4S]-cluster, was successfully ⁵⁷Fe-labeled. Paper IV⁴ demonstrates the selective labeling for one enzyme state, but it can be expanded to any other state. Apart from

⁵⁷Fe labeling, it is possible to label the active site with ¹³C and ¹⁵N.^{96,113} These investigations help to yield better insight into the electronic structures of the catalytic intermediates.

Paper II² and III³ focus on *in vivo* engineering approaches to enhance H₂ production activity in *Chlamydomonas reinhardtii*. *In vivo*, hydrogenase activity is diminished, because electrons, which are necessary for H₂ production, are delivered from the natural electron donor PetF mainly to FNR, not to HydA1. Weakening the FNR-PetF interaction could lead to an increased H₂ production of HydA1. Indeed, by identification and substitution of amino acid residues of PetF that are only important for FNR binding, an increased catalytic activity of HydA1 in the presence of FNR was achieved in a light-dependent H₂ production assay (paper II).² Due to a lack of crystal structures of *C. reinhardtii* PetF and the PetF-HydA1 complex, other ways must be found to investigate the PetF-HydA1 interaction. Therefore, a PetF NMR solution structure was determined. Furthermore, by substitution of the paramagnetic irons in PetF, which impede NMR spectroscopic investigations, with diamagnetic gallium, the whole PetF-HydA1 interface was identified. This served as basis for the calculation of a PetF-HydA1 docking model (paper III).³ The results presented in paper II and paper III provide the possibility to a knowledge based amino acid substitution in PetF that lead to an increased *in vivo* H₂ production rate of HydA1. Combined with other metabolic engineering approaches, *e.g.* modified *C. reinhardtii* strains, this knowledge can be used as basis for the design of H₂-producing organisms. In principle, *C. reinhardtii* is a suitable choice for an H₂-producing organisms since it photosynthetically produces H₂ and since it is a widely used model organism⁵³ of which the complete nuclear genome sequence is known.¹¹⁴ However, a limiting factor is that *C. reinhardtii* remains a difficult platform for conducting genetic alterations, because there is still a lack of tools for targeted gene insertion in green algae.¹¹⁵ Therefore, further developments in the microbiological field are necessary in order to apply the gained knowledge to increase biological hydrogen production in *C. reinhardtii*.

In summary, engineering an H₂-producing organism has the advantage over using the isolated hydrogenase as catalyst that improving the H₂ production activity *in vitro* seems more difficult. Furthermore, the high oxygen sensitivity of the hydrogenase causes problems. Even though the hydrogenase within the organism is also oxygen sensitive, it is more protected than the isolated hydrogenase. Additionally, the isolated hydrogenase is irreversibly damaged by oxygen, whereas in the organism, there can be repair mechanisms or an upregulated hydrogenase production. On the other hand, systems can be developed that protect the isolated hydrogenase. In 2014, Plumeré *et al.* showed that a specifically designed viologen-based redox polymer can protect hydrogenases from oxygen damage.¹¹⁶ Based on the detailed enzymatic understanding of hydrogenases, another possibility for future H₂ production is the development of chemical bioinspired models as catalysts.^{60,117}

Altogether, there has been good progress in understanding hydrogenases, but for a technological, large-scale application, still further development is necessary.

6 REFERENCES

- [1] Siebel, J. F.; Adamska-Venkatesh, A.; Weber, K.; Rumpel, S.; Reijerse, E.; Lubitz, W. *Biochemistry* **2015**, *54*, 1474.
- [2] Rumpel, S.; Siebel, J. F.; Fares, C.; Duan, J.; Reijerse, E.; Happe, T.; Lubitz, W.; Winkler, M. *Energ. Environ. Sci.* **2014**, *7*, 3296.
- [3] Rumpel, S.; Siebel, J. F.; Diallo, M.; Farès, C.; Reijerse, E. J.; Lubitz, W. *ChemBioChem* **2015**, accepted, DOI: 10.1002/cbic.201500130.
- [4] Gilbert-Wilson, R.; Siebel, J. F.; Adamska-Venkatesh, A.; Pham, C. C.; Reijerse, E.; Wang, H.; Cramer, S. P.; Lubitz, W.; Rauchfuss, T. B. *J. Am. Chem. Soc.* **2015**, accepted, DOI: 10.1021/jacs.5b03270.
- [5] Tertzakian, P. *A Thousand Barrel a Second*; McGraw-Hill: New York, **2006**.
- [6] Armaroli, N.; Balzani, V. *Angew. Chem. Int. Edit.* **2007**, *46*, 52.
- [7] Lubitz, W.; Reijerse, E.; van Gastel, M. *Chem. Rev.* **2007**, *107*, 4331.
- [8] Armaroli, N.; Balzani, V. *Energ. Environ. Sci.* **2011**, *4*, 3193.
- [9] Cook, T. R.; Dogutan, D. K.; Reece, S. Y.; Surendranath, Y.; Teets, T. S.; Nocera, D. *G. Chem. Rev.* **2010**, *110*, 6474.
- [10] Lewis, N. S.; Nocera, D. G. *P. Natl. Acad. Sci.* **2006**, *103*, 15729.
- [11] Armaroli, N.; Balzani, V. *ChemSusChem* **2011**, *4*, 21.
- [12] Crabtree, G. W.; Dresselhaus, M. S. *MRS Bulletin* **2008**, *33*, 421.
- [13] Olah, G.; Goeppert, A.; Prakash, G. K. S. *Beyond Oil and Gas: The Methanol Economy*; Wiley-VCH Verlag GmbH & Co. KGaA: Weinheim, **2006**.
- [14] Service, R. F. *Science* **2007**, *315*, 172.
- [15] Gordon, R. B.; Bertram, M.; Graedel, T. E. *P. Natl. Acad. Sci. USA* **2006**, *103*, 1209.
- [16] Karamanolis, S. *Wasserstoff – Energieträger der Zukunft*; Elektra Verlags-GmbH: München, **2001**.
- [17] Melis, A.; Happe, T. *Plant Physiol.* **2001**, *127*, 740.
- [18] Lubitz, W.; Ogata, H.; Rüdiger, O.; Reijerse, E. *Chem. Rev.* **2014**, *114*, 4081.
- [19] Vignais, P. M.; Billoud, B.; Meyer, J. *FEMS Microbiol. Rev.* **2001**, *25*, 455.
- [20] Tamagnini, P.; Axelsson, R.; Lindberg, P.; Oxelfelt, F.; Wünschiers, R.; Lindblad, P. *Microbiol. Mol. Biol. R.* **2002**, *66*, 1.
- [21] Vignais, P. M.; Billoud, B. *Chem. Rev.* **2007**, *107*, 4206.
- [22] Fontecilla-Camps, J. C.; Volbeda, A.; Cavazza, C.; Nicolet, Y. *Chem. Rev.* **2007**, *107*, 4273.
- [23] Shima, S.; Thauer, R. K. *Chem. Rec.* **2007**, *7*, 37.

- [24] Thauer, R. K.; Klein, A. R.; Hartmann, G. C. *Chem. Rev.* **1996**, *96*, 3031.
- [25] Frey, M. *ChemBioChem* **2002**, *3*, 153.
- [26] Adams, M. W. W. *BBA - Bioenergetics* **1990**, *1020*, 115.
- [27] Lenz, O.; Ludwig, M.; Schubert, T.; Bürstel, I.; Ganskow, S.; Goris, T.; Schwarze, A.; Friedrich, B. *ChemPhysChem* **2010**, *11*, 1107.
- [28] Huynh, B. H.; Czechowski, M. H.; Krüger, H. J.; DerVartanian, D. V.; Peck, H. D.; LeGall, J. P. *Natl. Acad. Sci.* **1984**, *81*, 3728.
- [29] Adams, M. W.; Mortenson, L. E. *J. Biol. Chem.* **1984**, *259*, 7045.
- [30] Peters, J. W.; Lanzilotta, W. N.; Lemon, B. J.; Seefeldt, L. C. *Science* **1998**, *282*, 1853.
- [31] Nicolet, Y.; de Lacey, A. L.; Vernède, X.; Fernandez, V. M.; Hatchikian, E. C.; Fontecilla-Camps, J. C. *J. Am. Chem. Soc.* **2001**, *123*, 1596.
- [32] Lemon, B. J.; Peters, J. W. *Biochemistry* **1999**, *38*, 12969.
- [33] Pierik, A. J.; Hulstein, M.; Hagen, W. R.; Albracht, S. P. J. *Eur. J. Biochem.* **1998**, *258*, 572.
- [34] Silakov, A.; Kamp, C.; Reijerse, E.; Happe, T.; Lubitz, W. *Biochemistry* **2009**, *48*, 7780.
- [35] Silakov, A.; Reijerse, E. J.; Albracht, S. P. J.; Hatchikian, E. C.; Lubitz, W. *J. Am. Chem. Soc.* **2007**, *129*, 11447.
- [36] Pereira, A. S.; Tavares, P.; Moura, I.; Moura, J. J. G.; Huynh, B. H. *J. Am. Chem. Soc.* **2001**, *123*, 2771.
- [37] Kuchenreuther, J. M.; Guo, Y.; Wang, H.; Myers, W. K.; George, S. J.; Boyke, C. A.; Yoda, Y.; Alp, E. E.; Zhao, J.; Britt, R. D.; Swartz, J. R.; Cramer, S. P. *Biochemistry* **2012**, *52*, 818.
- [38] Chernev, P.; Lambertz, C.; Brünje, A.; Leidel, N.; Sigfridsson, K. G. V.; Kositzki, R.; Hsieh, C.-H.; Yao, S.; Schiwon, R.; Driess, M.; Limberg, C.; Happe, T.; Haumann, M. *Inorg. Chem.* **2014**, *53*, 12164.
- [39] Vincent, K. A.; Parkin, A.; Armstrong, F. A. *Chem. Rev.* **2007**, *107*, 4366.
- [40] Siegbahn, P. E. M.; Tye, J. W.; Hall, M. B. *Chem. Rev.* **2007**, *107*, 4414.
- [41] Adamska, A.; Silakov, A.; Lambertz, C.; Rüdiger, O.; Happe, T.; Reijerse, E.; Lubitz, W. *Angew. Chem. Int. Edit.* **2012**, *51*, 11458.
- [42] Schütz, K.; Happe, T.; Troshina, O.; Lindblad, P.; Leitão, E.; Oliveira, P.; Tamagnini, P. *Planta* **2004**, *218*, 350.
- [43] Happe, T.; Naber, J. D. *Eur. J. Biochem.* **1993**, *214*, 475.

- [44] Melis, A.; Zhang, L.; Forestier, M.; Ghirardi, M. L.; Seibert, M. *Plant Physiol.* **2000**, *122*, 127.
- [45] Happe, T.; Hemschemeier, A.; Winkler, M.; Kaminski, A. *Trends Plant Sci.* **2002**, *7*, 246.
- [46] Winkler, M.; Hemschemeier, A.; Gotor, C.; Melis, A.; Happe, T. *Int. J. Hydrogen Ener.* **2002**, *27*, 1431.
- [47] Kennedy, R. A.; Rumpho, M. E.; Fox, T. C. *Plant Physiol.* **1992**, *100*, 1.
- [48] Hemschemeier, A.; Happe, T. *BBA - Bioenergetics* **2011**, *1807*, 919.
- [49] Happe, T.; Mosler, B.; Naber, J. D. *Eur. J. Biochem.* **1994**, *222*, 767.
- [50] Fukuyama, K. *Photosynth. Res.* **2004**, *81*, 289.
- [51] Winkler, M.; Kuhlger, S.; Hippler, M.; Happe, T. *J. Biol. Chem.* **2009**, *284*, 36620.
- [52] Medina, M.; Gomez-Moreno, C. *Photosynth. Res.* **2004**, *79*, 113.
- [53] Harris, E. H. *Ann. Rev. Plant Phys.* **2001**, *52*, 363.
- [54] Happe, T.; Kaminski, A. *Eur. J. Biochem.* **2002**, *269*, 1022.
- [55] Mulder, D. W.; Boyd, E. S.; Sarma, R.; Lange, R. K.; Endrizzi, J. A.; Broderick, J. B.; Peters, J. W. *Nature* **2010**, *465*, 248.
- [56] Pandey, A. S.; Harris, T. V.; Giles, L. J.; Peters, J. W.; Szilagyi, R. K. *J. Am. Chem. Soc.* **2008**, *130*, 4533.
- [57] Knörzer, P.; Silakov, A.; Foster, C. E.; Armstrong, F. A.; Lubitz, W.; Happe, T. *J. Biol. Chem.* **2012**, *287*, 1489.
- [58] Nicolet, Y.; Piras, C.; Legrand, P.; Hatchikian, C. E.; Fontecilla-Camps, J. C. *Structure* **1999**, *7*, 13.
- [59] Tard, C.; Pickett, C. J. *Chem. Rev.* **2009**, *109*, 2245.
- [60] Simmons, T. R.; Berggren, G.; Bacchi, M.; Fontecave, M.; Artero, V. *Coordin. Chem. Rev.* **2014**, *270–271*, 127.
- [61] Le Cloirec, A.; C. Davies, S.; J. Evans, D.; L. Hughes, D.; J. Pickett, C.; P. Best, S.; Borg, S. *Chem. Commun.* **1999**, 2285.
- [62] Lyon, E. J.; Georgakaki, I. P.; Reibenspies, J. H.; Darensbourg, M. Y. *Angew. Chem. Int. Edit.* **1999**, *38*, 3178.
- [63] Schmidt, M.; Contakes, S. M.; Rauchfuss, T. B. *J. Am. Chem. Soc.* **1999**, *121*, 9736.
- [64] Li, H.; Rauchfuss, T. B. *J. Am. Chem. Soc.* **2002**, *124*, 726.
- [65] Song, L.-C.; Yang, Z.-Y.; Bian, H.-Z.; Hu, Q.-M. *Organometallics* **2004**, *23*, 3082.
- [66] Camara, J. M.; Rauchfuss, T. B. *Nat. Chem.* **2012**, *4*, 26.

- [67] Felton, G. A. N.; Mebi, C. A.; Petro, B. J.; Vannucci, A. K.; Evans, D. H.; Glass, R. S.; Lichtenberger, D. L. *J. Organomet. Chem.* **2009**, *694*, 2681.
- [68] Beyler, M.; Ezzaher, S.; Karnahl, M.; Santoni, M.-P.; Lomoth, R.; Ott, S. *Chem. Commun.* **2011**, *47*, 11662.
- [69] Shepard, E. M.; Mus, F.; Betz, J. N.; Byer, A. S.; Duffus, B. R.; Peters, J. W.; Broderick, J. B. *Biochemistry* **2014**, *53*, 4090.
- [70] Broderick, J.; Byer, A.; Duschene, K.; Duffus, B.; Betz, J.; Shepard, E.; Peters, J. *J. Biol. Inorg. Chem.* **2014**, *19*, 747.
- [71] Johnson, D. C.; Dean, D. R.; Smith, A. D.; Johnson, M. K. *Annu. Re. Biochem.* **2005**, *74*, 247.
- [72] Peters, J. W.; Szilagyi, R. K.; Naumov, A.; Douglas, T. *FEBS Letters* **2006**, *580*, 363.
- [73] Posewitz, M. C.; King, P. W.; Smolinski, S. L.; Zhang, L.; Seibert, M.; Ghirardi, M. L. *J. Biol. Chem.* **2004**, *279*, 25711.
- [74] Driesener, R. C.; Challand, M. R.; McGlynn, S. E.; Shepard, E. M.; Boyd, E. S.; Broderick, J. B.; Peters, J. W.; Roach, P. L. *Angew. Chem. Int. Edit.* **2010**, *49*, 1687.
- [75] Shepard, E. M.; McGlynn, S. E.; Bueling, A. L.; Grady-Smith, C. S.; George, S. J.; Winslow, M. A.; Cramer, S. P.; Peters, J. W.; Broderick, J. B. *P. Natl. Acad. Sci.* **2010**.
- [76] Czech, I.; Silakov, A.; Lubitz, W.; Happe, T. *FEBS Letters* **2009**, *584*, 638.
- [77] McGlynn, S. E.; Shepard, E. M.; Winslow, M. A.; Naumov, A. V.; Duschene, K. S.; Posewitz, M. C.; Broderick, W. E.; Broderick, J. B.; Peters, J. W. *FEBS Letters* **2008**, *582*, 2183.
- [78] Kuchenreuther, J. M.; Myers, W. K.; Suess, D. L. M.; Stich, T. A.; Pelmeshnikov, V.; Shiigi, S. A.; Cramer, S. P.; Swartz, J. R.; Britt, R. D.; George, S. J. *Science* **2014**, *343*, 424.
- [79] Berggren, G.; Adamska, A.; Lambertz, C.; Simmons, T. R.; Esselborn, J.; Atta, M.; Gambarelli, S.; Mouesca, J. M.; Reijerse, E.; Lubitz, W.; Happe, T.; Artero, V.; Fontecave, M. *Nature* **2013**, *499*, 66.
- [80] Roseboom, W.; de Lacey, A. L.; Fernandez, V. M.; Hatchikian, E. C.; Albracht, S. P. *J. J. Biol. Inorg. Chem.* **2006**, *11*, 102.
- [81] Bethel, R. D.; Darensbourg, M. Y. *Nature* **2013**, *499*, 40.
- [82] Schilter, D.; Rauchfuss, T. B. *Angew. Chem. Int. Edit.* **2013**, *52*, 13518.
- [83] Esselborn, J.; Lambertz, C.; Adamska-Venkatesh, A.; Simmons, T.; Berggren, G.; Noth, J.; Siebel, J.; Hemschemeier, A.; Artero, V.; Reijerse, E.; Fontecave, M.; Lubitz, W.; Happe, T. *Nat. Chem. Biol.* **2013**, *9*, 607.

- [84] Roy, S.; Jones, A. K. *Nat. Chem. Biol.* **2013**, *9*, 603.
- [85] Adamska-Venkatesh, A.; Krawietz, D.; Siebel, J.; Weber, K.; Happe, T.; Reijerse, E.; Lubitz, W. *J. Am. Chem. Soc.* **2014**, *136*, 11339.
- [86] Lee, S. Y. *Trends Biotechnol.* **1996**, *14*, 98.
- [87] Shiloach, J.; Fass, R. *Biotechnol. Adv.* **2005**, *23*, 345.
- [88] Schmidt, T. G. M.; Skerra, A. *Nat. Protocols* **2007**, *2*, 1528.
- [89] Kuchenreuther, J. M.; Grady-Smith, C. S.; Bingham, A. S.; George, S. J.; Cramer, S. P.; Swartz, J. R. *ONE* **2010**, *5*, 15491.
- [90] Lottspeich, F.; Zorbas, H. *Bioanalytik*; Spektrum Akademischer Verlag: Heidelberg, Berlin, **1998**.
- [91] Weidlein, J.; Müller, U.; K., D. *Schwingungsspektroskopie*; Thieme Verlag: Stuttgart, New York, **1988**.
- [92] Chemical Department, U. o. C. B. *The Handbook for Organic Chemistry Lab, Online edition: Chapter 15, Infrared Spectroscopy: Theory* Boulder, **2002**.
- [93] Clayden, J.; Greeves, N.; Warren, S.; Wothers, P. *Organic Chemistry*; Oxford University Press: Oxford, New York, **2001**.
- [94] Barth, A. *BBA - Bioenergetics* **2007**, *1767*, 1073.
- [95] Pierik, A. J.; Roseboom, W.; Happe, R. P.; Bagley, K. A.; Albracht, S. P. J. *J. Biol. Inorg. Chem.* **1999**, *274*, 3331.
- [96] Adamska-Venkatesh, A.; Simmons, T. R.; Siebel, J. F.; Artero, V.; Fontecave, M.; Reijerse, E.; Lubitz, W. *Phys. Chem. Chem. Phys.* **2015**, *17*, 5421.
- [97] Marion, D. *Mol. Cell. Proteomics* **2013**.
- [98] Bax, A.; Grzesiek, S. *Acc. Chem. Res.* **1993**, *26*, 131.
- [99] Que, L. *Physical Methods in Bioinorganic Chemistry*; University Science Books: Sausalito, **2000**.
- [100] Atherton, N. M. *Principles of electron spin resonance*; Ellis Horwood PTR Prentice Hall: New York, **1993**.
- [101] Gülich, P.; Bill, E.; Trautwein, A. X. *Mössbauer Spectroscopy and Transition Metal Chemistry*; Springer: Heidelberg, **2011**.
- [102] Schünemann, V.; Winkler, H. *Rep. Prog. Phys.* **2000**, *63*, 263.
- [103] Pandelia, M.-E.; Lanz, N. D.; Booker, S. J.; Krebs, C. *BBA – Mol. Cell Res.* **2015**.
- [104] Melis, A.; Happe, T. *Photosynth. Res.* **2004**, *80*, 401.
- [105] Sun, Y.; Chen, M.; Yang, H.; Zhang, J.; Kuang, T.; Huang, F. *Int. J. Hydrogen Ener.* **2013**, *38*, 16029.

-
- [106] Decottignies, P.; Flesch, V.; Gérard-Hirne, C.; Le Maréchal, P. *Plant Physiol.* **2003**, *41*, 637.
- [107] Mulder, David W.; Shepard, Eric M.; Meuser, Jonathan E.; Joshi, N.; King, Paul W.; Posewitz, Matthew C.; Broderick, Joan B.; Peters, John W. *Structure* **2011**, *19*, 1038.
- [108] Sybirna, K.; Ezanno, P.; Baffert, C.; Léger, C.; Bottin, H. *Int. J. Hydrogen Ener.* **2013**, *38*, 2998.
- [109] Sybirna, K.; Bottin, H. *Int. J. Hydrogen Ener.* **2013**, *38*, 13164.
- [110] Volkov, A. N.; Bashir, Q.; Worrall, J. A. R.; Ullmann, G. M.; Ubbink, M. *J. Am. Chem. Soc.* **2010**, *132*, 11487.
- [111] Popescu, C. V.; Münck, E. *J. Am. Chem. Soc.* **1999**, *121*, 7877.
- [112] Rusnak, F. M.; Adams, M. W.; Mortenson, L. E.; Münck, E. *J. Biol. Chem.* **1987**, *262*, 38.
- [113] Adamska-Venkatesh, A.; Simmons, T. R.; Siebel, J. F.; Souvik, R.; Artero, V.; Fontecave, M.; Reijerse, E.; Lubitz, W. *J. Am. Chem. Soc.* **2015**, submitted.
- [114] Merchant, S. S.; Prochnik, S. E.; Vallon, O.; Harris, E. H.; Karpowicz, S. J.; Witman, G. B.; Terry, A.; Salamov, A.; Fritz-Laylin, L. K. *et al. Science* **2007**, *318*, 245.
- [115] Dubini, A.; Ghirardi, M. *Photosynth. Res.* **2015**, *123*, 241.
- [116] Plumeré, N.; Rüdiger, O.; Oughli, A. A.; Williams, R.; Vivekananthan, J.; Pöller, S.; Schuhmann, W.; Lubitz, W. *Nat. Chem.* **2014**, *6*, 822.
- [117] Artero, V.; Fontecave, M. *Coordin. Chem. Rev.* **2005**, *249*, 1518.

7 ACKNOWLEDGEMENTS

This thesis could not have been realized without the help of many people. I am deeply grateful for all of them:

- Prof. Wolfgang Lubitz for giving me the opportunity to work at the Max Planck Institute for Chemical Energy Conversion, to attend conferences and workshops, and for his constant support.
- Prof. Karl-Erich Jaeger for being my second supervisor as he is for so many of us from Mülheim.
- Dr. Edward Reijerse for his supervision, constant support, helpful discussions and for his patience and help in correcting and improving manuscripts and this thesis.
- Dr. Sigrun Rumpel for her supervision and guidance, especially in the early years of this thesis, for support, nice teamwork, manuscript and thesis corrections and helpful discussions.
- Dr. Katharina Weber and Dr. Agnieszka Adamska-Venkatesh for a fantastic teamwork. I wish I had co-workers like them all my life long.
- Dr. Eckhard Bill for giving me his time to explain Mössbauer spectroscopy and to discuss my projects.
- Julian Esselborn, Dr. Martin Winkler and Prof. Thomas Happe from the Ruhr University Bochum for introducing me to my hydrogenase HydA1, helpful discussions, a nice time in Szeged and shared publications.
- Dr. David Schilter, Dr. Ryan Gilbert-Wilson and Prof. Thomas Rauchfuss from the University of Illinois for the great synthetic work they did, which was the basis for very interesting projects, and for nice communication over the ocean.
- Cindy Pham, Dr. Hongxin Wang and Prof. Stephen Cramer from the University of California for realizing the NRVS project.

- Mamou Diallo for working in the laboratory for me for five months, doing a great job.
- Julian Jakobs, Agnes Stoer and Annika Gurowski for all the work they did for me. Without them, I would not have been able to work on so many different projects.
- Bernd Mienert not only for taking care of all my Mössbauer samples, but also for giving me the opportunity to participate in dragon boat races.
- Dr. James Birrell for general discussions and help in the English language.
- Norbert Dickmann for measuring all my samples in mass spectrometry.
- Gabriele Schmitz and Miriam Frenzer for constant help in gas chromatography.
- Michael Reus for advising me in UV/Vis spectrometers.
- Michael Reus, Yvonne Brandenburger and Patricia Malkowski for all the things they take care about and for any kind of help in the biochemistry laboratory.
- Birgit Deckers for always helping me in graphic design.
- Rita Gröver for any organization issues and for submitting manuscripts.
- The whole Lubitz group, especially Dr. Agnieszka Adamska-Venkatesh and Ania Nalepa, and the biochemistry laboratory for the enjoyable time at the institute.

Apart from all the help and support in the institute, there are many other people that contributed indirectly to realize this thesis. I want to thank my MPI friends for a great time we had together and permanent support, encouragements and much, much more. I also want to thank all my other friends. Although they are not in Mülheim, they are always present and a constant support. I'm thankful to my boyfriend for giving me the opportunity to discover special places on the world and for the time we shared. My deepest gratitude goes to my whole family, first of all to my parents, to my brothers including family, to my aunt and finally to my grandparents. They all supported me constantly.